The Influence of Overburden on Quantitative Time-Lapse Seismic Interpretation

Fabian Domes

Submitted for the Degree of Doctor of Philosophy

Institute of Petroleum Engineering
Heriot-Watt University

March 2010

Abstract

Time-lapse seismic data quality has improved over the past decade, which makes dynamic interpretation of the reservoir changes possible. To push the limits of this technique further, this thesis studies the time-lapse seismic noise generated by overburden heterogeneities, as well as its influence on quantitative seismic interpretation. This is done by testing the accuracy of a multi-attribute pressure and saturation inversion method in this context to gain insight into its performance in the case of seismic acquisitions not being perfectly repeated. Extensive seismic modelling studies are conducted in order to quantify the accumulated error for three different overburden complexities.

Channels in the overburden above the Nelson Field, North Sea, are found to cause errors in the time-lapse amplitudes. The magnitude of these amplitude errors decreases with increased repeatability of the monitor survey's source and receiver positions. On average, saturation change is estimated to an accuracy of less than 6% when affected by amplitude errors only. However, these mean errors significantly increase to more than 20% if the residual time shifts caused by the channels are not removed from the seismic data. Moreover, the maximum saturation change estimation error can exceed the production induced signal locally. In addition, a major finding of this study is that the shape of the channel in conjunction with the acquisition direction has a significant impact on the spatial distribution of the errors at the reservoir level. It is also shown that the commonly used repeatability measures of NRMS or $\Delta Source + \Delta Receiver$ do not correlate well with the spatial distribution of areas with increased saturation change estimation error.

Consequently, a layer stripping method is presented which reduces the amplitude errors caused by the overburden channel and the acquisition non-repeatability by a factor of two. Nevertheless, the limits of using post-stack data to invert for time-lapse changes become apparent and, as a result, it is strongly advised to do further research into applying this method to pre-stack seismic data.

Production-induced amplitude changes inside the stacked reservoirs of a deepwater West of Africa field constitute the second overburden complexity studied. These changes imprint on the lower reservoir channel and reduce the time-lapse amplitude change locally by up to 42%. Furthermore, time-lapse amplitude errors are as large as 38% in case that the velocity change inside the upper reservoir is not included in the monitor migration velocity model. In addition, an important conclusion of this study is that due to the high frequency assumption ray-tracing based seismic modelling does not perform well for cellular models such as this West of Africa example. Finite-difference modelling methods are strongly advised to be used instead.

Finally, the effect of overburden changes above the highly compacting Ekofisk chalk reservoir, North Sea, is investigated by combining reservoir simulation, geomechanical and ray-tracing models. The velocity change of the overburden rocks reduces the time-lapse amplitudes at the top reservoir predominantly in the zone of vertical displacements greater than six metres. In this zone, the mean time-lapse amplitude errors in the full and far offset stack data are 9.4% and 4.23%, respectively. These errors decrease below 2.3% in areas of less than six metres vertical displacement. Consequently, the full and far offset stack amplitudes are not suited for quantitative time-lapse interpretation. The time-lapse amplitudes for the near and mid offset stacks are significantly less affected and the mean errors are smaller than 1.5% across the entire reservoir. Therefore, these two partial stacks are recommended for quantitative time-lapse interpretation.

Three different overburden complexities in the North Sea and West of Africa are studied and prove to have a measurable impact on the time-lapse amplitudes. It is shown that these errors affect the ability to estimate the saturation change and in a way that is not entirely predictable from inferences using commonly used repeatability measures.

To my loved ones

There is no such thing as a long piece of work, except one that you dare not start.

Charles-Pierre Baudelaire, 1821-1867

Acknowledgements

That is it? Done? At the beginning it seemed such a long journey and now I should stop walking? The only thing that remains is to say thank you to all the great people that joined me during the past years and provided me support whenever I lost directions.

First I would like to express my gratitude to Colin MacBeth for his supervision, his comments on my work and that he truly kept me outside my comfort zone. However, looking back I can tell that I also truly enjoyed it and I would not have come to an end without his support. Many thanks go to Ingo Pecher for being my co-supervisor and making valuable comments from a different perspective. I am grateful to David Johnston and Patrick Corbett for reading and evaluating this thesis. As an Ian Jack/BP Amoco Scholarship recipient I would like to express my sincere thanks to Ian Jack and the SEG Foundation for supporting my study. I would also like to thank Michael Payne for making my internship at the ExxonMobil Upstream Research Company possible. Many thanks for all the help also goes to the members of the Quantitative Interpretation group at the URC.

Thanks to all the ETLP research students I met during the past years for discussing questions about science, software applications and the most efficient way to code programs.

Many friends kept me going through the hard times:
Philippa, I owe you a debt of gratitude for editing and correcting my English during the past months.
Suzannah, I miss the smoko times and the Danish pastry on weekends.
Andy, thank you for the pragmatic suggestions on research.

Uli, your never-ending stream of emails containing the most useless links of the world wide web was a great source of distraction.
Niki, I will always be thankful for your motivation to keep on trucking and I often remember the good words of your dad you sent me: ”Few people fail because they aim too high and miss. Many fail because they aim too low and hit”.
Jürgen, thanks for calling late in the night and keep me from falling asleep in the office.
Sigi, you have a very unique attitude towards life - thanks for your inspiration.
Xenia, if there is someone who makes me smile then it is you, even during the hardest times. My greatest gratitude for your support and for convincing me to not give up in times all seemed to be unreachable. I cannot imagine the past two years without you.
Mami, Papi, I would not be at this point without your endless support. It is an invaluable feeling to know that whatever happens you are there for me - Ich hoffe dass ich euch eines Tages einen kleinen Teil eurer Liebe zurück geben kann.

ACADEMIC REGISTRY
Research Thesis Submission

Name*:*	Fabian Domes		
School/PGI:	Institute of Petroleum Engineering		
Version: *(i.e. First, Resubmission, Final)*	Final	Degree Sought (Award **and** Subject area)	Doctor of Philosophy (Petroleum Engineering)

Declaration

In accordance with the appropriate regulations I hereby submit my thesis and I declare that:

1) the thesis embodies the results of my own work and has been composed by myself
2) where appropriate, I have made acknowledgement of the work of others and have made reference to work carried out in collaboration with other persons
3) the thesis is the correct version of the thesis for submission and is the same version as any electronic versions submitted*.
4) my thesis for the award referred to, deposited in the Heriot-Watt University Library, should be made available for loan or photocopying and be available via the Institutional Repository, subject to such conditions as the Librarian may require
5) I understand that as a student of the University I am required to abide by the Regulations of the University and to conform to its discipline.

* *Please note that it is the responsibility of the candidate to ensure that the correct version of the thesis is submitted.*

Signature of Candidate*:*		Date:	

Submission

Submitted By *(name in capitals):*	
Signature of Individual Submitting:	
Date Submitted:	

For Completion in Academic Registry

Received in the Academic Registry by *(name in capitals):*			
Method of Submission *(Handed in to Academic Registry; posted through internal/external mail):*			
*E-thesis Submitted (**mandatory for final theses from January 2009**)*			
Signature:		Date:	

Table of Contents

List of Tables

List of Figures

List of Abbreviations

AVO	Amplitude versus Offset
b/d	Barrels per Day
CALM	Catenary anchor-leg mooring buoy
CMP	Common Mid Point
CNS	Central North Sea
DMO	Dip Moveout
EOR	Enhanced Oil Recovery
ETLP	Edinburgh-Time-Lapse-Project
FD	Finite-Difference
FE	Finite-Element
FFT	Fast Fourier Transform
FPSO	Floating production storage and offloading
GoM	Gulf of Mexico
GOR	Gas oil ratio
HPHT	High Pressure High Temperature
Mb/d	Thousand Barrels per Day
MMb/d	Million Barrels per Day
NMO	Normal Moveout
NRMS	Normalised Root Mean Square

NTG ..... Net to Gross

OOWC ..... Original Oil Water Contact

OWC ..... Oil Water Contact

PDF ..... Probability Density Function

PS ..... Pseudospectral

PSDM ..... Pre-stack Depth Migration

PSTM ..... Pre-stack Time Migration

RMS ..... Root Mean Square

SEGY ..... Seismic data exchange format

SNR ..... Signal to Noise ratio

TLP ..... Tension-leg platform

TWT ..... Two Way Traveltime

UKOOA ..... United Kingdom Offshore Operators Association

UTM ..... Universal Transverse Mercator

WAG ..... Water Alternating Gas

List of Symbols

mD	milliDarcy
$\mathbf{V_p}$	P-wave velocity
$\mathbf{V_s}$	S-wave velocity
$\mathbf{S_w}$	Water saturation
$\mathbf{S_o}$	Oil saturation
$\mathbf{\Delta S_o}$	Oil saturation change
$\mathbf{P}$	Pressure
$\boldsymbol{\rho}$	Density
$\boldsymbol{\Delta I}$	Impedance change
$\boldsymbol{c_v}$	Coefficient of variation
$\boldsymbol{\sigma}$	Standard deviation
Zbml	Depth below mud line
Z	Impedance

Publications

Domes, F., MacBeth, C., and Brain, J. (2009). The Influence of Overburden on Time-Lapse Saturation Interpretation. In *71th Mtg.*, page Y002, Amsterdam, Netherlands. Eur. Assn. Geosci. Eng.

Chapter 1

Introduction

This chapter provides an introduction to the overburden problem in time-lapse seismic. Various domains, such as the acquisition, overburden and processing domain, are discussed and linked together in order to emphasise their combined importance for quantitative time-lapse interpretation. The challenges in studying overburden effects are in turn outlined, followed by the main contribution of this work.

1.1 Time-lapse seismic

Time-lapse seismic has matured in the North Sea and is now on its way to being routinely applied around the world. A recent overview on time-lapse seismic monitoring applications is published by Staples et al. (2006b). The authors point out that time-lapse seismic studies have evolved into a routinely applied reservoir monitoring tool over the last decade. Indeed, the success stories are convincing. A broad range of reservoirs and enhanced oil recovery (EOR) projects report economic success using time-lapse seismic. Its value is proven for monitoring steam injection at heavy oil reservoirs (Sigit et al., 1999; Theune et al., 2003), as well as for monitoring water flood in the Draugen and Gannet field, offshore Norway, the benefits of which are shown by Koster et al. (2000). Monitoring the waterfront in the Draugen field proves successful, while in the case of the Gannet field time-lapse seismic leads to identifying undrained compartments and infill drill locations. Gas flood monitoring has also matured, at least in high porosity reservoirs such as Troll West (Eikeberg and Rigmor, 2002). Besides proving its value for extracting hydrocarbons time-lapse seismic monitoring is also successfully applied in monitoring CO_2 injection into a marine aquifer above the Sleipner West Field, Norwegian North Sea (Eiken et al., 2000). However, all these success stories have one thing in common: A long production time between baseline and monitor survey and/or favourable reservoir rock and fluid parameters. These conditions make it easier to separate the production-induced effects, such as the change in the reservoir's reflectivity, from the noise contained in the time-lapse data. However, there are also examples where time-lapse surveys are acquired within just a few months, such as the Valhall Field, North Sea (van Gestel et al., 2008) and the Marimba Field, West of Africa (David Johnston, ExxonMobil, personal communication).

Hence, the main idea behind time-lapse seismic is that the production of hydrocarbons changes the elastic parameters of the reservoir rock. These changes affect the reflection coefficient at the top or base of the reservoir, which is in turn observed, for example, as an amplitude change in the monitor seismic data. A common scenario is when water replaces oil and thus increases the impedance of the reservoir rock in the water flood area. Furthermore, pore pressure changes in the reservoir alter

the effective pressure and thus change the stiffness of the rock, which in turn leads to a change in seismic velocity and thus impedance. Another example is when a waterfront replaces the oil in a piston-like manner. The sharp contrast between the water saturated rock and the oil saturated rock can also be identified in the time-lapse data as the spatial movement of the original oil water contact (OOWC). A large time-lapse signal is therefore related to considerable changes in the reservoir, which is in turn often related to many years of reservoir production.

Nowadays, the increasing seismic data fidelity, faster turnaround times for monitor surveys and companies acquiring time-lapse seismic even over carbonate reservoirs are pushing the limit of what can be detected by time-lapse monitoring. However, the limiting factor for detecting subtle reservoir changes is the noise contained in the data. Calvert (2005a,b) points out that time shifts as low as 0.5ms could be observed in noise free time-lapse data. Such time shifts are caused, for example, by a moving oil water contact (OWC) or geomechanical changes in the reservoir. However, detecting those tiny shifts and identifying them as signal is only possible in an almost noise free environment. Therefore, reservoir changes that are well below the current noise level could be observed in theory if the seismic data quality could be increased and thus the noise level reduced. In order to test the limits of current time-lapse seismic quantitative interpretation it is of paramount importance to identify the various sources of time-lapse noise as well as their respective origin and magnitude.

1.2 Time-lapse seismic noise quantification

Kragh and Christie (2002) introduce the NRMS (Normalised Root Mean Square) measure to quantify the repeatability of two seismic traces and thus to assess the noise level in time-lapse seismic data. The NRMS is a metric to express the likeness of two seismic traces (Kragh and Christie, 2002) and to quantify the repeat common signal between such two traces. It is calculated by taking the RMS (Root Mean Square) of the difference of two traces from the baseline, $b(t)$, and monitor survey, $m(t)$, within a given time window $t \in [t_1, t_2]$, which is in turn normalised by the

average RMS of both input traces. It is normally expressed as a percentage value:

$$\text{NRMS} = \frac{200 \cdot RMS[m(t) - b(t)]}{RMS[m(t)] + RMS[b(t)]} \tag{1.1}$$

The NRMS measure ranges from 0% for identical traces to 141% for randomly uncorrelated traces, and up to 200% for 180° out of phase traces. It is very sensitive to small changes between the two input traces, whether it is in the amplitude or phase. Any change in the NRMS measure can be attributed to noise, if it is calculated in a zone where no changes are expected to happen between the baseline and monitor survey. Calvert et al. (2002) relate this noise to various origins:

- Additive uncorrelated noise
- Convolution noise due to locally different wavelets
- Buried statics, velocity variation, focusing and defocusing effects and scattering
- Seismic processing artifacts

It is therefore important that changes in the reservoir reflect in an NRMS measure greater than that outside the reservoir zone in order to detect a usable time-lapse signal.

Figure 1.1 outlines how NRMS noise levels, calculated outside the reservoir zone, decreased over the last decade. Obviously, NRMS repeatability measures are high for time-lapse studies using legacy baseline surveys, that is surveys that were acquired for exploration or structural interpretation purpose and not dedicated for time-lapse interpretation. This is evident for the Gullfaks field in the Norwegian North Sea that is produced for nine years (1986 - 1995) before the first time-lapse monitor survey is shot. The main drive mechanism at the Gullfaks field is water injection and WAG (water alternating gas) injection. A high NRMS value of 34% is observed after taking the difference between the monitor survey (1995) and baseline survey (1985) (Landrø et al., 1999). However, a feasibility study shows that replacing oil with water leads to a 40% reduction in reflection strength (Landrø et al., 1999),

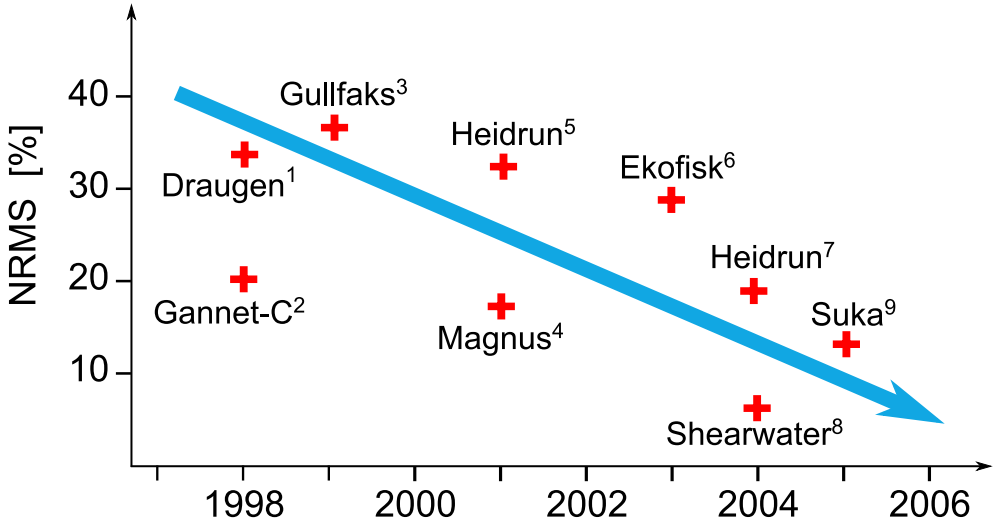

Figure 1.1: The evolution of NRMS values over the last decade. Examples from the North Sea. ([1]Koster et al. (2000); [2]Koster et al. (2000); [3]Landrø et al. (1999); [4]Ritchie et al. (2002); [5]Furre et al. (2003); [6]Byerley et al. (2006); [7]Furre et al. (2005); [7,8,9]Staples et al. (2007)). The x-axis indicates the time of the monitor survey being acquired. The blue arrow indicates the trend over the past years.

which is therefore sufficient to map changes of the original oil water contact at the top reservoir level despite this high NRMS measure of 34% outside the production zone.

Koster et al. (2000) report an NRMS level of 20% outside the reservoir at the Gannet-C field. The baseline survey is shot in 1993 and a monitor survey is subsequently acquired in 1998. The Gannet-C field is located at the edge of the North Sea Central Graben and consists of a thick oil rim with a gas cap at the top. The field's initial production is by aquifer drive and gas reinjection at the top. The main purpose of the time-lapse survey is to map the oil water contact movement to identify undrained fault blocks. In this case, the time-lapse seismic noise arises from the non-repeat source and receiver position of the monitor survey as well as from imaging problems due to the steep flanks around the salt dome (Staples et al., 2006a).

Another good example of high noise levels in earlier time-lapse studies is presented by Koster et al. (2000). The Draugen field is located in the Norwegian North Sea and has excellent reservoir properties (porosity 27%, net-to-gross ratio (NTG) 97%). Production is assisted by water injection to maintain the initial reservoir pressure.

Koster et al. (2000) report an NRMS level of 35% for a time-lapse monitor survey shot in 1998, eight years after the baseline survey is acquired. A similar high NRMS measure of 30% is reported for the Ekofisk field (Byerley et al., 2006) using a baseline survey from 1999 and a monitor survey shot in 2003. The oil production during that time is by water injection into the chalk reservoir rock. The high porosity chalk significantly compacts over the last decades of production, which leads to a complex time-lapse response due to amplitude and time differences at the top of the reservoir. Janssen et al. (2006a) show that the reservoir has to be produced for at least 48 months before oil saturation changes can be identified when there is an assumed NRMS level of 30% outside the reservoir zone.

The Heidrun field in the Norwegian North Sea consists of complex reservoir units of late Triassic to early/mid-Jurassic age. The main drainage strategy for the thick oil column of the Fangst group is by down flank water injection and gas reinjection at the top of the reservoir, to support the reservoir pressure (Furre et al., 2003). Time-lapse data acquired over the south flank of the Heidrun field reveal an NRMS level of 34% when using the baseline survey from 1986 and a monitor survey shot in 2001 (Furre et al., 2003). However, in this case the monitor survey is acquired using WesternGeco's Q-marine technology, where streamers are steered up to 3° against the natural feather (Eiken et al., 2002). A dramatic improvement in the noise level at the Heidrun field is seen after both baseline and monitor survey are acquired using steerable streamer technology (Q on Q acquisition). The Heidrun time-lapse study using Q on Q surveys shot in 2001 and 2004 significantly improves the NRMS repeatability measure to 21% (Furre et al., 2005).

Even greater improvement in the NRMS measure is reported from a time-lapse experiment carried out in 2001 over the Magnus field in the North Sea. Steerable streamer technology is again used, which reduces the NRMS measure in the overburden to 15% (Ritchie et al., 2002). Production from the Magnus Upper Jurassic sandstone reservoir is by a water alternating gas scheme. The key interpretation aim of the time-lapse study is the mapping of flow barriers and thin beds in the reservoir, which are below seismic resolution (Ritchie et al., 2002).

The latest reported time-lapse surveys have NRMS noise levels as low as 13%, for example, the Skua Field, North Sea (Staples et al., 2007). Moreover, the lowest NRMS measure reported in the literature to date is at the Shearwater field. Shell is operator of this high pressure high temperature (HPHT) field and claim an NRMS level of 7%, using a baseline survey shot in 2002 and a monitor survey shot in 2004 (Staples et al., 2007). The production from this deep North Sea field is by pressure depletion. The time-lapse signal is driven by the reservoir's compaction, thus causing time shifts between the baseline and monitor survey.

However, using just one NRMS value to describe an entire survey and thus the time-lapse seismic data quality is indeed a simplification. One has to bear in mind that the NRMS is not a unique measure, but depends on the time interval over which it is extracted from, the signal to noise ratio of the seismic data, as well as strength of the baseline reflectivity.

Therefore, the previous discussion is a simplified and qualitatively statement that the time-lapse NRMS level has steadily decreased over the past decade. This trend becomes evident in Figure 1.1 (blue arrow). The decrease in the NRMS measure is attributable to the improvements in acquisition repeatability, as well as to improved seismic data processing. The relation between the improved marine streamer acquisition technology (for example, steerable streamer, controlled source and better GPS positioning) and the decrease of noise levels in time-lapse seismic data is pointed out in this discussion. Therefore, it is important to have a closer look at the acquisition domain and how it actually affects the time-lapse noise level.

1.3 The seismic data acquisition domain

The preceding section shows that the time-lapse noise level, expressed as NRMS measure, is related to the acquisition technology, however not exclusively. To improve the time-lapse interpretability, the repeated survey should ideally match the acquisition geometry of the baseline survey. This means that the source- and receiver positions, the source signature and receiver responses should be repeated

exactly. In that way, changes in the seismic data can be attributed to changes in the subsurface and do not originate from any acquisition differences. This is an ideal world scenario, or better put in Rodney Calvert's words: "We should carefully repeat any problems we cannot solve" (Calvert and Wills, 2003). The following sections provide a more detailed view of the marine time-lapse acquisition and how it affects the time-lapse data quality.

1.3.1 Measuring the variation in marine acquisition geometry

The acquisition of seismic data in the marine environment is still dominated by the use of hydrophones and airguns towed behind seismic vessels. Hydrophones are attached to a cable, known as the streamer, and in turn, several streamers are placed parallel to each other to form a streamer swath (Figure 1.2, dotted lines). Thus, streamer recording provides a narrow three-dimensional coverage. Streamers are usually between 3000m and 5000m long, depending on the depth of the target to be imaged. When this shot and receiver configuration is towed behind the seismic vessel, ocean currents deviate the streamers from their pre-defined straight line (Figure 1.2). Such ocean currents vary in strength and direction either randomly or with predictable (seasonal) patterns. At the time the monitor seismic data are acquired, using marine streamer technology, ocean currents can be significantly different to the ones prevailing during the baseline acquisition. Consequently, streamers are deviated in a different direction compared to the baseline survey (Figure 1.2). The maximum streamer feathering is up to $\pm 10^{\circ}$ for typical North Sea surveys, with approximately 95% of the survey having a feathering within $\pm 6^{\circ}$ (Eiken et al., 2003a). In areas of strong ocean currents, such as the Gulf of Mexico, streamer feathering is as high as $\pm 15^{\circ}$ (Tura et al., 2005).

An absolute reference position is needed for each source and receiver in order to quantify the amount of streamer deviation compared to the pre-defined line as well as in between successive surveys. The positions of the seismic source as well as the front-, mid- and end position of each streamer are recorded using differential GPS measurements. These measurements are highly accurate within ± 2m (Kommedal

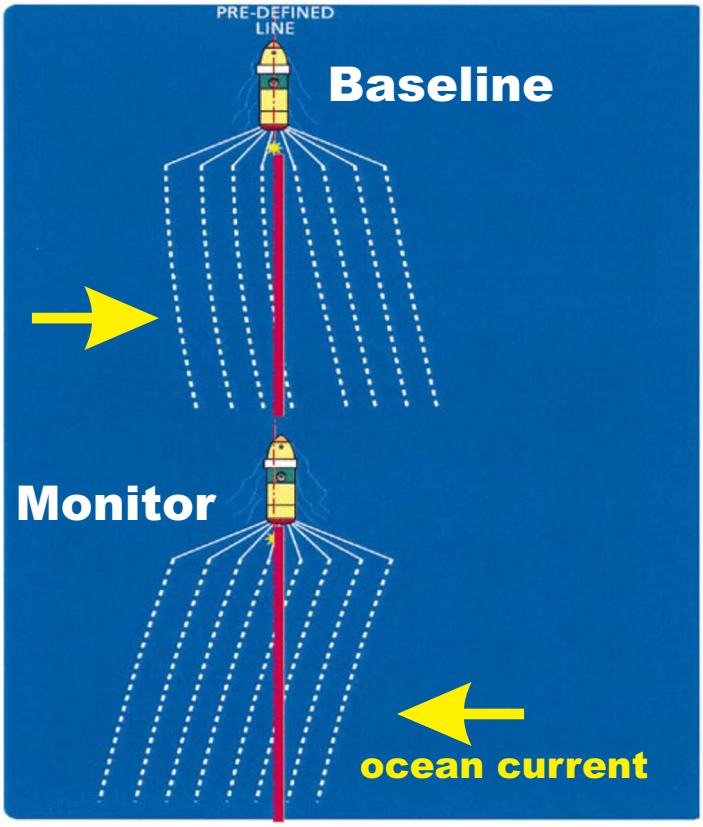

Figure 1.2: Marine time-lapse acquisition: Dotted lines indicate the streamers' position towed behind the seismic vessel for the baseline and monitor survey. The yellow arrows indicate the direction of the ocean current during the acquisition (modified from Eiken et al. (2003b)).

et al., 2005). The hydrophone positions along the streamer are in turn extrapolated from these GPS measurements utilising additional relative positioning information from a local acoustic network between the hydrophones (Bittleston et al., 2000). The mean error in determining each hydrophone position is ±5m, but can be as high as ±12m (Morice et al., 2000; Bittleston et al., 2000; Eiken et al., 2003b). These errors are inherent to the recording system and independent of the ocean currents. However, compared to the positioning errors caused by ocean currents these errors are insignificant. For example, 5° of feathering relates to a cross-line deviation of 261m at the far end of a 3000m streamer cable. The mid offset deviation is 130m and still considerably more compared to a maximum error of 12m in determining the exact hydrophone position.

One disadvantage of working with the feathering angle is that it relates the actual acquisition geometry to a pre-defined (planned) geometry. In time-lapse seismic, however, a measure is needed that quantifies the position difference of source and receiver between the baseline and monitor survey. The sum of the difference in source and the difference in receiver position, $\Delta Source + \Delta Receiver$, is therefore widely used to specify the quality of the geometric repeatability of source and receiver positions between the baseline and monitor survey. Figure 1.3 illustrates the concept of how to calculate this quantity. When binning time-lapse seismic data into common mid point (CMP) offset classes each bin is normally populated with at least two traces (two source and receiver pairs), one from the baseline and one from the monitor survey (Figure 1.3). The absolute value of the difference in source, $|\Delta Source|$, and receiver locations, $|\Delta Receiver|$ can thus be calculated based on the positioning data recorded during each survey. The sum of both absolute measures, the source and receiver mis-position, is commonly referred to as the $\Delta Source + \Delta Receiver$ repeatability measure. It is calculated in each CMP bin and for each offset class.

Another similar measure to quantify the geometric repeatability of source and receiver locations is the difference in azimuth, Δ Azimuth, between baseline and monitor source and receiver positions (Figure 1.3). In general, the smaller either one of the geometric repeatability measurements is, the better the monitor survey repeats the baseline survey's source and receiver positions. However, the com-

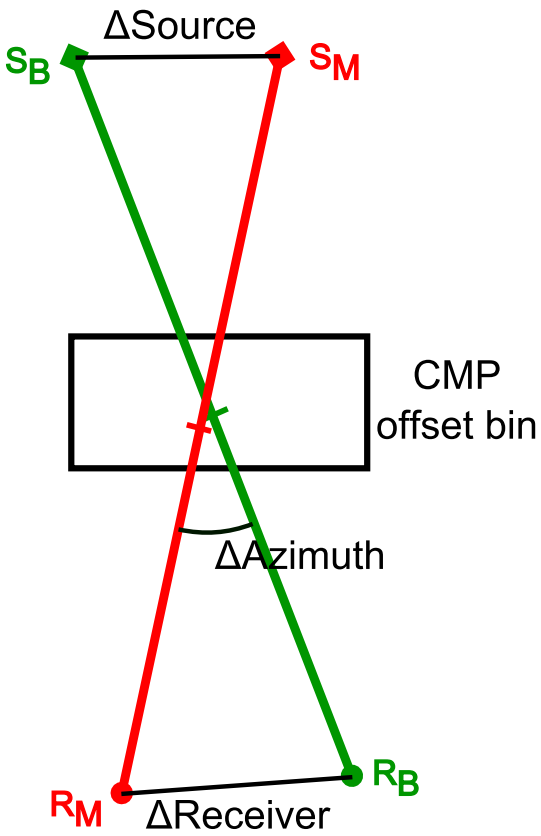

Figure 1.3: Geometric repeatability measure for time-lapse traces. The source and receiver location, S_B and R_B, of one baseline trace are connected by the green line. The respective source and receiver location, S_M and R_M, for the monitor trace are connected by the red line. The measured distance between repeat source and receiver location is Δ Source and Δ Receiver, respectively. Δ Azimuth is the azimuth difference between the baseline and monitor source and receiver positions.

mon midpoint separation of both source and receiver pairs can vary for the same $\Delta Source + \Delta Receiver$ measure. This increase in midpoint distance causes a decreasing overlap in the Fresnel zones and thus most likely a higher NRMS measure, as the common part of the subsurface reflection area decreases. The next section highlights the necessity to closely match the baseline survey geometry during the monitor acquisition, in order to reduce the time-lapse noise.

1.3.2 Relating NRMS variation with geometric acquisition repeatability

A relation between the NRMS measure and the repeatability of source and receiver locations is reported by Kragh and Christie (2002). They use the data from two repeat 2D seismic lines that are acquired in the Gulf of Mexico. No streamer control is used, therefore the shot and receiver positions are affected by the strong eddy currents in that region. NRMS values range from 18% to 90% and correlate very well with the source and receiver mid-point position error between the base and repeat sail line pass (Figure 1.4(d)).

The NRMS measure is calculated for every CMP bin of the baseline and monitor 2D line (Figure 1.4(b)). In turn, the authors calculate the distance between the respective CMP bin location of each line and plot these values against the NRMS measure (Figure 1.4(d)). The increase in the NRMS measure with increasing mispositioning of the CMP bins is evident. Furthermore, the two lines are acquired in a region of no production activity and within two days. Therefore, any effects in the difference data are related to the differences in the acquisition. It is apparent that the non-repeat monitor line gives rise to an increase in time-lapse noise. The larger the geometrical non-repeatability is, the larger the NRMS measure or noise. The former example is an early study of the relation between acquisition non-repeatability and time-lapse noise. The CMP bin difference between two repeat 2D lines is just an approximate measure (Fresnel zone overlap) for the non-repeatability of the source and receiver position, as outlined on the previous section. Moreover, 3D seismic surveys are the current industry standard. Consequently, Renoux and Lacombe (2005) present a study using full 3D seismic acquisition geometries. The

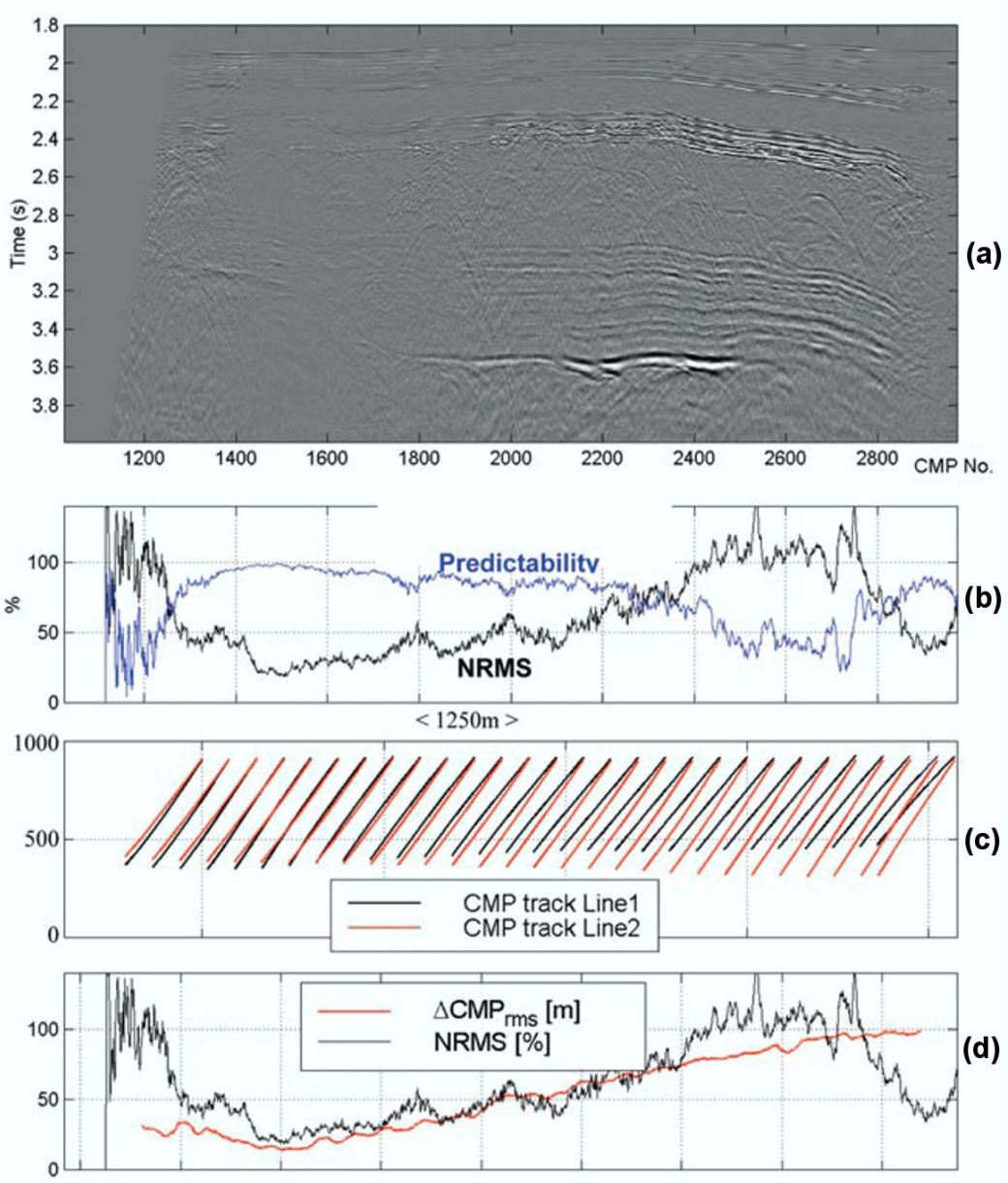

Figure 1.4: Relation between time-lapse noise and streamer positioning repeatability using a repeat 2D seismic line. (a) time-lapse difference of the seismic data. (b) NRMS measure calculated in a window from 2s to 4s for each CMP bin. (c) CMP bin position for base line (black) and repeat line (red) for every 30th shot. (d) Relation between the NRMS measure (black line) and the CMP mis-position (red line) (from Kragh and Christie (2002)).

authors compare real seismic data from a North Sea field with synthetic data, which are modelled using horizons and velocity parameters input from the same North Sea field. The variation of the NRMS measure with increasing $\Delta Source + \Delta Receiver$ positioning error follows the same characteristic pattern for the real data as well as the synthetic case (Figure 1.5). The authors report that both data sets exhibit an

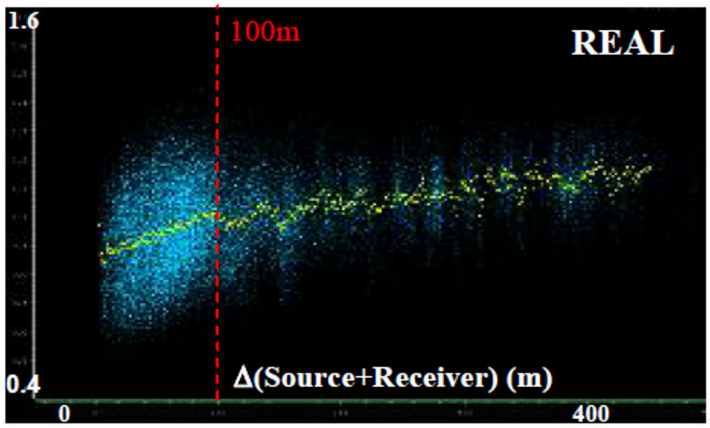

(a)

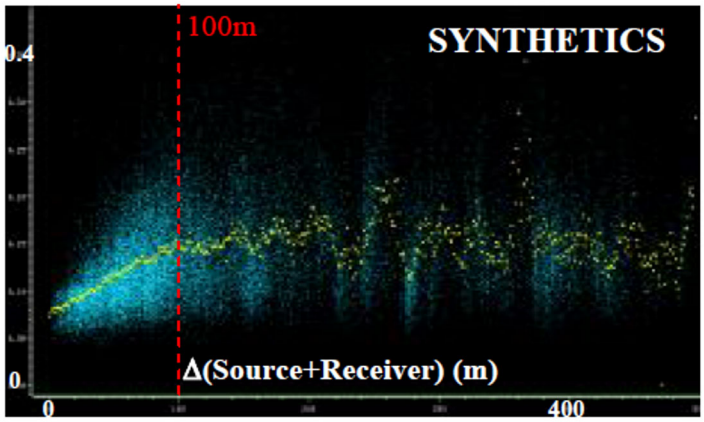

(b)

Figure 1.5: Change of the NRMS measure with increasing non-repeatability of source and receiver positions. (a) NRMS versus source and receiver mis-positioning calculated from a real North Sea data set. (b) NRMS variation with source and receiver mis-positioning calculated the synthetic model using input data from the real North Sea data set example. The yellow points represent the average curve. Heterogeneities in the model are described as lateral velocity variations and dipping layers, without further specification given by the authors (from Renoux and Lacombe (2005)).

initial linear increase of the NRMS measure with increasing $\Delta Source + \Delta Receiver$ (Figure 1.3), before reaching a plateau when $\Delta Source + \Delta Receiver$ equals 100m.

The NRMS level seems to be uncorrelated with source and receiver mis-positioning greater than 100 metres. Furthermore, the NRMS measure in the linear part is on average higher in the real data case (Figure 1.5(a)) than in the synthetic case (Figure 1.5(b)). The authors ascribe this to the fact that the synthetic case does not include multiples, varying source signatures or swell noise, which are all additional sources of noise and therefore increase the NRMS measure. However, a clear statement is made that the time-lapse data quality, expressed as NRMS quantity, is directly related to the geometric repeatability of source and receiver positions for time-lapse seismic data acquisition.

Naess (2007) explains the foregoing characteristic increase of NRMS versus $\Delta Source + \Delta Receiver$ measure. With the knowledge that the NRMS repeatability measure is sensitive to small phase shifts, the author splits the incoming wavefield of the baseline and monitor survey into its frequency components. The maximum NRMS error is reached when two recorded events are 180° out of phase. The receiver mis-position in the cross-line direction, however, introduces an additional path that the wave has to travel, thus resulting in a phase shift. Higher frequencies will reach the 180° out of phase criterion first, followed by the lower frequencies for the same additional path to travel. The author argues that the observed NRMS curve is the superposition of NRMS measures for each frequency component. The linear relation between the NRMS measure and the source and receiver mis-position is plotted for four single frequencies, k_1 to k_4, in Figure 1.6(a). The orange line is the superposition of NRMS measure of all frequencies recorded in the seismic trace and thus forms the characteristic linear increase until a plateau is reached. The black line in Figure 1.6(b) is the superposition of a larger number of frequency components, thus obtaining a smooth character. Naess (2007) further states that, for real data acquisition, the recorded wavefield arrives from more than one direction at the receiver and therefore a different average repeatability curve will represent each such direction. This is evident in the spread of data points in Figure 1.5. Lastly, Naess (2007) argues that the relation between the NRMS measure and the non-repeatability of source and receiver position varies with the type of subsurface geology. He explains that a much steeper NRMS versus $\Delta Source + \Delta Receiver$ curve is common offshore Norway, because of glacial scouring stripes on the sea floor giving rise to a large

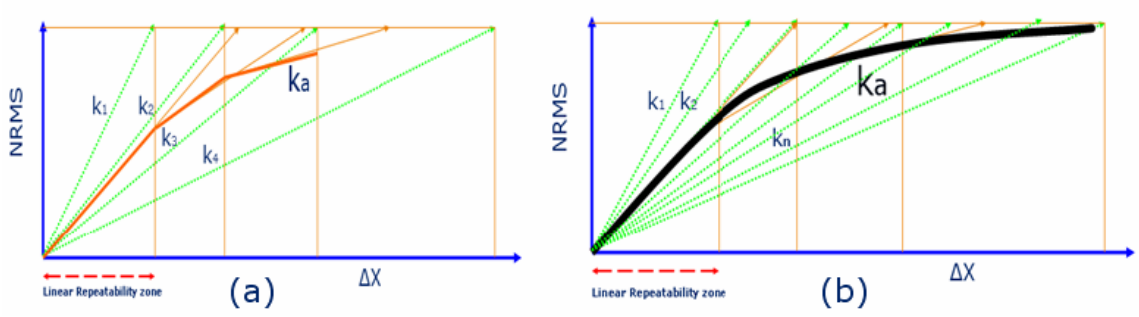

Figure 1.6: Each frequency component has a linear relationship (k_1-k_4) between the NRMS measure and the crossline variation of the receiver position, Δx (a). A large number of frequency components will superimpose and result in an average curve gradually reaching a plateau (b) (from Naess (2007)).

amount of sideways diffracted high frequency noise, even at small cross-line positioning shifts. Apparently, the time-lapse noise level is not only affected by the geometrical non-repeatability of source and receiver positions, but also by the type of subsurface geology.

The effect of overburden geology and shot mis-positioning is further studied by Landrø (1999b). The author looks at the influence of source position differences in a VSP survey on the RMS amplitude error at the reservoir. The survey is acquired over the Oseberg field, Norwegian North Sea, within just two days. No noticeable production changes in the reservoir are assumed to happen over this short time. Furthermore, the geophone position is fixed down-hole in the reservoir. The author sorts all shots (Figure 1.7) into groups based on their distance to the nearest neighbours. Subsequently, the RMS of the difference for each shot-receiver trace in every group is calculated and compared to the RMS value of either of the input traces. The RMS error is as low as 18% for shots with a separation of less than 5m. Additional filtering of high frequencies above 50Hz in the seismic data reduces the RMS error to 8% (Landrø, 1999b). The average RMS error is then calculated for shots within specific separation classes between 0m to 100m (Figure 1.8).
The RMS error increases with increasing shot separation. This shot separation can also be understood as a shot mis-position. Therefore, it is important to repeat the source location in the monitor survey as closely as possible in order to obtain good repeat seismic data.

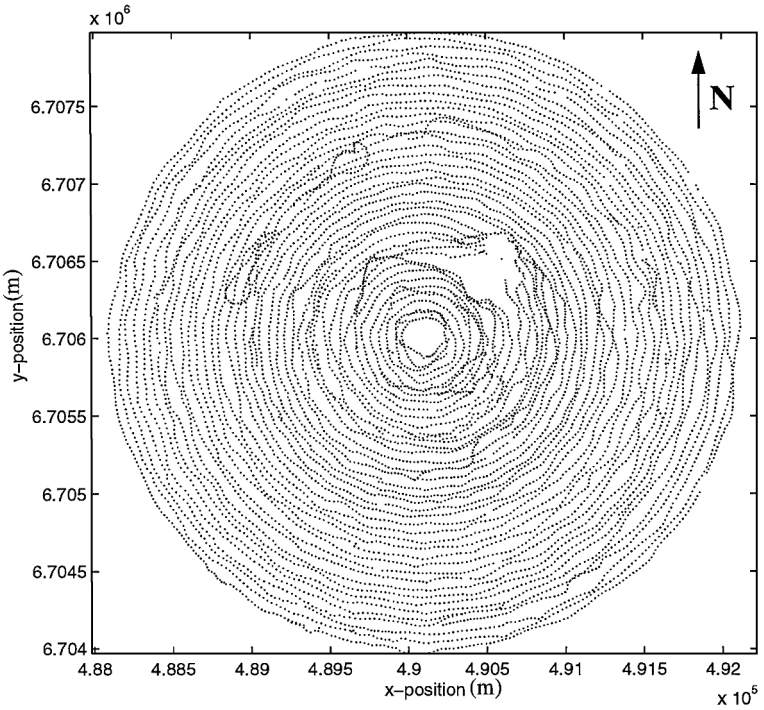

Figure 1.7: VSP survey at the Oseberg field, where dots indicate the shot positions. The nominal shot separation is 25m. Spacing between the concentric circles is approximately 40m (from Landrø (1999b)).

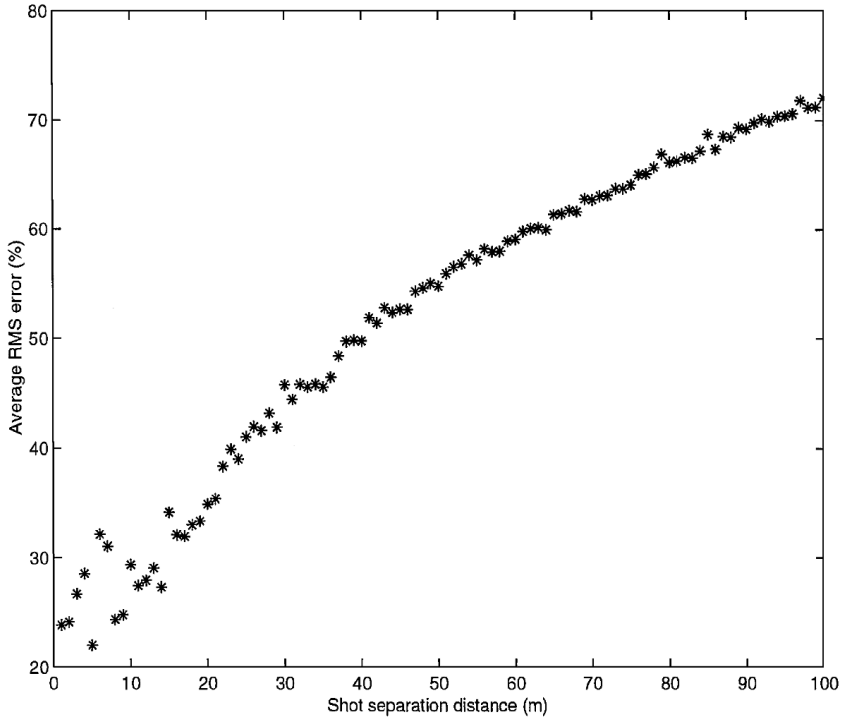

Figure 1.8: Average RMS error between seismic traces with increasing shot separation (from Landrø (1999b)).

A chart of NRMS versus $\Delta Source + \Delta Receiver$ measure for several North Sea time-lapse surveys is compiled by Smit et al. (2005). Each dot in Figure 1.9 represents one time-lapse seismic survey. Black lines connect points corresponding to the same field in cases where multiple surveys are acquired over the same field. There is a clear trend of decreasing NRMS values with decreasing positioning errors (Figure 1.9, dashed red line). This is particularly evident for the three fields (black lines) where multiple time-lapse surveys are shot. For the latter case, however, it is assumed that all time-lapse surveys acquired over the same field are reprocessed so that the decrease in NRMS is solely attributable to the decreasing positioning error and not to an improvement in the data processing. An important observation is

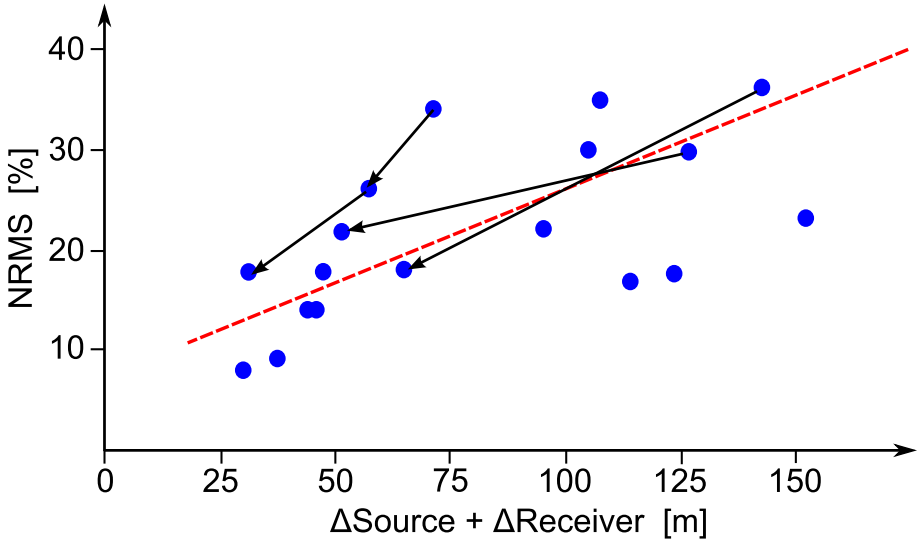

Figure 1.9: Each blue dot represents one acquired 4D survey. The average error in source plus receiver location is plotted against the NRMS level. Arrows connect surveys shot over the same field. The dashed red line marks the trend of the data (after Smit et al. (2005)).

that mis-positioning of source and receiver position during time-lapse acquisition is a controling parameter which affects the overall NRMS measure and thus the noise level in the seismic data. However, the positions of sources and receivers are increasingly well controlled with today's marine acquisition technology. The emergence of steerable streamer (Bittleston et al., 2000; Curtis et al., 2002; Eiken et al., 2003a; Tang et al., 2007) makes it easier to counteract the feathering due to ocean currents. In addition, significant improvements of the time-lapse data quality are achieved by various feather matching (time-lapse binning) strategies. This is contrary to the wide spread of data points in Figure 1.9. Thus, despite

the improving acquisition technology, Smit et al. (2005) conclude that the following parameters also contribute to the NRMS noise level:

- Overburden geology
- Processing quality
- Dominant frequency in the data

Consequently, Smit et al. (2005) come up with an alternative definition of the NRMS measure:

$$\text{NRMS} = \sqrt{2\pi^2(f\Delta t + k_x\Delta x)^2 + \sqrt{2}\frac{1}{(SNR)^2}} \tag{1.2}$$

To their understanding, the NRMS measure is dependent on the remaining time shifts, Δt, the dominant frequency, f, errors in the position repeatability, Δx, the lateral dominant wavelength, k_x, and the noise level of the data, SNR. Most interesting is the fact that the NRMS measure is assumed to be affected by the dominant lateral wavelength, which depends on the overburden geology.

1.4 Overburden domain

The previous section highlights the importance of a good repeat monitor survey in order to reduce the time-lapse noise level, expressed as NRMS measure. It is also shown that the overburden geology is an important factor that needs more consideration. Thus, the following section discusses the overburden domain to further evaluate its potential role for the time-lapse data quality.

1.4.1 Seawater velocity changes

The acoustic property of seawater varies spatially and vertically due to variations in the water temperature and salinity (Del Grosso, 1974; Chen and Millero, 1977). These variations occur over a wide frequency range from daily variations, due to sun intensity, to seasonal and yearly variations influenced by tides and ocean currents.

Velocity changes due to river currents are an issue especially in the West of Africa region. Bertrand and MacBeth (2003) investigate the effect of such velocity variations on time-lapse seismic data for the Teal-South field, Gulf of Mexico (GoM), as well as for the Foinaven field, West of Shetland. The impact of the seawater velocity variation on the seismic data at Teal-South is reported to be only moderate due to the shallow water depth of 90m. More pronounced effects are observed at the Foinaven field where water depth is between 500m and 600m. Bertrand and MacBeth (2003) model synthetic seismic data, assuming that the seawater velocity at the time of the monitor survey (Figure 1.10) is changed from the constant baseline velocity. Pre-stack traveltime differences from a subsurface reflection event are

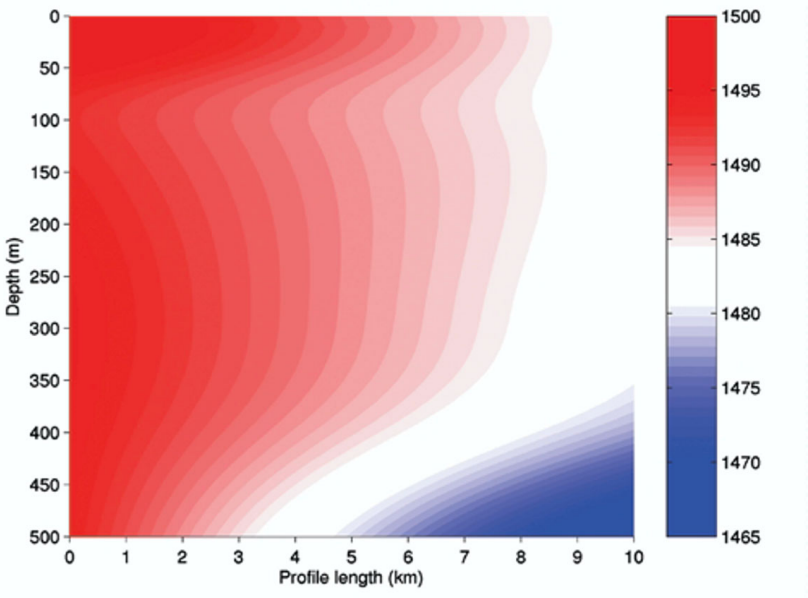

Figure 1.10: Seawater velocity model for the synthetic Foinaven modelling study. The velocity varies between 1500m/s at the surface and 1465m/s at the bottom (from Bertrand and MacBeth (2003)).

reported to be in the range of 1ms to 6ms. In addition, the magnitude of the RMS amplitude error is found to be 6% for the near offset stack and 35% for the far offset stack data (Figure 1.11). These RMS amplitude errors are extracted at the top reservoir reflection even after applying a cross-equalisation. This cross-equalisation process corrects for time and phase shifts as well as amplitude variations between the baseline and monitor data observed at a reference event outside the zone of production induced changes. Amplitude errors before cross-equalisation are as high as 70%. Further investigation reveals that the impact of the variation in seawa-

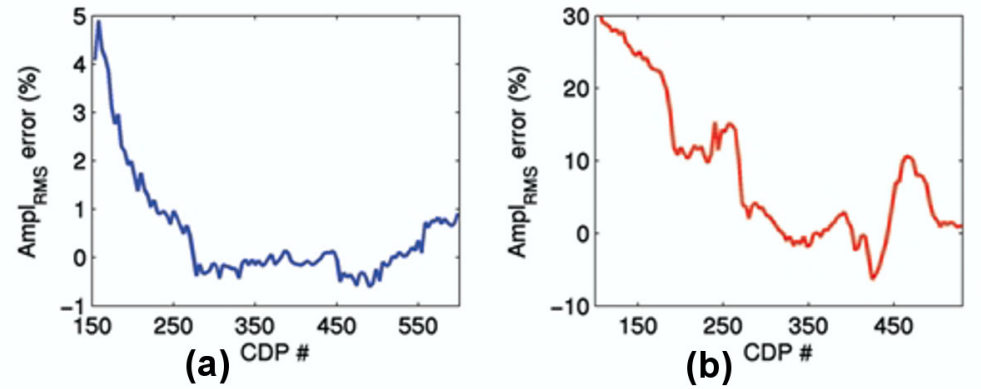

Figure 1.11: Modelled RMS amplitude error due to seawater variation at the Foinaven field. (a) amplitude error for the near offset stack, (b) amplitude error for the far offset stack (from Bertrand and MacBeth (2003)).

ter velocity on the NRMS measure is substantial. The NRMS measure is between 50% to 70% for the raw near offset difference data, but drops to 10% to 20% after cross-equalisation is applied (Figure 1.12). Bertrand et al. (2005) consequently demonstrate a method to dynamically account for such velocity variations in the case of permanent sensor installations.

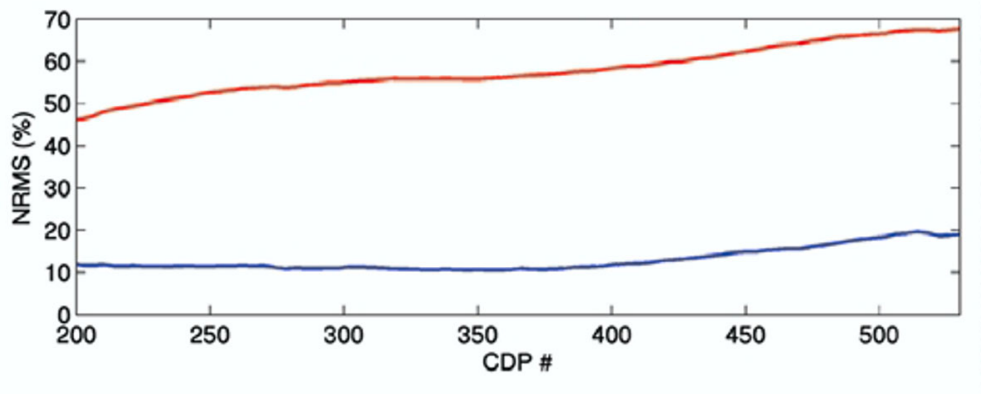

Figure 1.12: NRMS measure for the near offset stack difference. The red curve is obtained from the raw difference whereas the blue curve outlines the NRMS level after cross-equalisation (from Bertrand and MacBeth (2003)).

1.4.2 Scatterers, channels and faults in the subsurface

The effect of scatterers and faults in the overburden on time-lapse data has not yet been discussed in the literature. However, their impact on 3D seismic data interpretation has been investigated. It is the intention to discuss these possible

sources of error in 3D seismic data and question whether they impact the time-lapse data when their effects are not accurately repeated in a time-lapse experiment.

Malme et al. (2005) study the impact of randomly distributed point diffractors in the overburden on amplitude versus offset (AVO) analysis. The seismic response is modelled at various target levels below the scatterers using a full elastic finite-difference algorithm. They find that such diffractors cause interfering wavefronts, thus resulting in rapidly oscillating amplitude distortions of up to 30% in magnitude along the AVO curve. Simple smoothing of the distorted AVO curve recovers its true behaviour to an acceptable degree. In the next step, the authors replace the scatterers in the overburden with an elliptical shaped lens. Severe amplitude distortions of the AVO curve are observed along reflectors beneath the lens. The amplitude deviations from the true case, without the lens (Figure 1.13, blue line), are as high as 100% vertically below the centre of the lens, and still up to 50% at offsets greater than 1000m (Figure 1.13, red line). Note that the shot position, however, is slightly offset from the centre of the lens. Smoothing the distorted AVO response (Figure 1.13, black line) does not resolve the original response of the model where no overburden lens is present. Malme et al. (2005) believe that the amplitude distortions in the AVO response can be compensated if the velocity of the lens is included in an accurate migration velocity model, but no proof is given. Hatchell (2000) also investigates the origin of amplitude distortions in the AVO response in seismic data recorded at two different locations in the Gulf of Mexico. The first example is from the Mars field in water depth of 900m. Anomalous amplitude dimming is observed in pre-stack migrated AVO gathers, which is systematically varying with cross-line location. The amplitude variations are reported to be $\pm 25\%$ for near offsets and and decreasing with far offsets (Figures 1.14(a) and (b), respectively). The author uses the real acquisition geometry and ray-tracing methods to locate the origin of these amplitude anomalies near the top of the slump zone of the Mars basin, at 1800ms two way traveltime (TWT). He then postulates that these amplitude anomalies are caused by velocity changes across buried faults, arguing that the transmission of seismic waves is distorted when arriving at different sides of the fault and therefore resulting in a complex interference pattern. The time slice through the stacked data (Figure 1.14(a)), however, does not show any obvious reflection event at this depth.

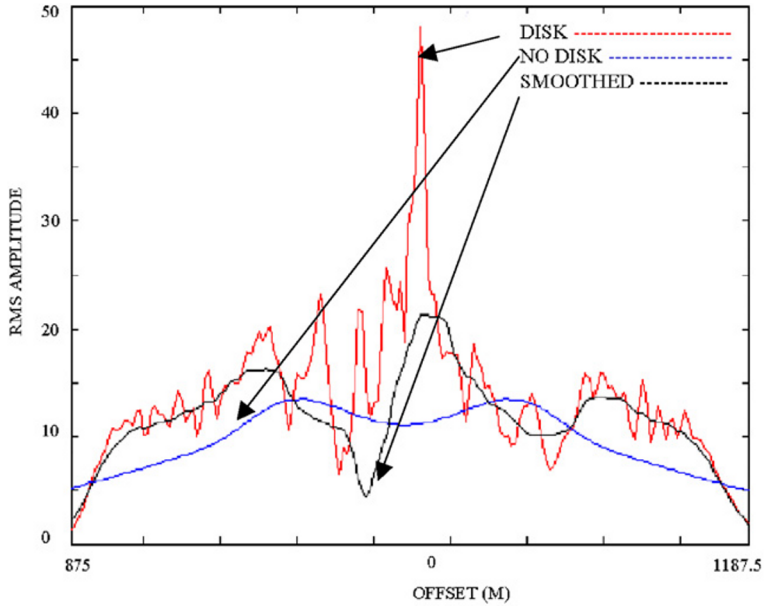

Figure 1.13: Amplitude versus offset response with (red) and without (blue) a lens in the overburden. The black line results after smoothing the red AVO curve (from Malme et al. (2005)).

Nevertheless, the author outlines that there is a favourable agreement between the orientation of faults and unconformities at the top of the slump zone and observed features in the amplitude anomaly map. The second example that Hatchell (2000)

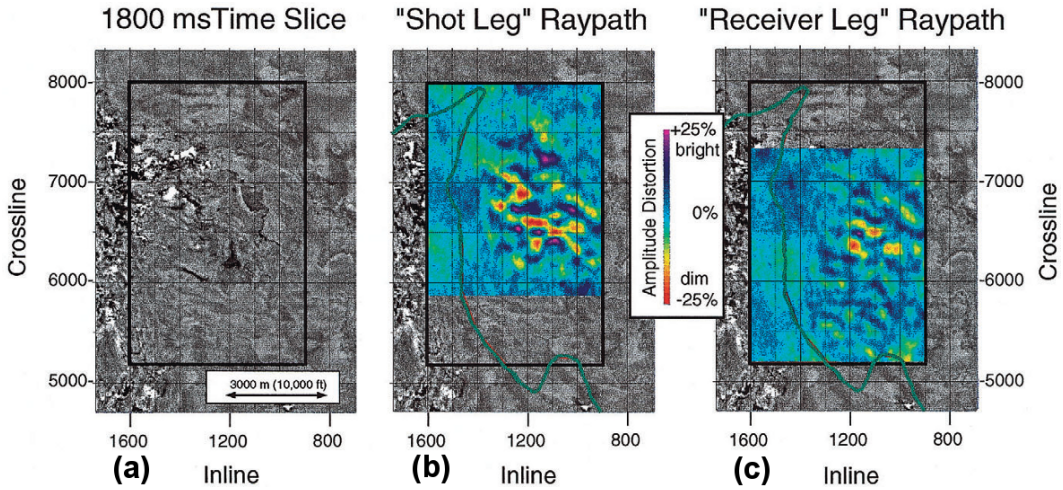

Figure 1.14: Amplitude distortions at the Mars field: (a) time slice at 1800ms through the stacked data. (b) amplitude dimming in the near offset data (shot leg) and (b) in the far offset data (receiver leg) (from Hatchell (2000)).

presents is from a shallow water (8m) Gulf of Mexico Shelf data set. The overburden geology is described as a Miocene Age prograding delta system with syndepositional faults. Amplitude distortions of ±25% are observed at a Miocene sandstone reflection event in the AVO volume created from the pre-stack seismic data. The author

assumes that these distortions also originate from velocity changes across faults, but stresses that not all faults give rise to such distortions. He confirms his assumptions in a synthetic seismic modelling study.

However, the scale of these faults is much smaller compared to the previously discussed overburden complexities (scatterers, overburden lens). Nevertheless, the amplitude error caused by these faults, as reported by Hatchell (2000), is of similar magnitude compared to the large scale overburden heterogeneities. Hence, it has to be questioned, whether these amplitude errors originate solely from displacements across faults, or if there are other controlling factors such as multiples involved as well.

Irrespective of the latter uncertainty in the effect of faults, the question that has to be asked is whether the presented amplitude distortions, caused by overburden heterogeneities, are sufficiently repeatable if source and receiver positions do not differ between the baseline and the monitor survey and thus cancel each other out in the time-lapse difference data.

1.4.3 Complex bodies in the overburden

Misaghi et al. (2007) study the effect of transmission errors in seismic data in relation to shot mis-positioning for a complex overburden at the Oseberg field. They use the same VSP data, acquired over the Oseberg field, as Landrø (1999b). A clear relation between shot separation distance and RMS amplitude error is described for this data in Section 1.3.2. This new study, however, shows that the RMS amplitude error at the reservoir is not only influenced by the separation distance of respective shots, but also by an overburden shale lens. One schematic drawing of the experiment and two cross sections through the stacked seismic data outline the position of the lens above the reservoir (Figure 1.15). Misaghi et al. (2007) sort the data again into shot separation distance classes, but now investigate the spread of the RMS amplitude error for shots less than 10m apart (Figure 1.16). The authors sort the shots into two additional classes, dependent on whether the seismic waves travel through the lens on the way to the receiver or not. Misaghi et al. (2007)

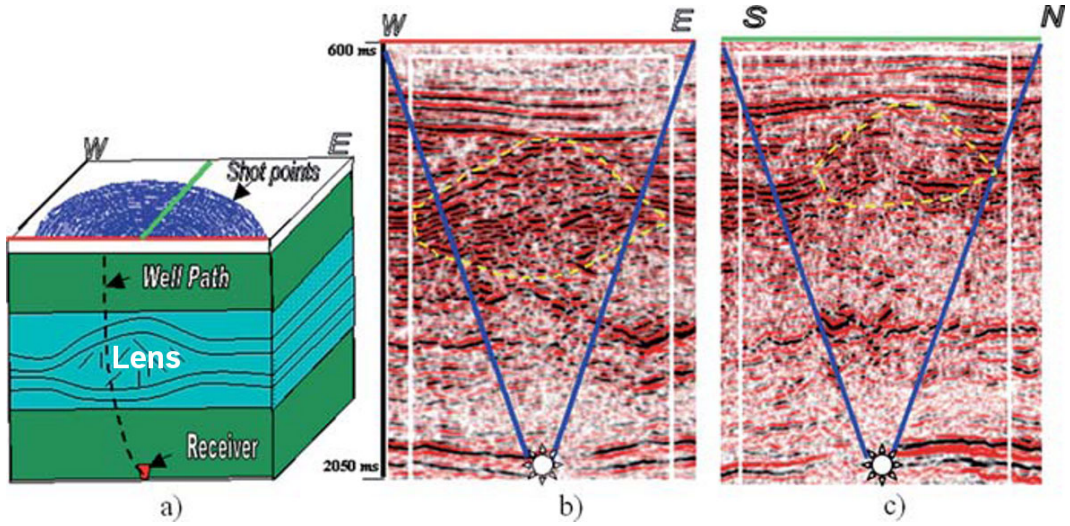

Figure 1.15: Overburden complexity at the Oseberg field. (a) Schematic view of the circular VSP shot pattern, the receiver position and the shale lens above the reservoir. (b) W-E section with the shale lens outline (dashed yellow line). (c) N-S section with the location of the lens marked (dashed yellow line) (from Misaghi et al. (2007)).

consequently demonstrate that the RMS error increases from 20% to 35% if the ray-path of the wave is passing through the lens (Figure 1.16) and shots are less than 10m apart. They therefore conclude that the upper limit of the RMS amplitude error cloud is due to transmission distortion of the seismic wave when it passes through the overburden lens in addition to the shot separation. The lower bound results from events where the waves do not pass through the lens and is therefore solely governed by the mis-position between shot points. This study provides strong evidence that the overburden shale lens adds additional error to the seismic data if waves are travelling through this complex zone. However, the authors stress that this VSP survey does not represent a proper time-lapse acquisition scenario and care has to be taken when extrapolating the observations into a general time-lapse framework. Besides considering a validation of the results by three-dimensional seismic modelling, the authors discard this option due to the lack of velocity and density parameters and also due to the fact that a substantial amount of work is needed to assemble such a detailed overburden model.

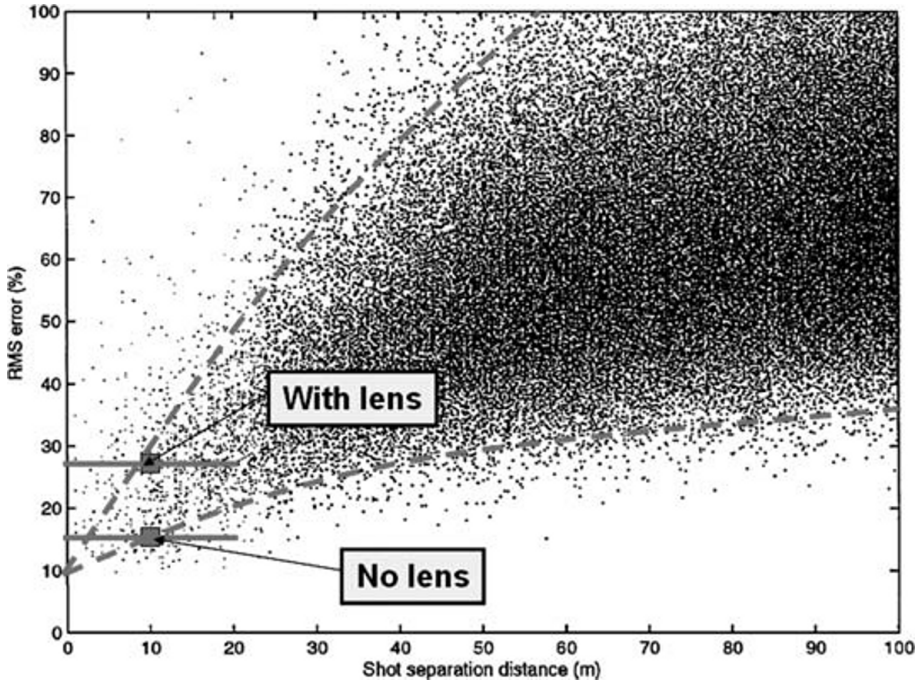

Figure 1.16: RMS amplitude error variogram for the Oseberg field. The upper and lower bounds of the amplitude error variability are outlined by dashed lines (from Misaghi et al. (2007)).

1.4.4 Dipping horizon

The previous sections focus predominantly on amplitude errors originating from overburden heterogeneities. However, traveltime errors caused by source and receiver mis-positioning as well as by overburden structure are discussed in this section. Fehmers et al. (2007) report on systematic residual time shifts observed at steep dips at the Curlew D gas condensate field, Central North Sea. An NRMS measure of 27% is obtained after processing the seismic data, which allows identification of time shifts greater than 1ms. This is indeed in line with an initial time-lapse feasibility study showing that time shifts due to reservoir depletion are expected to be between 1ms to 2ms and observable in the seismic difference data. However, large time shifts are observed at steep dips outside the reservoir when extracting the time shifts along a horizon just above the reservoir (Figure 1.17(a)). The authors postulate that a relative positioning error of 6.25m between the baseline and monitor survey causes those time shifts at steep gradients. They consequently shift the monitor survey by that amount and correct most of these large time shifts (Figure 1.17(b)). However, striping parallel to the acquisition sail line direction is still

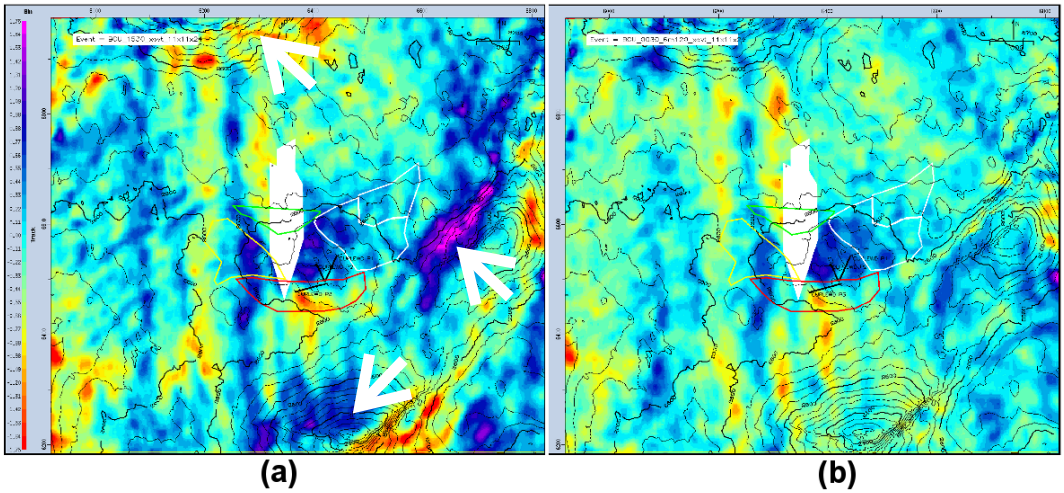

Figure 1.17: Time shifts measured over Curlew D at the top Kimmeridge event. The colour scale is between -1.75ms and 1.75ms. (a) Time shifts after cross correlation - white arrows indicate areas of large shifts and steep dip. (b) Time shifts after constant shift of 6.25m (modified from Fehmers et al. (2007)).

evident in the time shift map (Figure 1.17(b)). Fehmers et al. (2007) suspect that such residual time shifts are caused by differences in source and receiver position between the surveys, which could not be removed during processing.

1.4.5 Geomechanically active reservoir and overburden

The previous section shows that time shifts can be affected by positioning errors between the baseline and the monitor survey in conjunction with steep dipping horizons. A more detailed discussion on the origin of time shifts and how the overburden is involved is given in this section.

Indeed, time shifts are observed in many time-lapse studies and over many different reservoirs. Large time shifts in excess of 15ms are observed at chalk reservoirs, such as the Ekofisk field (Guilbot and Smith, 2002; Smith et al., 2002; Janssen et al., 2006b), the Valhall field (Barkved and Kristiansen, 2005; Hall et al., 2005; Hatchell et al., 2005) and the South Arne field (Schiøtt et al., 2008), all situated in the Norwegian North Sea. Furthermore, time shifts are also reported for clastic reservoirs. Heron, Skua, Shearwater, Elgin and Franklin are high pressure high temperature clastic North Sea reservoirs which exhibit shifts in the range of 0.5ms to 5.5ms (Staples et al. 2007 and Hawkins et al. 2007). Moreover, Olden et al.

(2001) suggest that time shifts are caused by production induced velocity changes in a Rotliegend oil reservoir, North Sea. These time shifts show up as a time "pull up" of the base reservoir reflection event and cause an abnormal time-lapse amplitude signal due to the misalignment of the seismic reflection event in the monitor survey. Significant time shifts of up to 8ms are also reported outside the North Sea, for example, at the deep water Genesis field in the Gulf of Mexico (Hudson et al., 2005; Rickett et al., 2007), the Mars field (Schutjens, 2005) and the Holstein field (Ebaid et al., 2008).

Staples et al. (2007)) use a particularly illustrative figure to explain the origin of these time shifts (Figure 1.18). When the pore pressure in the reservoir decreases in case there is no pressure support during hydrocarbon production, the effective vertical stress on the reservoir rock increases, thus giving rise to compaction. This compaction of the reservoir rock provides void space, into which the overburden and underburden expands. The seismic velocity thus increases inside the reservoir due to the compaction and decreases in the overburden and underburden due to extension (Figure 1.18). The slowing down of the velocity in the overburden gives rise to an

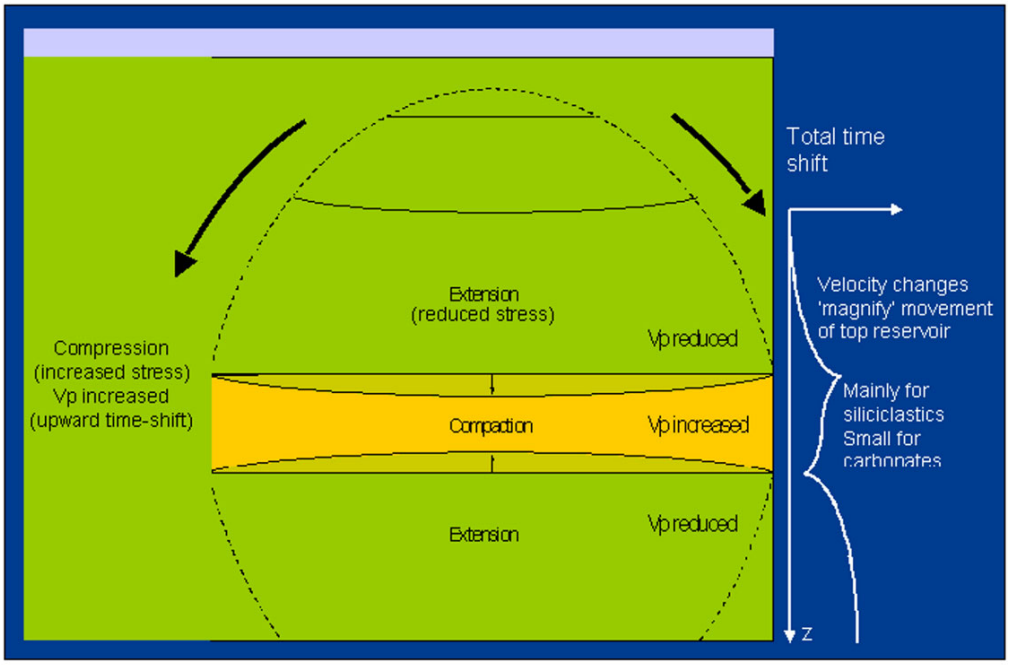

Figure 1.18: Schematic velocity change for a compacting reservoir. The left-hand figure outlines the areas of compaction and extension. The right-hand side shows the time shift versus depth measured on a vertical line through the centre of the reservoir (from Staples et al. (2007)).

increase in two way traveltime in the monitor survey, thus causing the bulk of the time shifts observed above the reservoir. In addition to those vertical time shifts, Cox and Hatchell (2008) also observe apparent lateral shifts in time-lapse data of the Shearwater field. They question whether the velocity change in the overburden impacts the wave propagation and therefore causes these apparent shifts, because of the common practice of using the baseline velocity model to migrate the monitor seismic data. Cox and Hatchell (2008) consequently prove in a study that the observed lateral shifts are most likely caused by using the baseline velocity model during data processing, thus not accounting for the overburden velocity change. However, the authors are still unsure if the seismic amplitude at the reservoir level is also affected when using an incorrect migration velocity model. Moreover, Landrø and Stammeijer (2004) describe a technique to estimate the velocity change inside of a compacting reservoir, from post-stack seismic data. They also believe that their method is limited if the data processing of the monitor seismic data is carried out with the baseline velocity and therefore does not account for the velocity change in the overburden rock.
To summarise, compacting reservoirs induce stress and strain changes in the overburden rock which might impact the time-lapse amplitude attribute if not properly taken care of during data processing.

1.5 The influence of the seismic processing domain on time-lapse seismic attributes

The importance of using a proper migration velocity model in order to capture velocity changes in the overburden is outlined in the previous section. Thus, it is necessary discuss other possible sources of error which might originate from the processing sequence applied to the seismic data.

The paradigm of processing data for time-lapse interpretation is considerably different from processing data for exploration studies. The seismic interpreter working on an exploration project is mainly interested in an accurate image of the subsurface

structure in order to identify new hydrocarbon traps. However, during time-lapse seismic data processing care is taken to process the baseline and monitor survey in the very same way, often called parallel processing. This means that time-lapse processing does not aim for obtaining the best result for each individual seismic data set, but rather aims for the result that optimises the time-lapse difference data. For example, it is not necessary to eliminate multiples in the baseline survey if they repeat exactly in the monitor survey, thus cancelling out when taking the difference. To monitor the time-lapse data quality during processing, quality control is performed in order to determine the improvement in the time-lapse data quality measured as NRMS quantity. The NRMS measure should decrease after each processing step to reflect the enhancement in data quality and therefore the ability to detect time-lapse changes.

An example of such quality control is given by Taylor et al. (2007). They describe how the NRMS measure is lowered during the parallel processing applied to the base and monitor survey shot over the Elgin and Franklin field. An initial NRMS measure of 80% is observed in the raw pre-stack shot gathers, which continuously decreases to 18% for the final post-stack time-lapse data (Figure 1.19). Phase, time and amplitude corrections are only applied to the monitor data in a final cross correlation step (Taylor et al., 2007). Another example for time-lapse processing is described by Magesan et al. (2005). The authors discuss the time-lapse processing flow applied to the Genesis field (GoM) in great detail. Table 1.1 summarises the various steps. Items in italics use the baseline and monitor data set to derive common processing parameters. All remaining steps optimise each data set individually.

Kvalheim et al. (2007) look more closely at a single but very important processing step out of these preceding sequences: the data migration. They investigate the impact of pre-stack depth migration (PSDM) versus pre-stack time migration (PSTM) on the time-lapse difference data at the Brage field, Norwegian North Sea. The following four migration trials are conducted:

- Conventional straight ray Kirchhoff pre-stack time migration with a smoothed version of the RMS stacking velocity field

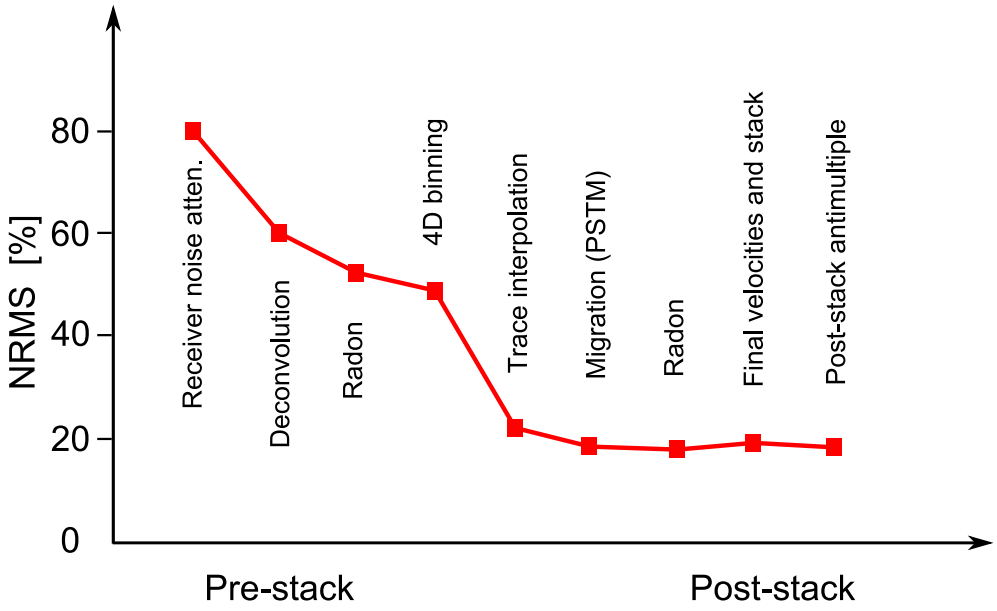

Figure 1.19: NRMS repeatability measure at the Elgin and Franklin field calculated in a time window from 3000ms to 5000ms after each processing step (after Taylor et al. (2007)).

reformat and navigation
denoise
zero phasing with Q-related phase correction
spherical divergence correction
surface consistent amplitude correction
source and receiver statics
navigation QC and corrections
global amplitude scaling
data regularisation and bin centering
multiple attenuation
global spectral matching
offset amplitude calibration
time alignment
spatial resampling of data for migration
prestack migration velocity analysis
prestack migration
cross-equalisation

Table 1.1: Time-lapse processing steps applied to the seismic data of the Genesis field. Items in italics are processes that need both baseline and monitor data to derive the input parameters (after Magesan et al. (2005)).

- 3D curved ray Kirchhoff pre-stack time migration, partially honouring ray bending
- 3D Kirchhoff pre-stack depth migration using an interval velocity model
- Pre-stack depth migration using a wave equation migration scheme

The depth migrated sections are converted back into the time domain for direct comparison of attribute maps extracted along the oil water contact. Subtle as well as significant differences in amplitude and positioning of events are observed across all different maps. The time-lapse attribute map from the pre-stack depth migration

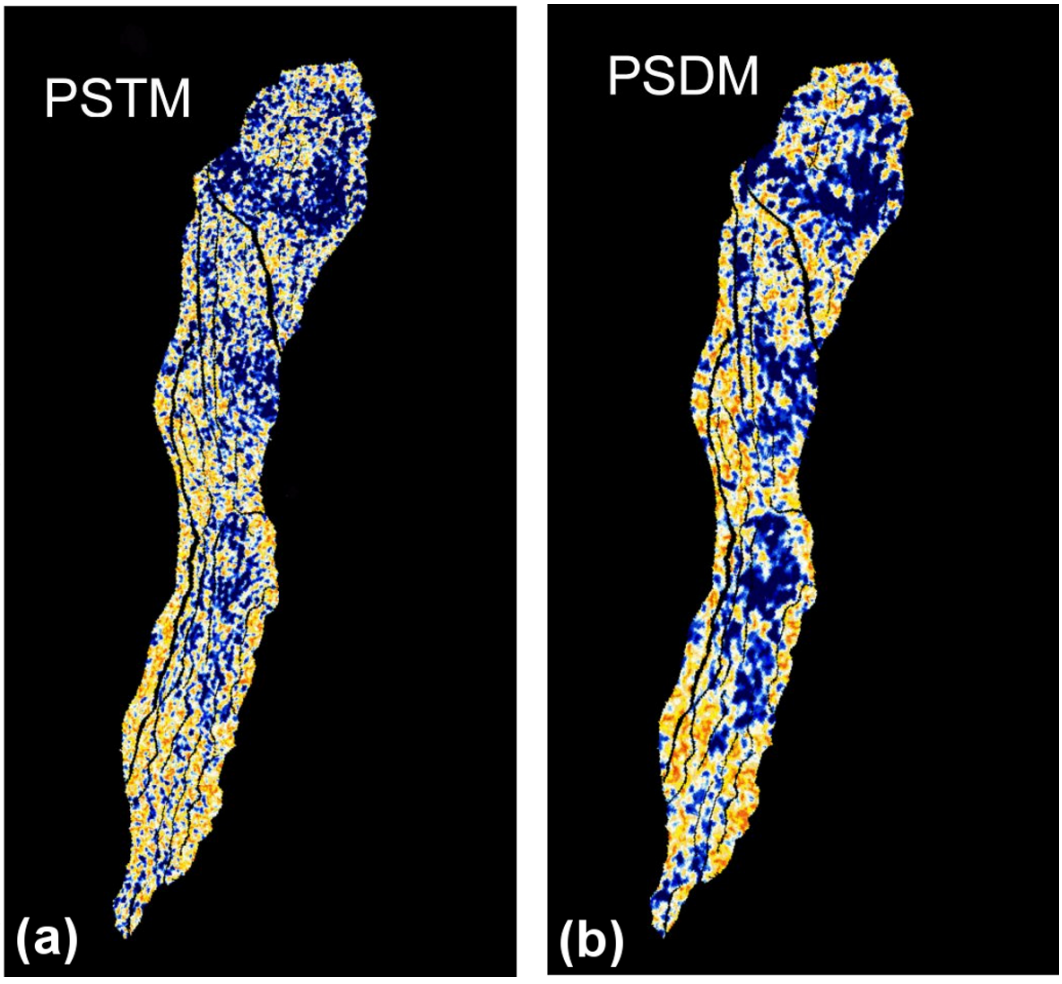

Figure 1.20: PSTM versus PSDM at the Brage field. Time-lapse attribute maps are extracted along the OWC. Blue colours indicate water flood while yellow colours indicate possible remaining oil columns (from Kvalheim et al. (2007)).

trial (Figure 1.20(b)) shows better coherency compared to the pre-stack time migration trial (Figure 1.20(a)). The clusters of correlated colour are larger and spatially

more continuous in the pre-stack depth migration trial (Figure 1.20(b)), hence water flooded areas are much easier to identify. The authors relate the increase in spatial coherency, when using depth migration methods, to the use of an accurately built velocity model which gives rise to the improved lateral and vertical positioning of the subsurface structures. Furthermore, Behrens et al. (2009) report an improved interpretability of the time-lapse difference data at the Gannet D field, North Sea, after refining the velocity model and applying a pre-stack depth migration to the baseline and monitor seismic data.

Thus, each processing step changes the time-lapse data quality which needs to be monitored throughout the processing sequence and in addition, it is highlighted that the time-lapse data quality significantly improves when very advanced migration algorithms are used, along with accurate velocity models.

1.6 Land seismic - Near surface

The previous sections only look at applications of time-lapse seismic in the marine environment. It should, however, be acknowledged that a considerable amount of the world's hydrocarbon production is from onshore reservoirs. The near surface (weathering layer) is of particular interest in seismic experiments on land, as the data quality suffers considerably from scattered energy in the near surface, varying water tables or datum corrections due to the topography. These problems are challenging enough for three-dimensional data interpretation and a great amount of research is carried out to solve these problems. It is thus understood that time-lapse seismic on land and in particular the influence of overburden on time-lapse seismic onshore requires a great amount of research, which easily fills many PhD theses. However, this topic is not the focus of this study.

1.7 Quantitative time-lapse interpretation

Possible errors in seismic data which originate from overburden heterogeneities are outlined in the previous sections. It is subsequently discussed whether these errors also affect the (quantitative) time-lapse data interpretation.

In the past, studying reservoir changes using time-lapse data was done qualitatively by interpreting attribute maps derived from the the baseline and monitor data. For example, Landrø et al. (1999) compare baseline and monitor amplitude maps at the Gullfaks field to detect anomalies which they in turn relate to saturation changes inside the reservoir (Figure 1.21). Another example of qualitative time-

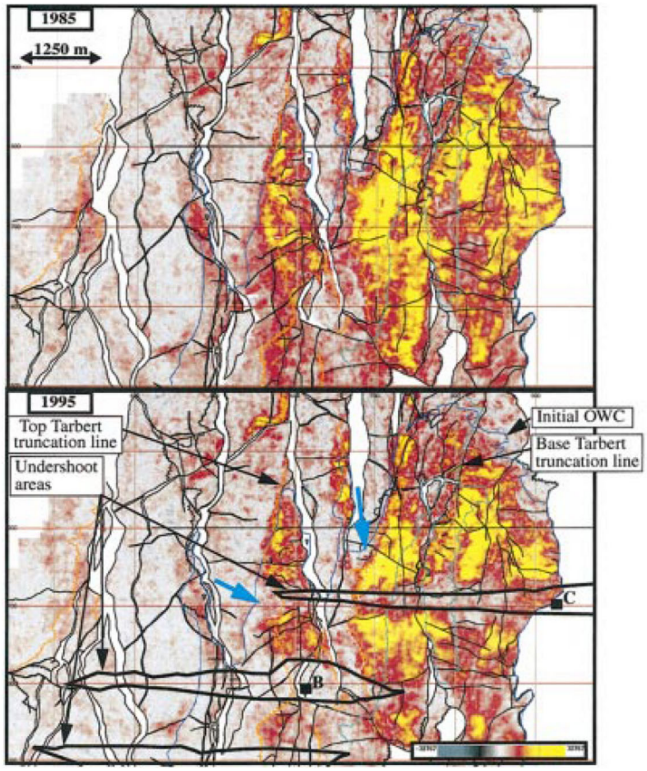

Figure 1.21: Qualitative interpretation of time-lapse amplitude maps. Areas with significant changes are marked with cyan arrows (from Landrø et al. (1999)).

lapse interpretation is given by Furre et al. (2003). The authors use time-lapse amplitude maps to monitor gas injection at the Heidrun field, offshore Mid-Norway. However, recent advances in the field of time-lapse seismic interpretation made it possible to use time-lapse attributes to quantify the changes in the reservoir.

Landrø (1999a) and Landrø (2001) uses AVO attributes and core measurements to discriminate between pressure and saturation changes at the Gullfaks field. Moreover, Lumley et al. (2003) present a method which uses two attributes, such as near and far offset stacks, to separate saturation and pressure changes in the reservoir. Floricich et al. (2005, 2006a) use multiple time-lapse attributes, such as near, mid and far offset stacks, together with well data to apply a multi-attribute inversion scheme and estimate the change in pressure and oil saturation inside the reservoir. Successful use of this method is demonstrated for the Schiehallion field (Figure 1.22), where the quantitative estimate of pressure and saturation change is used to support the decision to drill a new infill well (Floricich et al., 2006b). Moreover,

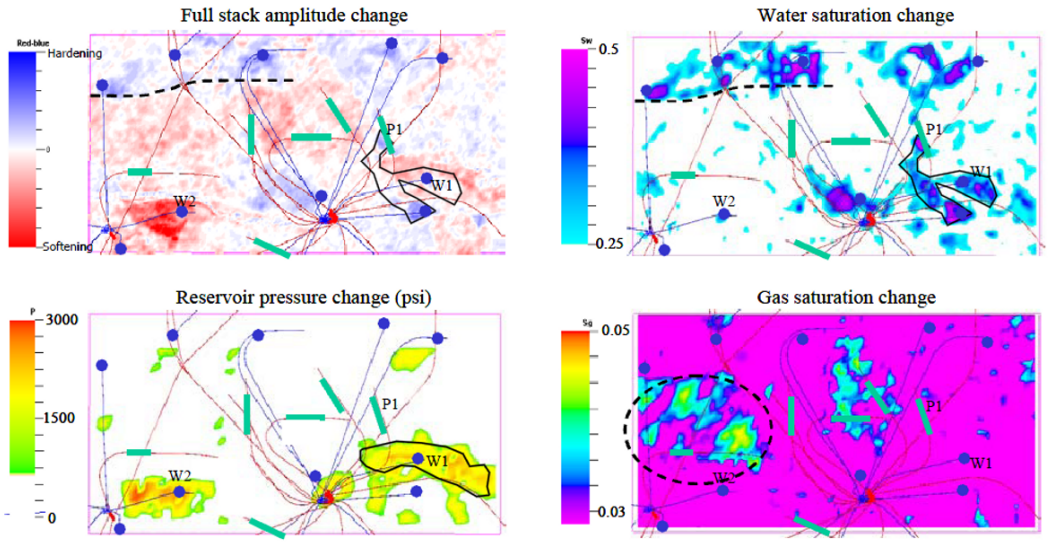

Figure 1.22: Time-lapse amplitude changes as well as pressure and saturation change estimates for the Schiehallion field (from Floricich et al. (2006b)).

Corzo and MacBeth (2006) use time-lapse amplitude information to derive pore pressure changes inside the compacting Valhall reservoir chalk. However, Corzo and MacBeth (2006) conclude that the dominant overburden effect on the RMS amplitude attributes, arising from complex velocity changes above the compacting reservoir, needs to be removed first before an accurate prediction on the pressure change can be made. This is also the conclusion of Angelov et al. (2007) who show that the reservoir pore pressure estimation, using AVO attributes, is highly erroneous if affected by production-induced overburden changes. But not only seismic amplitude or AVO information is used for quantitative interpretation of reservoir changes. Brevik (1999) describes a method which uses the change in P- and S-wave

traveltime along with amplitude attributes to invert for the change in oil saturation and pressure. Furthermore, Hodgson et al. (2007) use time shifts measured in the overburden to predict the pressure change inside the reservoir sands of the Genesis field, Gulf of Mexico.

All the above examples highlight that quantitative time-lapse interpretation methods depend on accurate input data for good performance. However, the preceding sections outline various overburden heterogeneities which affect exactly these time-lapse attributes: amplitude, the AVO response, the seismic velocity of overburden rocks and the measured time shifts above the reservoir.

Thus, it is crucial to investigate how errors in the time-lapse seismic data impede the ability to quantitatively interpret time-lapse changes. No study about the sensitivity of such pressure- and saturation change inversion methods on the seismic attribute errors caused by overburden heterogeneities has yet been done. Up to now, the commonly used measure to quantify the overburden influence on time-lapse data quality is the NRMS measure. However, this measure does not quantify the actual error in the time-lapse attribute nor in the pressure and saturation change estimates, when a complex overburden affects the seismic data quality. Consequently, this study investigates the impact of overburden heterogeneities on the time-lapse amplitude and thus on the oil saturation change estimation (Domes et al., 2009).

1.8 Summary

Various origins of time-lapse noise are discussed. It is first outlined that acquisition non-repeatability affects the time-lapse data quality. Furthermore, the error introduced into the seismic attributes increases when overburden complexities such as scatterers, a shale lens or seawater velocity variations distort the wavefield. Also, several authors state that velocity changes of the overburden rock above a compacting reservoir affect the time-lapse seismic amplitude attribute.

Seismic attributes, however, are more frequently used to quantitatively estimate the pressure and oil saturation changes inside the reservoir. Thus, there is need

to study the influence of the overburden on time-lapse seismic attributes, and in turn on the quantitative interpretation of reservoir changes, in more detail. Apart from the influence of seawater velocity variations on time-lapse amplitude changes, no study on the influence of the overburden on quantitative interpretation of time-lapse amplitude or pressure and saturation change estimates has yet been published to the knowledge of the author. It is important to understand how the errors, which originate from overburden heterogeneities, affect the final time-lapse interpretation data, such as the estimate of oil saturation change inside the reservoir. It is necessary to establish error bounds and to relate the amount of error which can be expected in the time-lapse interpretation to specific overburden complexities.

1.9 Main challenges of the thesis

The main challenge of this work is to test what state-of-the-art quantitative time-lapse seismic interpretation methods can achieve, in the light of noise originating from the overburden in conjunction with acquisition non-repeatability. Three-dimensional subsurface models are built which are conditioned with real field data in order to model seismic pre-stack shot gathers that are comparable to real data. In turn, a time-lapse processing and interpretation workflow is run on the synthetic data. Due to the control over the input parameters, time-lapse interpretation results are compared to reference models in order to quantify the error for a given overburden complexity. Those time-lapse interpretation errors are finally related back to their main origin, whether it is the heterogenous overburden, the non-repeat monitor acquisition geometry or due to seismic data processing. The influence of overburden noise on the saturation change inversion method is investigated for the first time and this research requires a sound understanding of a wide range of geophysical applications, from seismic modelling over time-lapse seismic data processing to the application of the pressure and saturation change inversion method. This work is also challenging with respect to the fact that the study exclusively focuses on building, modelling and interpreting large three-dimensional data sets. Conditioning these models with the right parameters that honour the geology as well as the

physics is not always straightforward.

1.10 Thesis outline

The remainder of this work is divided into the following chapters:

Chapter 2

A general overview of different seismic modelling techniques is provided so that the reader understands the reason for the choice of the NORSAR3D^{TM} ray-tracing package. The general workflow for building an accurate subsurface model is outlined as well as the methodology of how to quantitatively assess the overburden influence on time-lapse interpretation.

Chapter 3

The influence of two distinct sand channels in the overburden on the time-lapse amplitude attribute at the top reservoir level is investigated. The errors in the time-lapse amplitude attribute are separated into errors originating from the acquisition non-repeatability and amplitude errors which are due to the overburden channel. The impact of those errors is assessed by setting the errors in relation to the production signal. The study is further extended to investigate the impact of the two overburden channels on the multi-attribute saturation change estimation method. The derived oil saturation change estimates are compared to the input data of the subsurface model, in order to quantify the effect of overburden and non-repeatable monitor acquisition geometry. A final recommendation is made on how to best extract the time-lapse amplitude attribute from the seismic data in order to minimise overburden effects.

Chapter 4

A layer stripping method is presented which allows to estimate the reservoir reflectivity change without the effects caused by the overburden and non-repeated monitor acquisition. The method is tested on synthetic data and its results are in turn used to improve the oil saturation change estimates. Initial results show that errors caused by overburden channels are favourably reduced.

Chapter 5

This chapter investigates two deepwater stacked reservoir channels. It is tested whether an accurate migration velocity, which includes the velocity changes due to the reservoir production, is necessary to interpret the time-lapse changes. The observed amplitude effects when using the baseline velocity model for migrating the monitor data are quantified and their origin is discussed.

Chapter 6

A ray-tracing model for a compacting North Sea chalk reservoir is set up to study the effect of overburden velocity changes on the time-lapse amplitude attribute. Accurate information about the deformation of subsurface horizons as well as strain in the overburden rocks is obtained from a geomechanical simulation model. Pre-stack shot gathers are modelled and processed to limited stacked cubes. The amplitude effects due to the expanding overburden are then studied at various offsets and finally ranked according to the severity of the distortion.

Chapter 7

The last chapter presents a summary of the conclusions for this work. Moreover, recommendations for future research are suggested.

1.11 Contribution of this work

This work contributes to the knowledge of how accurate current quantitative time-lapse interpretation can be in the presence of overburden "noise". The work provides information on the error in time-lapse amplitude interpretation for three different overburden heterogeneities: Overburden sand channels, stacked deepwater reservoir channels and a geomecanically active overburden. The error is compared to the production signal as well as to commonly used acquisition non-repeatability measures. Furthermore, the limits of a current saturation change estimation method are discussed in detail and error bounds are given depending on the input time-lapse attribute used. It is briefly shown where the current multi-attribute inversion method breaks down and therefore outlines areas of future research to improve the stability of such methods in the presence of noise.

A layer stripping method which removes overburden errors is presented and tested on synthetic time-lapse data. The results are promising and significantly improved over an earlier application of such an approach. The ability to correct for overburden errors in time-lapse data may be helpful in the future development of quantitative time-lapse interpretation methods. Finally, velocity changes due to vertical straining of the overburden rocks are studied for a compacting chalk reservoir. The hypothesis of several authors that the time-lapse amplitude is affected by such overburden velocity changes if they are not included in the monitor migration velocity model is confirmed.

Chapter 2

Modelling the overburden influence

This chapter provides a review of different seismic modelling methods. Furthermore, reasoning is given for the specific choice of the NORSAR3D^{TM} ray-tracing package for modelling the seismic pre-stack data used during later studies. The principal workflow which is used to study overburden effects on time-lapse data is presented. Finally, pitfalls and limitations that exist in such a modelling approach are addressed.

2.1 Methodology

Modelling wave propagation in the earth has a lengthy history. One of the early applications of modelling seismic wave propagation is described by Lysmer and Drake (1972), and discrete solutions to the elastic wave equation were already developed forty years ago (Alterman et al., 1970). Apart from the application of finite-difference schemes in the seismic forward modelling step, much work has been done on the reverse time migration, using finite-differences as well (Baysal et al., 1983). Over the last decades, various modelling techniques that allow for calculating the seismic response of the earth have been developed. An overview of this wide research area is given in the SEG reprint series on seismic modelling (Kelly and Marfurt, 1990).

Before starting with the investigation of overburden effects on time-lapse seismic attributes, the methodology and the principal workflow for the studies is outlined. There are several questions that need to be answered in order to understand the approach taken and the data used for this project. The most important questions are:

- What is the overburden and why is it important at all?
- What generalised workflow is used to provide the answers?
- What software requirements are needed in order to obtain conclusive results?
- What data will be used and how will it be conditioned?

First the most obvious question: What is considered to be overburden? Section 1.4 summarises the major overburden features important in hydrocarbon exploration, but how does this fit into the research presented here? For simplicity, everything that lies above the reservoir under investigation is considered overburden. Whether it is sea water, unconsolidated sediments, rock or another reservoir. Therefore, in order to study the influence of the overburden in time-lapse seismic, either of the following scenarios have to happen between baseline and monitor survey:

- Change in the overburden, no change in the acquisition parameters
- No change in the overburden, change in the acquisition parameters
- Change in the overburden, change in the acquisition parameters

The most common thought about the influence of the overburden on time-lapse seismic data is that the overburden undergoes physical changes due to production from the reservoir. However, repeat seismic measurements can only be considered ideal if the acquisition parameters are kept the same for any repeat survey. Therefore, a change in the acquisition parameters in conjunction with a complex overburden will also be considered to be an overburden effect. Studying overburden effects in a systematical manner requires time-lapse data which can be controlled and quantitatively described. Overburden effects might be inherent in real data, but we lack the possibility to compare such data against data without overburden effects. Consequently, modelling of synthetic pre-stack seismic data is used in order to quantitatively interpret the impact of the overburden on time-lapse seismic data. The modelling approach should be of such a nature that any conclusions drawn are also applicable to real time-lapse data. That involves assembling subsurface models from real input data, such as interpreted horizons from seismic sections, but not only in a two-dimensional sense but as a full three-dimensional model. In the next step, synthetic seismic data are generated using the assembled subsurface model and real seismic acquisition geometries, in order to incorporate actual streamer feathering issues into the synthetic data. Any change in the parameters of the overburden/subsurface model or the seismic acquisition geometry can now be quantitatively related to changes in the time-lapse seismic response. The challenge now is to set up three-dimensional subsurface models and generate seismic data which are accurate enough to draw meaningful conclusions as well as highlight even subtle changes. The next sections further explain the choice for the seismic modelling algorithm used, which in turn demands a specific subsurface model assembly. Comparison is made between different approaches and the reasoning is given for the specific choice.

2.2 Seismic modelling techniques

Modelling the overburden has to take into account the real structure and parameters of the overburden and the reservoir. Therefore, the seismic modelling algorithm has to be sophisticated enough to correctly handle the complexity of three-dimensional models and complex wave propagation. In addition, seismic modelling should also be feasible with the computational resources that are available within the Edinburgh-Time-Lapse-Project (ETLP) research group. Several methods for seismic modelling have been developed to date and each has its unique advantages and disadvantages. Table 2.1 summarises the most common techniques for seismic modelling (Carcione et al., 2002; Krebes, 2004; Kennett and Harding, 1985).

Direct Methods	Finite-Difference (FD) Pseudospectral (PS) Finite-Element (FE)
Integral-Equation Methods	Huygens' Principle: Domain Integral-Equation Method Boundary Integral-Equation Method
Matrix Methods	Propagator Matrix Method Reflectivity Method Recursive Reflectivity Method
Asymptotic Methods	Ray-Tracing Wavefront Construction

Table 2.1: Seismic modelling methods

2.2.1 Direct seismic modelling methods

The most direct approach to seismic modelling is to numerically solve the appropriate wave equation (2.1).

$$\left[\rho c^2 \nabla \cdot (\frac{1}{\rho}\nabla)\right] p + f = \frac{\partial^2 p}{\partial t^2} \tag{2.1}$$

This is a second-order partial differential equation, where p is the pressure, c the compressional wave velocity, ρ the density and f the body force (Aki and Richards, 2002). The main idea behind all direct methods is to compute the wavefield (pressure

or displacement) at a discrete set of closely spaced grid points by approximating the derivatives occurring in the wave equation with finite-difference formulas and recursively solving the resulting difference equations. Differential operators are evaluated in the space and time domain for the finite-difference (FD) and the finite-element (FE) method. Pseudospectral (PS) methods make use of evaluating one of the difference operators in the wavenumber domain. Details on the mathematics of these methods can be found in, for example, Carcione et al. (2002), Kelly et al. (1976) and Kelly and Marfurt (1990).

The application of direct numerical methods is not trivial and involves a careful gridding of the model in space and time in order to suppress numerical grid dispersion or instability. Furthermore, setting proper absorbing boundary conditions is not straightforward. However, besides those more technical disadvantages, direct methods also have advantages. The main one is that finite-difference schemes produce the full wavefield without additional work done by the user to specify the wave types at each interface. All different types of waves such as reflection, refraction, multiples, converted waves and surface waves are computed with the correct amplitudes and phases. Depending on the point of view, the advantage of modelling all wave conversions without explicit user interaction might also be seen as a weakness. It is not possible to select only one specific wave conversions type at an interface of interest. An example of a full wavefield synthetic shot record is displayed in Figure 2.1. Direct methods can also handle a sharp contrast in material properties in the subsurface model. There are no smoothness constraints for this method. However, finite-difference methods are very costly in computer resources and CPU time. Indeed, computing power has always been the limiting factor ever since finite-difference methods were introduced. Nowadays, two-dimensional computations take only a matter of minutes, but calculating the wavefield in a three-dimensional model is still a tremendous task and only feasible on large high-performance computing grids. In a recent study, Houbiers et al. (2008) describe the use of finite-difference modelling to understand imaging problems at a reservoir in the Norwegian Sea. Modelling one shot record in three dimensions took one whole day on one CPU. A typical minimum number of shots for a full survey is in the region of 5000. Therefore, full wavefield modelling is done within twelve days on 420 computer nodes.

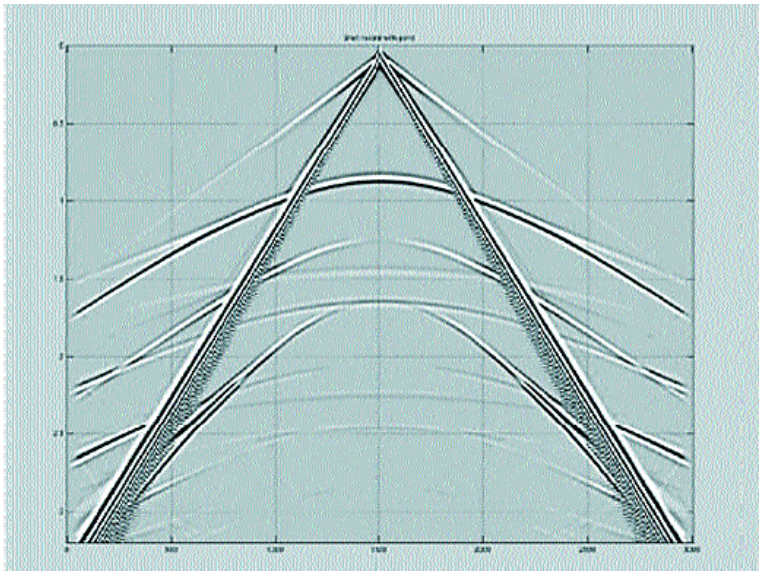

Figure 2.1: 2D synthetic seismic shot record produced by a finite-difference method (from Krebes (2004)).

Besides this long runtime, only frequencies up to 23Hz are modelled. Even more CPU time is needed in order to model higher frequencies in the synthetic seismic data, because the modelling grid has to be refined in order to avoid instability and dispersion with increasing frequency content. Therefore, the limiting factor for applying direct modelling methods is the number of CPUs available.

2.2.2 Integral equation methods

Integral equation methods are derived from Huygens' Principle, which states that a wavefield can be thought of as superposition of waves originating from point sources. The main application of this method is to solve scattering problems. The method is well suited to study wave propagation in media with explicit boundary conditions or discontinuities in properties, such as fractured rock (Liu et al., 1997) or the radiation of seismic sources on boreholes (Dong et al., 1995).

2.2.3 Matrix methods

Matrix methods are ideal for computing synthetic seismograms for a vertically heterogenous stack of layers. In addition to the condition of being a laterally homoge-

nous stack of layers, each layer in the stack has to be in welded contact with its subsequent layer. Thus, the x, y and z components of displacement, $\mathbf{u}$, and traction, $\mathbf{T}$, are continuous across the interface. The displacement and traction components can be continued through the stack of layers for plane wave propagation. Using the propagation matrix, $\mathbf{P}(\mathbf{z}, \mathbf{z_0})$, displacement and traction can be computed anywhere in the medium (Equation 2.2).

$$\mathbf{f}(\mathbf{z}) = \mathbf{P}(\mathbf{z}, \mathbf{z_0})\mathbf{f}(\mathbf{z_0}), \quad \mathbf{f} = \begin{bmatrix} \mathbf{u} \\ \mathbf{T} \end{bmatrix} \tag{2.2}$$

The propagator matrix contains the medium parameters, frequency, ray parameter and the phase factors for the plane waves. Figure 2.2 is a schematic representation of the reflection and transmission response for a stack of three layers. The total reflection of the stack is the sum of all upgoing plane waves (including multiples). The total transmission is the sum of all transmitted, downgoing plane waves. The

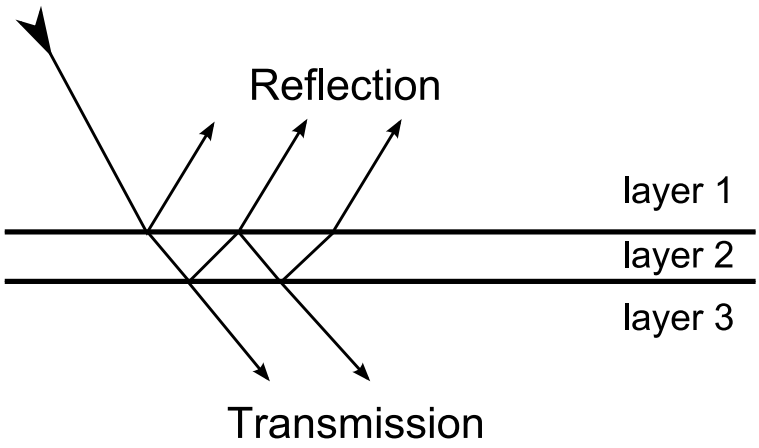

Figure 2.2: Schematic representation of the stack's reflection and transmission component

stack's reflection and transmission coefficients are a function of the ray parameter, p, and the frequency, ω. The reflected waveform recorded at a receiver is obtained by integrating over all ray parameters and frequencies of plane waves reflected at the layer boundaries. Similarly, the transmitted wavefield is obtained by integrating over all plane waves transmitted through the stack. The recursive reflectivity method (e.g. Kennett (1983)) evaluates the transmission and reflection matrices for individual layers and interfaces in the model. This has the advantage of being numerically stable, in contrast to former approaches which used the exponential decay

of wave amplitudes in individual layers instead (Gilbert and Backus, 1966). Furthermore, better control over different wave types is given at each interface, as well as better control over the inclusion of multiples in the stack reflection and transmission matrix coefficient. Matrix methods are mostly used for wavefield extrapolation and wave equation migration methods. Although the summation over all possible plane waves can be used to represent a curved wavefront, matrix methods are not well suited for modelling pre-stack seismic gathers in an heterogenous earth for arbitrary cases. The assumption of a laterally homogeneous velocity and density field is not well suited when modelling a heterogeneous earth response.

2.2.4 Asymptotic methods

Ray-tracing methods are also called asymptotic methods, because approximations from geometrical optics can be used if the frequency is high enough. However, defining "high frequency" is still a rule of thumb. In general, medium parameters should not change much over the distance of the dominant wave length (Krebes, 2004). Under the condition of high frequency the traveltime, τ, of the wave from the source to a point $\mathbf{x} = (\mathbf{x}, \mathbf{y}, \mathbf{z})$ can be calculated using the eikonal equation (2.3), where $c(\mathbf{x})$ is the velocity of the P- or S-wave at point $\mathbf{x}$.

$$(\nabla\tau)^2 = \frac{1}{c(\mathbf{x})}\,. \tag{2.3}$$

In order to calculate the ray amplitude, $A(\mathbf{x}, \mathbf{x_S})$, for a wave travelling from the source location, $\mathbf{x_S}$, to a point, $\mathbf{x}$, one has to solve the transport equation (2.4)

$$2\nabla A \cdot \nabla\tau + A\Delta\tau = 0\,. \tag{2.4}$$

Tracing rays between known source and receiver points in a complex, heterogenous media is done by an iterative method. A range of rays leaving the source location with different take-off angles are traced through the model and their respective arrival location is determined. If the rays do not hit the receiver location, the take-off angle is adjusted and new rays are traced. This can be quite a tedious trial and error

approach which is not recommended for fast ray-tracing in structurally complex models. Ideally, one wants to solve the eikonal and transport equation numerically on a regular grid in the model. In that way, information about the traveltime, $\tau(\mathbf{x}, \mathbf{x_S})$, and amplitude, $A(\mathbf{x}, \mathbf{x_S})$, is known without the need of iteratively changing the take-off angle of the rays. There are two major methods of doing this:

- FD methods for solving the eikonal and transport equation on a regular grid
- Wavefront construction to solve the eikonal and transport equation on a regular grid

FD methods used to solve the eikonal and transport equation are extensively studied (e.g. Vidale (1990) and Kim and Cook (1999)). The traveltimes and amplitudes are directly calculated on a defined grid. The FD methods are computationally very efficient and not affected by shadow zones in the model. The biggest disadvantage is that only the traveltime of the first arrivals is easily calculated. Also, the implementation of multivaluedness due to caustics is not trivial. The propagation of a wavefront calculated with the finite-difference solution to the Eikonal equation is shown in Figure 2.3(a). Only first arrivals are determined with this method.

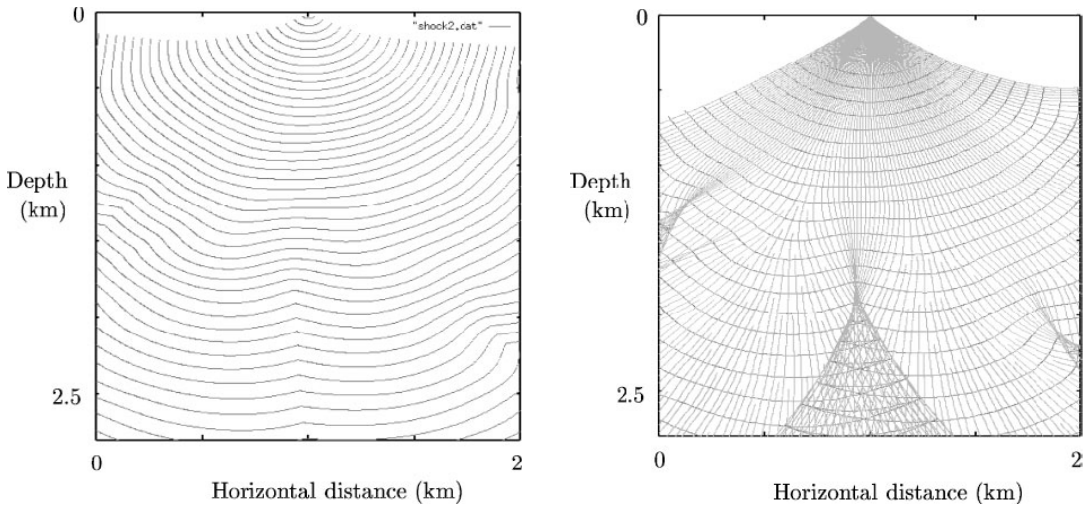

(a) Finite-difference solution of the Eikonal equation

(b) Wavefront construction

Figure 2.3: Propagating wavefront using the finite-difference solution to the Eikonal equation (a) and the wavefront construction method (b) (from Carcione et al. (2002)).

The wavefront construction method (Vinje et al., 1993, 1996a,b) is able to calculate higher order arrivals for the same model (Figure 2.3(b)). The idea behind the wavefront construction method is that rays are traced from a source location into the medium in small time steps, Δt. The wavefront is therefore calculated at discrete times, $t = m\Delta t$. The distance between two adjacent rays is evaluated after each time step. If rays are too far apart, a new ray is started inbetween in order to obtain an even distribution of rays in the subsurface model. New rays are also interpolated if traced rays hit pinch-outs in the model, in order to avoid artificial shadow zones. Parameters controlling the divergence of rays and therefore the ray coverage in the model have to be defined by the user. Finally, a synthetic seismogram is computed using the registered events at the receiver location. Not only is the wavefront construction method able to calculate higher order arrival times at the receiver locations, its implementation by Vinje et al. (1993) is also more accurate in calculating the traveltime compared to the finite-difference method for solving the Eikonal equation, as described by Vidale (1990) (Figure 2.4). The error is calculated from the same data shown in Figure 2.3. The wavefront construction

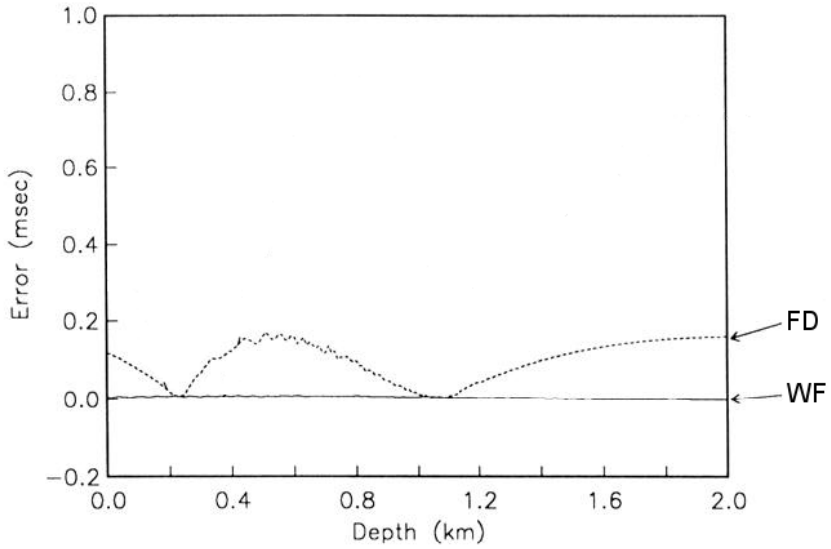

Figure 2.4: Error in traveltime calculation between a finite-difference solution to the Eikonal equation (FD and the wavefront construction method (WF) (modified from Vinje et al. (1993)).

method is therefore the preferred choice of all ray-tracing methods. The method is capable of computing all necessary kinematic and dynamic parameters to generate synthetic seismograms at any given receiver location in the model. Moreover, the

wavefront construction method is implemented in the NORSAR3D^{TM} ray-tracing package.

However, as mentioned earlier, all ray-tracing methods are high frequency methods, which implies that the model parameters have to be smoothly varying. Densities, P- and S-wave velocities have to be smoothed in order to avoid failure of the ray-tracing algorithms. Unfortunately, there is no mathematically-derived definition of what to consider smooth. As a rule of thumb, parameters should not significantly change over the distance of one quarter of the seismic wavelength. This smoothness criterion illustrates another drawback of ray-tracing methods. Sharp discontinuities can not be handled accurately. In addition, diffractions at an interface pinch-out are not modelled. Multiples and converted waves can be modelled using ray-tracing algorithms, but the type of conversion or reverberation has to be explicitly defined for each interface in the subsurface model. Building an appropriate subsurface model for ray-tracing therefore requires more work, because horizons have to be explicitly defined and included in the model. The main advantages and disadvantages for finite-difference seismic modelling of the wave equation and ray-tracing using wavefront construction are gathered in Table 2.2. Beside the limitations in the ray-

FD seismic modelling		WF seismic modelling	
Pros	Cons	Pros	Cons
Full wavefield including all multiples and wave conversion	Slow computation time	Very fast computation time	Smooth model
Very accurate	No identification of wave types	Accurate in traveltime and amplitude	No diffractions; multiples and wave conversion explicitly defined
Fast model setup	Problematic boundaries	Identification of wave types	Labour-intensive model building

Table 2.2: Advantages and disadvantages for direct seismic modelling using finite-differences and ray-tracing using the wavefront construction method.

tracing method, the software package NORSAR3D^{TM} is chosen for generating the pre-stack synthetic seismic gathers in the proceeding studies. The computation time

of three-dimensional finite-difference seismic modelling is prohibitive on a large scale which is why it is seldom used for modelling full field synthetic seismic data. The next section discusses the general workflow for assembling valid ray-tracing models.

2.3 Assembly of the 3D subsurface model

The NORSAR3D^{TM} software package is chosen as the best available option to conduct the seismic modelling for the overburden studies. Limitations and constraints for the ray-tracing method are outlined in Section 2.2.4. This section provides an overview of how subsurface models are assembled, what data are used and how such data are generated or obtained. Using the subsequent information the reader would be able to reproduce the subsurface model with the right data at hand. It is the intention to describe any data that are used or derived in a way that the reader is fully informed about assumptions included in the model building process which might later also affect the synthetic data and any derived attribute. The following data are needed to assemble a subsurface model:

- Horizons (Interface) in depth
- Velocity (P- and S-wave) information
- Density information

The simplified workflow for building a ray-tracing model consists of first importing depth horizons, then filling the space in between the interfaces with velocity and density information. Having a common coordinate system is of uttermost importance. A single Universal Transverse Mercator (UTM) projection is used throughout all data imported into the subsurface model. That way horizons, velocity and density fields lie on top of each other with an accuracy of $\pm$1m. The common coordinate grid problem should not be underestimated. Data from different domains, such as reservoir engineering data, seismic volumes or surface acquisition data are seldom on a common reference grid. It is common to have the data on a grid that is best suited for the task:

- Seismic interpretation horizons on an inline/crossline grid
- P1/90 navigation data on local UTM projections
- Reservoir simulation on i, j, k corner point grid (i, j, k $\in \mathbb{N}$)

If legacy data are involved, it becomes even more difficult to get hold of the exact grid-coordinate system information.
In addition, there are important assumptions when using this ray-tracing approach:

- Smoothness of the ray-tracing velocity and density field
- Smoothness of the ray-tracing model horizons
- The migration velocity model is derived from the ray-tracing velocity field in this study, hence a smooth velocity is also used for the seismic data processing

Horizons for the model building

The challenge in this overburden study is to accurately assemble a three-dimensional subsurface model that contains the most important structural features and preserves the complexity, but is simple enough to work with. Real data is therefore ideally suited to be incorporated into the process. Interpreted seismic reflection events in post-stack seismic cubes are used to define the interfaces in the subsurface model. In most cases, seismic interpretation horizons are extracted from the depth migrated or depth converted post-stack seismic data. In the workflow, the Petrel^{TM} software is used as a hub to visualise input as well as the output data of this study. Thus, the interpreted depth horizons are loaded into a Petrel^{TM} project where they are regridded on a user-defined regular grid with dimensions of 10m x 10m (Figure 2.5). In the next step, those horizons are exported to IRAP^{TM}-ascii files which can then be imported into the NORSAR3D^{TM} model building tool. Further smoothing is done with a filter of width 200m for the overburden horizons, while the reservoir horizons are smoothed using a filter of width 50m. Hence, much of the reservoir surface structure is conserved, whilst honouring the smoothness constraint for the ray-tracing. A considerable amount of work has to be done on the quality control

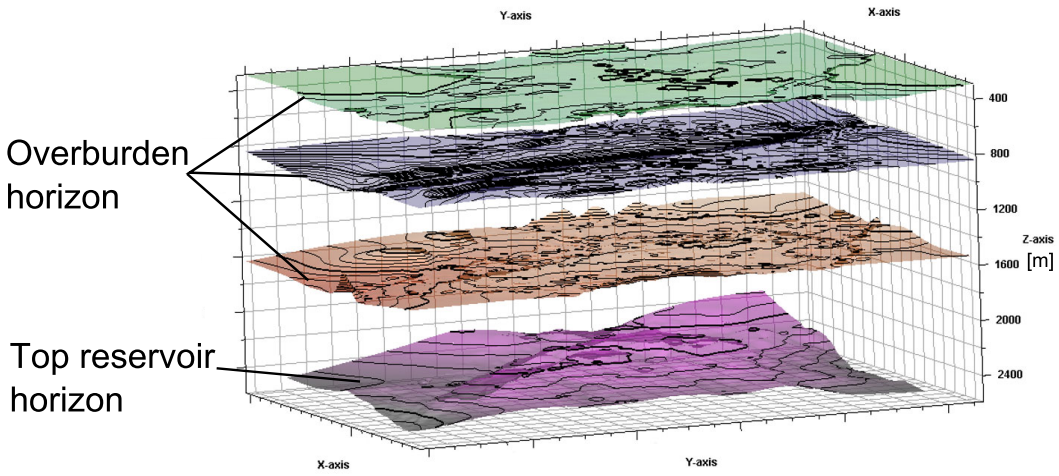

Figure 2.5: Typical un-smoothed depth horizons interpreted from seismic data and used for assembling the ray-tracing model.

and processing of the meshed horizons. The reservoir horizons are checked for any points where they cut each other due to imperfect meshing. Those points are in turn edited out, otherwise the ray-tracing algorithm breaks down in this area. Additional work is done on editing overburden features, such as overburden channels. In order to build an overburden sand channel, or a reservoir channel, surfaces have to be cut and intersected in a way that the resulting structure is a closed block (Figure 2.6). It is a special requirement of the software that the velocity and density properties can only be defined inbetween interfaces or within a closed box. As this is not an automated process it has to be done for each closed structure in the model. It is obvious that the workload increases with increasing overburden or reservoir model complexity.

Importing properties into the subsurface model

Velocity information for the overburden is extracted from a pre-stack depth migration velocity model and smoothed with a lateral filter width of 250m. P-, S-wave velocity and the density for the reservoir layers is obtained from a reservoir simulation model after petro-elastic transformation. Smoothing is performed with a lateral filter width of 100m in order to preserve most of the changes occurring in the reservoir. Lateral smoothing of the properties ensures that the high frequency assumption is valid and synthetic seismograms generated are accurate. Nevertheless,

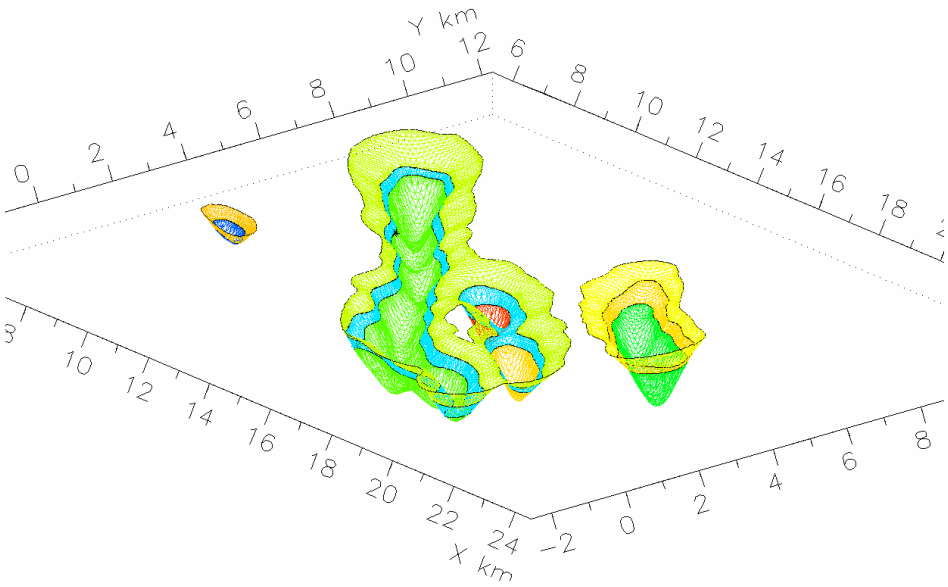

Figure 2.6: Editing complex structures in the ray-tracing model. A channel cutting through model layers is split up into various segments indicated by individual colours.

the lateral scale of the heterogeneities that are studied should be large enough, so that the smoothing of the velocity and density field does not render them indistinguishable from the background trend. Therefore, the high frequency assumption of the ray-tracing seismic modelling requires a minimum size and velocity contrast for the model elements. This in turn affects the modelled seismic data, which sample the major heterogeneities, but lack more subtle events such as scattered or diffracted seismic wave energy in the recorded seismograms. These subtle effects might cause additional errors in the seismic time-lapse data, however, it is assumed that these effects are not the dominant source of overburden induced error. However, only a finite-difference seismic modelling study using the same input data could provide insight to whether or not these small scale effects change the overall overburden induced errors. Figure 2.7 shows a depth slice through a smoothed P-wave velocity field imported into a three-dimensional ray-tracing model. A description of the petro-elastic transformation applied to the Nelson simulation data can be found in MacBeth et al. (2005), it is not discussed in this thesis. Furthermore, many authors contributed in general to this topic with either laboratory measurements, field data examples or theoretical work. A comprehensive overview of this topic is summarised by Mavko et al. (2009).

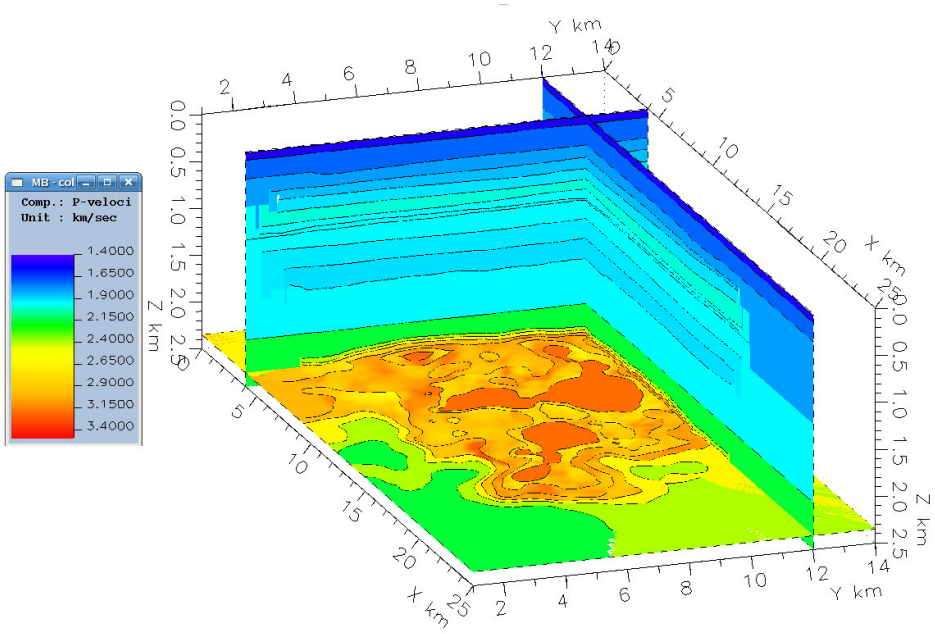

Figure 2.7: Smooth P-wave velocity field used in the ray-tracing model.

2.4 Generating pre-stack seismic data

The next step after building a ray-tracing model is the ray-tracing itself. Generating synthetic seismic data requires calculation of the traveltimes and amplitudes for given source- and receiver locations. There are a handful of important parameters that need to be set before the ray-tracing can start. The maximum distance and maximum angle between rays in the model and the time interval between wavefronts significantly influence the ability to trace rays to every point in the model as well as the overall time for the calculation. Therefore, test shots are set up at various locations throughout the model in order to determine the trade-off between the CPU time required per shot and a uniform ray coverage of the subsurface. Figure 2.8 shows a series of shot gathers recorded at the same shot location, but using different ray-tracing parameters. In each shot gather, traveltimes are recorded for events arriving at the receiver locations. If these traveltime curves are not continuous and show holes, it is an indication that events are missing at the receiver location (Figure 2.8(a)). This can either be due to wrong ray-tracing parameters or an actual shadow zone in the model. The randomness in which such holes occur in Figure 2.8(a), however, indicates that the chosen ray-tracing parameters need refinement. Figures 2.8(b) to 2.8(f) demonstrate that those missing events are recorded if proper

parameters are chosen. Therefore, the trade-off is between the time one shot needs to be computed and the maximum number of events being recorded.

Table 2.3 relates the number of recorded events to the overall CPU time used to trace each shot. The aim is to record the maximum number of events within the shortest computational time. Various test shots and adjustments of parameters throughout the model are therefore needed in order to obtain the most suitable set of ray-tracing parameters. The variation in computational time is large with the fastest run being less than ten minutes and the slowest twenty six minutes. An upper boundary for the maximum number of events which can be recorded is obtained by multiplying the number of interfaces in the model by the number of receivers. In case of the presented Nelson model, 4800 (20 layers x 240 receivers) events would be the maximum number. The numbers of traced events in Table 2.3 are close to this maximum number, considering that shallow layers (e.g. seabed) only have reflection events in the near offset range due to missing reflections beyond the critical angle. Therefore multiplying the number of receivers with the number of layers is always an overestimate. Real seismic navigation data are used in the modelling study in

Figure	Number of events recorded	CPU time [min:sec]
2.8(a)	3765	09:40
2.8(b)	3954	26:43
2.8(c)	3954	26:39
2.8(d)	3956	18:42
2.8(e)	3964	14:31
2.8(f)	3984	11:41

Table 2.3: Determining the trade-off between recorded events and ray-tracing parameters.

order to accurately investigate the effect of non-repeatable acquisition geometry. The navigation data files use a common format called P1/90 which is defined by the United Kingdom Offshore Operators Association (UKOOA). Those files should be on a common coordinate system, however, as many years pass between repeat surveys, the navigation data tend to be recorded in different coordinate projections.

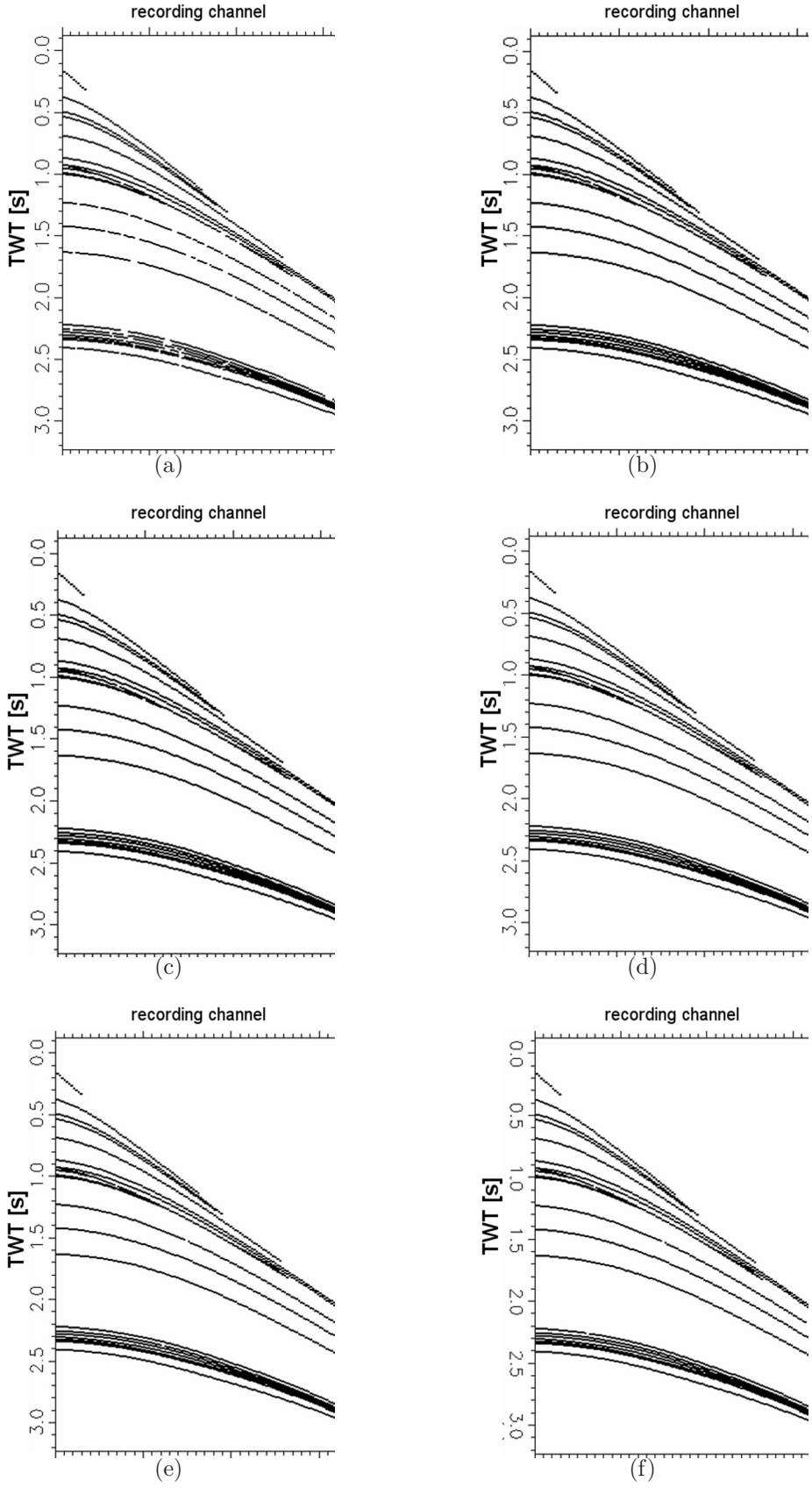

Figure 2.8: Synthetic test shot gathers to determine suitable ray-tracing parameters. Plot (a) to (f) show traveltime curves for the same shot location but with different ray-tracing parameters.

An extensive number of tools have been written during this study in order manipulate those data files. Major tasks when preparing the navigation data for import into the ray-tracing model are:

- Process shot and receiver coordinates of repeat surveys to match the baseline reference coordinate system
- Select specific shot and receiver pairs to be included in the seismic modelling

2.5 Seismic processing applied to the synthetic pre-stack data

Processing the pre-stack synthetic gathers to stacked volumes is done in a straightforward way, and use is made of the known interval velocities extracted from the ray-tracing model. The general processing flow is described in the next section, however, detailed information on the processing is provided in the subsequent chapters where appropriate.

First, a zero phase wavelet (e.g. Ricker 30Hz zero phase) is used to generate the pre-stack seismic gathers. This eliminates the need to process the seismic data to zero phase using deconvolution methods. The pre-stack data are imported into the ProMAX^{TM} processing software where the proper CMP bin spacing and geometry is assigned. The migration velocity is obtained by converting the ray-tracing subsurface P-wave interval velocities in depth into root mean square (RMS) velocities in time using the Dix formula (Dix, 1955):

$$V_{rms}^2 = \frac{\sum_{i=1}^{n} V_i^2 \Delta t_i}{\sum_{i=1}^{n} \Delta t_i} \quad . \tag{2.5}$$

V_i and Δt_i are the interval velocity and the normal incidence traveltime of the ith layer, respectively. V_{rms} is the RMS velocity of the stack of layers ($i = 1...n$) at two-way traveltime, $\sum_{i=1}^{n} \Delta t_i$.

This RMS velocity can then be used for the migration of the seismic shot gathers.

The time intensive task of picking the migration velocities in semblance analysis plots is therefore eliminated. Additional smoothing of the RMS velocity field ensures that the migration operator applied to the seismic data performs properly. Finally, post-stack regridding prepares the data for further time-lapse studies.

This workflow yields a very accurate (best case) migration velocity model, which cannot be resolved by means of conventional velocity analysis. Perturbation of this highly accurate velocity field might thus be done in an additional study in order to investigate the impact of the geometric repeatability in conjunction with a less well resolved velocity field. It is assumed that the error in the seismic data and thus the impact of the geometric mis-positioning increases in case that the subsurface velocities are not well known, but additional research is needed to verify this assumption.

2.6 How to assess the overburden influence?

Chapter 1 shows that errors originating from sand channels, faults or geomechanical changes above the reservoir are supposed to impact the time-lapse data. However, such errors are not easy to extract from real data, because they are inherent in the data and no comparison to a "no overburden heterogeneity" reference case can be drawn. Therefore, it is a natural choice to model those overburden complexities due to the great control one has over the model setup. The main methodology behind using synthetic models in order to study overburden effects is outlined for the proceeding overburden channel study of the Nelson Field (see Chapter 3). Sand channels of lower and higher velocity compared to the surrounding rock sit above this reservoir and are known to affect the seismic data quality. Figure 2.9 outlines the essential steps to evaluate the influence of overburden channels on the time-lapse seismic data using four synthetic ray-tracing models. The first pair of ray-tracing models contains changes in the reservoir between baseline and monitor survey due to production, but no channels in the overburden (Figure 2.9, left-hand side). These two models provide a reference case for later comparison and will be denoted as models excluding overburden complexity (ExclOB) in the proceeding text. A second

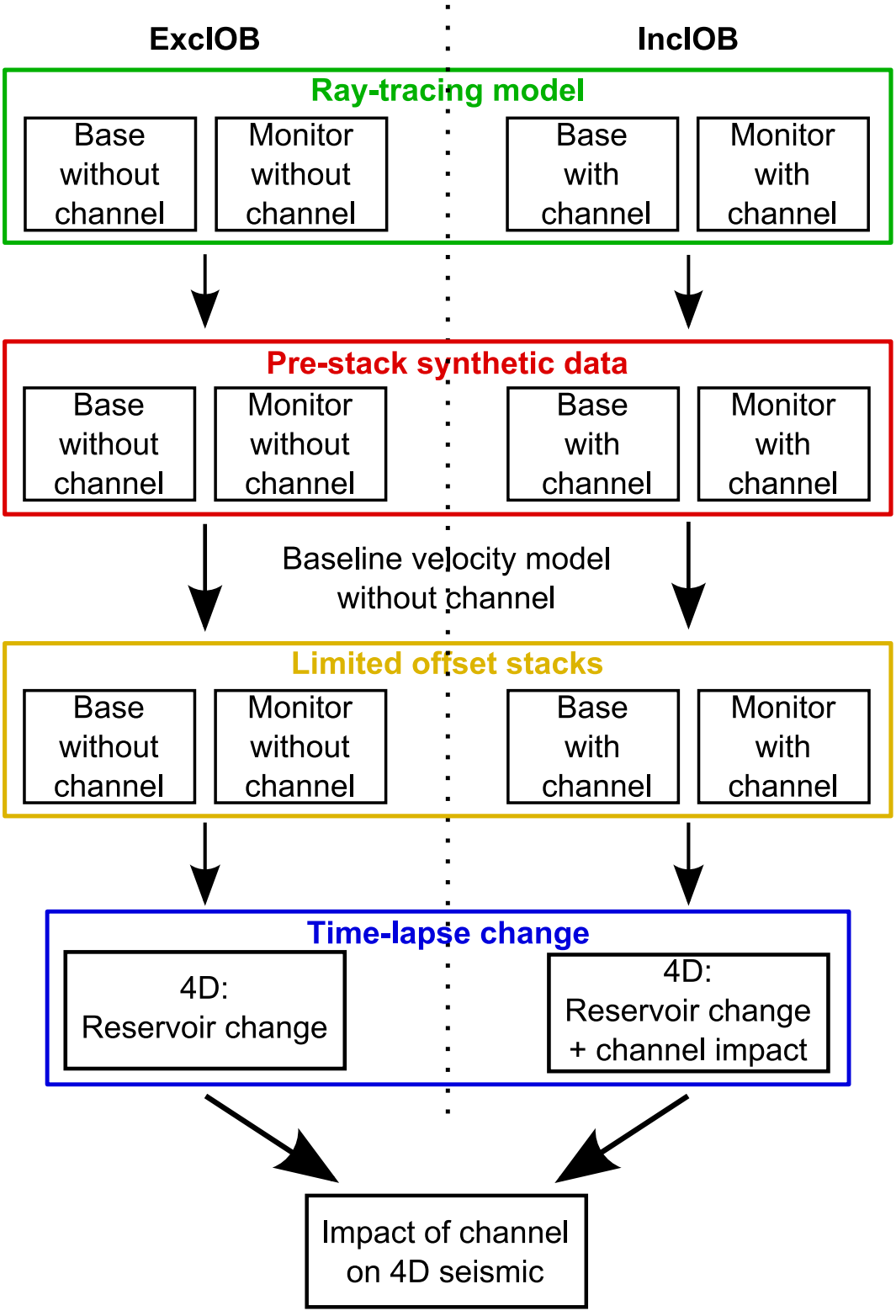

Figure 2.9: Modelling methodology for separating the overburden response from the reservoir response using synthetic ray-tracing models.

pair of ray-tracing models contains the same reservoir changes and in addition, the sand channels in the overburden (overburden complexity) (Figure 2.9, right-hand side). This case will be referenced as models including overburden complexity (InclOb). In turn, pre-stack synthetic shot gathers are generated for all of the four models (Figure 2.9, red box). The next step is crucial to understand. Only one velocity model (Baseline ExclOB) is used to image all four pre-stack seismic volumes. It is common industry practice to use the baseline velocity model even for processing the monitor seismic data. Updating any velocity changes in the migration velocity model due to reservoir changes is not feasible. In addition, those velocity models are coarse and do not contain small wavelength overburden features such as the overburden channels.

The ExclOB baseline velocity model represents such a coarse scale velocity model due to the fact that it does not contain information about the overburden channels. The imaging of base and monitor ExclOB data with the baseline ExclOB velocity model thus represents the standard approach in time-lapse studies. The baseline ExclOB velocity model is also used to migrate the InclOb case in order to reproduce this inability of accurately capturing the overburden complexities in the velocity model. The effect of the overburden channel on the wavefield propagating in the subsurface is therefore not fully accounted for in the InclOb case, because the velocity information about the channel is missing. The processed seismic InclOb data therefore contains the possible channel imprint in addition to the reservoir changes. The ExclOB, however, contains only the production effects, not the overburden channel imprint. Therefore, taking the difference between base and monitor ExclOB reveals the changes solely from reservoir production, whereas the difference of base and monitor InclOb reveals changes due to reservoir production as well as the overburden imprint (Figure 2.9, blue box). Consequently, subtracting the two time-lapse datasets eliminates the common signatures due to the reservoir production and highlights the impact of the overburden channel in the time-lapse data. It is stressed once more that the difference of two time-lapse differences highlights the overburden influence; a reference case with no overburden heterogeneity is always needed in addition to the models including the overburden complexity.

2.7 Why is 3D modelling imperative for the study?

A natural question after discussing all the work involved to generate synthetic three-dimensional pre-stack data is if such effort is really necessary, or if more simplistic two-dimensional modelling would do as well? First, the study should be realistic, therefore shooting 3D seismic is the industry standard for time-lapse studies. This qualitative argument can be backed up with facts. Varying acquisition geometries are an integral part of this study. However, a non-repeat 2D line cannot accurately capture the time-lapse change in the reservoir, because it illuminates different subsurface points. Figure 2.10 shows part of a CMP grid with the baseline and monitor streamer position. The monitor line has a feathering angle of 10° against the baseline and therefore mostly illuminates different subsurface points. Only a few CMP bins are in common between both surveys (Figure 2.10, green cells). This feathering angle is on the high side of what is observed in the North Sea, but certainly well within the expected feathering angles for surveys acquired in the Gulf of Mexico (see Section 1.3.1). Taking the difference between these two datasets will not result in the difference of the same subsurface points and is therefore erroneous. Shooting 3D

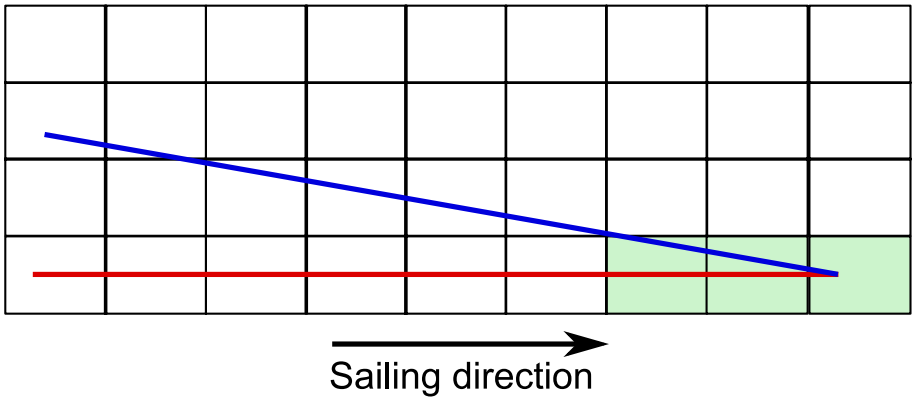

Figure 2.10: Schematic CMP bin cell coverage for a 2D non-repeat line. The red line indicates the baseline streamer position, the blue line the monitor streamer position. The feathering angle is 10°. Common CMP bin coverage is marked by pale green cells.

seismic surveys overcomes this issue of imaging the same subsurface points for non-repeat monitor acquisition geometries. Figure 2.11 shows that a monitor streamer feathering of 10° still results in illuminating the common mid-points. However, those common mid-points have different source and receiver positions, or azimuth for the

baseline and monitor survey. The difference in azimuth in conjunction with a com-

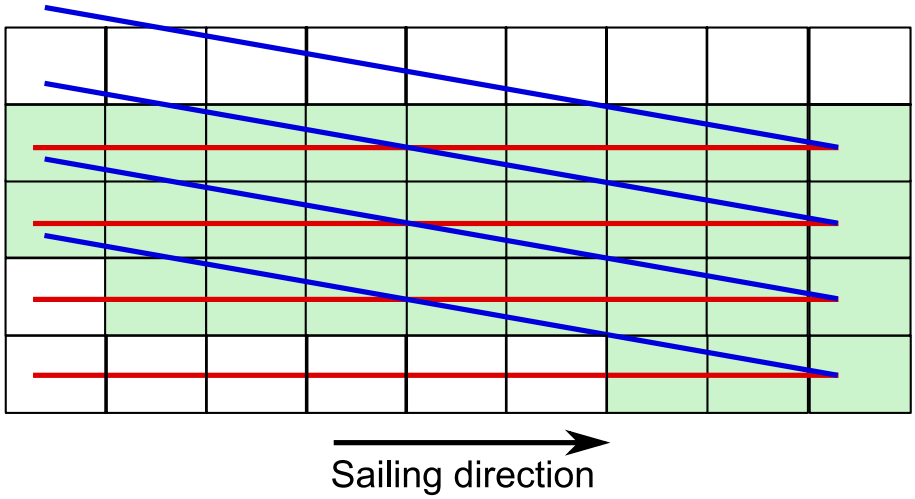

Figure 2.11: Schematic CMP bin cell coverage for a three-dimensional time-lapse experiment. The red lines indicate the baseline streamer positions, the blue lines the monitor streamer positions. The feathering angle is 10°. Common CMP bin coverage is marked by pale green cells.

plex overburden, however, is believed to introduce overburden noise in time-lapse data and is therefore only taken care of in 3D seismic modelling. Hence, 2D seismic modelling is not an option for this overburden study, certainly not if the effect of a non-repeatable acquisition geometry in conjunction with a complex overburden is investigated.

2.8 Summary

Modelling realistic three-dimensional time-lapse seismic data is not yet done on a regular basis. Assembling a subsurface model and computing seismic data is still very time consuming. A workflow is presented that allows to generate synthetic data with a reasonable workload in order to study time-lapse noise originating from overburden heterogeneity. The freedom to arbitrarily change and control the synthetic subsurface model is key to distinguishing between overburden effects and reservoir production-induced changes in time-lapse seismic data. However, seismic modelling is limited to smooth subsurface parameters, such as velocity and density. Realistic subsurface models therefore require careful editing of real input data in order to preserve the major geological features.

Chapter 3

The Nelson Field: Sand channels in the overburden

Two sand channels at various depths above the Nelson Field, North Sea, are studied in detail in this chapter. The effect of these overburden channels on the time-lapse amplitude interpretation at the top reservoir level forms the first part. The second part uses the time-lapse amplitude attributes to estimate changes in oil saturation in the top reservoir layer. The aim is to assess the accuracy of the oil saturation change inversion method in the presence of overburden heterogeneities which affect the wave propagation. Furthermore, the errors in the seismic attributes as well as the oil saturation change estimates are related to commonly used and well known repeatability measures.

3.1 The Nelson Field

The Nelson Field is located about 180km east of Aberdeen, in the UK Central North Sea (CNS), at a water depth of approximately 85m (Figure 3.1). The field lies on the well-defined basement horst known as the Forties-Montrose High (Whyatt et al., 1992). The reservoir is a four-way dip closed structure occurring within the

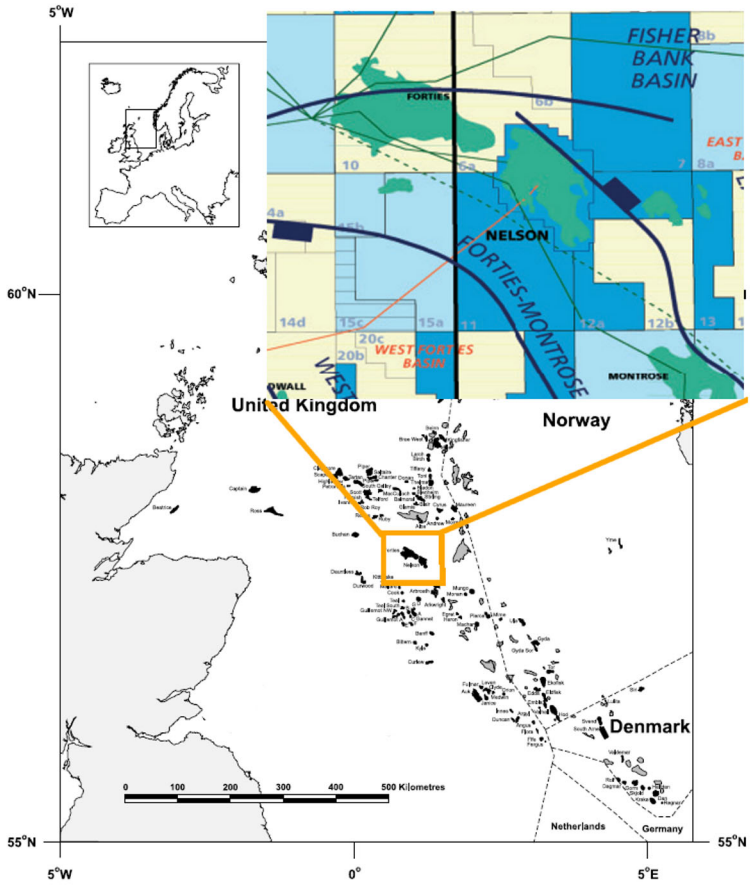

Figure 3.1: Nelson Field located in the Central North Sea on the Forties-Montrose ridge (modified from McInally et al. (2003) and Klett and Gautier (2005)).

Forties Sandstone Member of the Sele Formation. It covers an area of about 15 x 8 kilometres, with the producing horizon lying at a depth of approximately 2200 metres below mean sea level (Boyd-Gorst et al., 2001). The reservoir is divided into three main axial sand fairways: the eastern channel, the central channel and the western channel complexes (Figure 3.2). Figure 3.3 further highlights the structural cross section of the Nelson reservoir. The three main reservoir sands are divided by shale prone interchannel zones (Whyatt et al., 1992). The reservoir channels are submarine, turbidite sands of Paleocene age and are of excellent quality with

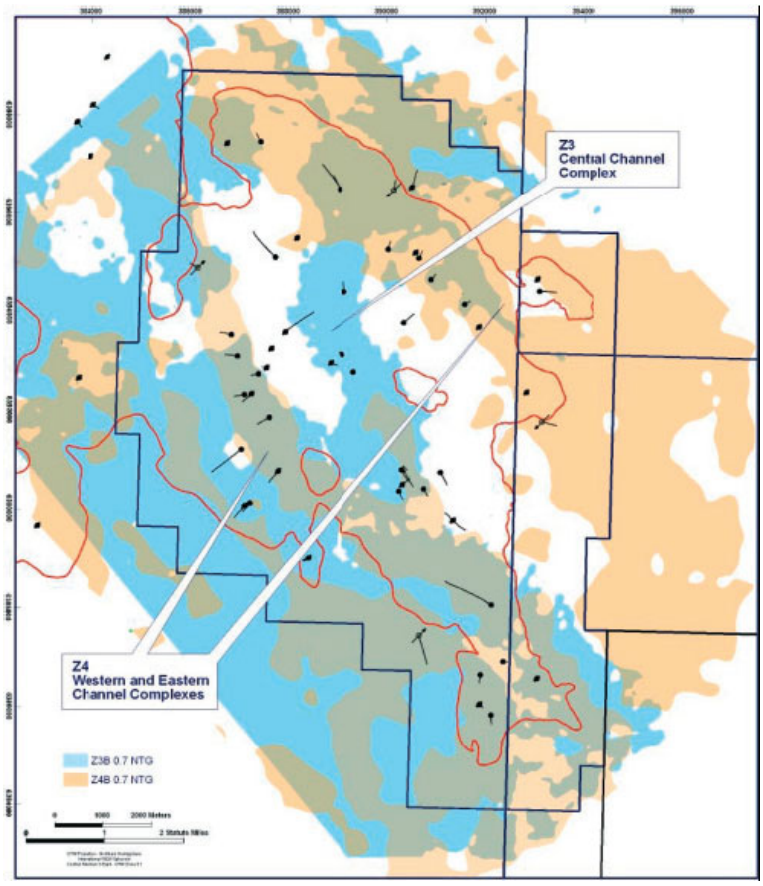

Figure 3.2: The eastern, western and central channel complexes (blue and orange) overlain on the Nelson Field outline (red line) (from McInally et al. (2003)).

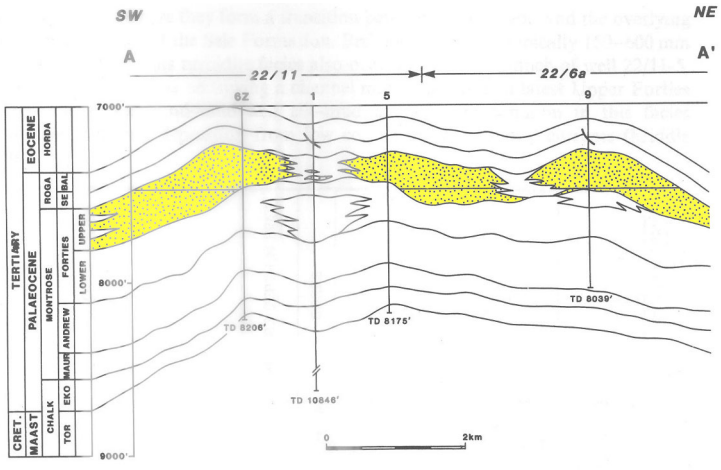

Figure 3.3: Structural cross section of the Paleocene sequence across the Nelson Field. The main reservoir sands (yellow colour) are separated by shale prone inter-channel zones (modified from Whyatt et al. (1992)).

an average porosity of 23% and permeability ranging between 200mD to 1000mD. The Nelson Field was discovered in 1988 and by 1990 thirteen appraisal wells had been drilled. Production commenced in 1994 with a plateau production rate of 150,000b/d being maintained between 1994 to 1996. The reservoir seal consists of shales of the Sele formation (McInally et al., 2003). The baseline seismic survey is acquired pre-production in 1990 with subsequent monitor surveys being acquired in 1997, 2000, 2003 and 2006. Since production commenced in 1994 more than 30 wells have been drilled. The main production drive is aquifer-supported oil displacement coupled with flank water injection (Boyd-Gorst et al., 2001). The Nelson Field has a good time-lapse signal with a significant contrast between the oil and the formation water (MacBeth et al., 2005). Moreover, the time-lapse response is mainly saturation-driven despite an initial pressure decrease of approximately 200psi (1.38MPa) (Boyd-Gorst et al., 2001). The Oil-water contact movement in the Top Forties formation is indicated by an increase in the impedance contrast with the overlying Sele shale.

3.2 Nelson Field - Overburden

The generalised stratigraphic section of the Montrose High (Figure 3.4) shows that the overburden at the Nelson Field is dominated by shale and mudstone. In addition, there is no major tectonic deformation and reflectors are near horizontal. Overburden complexity arises from sand-filled incisions of distinctive ages:

- Lower velocity channels of Quaternary age below the seabed
- Faster velocity channels of Mio-Pliocene age at around 1000ms TWT midway to the reservoir
- Faster velocity Tay sand channels just above the reservoir

Typical lateral and vertical dimensions of overburden channels in the Central North Sea are illustrated in Figure 3.5 and Figure 3.6. The Quaternary channels are just below the seabed and are approximately 2000m wide. Their thickness varies between

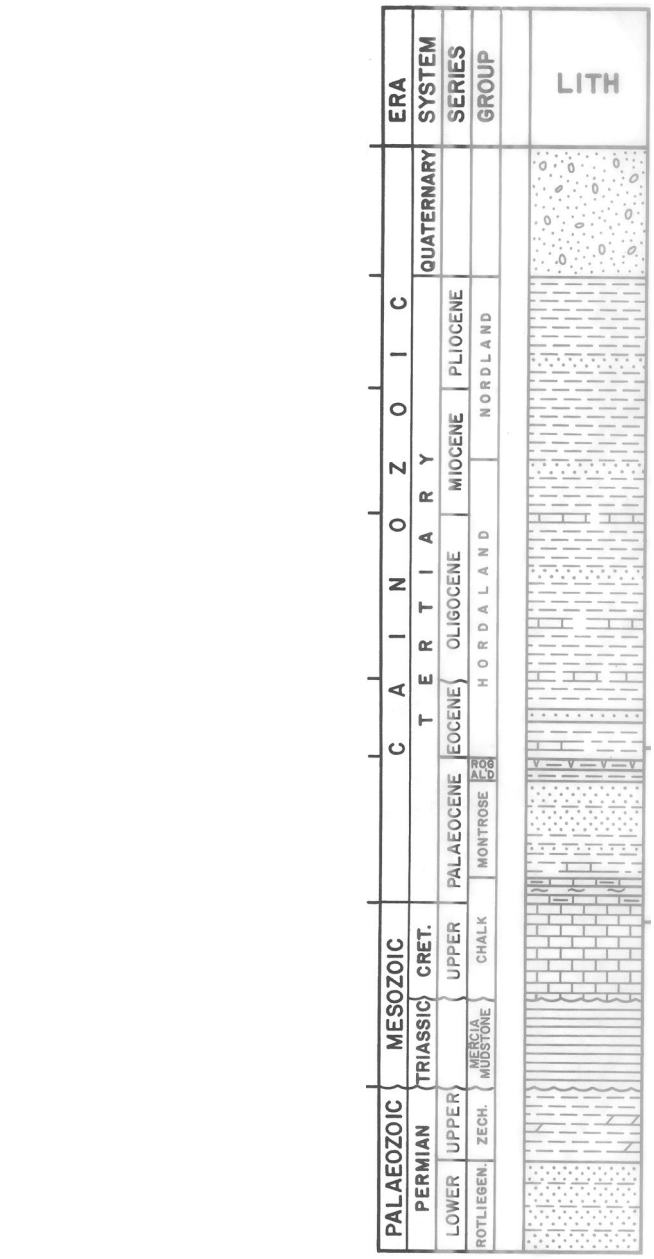

Figure 3.4: Stratigraphical section of the Montrose High (from Whyatt et al. (1992)).

50ms (TWT) and 300ms (TWT) with no apparent structure within the channels. The Mio-Pliocene age channels are at a depth of around 1000ms (TWT) and their typical width in the Central North Sea region is less than 1000m (Figure 3.6). Furthermore, their thickness is up to 250ms (TWT) which is in very good agreement with the Mio-Pliocene channels above the Nelson Field. Figure 3.5 outlines the near horizontal layering of overburden rocks in the Central North Sea with the overburden channels marked. The overburden channels observed at the Nelson Field are very similar in size and also at the same depths. The Quaternary age channels

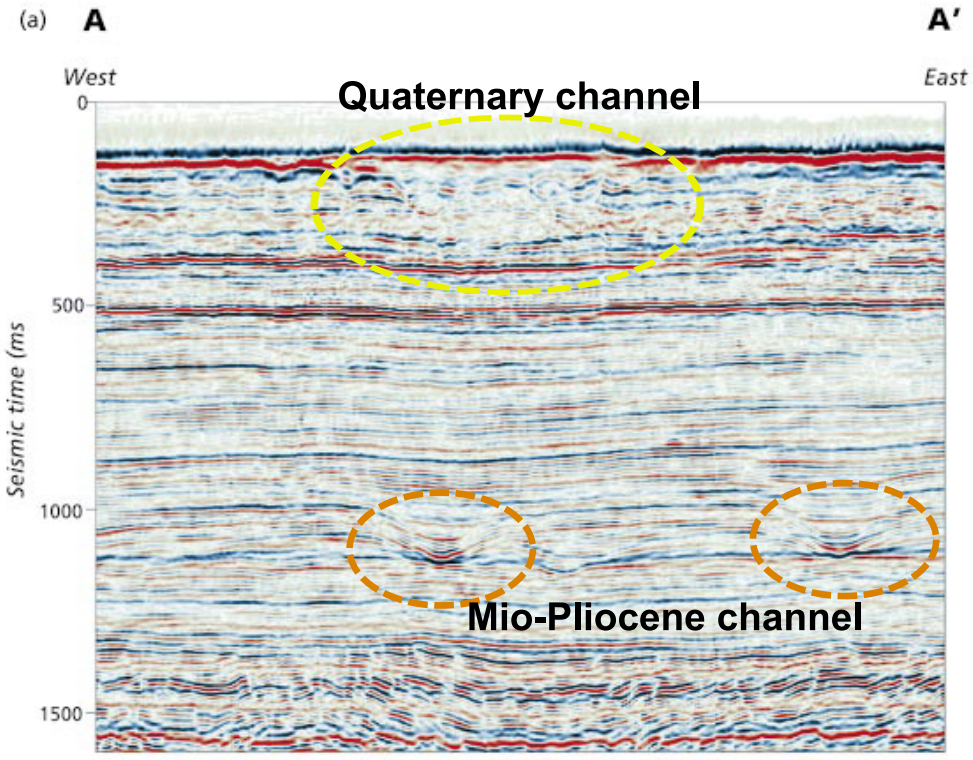

Figure 3.5: Typical Central North Sea seismic cross section. One Quaternary channel (yellow dashed line) and two Mio-Pliocene channels (brown dashed line) are marked (modified from Armstrong et al. (2001)).

are situated just below the seabed in very shallow depths of approximately 150m below mean sea level. Estimating the correct migration velocity for such shallow structures is challenging when using common tomography velocity model-building tools, because the acquisition streamer layout is not designed for a good ray coverage at such shallow depths. Only computational expensive full wavefield inversion algorithms accurately resolve these channels in the velocity model. Besides the lack of a proper velocity estimate for those shallow structures, additional imaging and

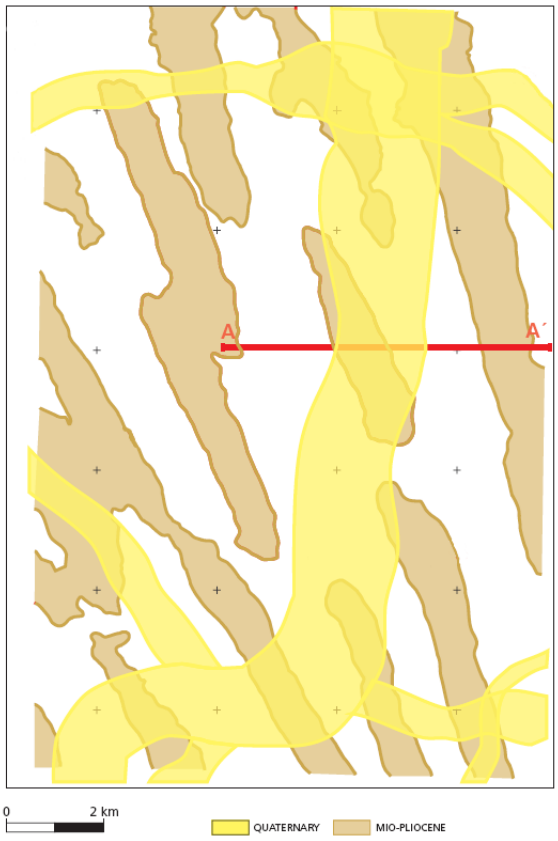

Figure 3.6: Spatial distribution of overburden channels in the Central North Sea. Quaternary channels below the seabed are marked in yellow. Mio-Pliocene channels are marked in brown. The seismic cross section AA' is displayed in Figure 3.5 (modified from Armstrong et al. (2001)).

scattering problems arise from them due to their lack of internal structure (Figure 3.7). The Tay sand channels can have a large impact on the time-lapse attributes

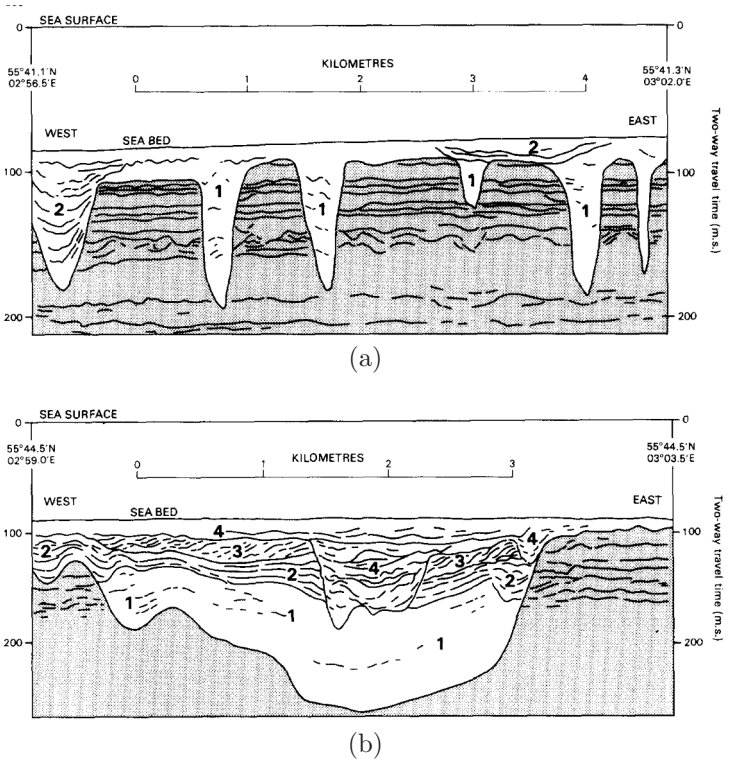

Figure 3.7: Quaternary channel cross sections interpreted from Central North Sea seismic data. The channels are of various width, (a) and (b), and with varying facies: Chaotic (1), Draped (2), Cross-Stratified (3), Variegated (4) (modified from Wingfield (1990)).

but are not the focus of the current study. These thin, sheet-like channels are the source of intra-channel multiples. However, multiple removal techniques are still an area of very active research and including these channels in the current work would deviate the research focus of this thesis. Nevertheless, it is understood that multiples originating from the overburden are a common problem in time-lapse seismic studies and need careful attention.

Overburden channels are not only a problem confined to the Central North Sea but also a common complexity in the Gulf of Mexico. Tura et al. (2005) reports on the frequent appearance of channels above the deepwater Europa Field (Figure 3.8) which impact the time-lapse interpretation. Moreover, faults and scatterers are observed to degrade the time-lapse data. The common problem to these channels is that they are not accurately represented in the migration velocity model. Certainly,

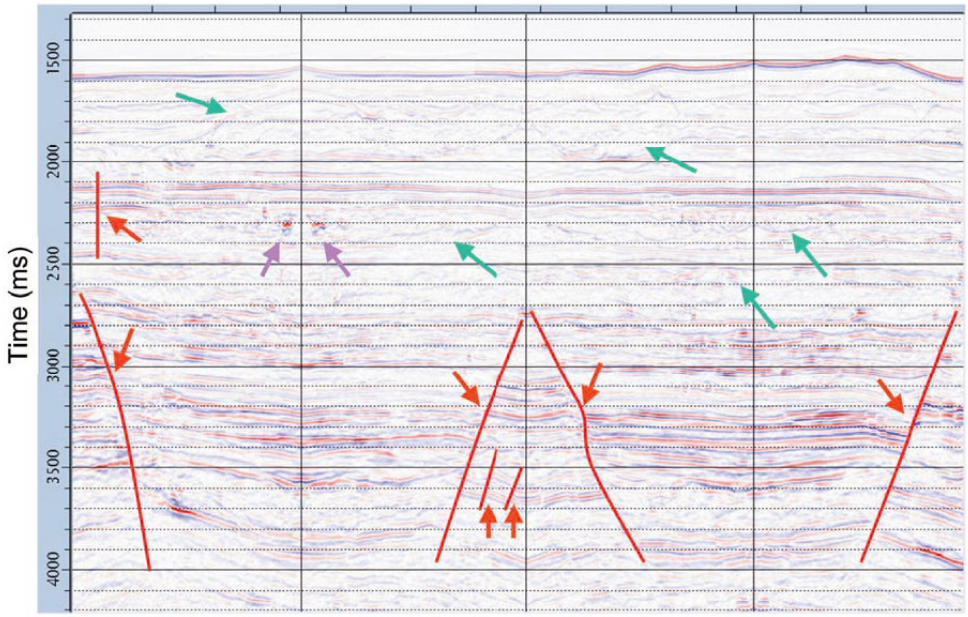

Figure 3.8: Overburden complexity at the Europa Field, Gulf of Mexico, arises from channels (green), faults (red) and scatters (purple) (modified from Tura et al. (2005)).

this does not matter for structural interpretation purposes, because these channels are still imaged reasonably well using a smooth background velocity model. However, transmission and time distortions of the wavefield of varying magnitude are the results of inaccurately capturing these channels in the migration velocity model. Even if these channels are accurately captured in the migration velocity model and very advanced imaging such as pre-stack depth migration is applied, transmission distortions still remain in the 3D seismic data. However, the common migration velocity grid spacing is 500m x 500m x 50m for the x, y and z direction. Therefore, overburden features with a spatial wavelength less than the grid spacing are not resolved. Only the largest of the North Sea overburden channels are thus mapped in the migration velocity cubes, but are still considerably smooth.

Furthermore, the overburden problem is assumed to arise from the non-repeated source and receiver position when acquiring the monitor seismic data, thus the ray path in the subsurface is changed. Hence, transmission and time distortions caused by the overburden channels might be different in the baseline and monitor seismic data and cause errors in the time-lapse difference data. The aim of the study is to investigate the impact of Quaternary and Mio-Pliocene channels on the amplitude and residual time shifts due to a non-repeat monitor acquisition.

3.3 Modelling the seismic response at the Nelson Field

The ray-tracing models are assembled as described in Section 2.3. Surfaces for both channels and reflection horizons are extracted from a depth-migrated seismic section. Models with and without the channel in the overburden are set up to study the channel's influence on time-lapse interpretation. Figure 3.9 shows the spatial

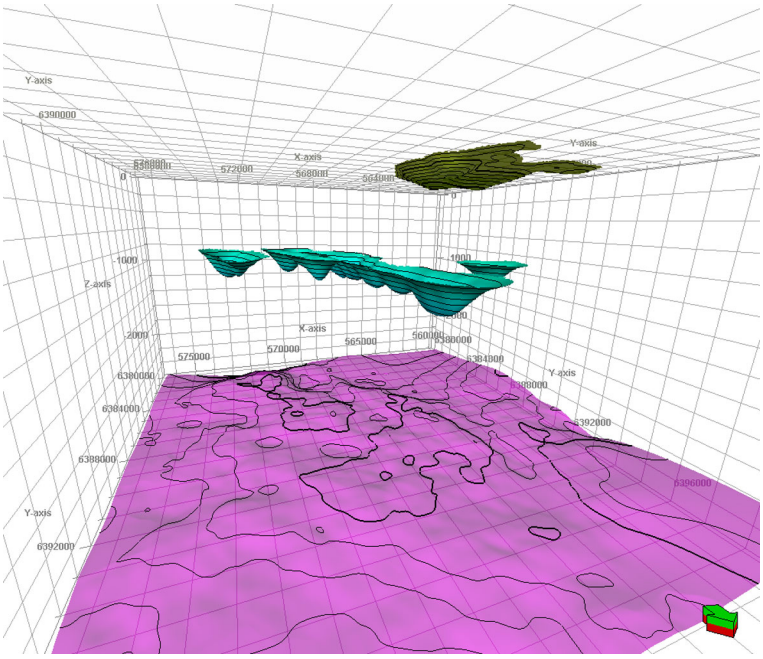

Figure 3.9: Subsurface model showing the Quaternary channel (dark green) below the seabed and the Mio-Pliocene channel (turquoise) midway to the reservoir (pink surface).

position of both channels above the top reservoir horizon. Separate models are set up for the Quaternary and the Mio-Pliocene channel in order to study the effect of each channel individually. In addition to the channel top and base horizons, a total of twenty horizons are inserted into the model. Fifteen horizons constitute the overburden and four horizons make up the reservoir. One horizon below the reservoir marks the lower bound of the ray-tracing model. Table 3.1 summarises the P-wave velocity, V_p, density, ρ, and V_p/V_s ratio used to populate the subsurface models. The density for each overburden layer is extracted from one well log by averaging the value over the layer interval, thus it is constant in each of the layers. P-wave

velocities on the other hand are extracted from a pre-stack depth migration velocity model but are also averaged to be constant in each overburden layer. Moreover, the velocity for the Quaternary and Mio-Pliocene channel is based on information from the pre-stack depth migration velocity model. However, the channels are not well resolved in this model, but rather represented as a very smooth velocity perturbation. Therefore, the velocities used for both channels are approximated and much simplified, but in agreement with common observations of being slower or faster than the surrounding rock for the Quaternary and Mio-Pliocene channel, respectively. Velocity and density information for the three reservoir layers in the

Model layer	V_p [m/s]	V_p/V_s	Density [kg/m^3]	Impedance change [%]
Overburden	1500-2640	2.5	1000-2250	–
Quaternary channel	1660	1.5	1600	-25
Mio-Plioccene channel	2070	1.6	2250	11
Model layer	V_p [m/s]	V_p/V_s	Density [kg/m^3]	Thickness [m]
Reservoir top layer	2531-3327	1.88-2.44	2349-2440	24 - 71
Reservoir middle layer	2646-3253	2.03-2.38	2352-2422	3 - 96
Reservoir bottom layer	2535-3461	1.98-2.45	2330-2446	12 - 127
Underburden	3200-3800	2.5	2400	–

Table 3.1: Summary of elastic property values used in the subsurface ray-tracing model. The range of overburden values indicates that the property varies in each separate layer. The impedance contrast is only given for the two overburden channels.

ray-tracing model are derived from the reservoir simulation model, by petro-elastic transformation, on two distinct occasions: the beginning and after four years of production. In turn, the elastic parameters are assigned to the following reservoir layers:

- T80-T75: Top reservoir layer
- T75-T70: Middle reservoir layer
- T70-T65: Bottom reservoir layer

The top and base reservoir horizon is denoted with T80 and T65, respectively. Two intra-reservoir reflection events are referenced as T75 and T70. Each of the three reservoir layers in the ray-tracing model is upscaled from multiple layers in the reservoir simulation model, because this fine layering of the reservoir simulation model in the vertical direction cannot be imported into the ray-tracing model. Hence, the reservoir model is divided into three main production units: top, middle and bottom layer. Upscaling of the velocity and density information is done by a porosity weighted vertical averaging over all active cells within each of the three units. The P-wave velocity, S-wave velocity and density values vary laterally, but are vertically constant in each of the three reservoir layers (Figure 3.10(a) and 3.10(b)). Therefore, the lateral production-induced changes are well resolved in the ray-tracing model.

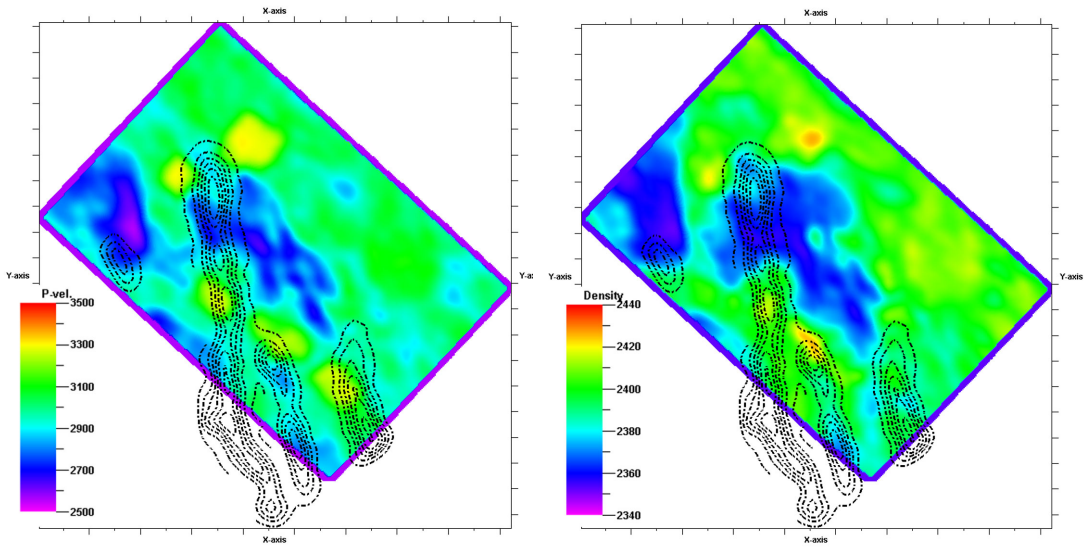

(a) P-wave Velocity top reservoir (b) Density top reservoir

Figure 3.10: The laterally varying velocity (a) and density field (b) in the top reservoir layer. The position of the Mio-Pliocene overburden channel is marked by the dotted line.

The next step is to chose a limited seismic modelling area, that contains the overburden channels as well as characteristic production-induced changes of the Nelson reservoir. Choosing such a subset is necessary, because of computational limitations. Modelling pre-stack shot gathers data in an area of 3km x 8km results in data files as large as 50GB and will run for several days on multiple CPUs. In addition, synthetic seismic data for several models with and without the channels in the overburden are generated. Processing these pre-stack data to limited offset stacks requires additional time and is limited by the storage capacity and the data throughput of the computational resources at hand. Hence, the source positions of the three seismic surveys which are used in this study as well as the Mio-Pliocene channel are overlain on the reservoir reflectivity change map (Figure 3.11(a) and 3.11(b)). All surveys are recorded with alternating sail directions and only shot points with a common acquisition direction in the 1990 survey are plotted on top of the reservoir reflectivity change in Figure 3.11(a). The blue rectangle outlines the area chosen for pre-stack seismic modelling. Figure 3.11(b) shows the 2000 (red lines) and the 2003 (yellow lines) shot locations on top of the reservoir reflectivity change map whereby the blue rectangle again indicates the seismic modelling area. The chosen modelling area contains a large part of the updip oil movement due to water injection, thus capturing the largest changes in the Nelson Field. Both channels (not shown for the Quaternary channel) are situated in the centre of the modelling area and are well imaged. The three seismic surveys provide two acquisition cases. For the poor repeat case (2000 - 1990) no attempt is made to repeat the baseline (1990) shot and receiver positions during the 2000 monitor survey. The 2003 survey is a dedicated (good) repeat survey as the towing configuration of the 2000 survey is matched and baseline source locations are repeated (Figure 3.11(b)), hence referred to as the good repeat case. The basic towing configurations for each survey are shown in Table 3.2.

The $\Delta Source + \Delta Receiver$ repeatability measure for traces with 1550m offset from the poor repeat case is shown in Figure 3.12(a). Acquisition stripes are clearly visible with $\Delta Source + \Delta Receiver$ ranging between zero metres and 500 metres. The average $\Delta Source + \Delta Receiver$ measure for this poor repeat case is 180m. The improvement in repeating the source and receiver position in the good repeat

Survey	1990	2000	2003
Number of sources	2	2	2
Source separation	50m	50m	50m
Shot interval	26.66m	18.75m	18.75m
Active cable length	2 x 3000m	6 x 3000m	8 x 5400m
Streamer separation	100m	100m	100m
Group interval	26.66m	12.5m	12.5m
Near trace offset	∼200m	∼200m	∼200m
	Poor repeat case $\Delta Source + \Delta Receiver = 180$m		
		Good repeat case $\Delta Source + \Delta Receiver = 65$m	

Table 3.2: Summary of towing parameters for the three seismic surveys used in the Nelson study. The $\Delta Source + \Delta Receiver$ is expressed as average values calculated from the 1550m offset traces.

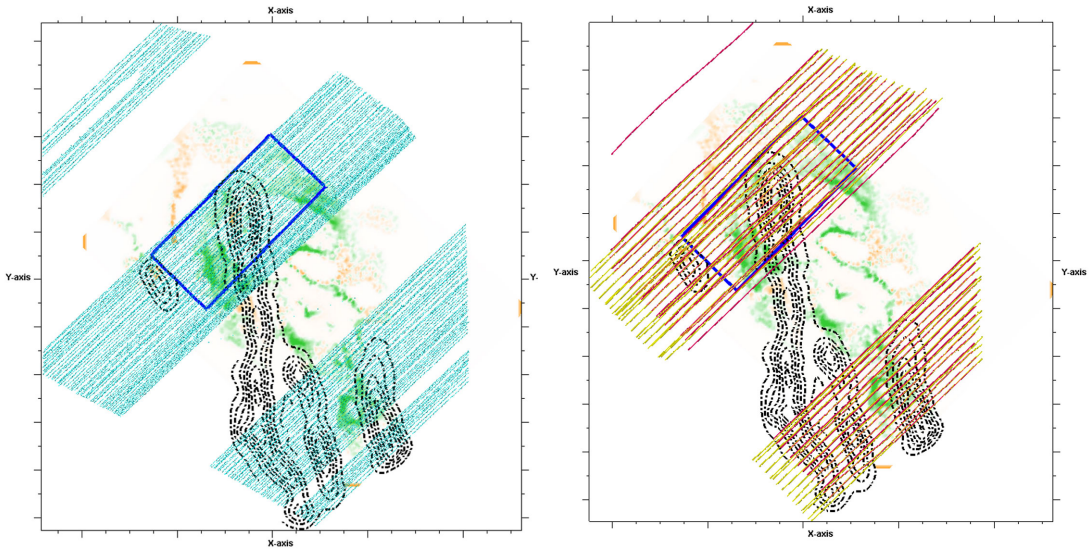

Figure 3.11: Shot points overlain on the top reservoir reflectivity change. The blue rectangle marks the chosen seismic modelling area. (a) Shot points with common sailing direction from the 1990 survey. (b) Shot points with common sailing direction from the 2000 survey (red lines) overlain by shot point locations from the 2003 repeat survey (yellow lines).

case is significant and the acquisition footprint noticeably reduced (Figure 3.12(b)). Hence, the average source and receiver misposition decreases by almost a factor of three to 65m for the dedicated time-lapse survey and is even lower than the average non-repeatability for North Sea time-lapse surveys.

The two acquisition cases therefore represent the two very common cases of a legacy time-lapse survey (poor repeat case) and a dedicated time-lapse survey (good repeat case) designed for the purpose of time-lapse interpretation. The first step in analysing the impact of the Quaternary and the Mio-Pliocene channel on the time-lapse seismic interpretation is to analyse the channel's impact on the amplitude attribute at the top reservoir horizon.

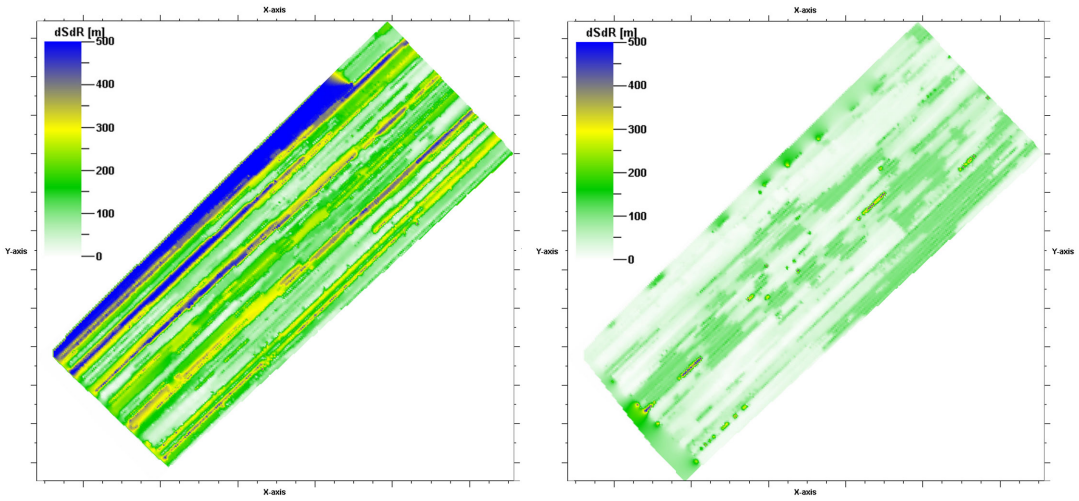

(a) Poor repeat case (b) Good repeat case

Figure 3.12: Positioning repeatability measure, $\Delta Source + \Delta Receiver$, for the poor repeat case (a) and the good repeat case (b). The minimum source and receiver positioning difference is calculated for each CMP bin at 1550m offset.

3.4 Amplitude analysis for the Nelson Field

The workflow to study the impact of the the overburden channel on the seismic data is outlined in Figure 3.13. The baseline and monitor ray-tracing model is set up with the overburden channel included in the velocity model. Therefore, the channel affects the wave propagation in the subsurface when it travels from the source, S, to the receiver position, R. In addition, the monitor model contains the changes in the reservoir caused by production. The pre-stack data are subsequently migrated using a velocity model that does not contain the overburden channel. This simulates the real case, where resolving such overburden complexities in the velocity model is not possible. Moreover, the reservoir production is not included either in the velocity model, when migrating the monitor seismic data. This is also in line with the common approach to use the baseline velocity model for processing both time-lapse seismic data sets.

This workflow is applied in the Nelson study in order to investigate the impact of overburden channels on the seismic amplitude at the reservoir level. The synthetic seismic pre-stack data are processed to full offset stacked sections from which the amplitude distortions at the top reservoir level are analysed. No steep dipping events

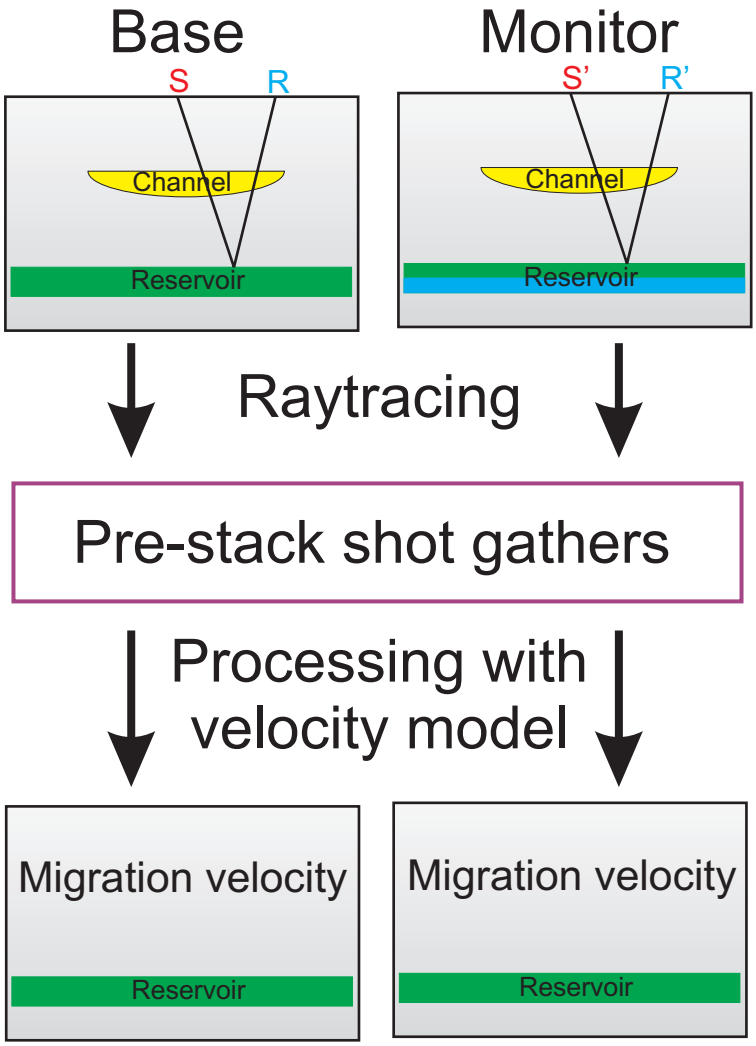

Figure 3.13: Schematic workflow to simulate the overburden effect on seismic data. S and R denote the source and receiver position.

or faults occur in the overburden of the Nelson Field and therefore a fast processing flow is chosen. The migration velocity model is extracted from the ray-tracing model on an xyz-grid with dimensions of 100m x 100m x 10m. The velocity cube is then converted from depth to time using the Dix formula followed by smoothing and regridding to 200m x 200m x 25ms. The synthetic seismic data are subsequently NMO corrected and stacked to full offset. Finally, post-stack Kirchhoff time migration is applied. Amplitudes are extracted and analysed at the top reservoir (T80) reflection event. Intra-reservoir reflections are difficult to identify and pick in the post-stack seismic volume, which is also in accordance with the real Nelson data set. The reservoir reflection events are highlighted in the seismic cross section (Figure 3.14) along with the reservoir sealing Sele formation. The Mio-Pliocene channel is

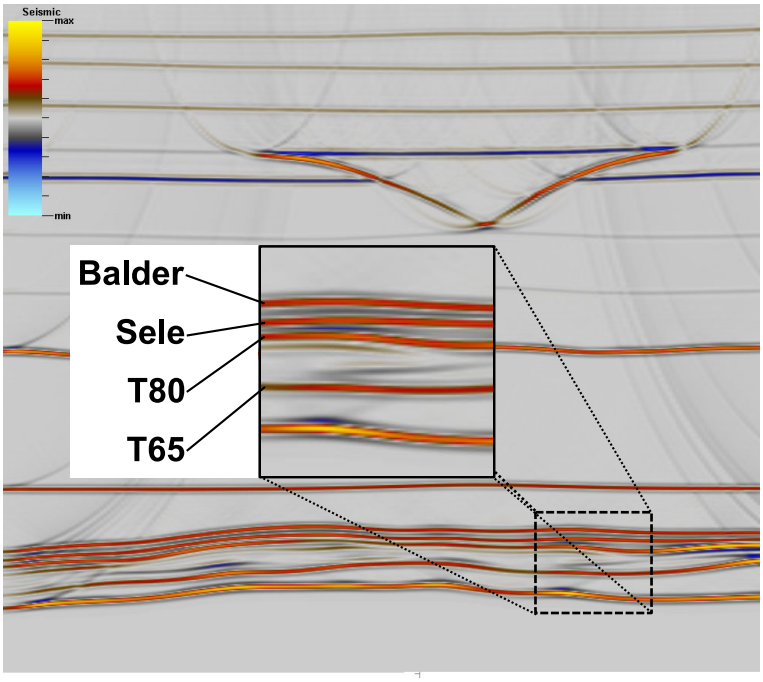

Figure 3.14: Seismic cross section through the full stack data. The inset diagram highlights the top and bottom reservoir reflection events, T80 and T65, as well as the Sele and Balder overburden reflections. The Mio-Pliocene channel and various other reflection events in the overburden are also shown.

clearly imaged although its velocity information is missing in the migration velocity model. Minor migration artefacts are seen at the edges of the seismic section due to the truncation of the migration operator. In addition, the inability of the ray-tracing to model diffractions causes mild migration artefacts around the channel margin (see Section 2.6).

3.4.1 Time-lapse difference

The common method of interpreting changes between the seismic baseline and monitor data is to subtract the post-stack baseline volume from the monitor volume, then work on the difference cube for quantitative time-lapse interpretation. Applying a time shift, derived by cross-correlating base and monitor data, to each monitor trace before the subtraction assures alignment of the reflection events. However, small residual time shifts which are not resolved by the cross-correlation still affect the difference traces, thus changing both their amplitude and phase information. On the other hand, seismic attributes (for example RMS amplitude) can be calculated

separately in each of the seismic volumes (baseline and monitor), then subtracted. Both methods will yield the same result if there is no time shift between the monitor and baseline trace. Ross et al. (1996) describe how the time-lapse difference trace is changed by small time shifts, which is now briefly discussed using two Ricker wavelets. A 30Hz Ricker wavelet of unity amplitude represents the baseline seismic event, whereas the monitor event is represented by a shifted version of the baseline wavelet (Figure 3.15). A non-zero difference signal (Figure 3.15, black line) results

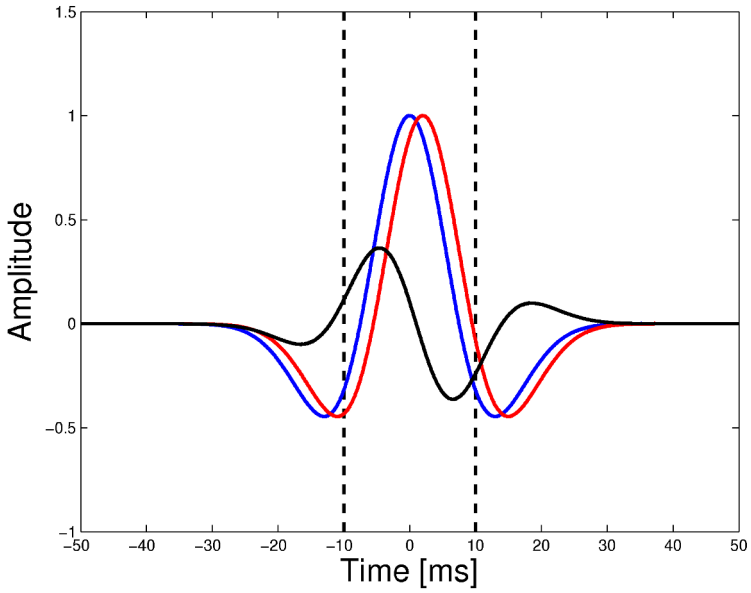

Figure 3.15: Two 30Hz Ricker wavelets (blue and red line) with the same unity amplitude and frequency content are shifted by 2ms. The black line indicates the difference signal of both Ricker wavelets. Dashed lines indicate the fixed time window used to calculate the RMS amplitude.

if both wavelets do not peak at the same time and thus resulting in a residual RMS amplitude signal. This residual amplitude is obtained by relating its RMS value calculated in a fixed 20ms window, to the RMS amplitude value of the baseline wavelet in the same window. Thus a relative amplitude error is obtaining. When making this calculation whilst incrementally increasing the time-shift one obtains a tuning curve for the relative amplitude error (Figure 3.16, black curve). A time shift of 1ms thus results in an amplitude error exceeding 15% and a time shift of 0.5ms still in an errors of 5%. Such small residual time shifts are common in time-lapse data, even after elaborate time-lapse seismic processing. In contrast, if the RMS amplitude is calculated separately for the baseline and monitor survey, then subtracted, the relative amplitude error is significantly reduced (Figure 3.16, red line). Hence,

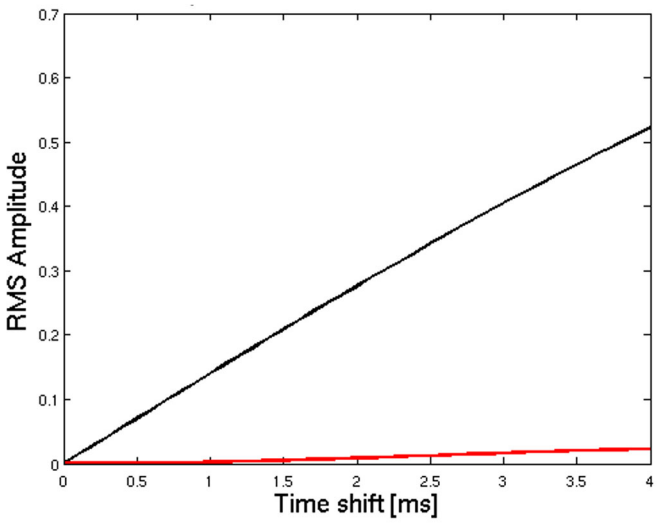

Figure 3.16: Relative RMS amplitude error for the RMS of the difference amplitude between baseline and monitor event (black curve) as well as for the difference of the RMS amplitude (red curve).

the difference of the RMS amplitudes is not sensitive to small time-shifts, whereas the RMS amplitude of the difference is significantly affected even by small time shifts. The difference of the RMS amplitudes is taken in the subsequent amplitude study, therefore eliminating most of the time shift related effects and focusing on the amplitude effects.

3.4.2 Working with normalised amplitude maps

The following sections outline how the overburden channel effect can be separated from the production as well as acquisition induced amplitude change by using different ray-tracing models. Consequently, these amplitude effects are ranked and compared to each other. The RMS amplitudes which are used in this study are extracted in a 20ms window centred around the top reservoir reflection event (T80 horizon).

Separating the production-induced amplitude changes

In order to compare and manipulate spatial amplitude maps, $A(x, y)$, derived from different ray-tracing models, they are normalised by their mean value, $\bar{A}$:

$$A_{Norm}(x, y) = \frac{A(x, y) - \bar{A}}{\bar{A}} \tag{3.1}$$

Hence, it is possible to add or subtract the normalised amplitude maps in order to assess the channel, acquisition or production effect. The total amplitude response can be thought of as a superposition of the acquisition imprint (Acq), production imprint (Prod) and the channel imprint (Chan). Combinations of these three components are investigated in this chapter using various ray-tracing models. The assumption that those components are additive, thus separable when subtracting the normalised amplitude maps, is tested first. The production-induced amplitude changes are obtained by the following combination of normalised amplitude maps:

$$(\text{Acq} + \text{Chan} + \text{Prod})_{\text{monitor}} - (\text{Acq} + \text{Chan} + \text{Prod})_{\text{base}} \tag{3.2a}$$

$$(\text{Acq} + \text{Chan} \quad)_{\text{monitor}} - (\text{Acq} + \text{Chan} \quad)_{\text{base}} \tag{3.2b}$$

$$(3.2\text{a}) - (3.2\text{b}): \quad \text{Prod}_{\text{monitor}} - \text{Prod}_{\text{base}} \tag{3.2c}$$

Normalised amplitude maps derived from the subsurface models with the overburden channel as well as production-induced changes between the baseline and monitor survey, are used in Equation 3.2a. On the other hand, normalised amplitude maps generated from ray-tracing models without production-induced changes are subtracted in Equation 3.2b, in order to isolate the combined acquisition and overburden channel effect. By assuming that the effects are independent, the influence of the acquisition and the overburden channel on the time-lapse amplitude attribute is removed by subtracting Equation 3.2a from 3.2b (Equation 3.2c). Therefore, the amplitude changes caused by production are isolated and consequently compared to the production-induced normal incidence reflectivity change at the top reservoir layer, which is calculated from the model's input parameters. Hence, the match of the extracted amplitude change, which is caused by the production, and the calcu-

lated reflectivity change is qualitatively assessed. Moreover, the previously discussed separation of the production effect can also be assessed using the poor and the good acquisition repeatability cases.

The coefficient of variation is used to compare the amplitude effects of various cases. The coefficient of variation, c_v, of a distribution, A, is the ratio of its standard deviation, $\sigma(A)$, divided by its mean, $\bar{A}$:

$$c_v(A) = \frac{\sigma(A)}{\bar{A}} \tag{3.3}$$

It is is a dimensionless number that allows comparison between different data sets. The standard deviation of the normalised amplitude maps, $A(x,y)_{Norm}$, thus is the coefficient of variation of the original RMS amplitude maps, $A(x,y)$. It is therefore possible to compare the RMS amplitude maps for the various cases of the poor and good repeat case as well as the Mio-Pliocene and Quaternary channel.

The production-induced amplitude changes are first looked at, in order to test whether the production, overburden channel and acquisition induced amplitude imprints are indeed separable. Therefore, ray-tracing models with the Mio-Pliocene channel, the poor acquisition repeatability and production-induced changes in the reservoir are used in order to determine the normalised amplitude changes caused by production (Equation 3.2a to 3.2c). The normalised amplitude map of the production imprint (Figure 3.17(b)) compares well to the normal incidence reflectivity change at the top reservoir horizon calculated from the simulation model (Figure 3.17(a)). The reflectivity change due to water flooding (green area in Figure 3.17(a)) matches spatially with the amplitude deviations in the normalised amplitude map (green area in Figure 3.17(b)). No apparent acquisition footprint nor any distortions caused by the Mio-Pliocene channel are visible. Indeed, these effects cancel each other out, thus justifying that subtracting normalised amplitude maps, in order to quantify the production-induced amplitude changes, is an appropriate approach The standard deviation of the production-induced amplitude change is 0.024 and the absolute maximum is 0.065. Furthermore, Figure 3.17(c) shows the extracted production-induced amplitude change in case of the good repeat survey and the

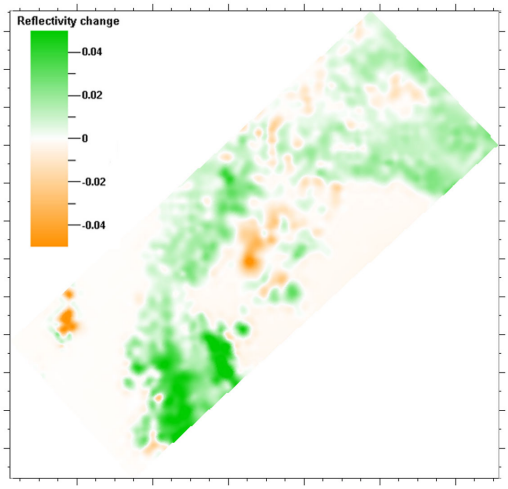

(a) Reflectivity change at T80

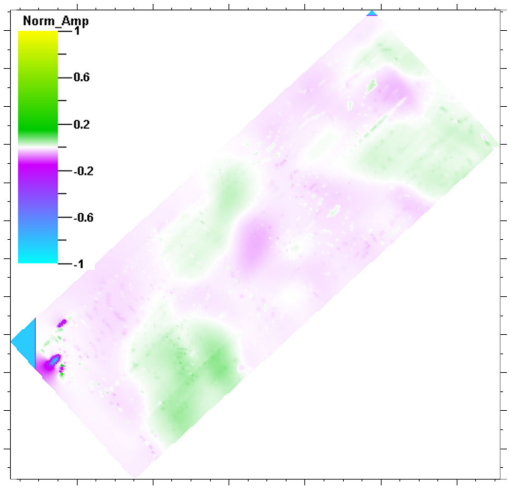

(b) Production imprint Mio-Pliocene channel (poor repeat case)

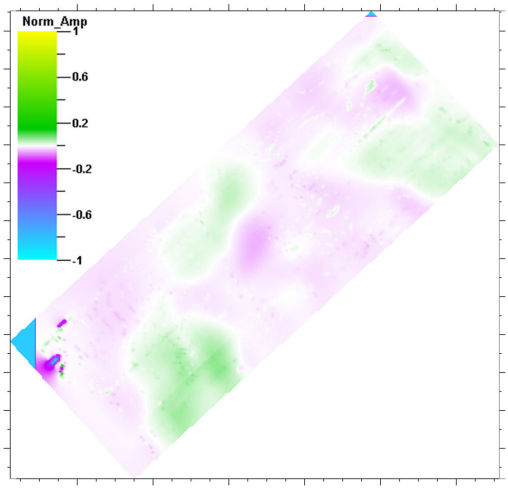

(c) Production imprint Mio-Pliocene channel (good repeat case)

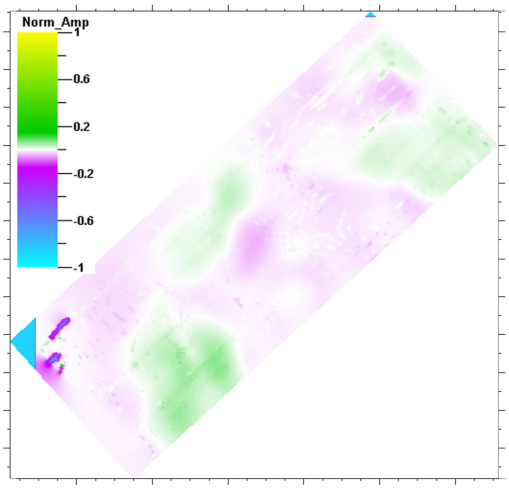

(d) Production imprint Quaternary channel (poor repeat case)

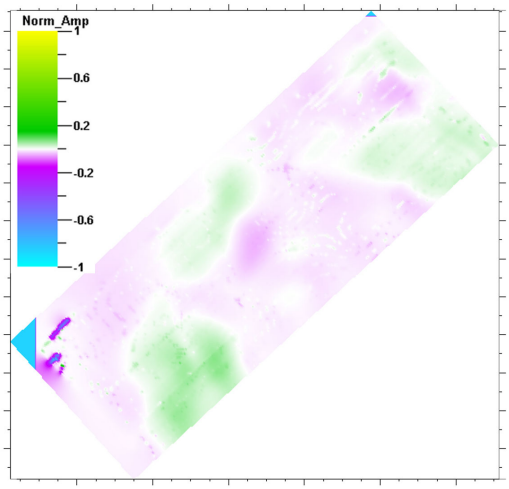

(e) Production imprint Quaternary channel (good repeat case)

Figure 3.17: (a) Production induced reflectivity change at the top reservoir. The production-induced normalised amplitude change derived from the following ray-tracing models: (b) Mio-Pliocene channel and poor repeat case. (c) Mio-Pliocene channel and good repeat case. (d) Quaternary channel and poor repeat case. (e) Quaternary channel and good repeat case. The similarity of the Figures (b) to (e) confirms that the amplitude change is consistently recovered from the various input data.

Mio-Pliocene channel in the overburden. The match with the reflectivity change at the top reservoir is excellent. The standard deviation of the map is 0.024 and the absolute maximum amplitude is 0.0652. Even though the acquisition footprint for the good repeat survey is different from the poor repeat case (Figure 3.22), the extracted normalised amplitude changes caused by production are very similar. Hence, the changed acquisition geometry of the good repeat case does not impact the extracted production-induced amplitude change compared to poor repeat case, shown in Figure 3.17(b).

Furthermore, the production-induced amplitude changes are extracted from data which are generated using the ray-tracing model with the Quaternary channel in the overburden and the poor repeat case (Figure 3.17(d)). Even though the overburden channel is included in the ray-tracing model but not in the migration velocity, production-induced amplitude changes are accurately resolved and compare very well with the normal incidence reflectivity change (Figure 3.17(a)) and the previously discussed production changes. The absolute maximum is 0.067, slightly more than for the Mio-Pliocene cases and the standard deviation is 0.027. Finally, the production effect on the normalised RMS amplitudes for the Quaternary channel and the good repeat survey are displayed in Figure 3.17(e). The amplitude change is very similar to the previous production-induced amplitude changes as well as to the reflectivity change. The standard deviation is 0.027 and the absolute maximum is 0.0668, almost identical to the poor repeat case with the Quaternary overburden cannel. This excellent consistency in between the various cases outlines that the production-induced changes are indeed separated from the acquisition and overburden effects using the above outlined equations, and thus provides assurance that this specific approach is a good tool to separate not only the production-induced changes, but also the overburden channel effect on the amplitude.

Figure 3.18 plots the absolute maximum of the normalised amplitude against the normalised standard deviation to summarise the consistency of the resolved production-induced amplitude changes. The amplitude change extracted from the Mio-Pliocene as well as the Quaternary channel model are clustered together. The difference between these estimates is less then 3% in the maximum amplitude. Moreover, this

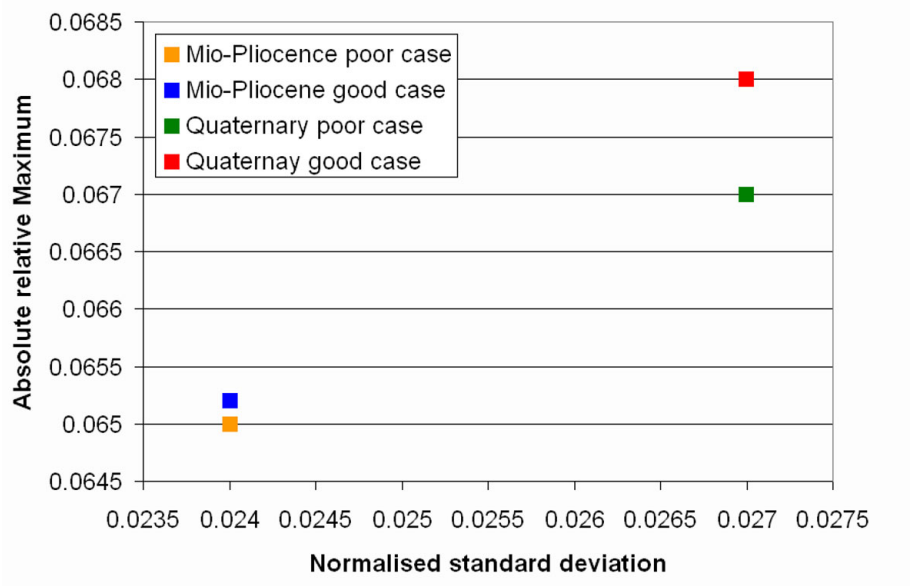

Figure 3.18: Production induced amplitude change for different overburden channels and acquisition geometries set up in the ray-tracing model.

small difference in the production-induced amplitude change is a good indication that the seismic modelling as well as the seismic processing are very repeatable processes. Therefore, use of the different combinations of subsurface models, which include or exclude the overburden channel, the acquisition or the production effect, is made to estimate the impact of the overburden channel on the time-lapse seismic amplitude attribute.

The production-induced amplitude changes are also derived using the following set of normalised amplitude maps:

$$(\text{Acq} + \text{Prod})_{\text{monitor}} - (\text{Acq} + \text{Prod})_{\text{base}} \tag{3.4a}$$

$$(\text{Acq} \quad)_{\text{monitor}} - (\text{Acq} \quad)_{\text{base}} \tag{3.4b}$$

$$(3.4\text{a}) - (3.4\text{b}): \quad \text{Prod}_{\text{monitor}} - \text{Prod}_{\text{base}} \tag{3.4c}$$

The overburden channel is not included in either one of the models; only production and acquisition effects are considered. The production-induced normalise amplitude changes estimated using the above equations are similar to the ones in Figure 3.17. No significant deviation is observed and thus these maps are not explicitly shown here.

3.4.3 Separating the overburden channel induced amplitude changes

The excellent results when separating the production-induced amplitude effects from the acquisition and overburden channel effects in the previous section provide enough confidence to look at the overburden channel effects. The following two methods are used to separate the overburden channel effect from the acquisition and production effect.

Normalised amplitude maps of the ray-tracing models with the channel in the overburden, but no production change occurring between baseline and monitor survey, are used in Equations 3.5a to 3.5c. Equation 3.5b is the difference of the normalised amplitude maps extracted from the subsurface model without the overburden channel and without any production between the baseline and the monitor survey, thus only containing the acquisition footprint. Assuming that the effects are independent, the influence of the overburden channel on the time-lapse data is separated (Equation 3.5c).

$$(\mathrm{Acq} + \mathrm{Chan})_{\mathrm{monitor}} - (\mathrm{Acq} + \mathrm{Chan})_{\mathrm{base}} \tag{3.5a}$$

$$(\mathrm{Acq} \quad)_{\mathrm{monitor}} - (\mathrm{Acq} \quad)_{\mathrm{base}} \tag{3.5b}$$

$$(3.5a) - (3.5b): \quad \mathrm{Chan}_{\mathrm{monitor}} - \mathrm{Chan}_{\mathrm{base}} \tag{3.5c}$$

The channel's impact can also be isolated if production-induced changes between the baseline and monitor survey are taken into account (Equations 3.6).

$$(\mathrm{Acq} + \mathrm{Chan} + \mathrm{Prod})_{\mathrm{monitor}} - (\mathrm{Acq} + \mathrm{Chan} + \mathrm{Prod})_{\mathrm{base}} \tag{3.6a}$$

$$(\mathrm{Acq} + \mathrm{Prod} \quad)_{\mathrm{monitor}} - (\mathrm{Acq} + \mathrm{Prod} \quad)_{\mathrm{base}} \tag{3.6b}$$

$$(3.6a) - (3.6b): \quad \mathrm{Chan}_{\mathrm{monitor}} - \mathrm{Chan}_{\mathrm{base}}$$

Mio-Pliocene channel

Equations 3.5a to 3.5c are first used on the normalised amplitudes extracted from the Mio-Pliocene channel, poor repeat data. The condition of no production in the reservoir is fulfilled by using the same elastic reservoir parameters in the baseline and monitor ray-tracing model. The normalised amplitude errors caused by the Mio-Pliocene channel in conjunction with the poor repeat survey are clearly seen in Figure 3.19(a). The Mio-Pliocene channel contour lines are superimposed on the map to outline the channel location. The amplitude distortion is largest beneath and closely around the channel. Only minor residual amplitude is seen far away on the left side of the channel (Figure 3.19(a)). The maximum absolute amplitude error is 0.184 and the standard deviation of the error is 0.016. Apart from small differences at the edge of the seismic modelling area, these amplitude errors do not change if estimated from the Mio-Pliocene channel poor repeat data which also includes the production-induced changes (Figure 3.19(b)), as outlined in Equation 3.6. The standard deviation slightly decreases to 0.015 and the absolute error increases to 0.197. This proves once more that subtracting the normalised amplitude maps indeed removes the production as well as the acquisition effect.

The normalised amplitude errors caused by the Mio-Pliocene channel are significantly reduced in the case of the good repeat survey (Figure 3.19(c) and 3.19(d)). The maximum error caused by the overburden channel reduces to 0.056 and the standard deviation reduces to 0.0131, if no production in the reservoir is taken into account. These errors increase marginally if production-induced amplitude changes are included in the seismic data as well. The maximum absolute error and the standard deviation are 0.064 and 0.0124, respectively (Figure 3.19(d)). However, the normalised amplitude error caused by the Mio-Pliocene channel has a similar appearance to the acquisition footprint. It is thought that the reason for this is a slight difference in the raypaths when traversing the channel in the baseline and monitor seismic data, compared to the case when no overburden channel is present. However, such subtle positioning differences are not compensated for by the seismic processing if the migration velocity does not resolve the channel or only time migration is applied. This can also be seen by the good correlation of the amplitude

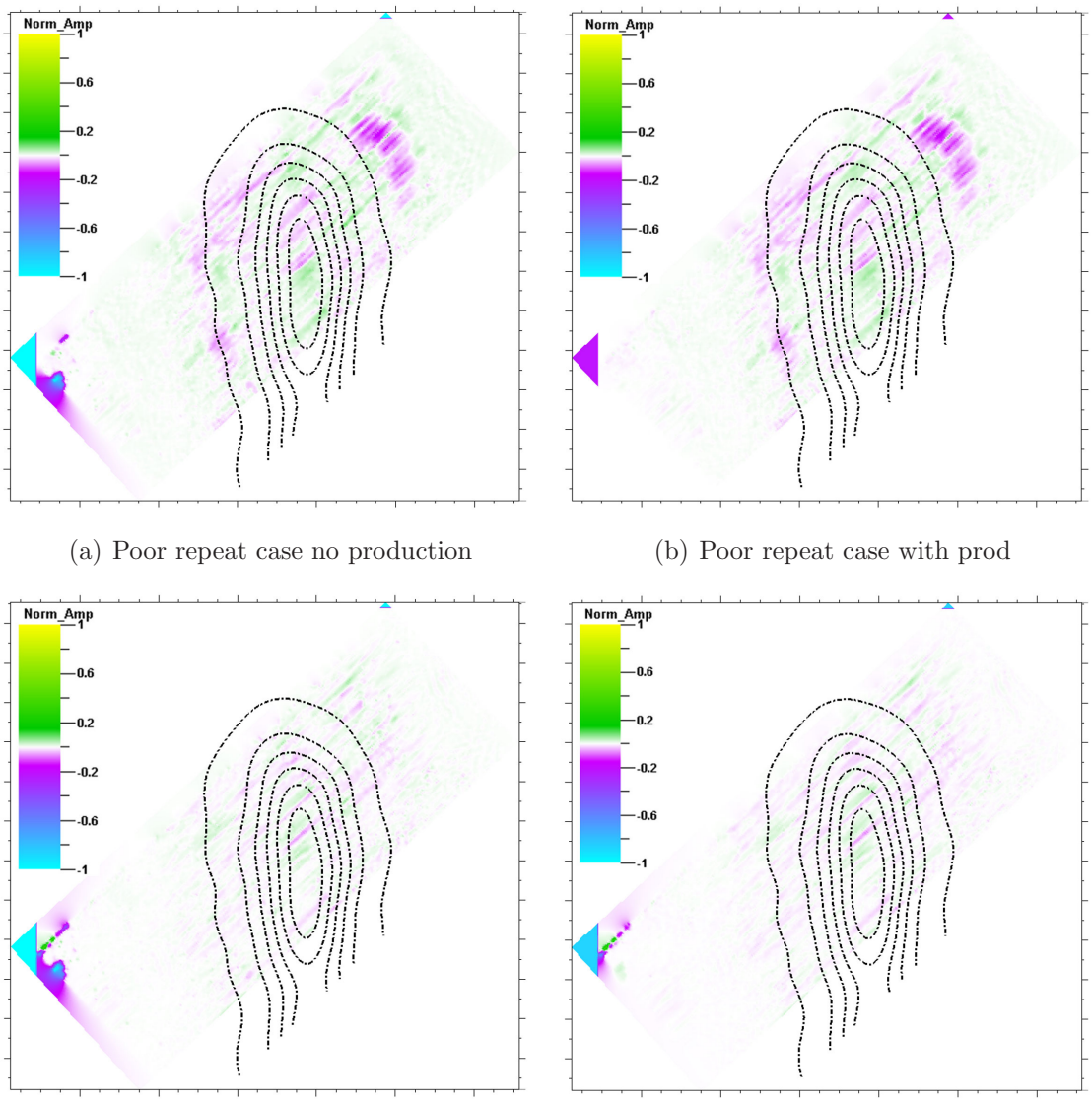

(a) Poor repeat case no production

(b) Poor repeat case with prod

(c) Good repeat case no production

(d) Good repeat case with production

Figure 3.19: Normalised amplitude errors caused by the Mio-Pliocene channel and the poor repeat as well as good repeat survey. The similarity between Figures (a) and (b), as well as (c) and (d) confirms that the amplitude error caused by the channel is consistently recovered whether or not production induced reservoir changes are included in the model.

errors to the $\Delta Source + \Delta Receiver$ measure (compare with Figures 3.29(a) and 3.29(b)). On the other hand, all effects cancel out far away from the channel, thus are perfectly repeated in the ray-tracing models. Furthermore, initial studies (not shown here) outline that the amplitude error is significantly reduced if the acquisition direction is parallel to the channel axis, hence in case when there is little variation of the channel's topography in the shooting direction.

Therefore, an acquisition direction parallel to the dominant orientation of the overburden channels would certainly reduce the amplitude error.

It is further believed that a pre-stack depth migration applied to the seismic data would reduce the amplitude error, as it accounts for ray-bending in the subsurface and also takes the actual source and receiver position into account. However, such pre-stack depth migration algorithms depend on an accurate velocity model in order to place the seismic energy at the correct position in depth and also correctly handle reflection and transmission effects. Hence, it is not just the imaging algorithm that needs to be changed, but also the workflow to obtain a highly accurate outline of the overburden channel in the velocity model. It is questioned whether it is feasible to derive such an accurate velocity model in order to make full use of the improved imaging capabilities of pre-stack depth migration. The advantage of the pre-stack time migration algorithms is that they work satisfactorily well with a smooth velocity model. Some of these time migration algorithms can also take ray-bending into account, but still lack the possibility to account for the actual source and receiver position. Moreover, it is thought that the use of a pre-stack time migration algorithm, as opposed to the post-stack time migration algorithm used for this study, would improve the data. However, the extend of the improvement is not known. In general, pre-stack time-migration outperforms post-stack time migration when steeply dipping events, or events with conflicting dips need to be imaged. The Nelson data are, apart from the overburden channels, structurally simple with layers having moderate dips. The overall reduction of the amplitude errors is thus considered to be marginal if pre-stack time migration is applied to the data. Nevertheless, migration trails using above discussed migration algorithms should be performed in order to obtain well grounded conclusions. Finally, it is mentioned that these results are obtained from full offset stack seismic data. Additional studies to look into the variability of the amplitude error when using partial offset stacks have not been conducted. This also remains an area for additional research.

Quaternary Channel

The same comparisons of the overburden channel imprint on the normalised time-lapse amplitude attribute are now discussed for the Quaternary channel. The normalised amplitude error caused by the Quaternary channel is first calculated from seismic data that do not include production-induced changes (Equation 3.5). The largest amplitude distortions occur beneath the areas of steep dipping channel margins, with an maximum absolute error of 0.118 and a standard deviation of 0.016 (Figure 3.20(a)). Secondly, the channel imprint is calculated using seismic data containing the production changes in the reservoir, but still using the poor repeat surveys (Figure 3.20(b)). Qualitative comparison does not reveal any significant difference compared to the previous case without reservoir production. The largest normalised amplitude distortions occur again beneath the steep dipping channel margins and are close to zero further away from the channel. The maximum error is 0.12 and the standard deviation of the map is 0.016. These measures also confirm that the approach of using differences of normalised amplitude maps works well and independent of the production or non-repeat acquisition induced amplitude changes.

The maximum amplitude error caused by the Quaternary channel significantly reduces to 0.053 when the acquisition repeatability improves in the good repeat case. However, the standard deviation slightly increases to 0.018 (Figure 3.20(c)). No production change occurs in the reservoir in the ray-tracing models used for this case. On the other hand, if production changes in the reservoir are included in the seismic modelling (Equation 3.6), the maximum absolute amplitude error stays about the same at 0.046. But the standard deviation of the map is reduced to 0.08. The maximum error for both good repeat cases occurs again beneath the steep dipping channel margins. Interestingly, amplitude distortions are minimal below the thickest part of the Quaternary channel for all cases (Figure 3.20(a) to 3.20(d)), which is different from the Mio-Pliocene overburden channel errors.

Figure 3.21 summarises the amplitude errors caused by the Mio-Pliocene as well as the Quaternary channel. The absolute maximum amplitude error caused by the overburden channel reduces by more than 55% in case of the Quaternary channel

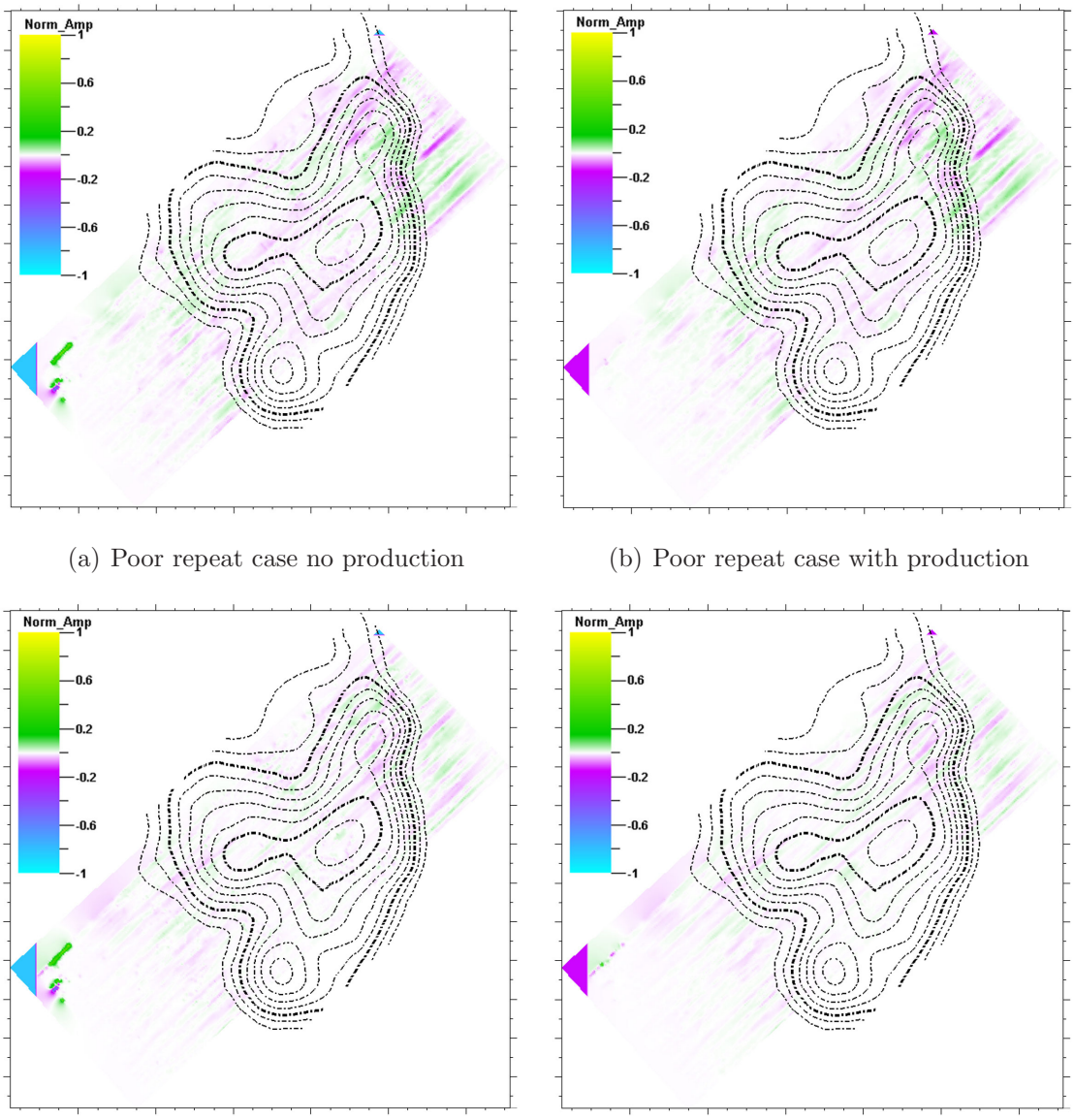

(a) Poor repeat case no production

(b) Poor repeat case with production

(c) Good repeat case no production

(d) Good repeat case with production

Figure 3.20: Normalised amplitude errors caused by the Quaternary channel and the poor repeat as well as good repeat survey. The similarity between Figures (a) and (b), as well as (c) and (d) confirms that the amplitude error caused by the channel is consistently recovered whether or not production induced reservoir changes are included in the model.

(circles) and by more than 65% in case of the Mio-Pliocene channel (triangulars), when using the good repeat survey compared to the poor repeat one. A more detailed comparison between the error caused by the overburden channels and the magnitude of the production and acquisition effect is presented in due course.

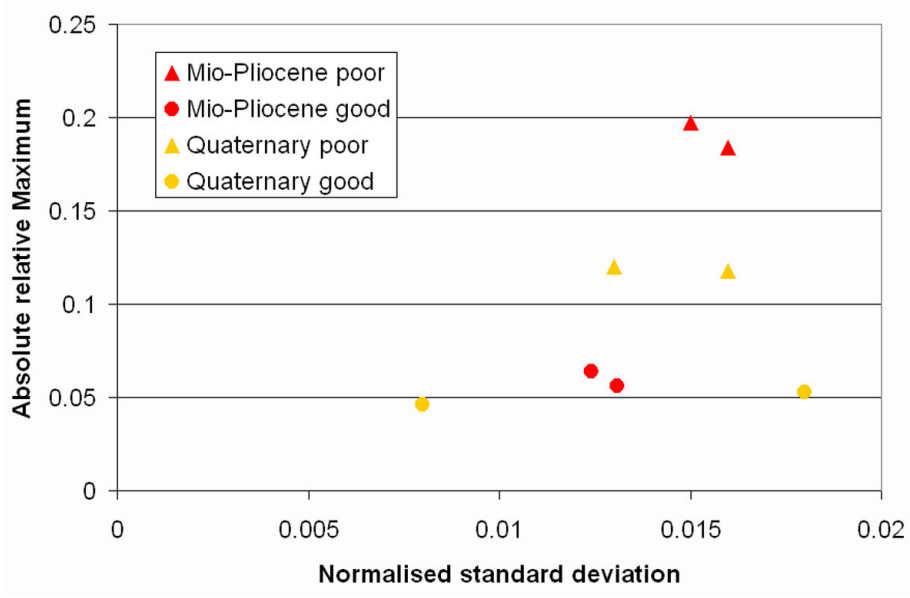

Figure 3.21: Amplitude errors caused by the Mio-Pliocene and Quaternary channel in case of the poor and good repeat survey.

3.4.4 Separating the acquisition imprint

Finally, the acquisition footprint is obtained from ray-tracing models without production changes and without the overburden channel included. Thus, any change at the top reservoir is attributable to the differences in the acquisition geometry. The poor repeat acquisition geometry results in a severe acquisition footprint, with a

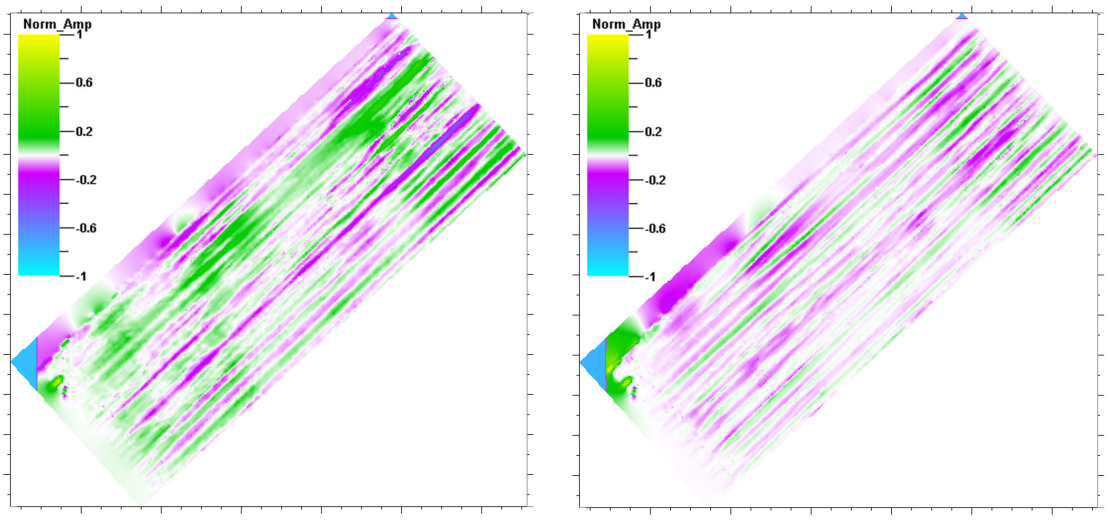

(a) Poor repeat survey

(b) Good repeat survey

Figure 3.22: Normalised amplitude error caused by the acquisition footprint of the poor (a) and good (b) repeat case.

maximum amplitude error of 0.55 and a standard deviation of 0.077 (Figure 3.22(a)). This error reduces by 54% to 0.25 for the good repeat case. The standard deviation reduces to 0.06 (Figure 3.22(b)).

3.5 Summary of amplitude analysis

The previous sections investigate the influence of two different overburden channels on the amplitude attribute at the top reservoir horizon. The amplitude error caused by the channels is separated from the production-induced amplitude change and the acquisition footprint by making use of various combinations of ray-tracing models. Hence, the maximum absolute normalised amplitude error is plotted against the respective standard deviation to rank the magnitude of the different effects (Figure 3.23). Overall, the acquisition footprint dominates both the good and the poor

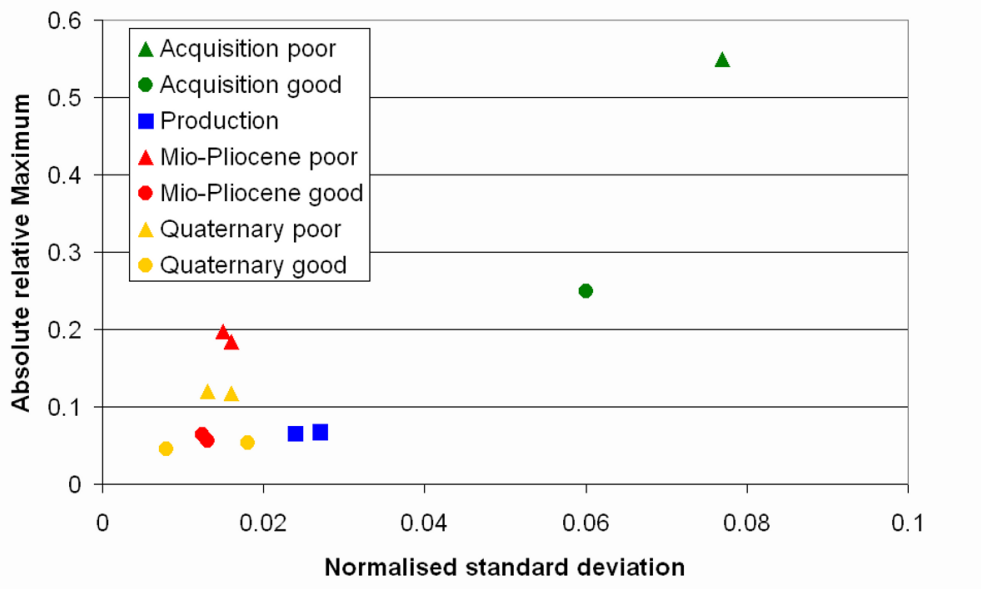

Figure 3.23: Magnitude of the overburden channel effect in relation to the production and acquisition effects. The standard deviation of the normalised amplitude maps is plotted versus the maximum absolute amplitude.

repeat case (Figure 3.23, green triangle and circle) and is several time bigger than the production-induced amplitude changes. This conclusion also points out the importance of developing accurate footprint removal techniques (for example Coléou et al. (2002)) and fold compensation during the time-lapse processing flow. However, it is shown in the previous sections that this acquisition footprint is cancelled out by

the specific combination of various ray-tracing models. Therefore, the acquisition impact is taken out of the comparison in order to focus on the error caused by the overburden channels in relation to the production signal (Figure 3.24). The

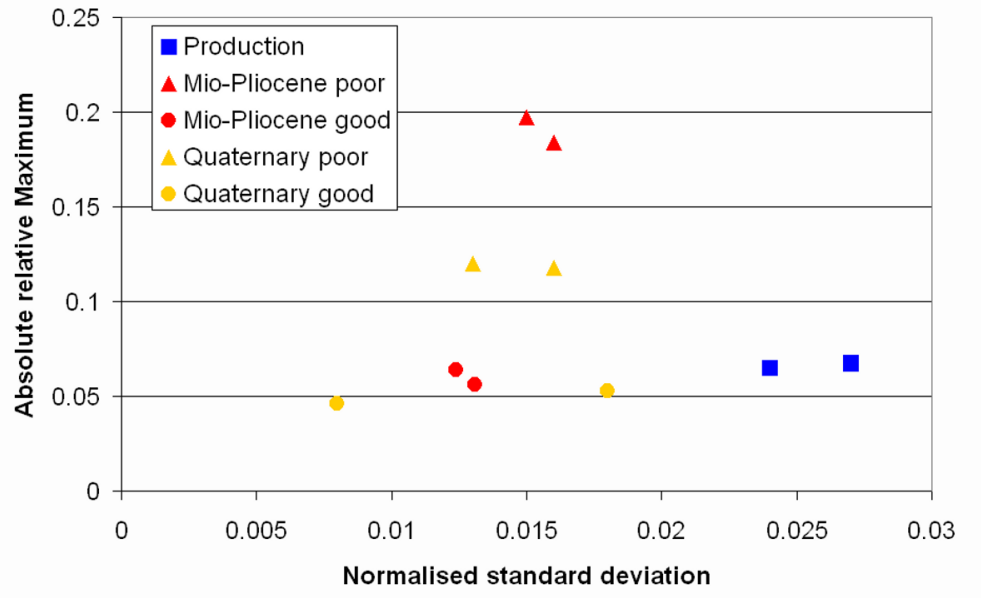

Figure 3.24: Normalised standard deviation versus the maximum absolute normalised amplitude for the overburden channel and production-induced amplitude effects.

production effects which are extracted from the poor and good repeat data (Figure 3.24, blue squares) are at a stable maximum amplitude of 0.065 and have a slightly varying standard deviations around 0.025. This indicates that the production effect is consistently recovered from the data regardless of the overburden channel or acquisition effects. The maximum amplitude errors caused by the Quaternary and Mio-Pliocene overburden channel are of the same magnitude as the production-induced amplitude changes for the good repeat case (Figure 3.24, red and yellow circles). The decrease in the standard deviation for this case indicates that the amplitude errors are more localised, which is seen in the respective maps. On the other hand, the overburden channel errors significantly increase for the poor repeat acquisition geometry. The Mio-Pliocene channel in conjunction with the poor repeat survey causes maximum errors in excess of 180% compared to the production-induced amplitude changes (Figure 3.24, red triangles). This error decreases to 79% in case of the Quaternary channel affecting the wavefield in conjunction with the poor repeat survey (Figure 3.24, yellow triangles). Standard deviations for the

errors caused by the overburden channels are approximately 40% less compared to the production case, which again indicated that these errors are localised at certain areas. Thereby this is in good agreement with amplitude deviations mostly occurring below the steep dipping channel margins for the Quaternary channel and beneath the thickest part for the Mio-Pliocene channel. Therefore, it is concluded that the Mio-Pliocene and Quaternary channel induce locally significant amplitude errors, equal or greater than production-induced amplitude changes, thus impeding the time-lapse interpretation. Consequently, the impact of such amplitude errors on the quantitative saturation estimation is studied in the following sections.

3.6 Pressure and saturation inversion - application to the Nelson data

The ultimate aim of the study is to understand what impact overburden complexity, such as an overburden channel, has on estimating the pressure and saturation change in the reservoir, using time-lapse seismic attributes. There are various methods that allow one to invert seismic attributes to pressure and saturation changes in the reservoir (Landrø, 2001; Floricich et al., 2005, 2006a,b; MacBeth et al., 2006). The multi-attribute inversion technique used for the proceeding study is the one described by MacBeth et al. (2006) and Floricich et al. (2006b). A brief introduction is given first to familiarise the reader with the basic terms and workflow. A more detailed discussion about this method and its limitations is provided in Appendix A.

When a reservoir is produced, its oil saturation as well as the pore pressure changes, which in turn changes the elastic properties of the reservoir rock, such as velocity and density. These changes in velocity and density can be calculated with the well known relations for changes in pore fluids (Batzle and Wang, 1992) and their effect on the overall rock matrix (Gassmann, 1951a,b). Certainly, these changes in the elastic properties give rise to changes in the monitor seismic data and thus time-lapse changes are observed. Therefore, the idea is that time-lapse attributes are used to invert for changes in the pressure and oil saturation caused by the reservoir

production. To make things simple, consider a non-compacting reservoir with two phases, oil and water. The seismic attribute, A, extracted from the reservoir reflection event is assumed to depend on the reservoir thickness, τ, lithology, L, porosity, ϕ, reservoir pressure, P and oil saturation, S_o.

$$A = A(x, y, \tau, L, \phi, P, S_o) \tag{3.7}$$

Furthermore, A is defined at each location, x and y, of the reservoir. If the reservoir thickness does not change between the base and monitor survey and the porosity is also constant (e.g. no facies changes), the repeat survey's seismic attribute response, A_r can be written in terms of the baseline response, A_b, and the change of the seismic attribute due to oil saturation change, ΔS_o, and pressure change, ΔP, by use of a first order Taylor expansion:

$$A_r(x, y, \tau, L, \phi, P, S_o) \approx A_b(x, y, \tau, L, \phi, P, S_o) + \frac{\partial A}{\partial S}\Delta S_o + \frac{\partial A}{\partial P}\Delta P \tag{3.8}$$

Consequently, the time-lapse seismic attribute, $\Delta A(x, y)$, is defined as the difference between the monitor and the baseline seismic attribute, and thus related to the change in oil saturation and pressure:

$$\Delta A(x, y) \approx C_S \Delta S_o(x, y) + C_P \Delta P(x, y) \tag{3.9}$$

where C_S and C_P are constants which are either derived from laboratory core measurements (Landrø, 2001), or from engineering data (Floricich et al., 2005). The latter case is closer looked at in the following study. Engineering data are repeat pressure and saturation measurements at well locations, which provide information about the changes in the reservoir in an area around the well location. Hence, the coefficients C_S and C_P are obtained by calibrating the time-lapse attribute at the well location to the repeat measured engineering data. For example, if the pressure and oil saturation is repeatedly measured at the four wells in Figure 3.25 and assuming that C_P and C_S are invariant across the reservoir one can estimate the

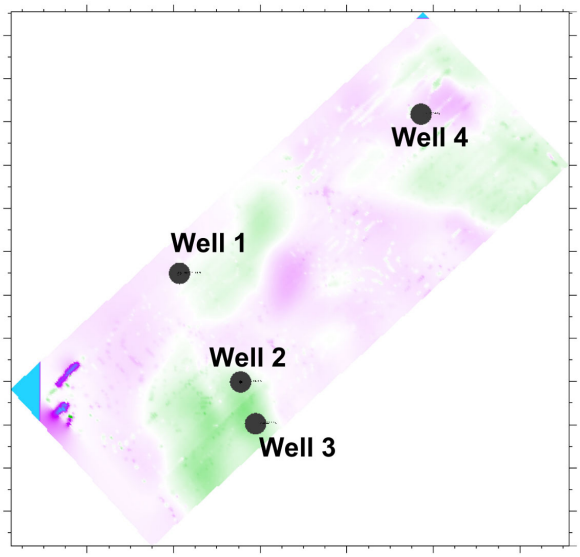

Figure 3.25: Schematic calibration of time-lapse seismic attributes to engineering well data.

calibration coefficients by solving the linear system:

$$\begin{bmatrix} \Delta S_{o1} & \Delta P_1 \\ \Delta S_{o2} & \Delta P_2 \\ \Delta S_{o3} & \Delta P_3 \\ \Delta S_{o4} & \Delta P_4 \end{bmatrix} \begin{bmatrix} C_S \\ C_P \end{bmatrix} = \begin{bmatrix} \Delta A_1 \\ \Delta A_2 \\ \Delta A_3 \\ \Delta A_4 \end{bmatrix} \tag{3.10}$$

in a least squares sense. ΔA_1 to ΔA_4 represent the time-lapse attributes extracted at the well location (Well 1 to Well 4). An additional set of correlation coefficients, C'_S and C'_P, is estimated from a different time-lapse attribute, $\Delta A'$, evaluated at the same well locations using Equation 3.10. The change in the seismic attribute is now linked to the pressure and saturation change at each x- and y-location of the reservoir:

$$\Delta A(x, y) \approx C_S \Delta S_o(x, y) + C_P \Delta P(x, y) \tag{3.11a}$$

$$\Delta A'(x, y) \approx C'_S \Delta S_o(x, y) + C'_P \Delta P(x, y) \tag{3.11b}$$

Consequently, the above system of linear equations is solved for the pressure and oil saturation change. Moreover, this system is easily generalised to multiple time-lapse attributes, ΔA^n, with different calibration coefficients, C^n_S and C^n_P ($n \in \mathbb{N}$). A least

squares inversion is thus employed to solve the over-determined linear system 3.12 for the pressure and oil saturation change, $\Delta P(x, y)$ and $\Delta S_o(x, y)$, respectively.

$$\begin{bmatrix} \Delta S_o \\ \Delta P \end{bmatrix} = \left(\begin{bmatrix} C_S^1 & C_P^1 \\ C_S^2 & C_P^2 \\ \vdots & \vdots \\ C_S^n & C_P^n \end{bmatrix}^{\mathrm{T}} \begin{bmatrix} C_S^1 & C_P^1 \\ C_S^2 & C_P^2 \\ \vdots & \vdots \\ C_S^n & C_P^n \end{bmatrix} \right)^{-1} \begin{bmatrix} C_S^1 & C_P^1 \\ C_S^2 & C_P^2 \\ \vdots & \vdots \\ C_S^n & C_P^n \end{bmatrix}^{\mathrm{T}} \begin{bmatrix} \Delta A^1 \\ \Delta A^2 \\ \vdots \\ \Delta A^n \end{bmatrix} \tag{3.12}$$

This brief mathematical background summarises the workflow (Table 3.3) for estimating pressure and saturation changes from time-lapse attributes. The intermedi-

Input seismic attributes
$\Downarrow$
Calibrate C_S and C_P at well locations
$\Downarrow$
Compute the cross-validation error at the well locations
$\Downarrow$
Estimate ΔS_o and ΔP

Table 3.3: Workflow for estimating pressure and saturation changes from time-lapse seismic attributes.

ate step that determines the attribute combination with the lowest overall error at all well locations is discussed in Appendix A.

3.7 Estimating oil saturation changes

The Mio-Pliocene channel effect on the full stack RMS amplitude attribute is discussed in the previous sections. Now amplitude attributes are extracted from five limited offset stacks, 1m-400m, 400m-800m, 800m-1200m, 1200m-1800m, 1800m-3000m, to investigate the overburden channel effect on the oil saturation change estimation. These five offset stacks are roughly equivalent to the following angle stacks: 0°-6°, 6°-12°, 12°-18°, 18°-24° and 24°-32°. The RMS amplitude is calcu-

lated in a 20ms window centred around the top reservoir reflection event (T80) in each of the limited offset stacks. Subsequently, after calibrating the attributes to the well data, RMS amplitude attributes extracted from the following three limited offset stacks, 400m-800m, 800m-1200m and 1200m-1800m, are chosen to estimate the oil saturation change in the top reservoir layer. However, it is found that the attribute combination with the lowest cross validation error does not automatically yield the best inversion results, thus needs the user's interaction. This problem is further discussed in Appendix A.

Moreover, the following study discusses only the oil saturation change estimates, not the pressure changes. This is mainly because of the saturation driven time-lapse signal, caused by water replacing the oil, at the Nelson Field and only small pressure changes due to a good pressure support. There are no major compartments or sealing faults observed in the reservoir, thus no significant pressure buildup or draw down exists. This field characteristic is also incorporated into the history matched reservoir simulation model, where the elastic reservoir parameters for the ray-tracing model are extracted from. Indeed, the simulated pressure draw down in the top reservoir layer (Figure 3.26) is almost a constant 200psi (1.38MPa) throughout the study area. Significant pressure changes are observed only at the two water injection wells (Figure 3.26, blue dots). To resolve this small and constant pressure change is below the detection ability of the multi-attribute inversion technique. The dominant oil saturation change is therefore always imprinted on the pressure change estimate. As a result, any quantitative interpretation of the overburden channel effect on the pressure change estimation would be highly biased by the oil saturation change and is not discussed in this chapter. Further discussion of this problem can be found in Appendix A.

The error in oil saturation change estimation caused by the overburden channel is assessed in a similar way to the amplitude study in section 3.4.2. Therefore, for either the good or the poor repeat case, saturation change estimates from the model data without the channel in the overburden are assumed to represent the reference case, or best case. The same time-lapse seismic attributes are in turn extracted from the model data with the channel in the overburden and subsequently inverted

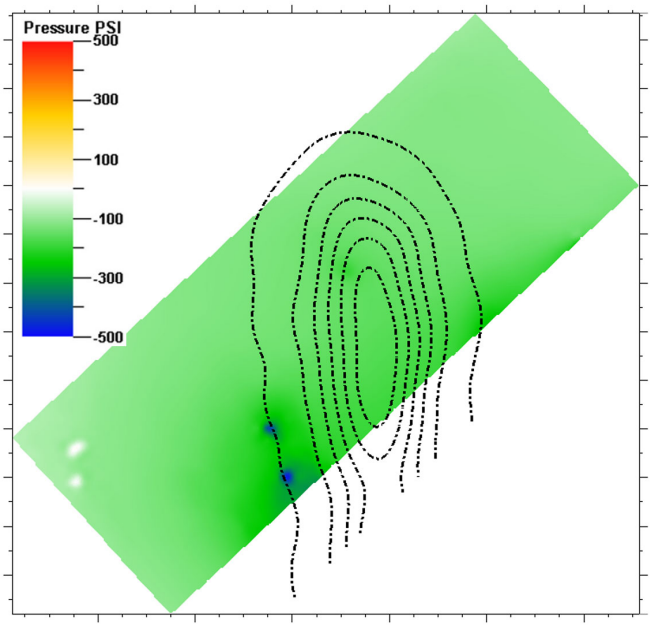

Figure 3.26: Simulation model pressure change for the first four years of production. The Mio-Pliocene channel is overlain for orientation.

for oil saturation changes, thus containing errors caused by the overburden channel. The difference between these two oil saturation change estimates isolates the error in saturation change estimate caused by the overburden channel. Moreover, the error in the oil saturation change estimate is assessed for two different ways the time-lapse attribute is derived (compare Section 3.4.1):

- Amplitude effects of the channel only: the differences of the RMS amplitudes are inverted for oil saturation changes
- Amplitude and time shift effects: the RMS amplitudes of the time-lapse seismic difference data are evaluated for oil saturation changes.

First, it is tested whether the multi-attribute inversion method is capable to estimate the oil saturation change correctly in the event of an identical repeat acquisition geometry. Therefore, a ray-tracing model is set up which contains the Mio-Pliocene channel and the reservoir changes caused by four years of production. The same acquisition geometry is used for the baseline and monitor survey, thus eliminating any acquisition-related artefacts. The seismic data for the baseline as well as the monitor survey are migrated with a velocity model that does not contain information about the overburden channel. However, migration errors should cancel out if they are re-

peated exactly. The oil saturation change as extracted from the simulator is shown in Figure 3.27(a), whereas the oil saturation change estimated from the difference of the RMS amplitude is shown in Figure 3.27(b). The result of estimating the oil

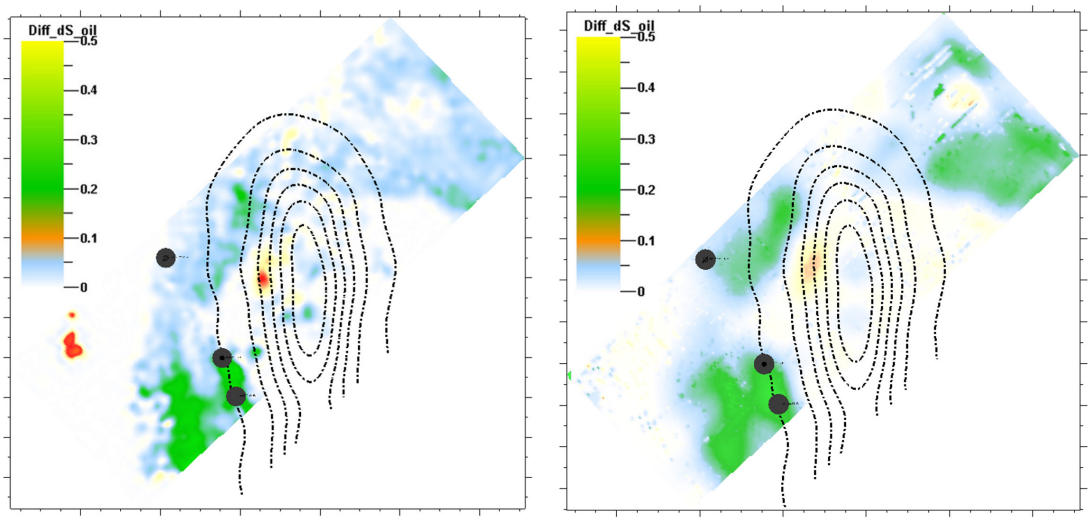

(a) Simulation model (b) Estimate

Figure 3.27: (a) Oil saturation change inside the top reservoir layer extracted from the simulation model. (b) Estimate of oil saturation change in the top reservoir layer using ideal repeat acquisition geometry. The position of the Mio-Pliocene channel is marked by its contour lines, whereas the black circles mark the wells used to calibrate the seismic attributes.

saturation change from time-lapse data when using the same acquisition geometry is very favourable. Overall, the estimated changes are smoother compared to the simulated changes (Figure 3.27(a)), which is a result of smoothing the reservoir parameters before ray-tracing (see Section 2.3) and due to the migration applied to the seismic data. The location of the three wells which are used for the inversion process is marked with black circles. The main areas of oil saturation change are recovered well, however, oil saturation change is slightly overestimated. The oil saturation change estimates for this ideal case show that the inversion method delivers accurate results within acceptable error limits, in case of a perfect repeat survey and even in the case of neglecting the overburden channel in the migration velocity. The next sections discuss the errors in estimating the saturation change if seismic attributes from a non-repeat monitor survey are used.

3.7.1 Error caused by amplitude effects

Mio-Pliocene channel

First, the impact of amplitude effects on the saturation change estimation is investigated. Hence, the RMS amplitude attribute is extracted from the baseline and monitor seismic data separately, then subtracted. Different ray-tracing models are used to isolate the error caused by the overburden channel. The first saturation change inversion utilises RMS amplitudes generated from the ray-tracing model without the Mio-Pliocene channel in the overburden (Figure 3.28(a)). Therefore,

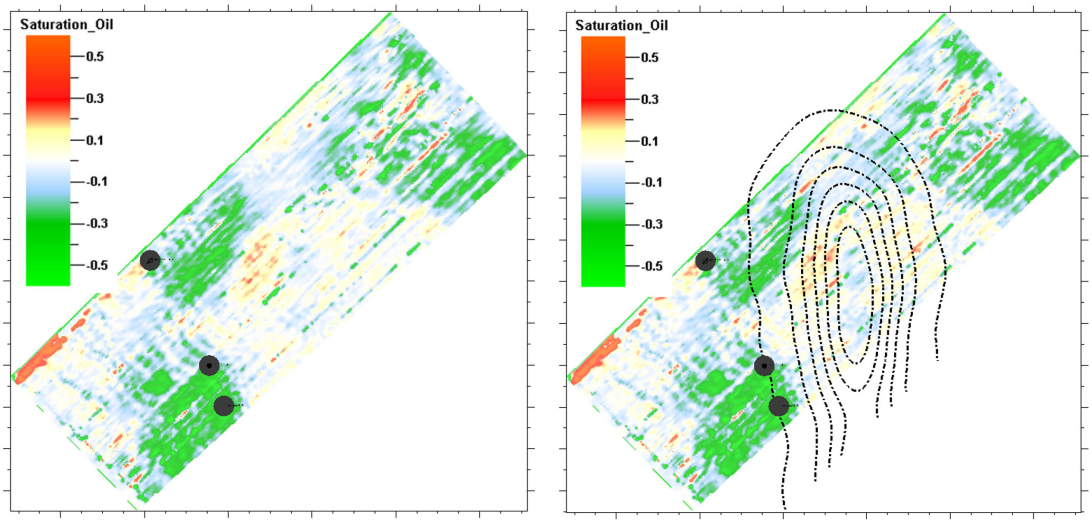

(a) Without Mio-Pliocene channel (b) With Mio-Pliocene channel

Figure 3.28: The oil saturation change estimate for the poor repeat baseline and monitor seismic data: (a) without the Mio-Pliocene channel in the the ray-tracing model. (b) with the Mio-Pliocene channel in the the ray-tracing model.

the Mio-Pliocene channel contour lines are not overlain on the saturation change estimates. This case represent the best possible estimate in case of no overburden channel distortion. Consequently, the second oil saturation change estimate is based on RMS amplitudes from the ray-tracing model where the Mio-Pliocene channel is present, thus affects the time-lapse amplitude attribute (Figure 3.28(b)). For this case, the position of the Mio-Pliocene channel is outlined by its contour lines overlain on the saturation change estimate. The acquisition footprint caused by the poor repeat monitor survey is visible in both estimates by the striping in the data.

However, comparison with the simulated oil saturation change (Figure 3.27(a)) reveals that the main areas of saturation change are recovered. Visual comparison of both estimates, with and without the overburden channel present, does not reveal any obvious differences. Therefore, both estimates are subtracted in order to cancel out the common features such as the acquisition footprint and isolate the error in oil saturation change estimate caused by the overburden channel (Figure 3.29(c)). The absolute value of this difference is displayed to highlight the error caused by the Mio-Pliocene channel, whether it is a positive or negative deviation from the best case. The largest errors in estimating the saturation change caused by the Mio-Pliocene channel in conjucntion with the poor repeat survey are up to 0.3 saturation units and located mostly underneath and to the right hand side of the channel (Figure 3.29(c)). Furthermore, the mean of the errors caused by the Mio-Pliocene channel and the poor repeat case is 0.03 saturation units and the standard deviation of the error is 0.04 saturation units, hence equating to a coefficient of variation of 1.33. These errors should always viewed in comparison to a maximum absolute oil saturation change of 0.45 saturation units occurring in the simulation model.

There is some degree of correlation between the oil saturation change inversion errors and the $\Delta Source + \Delta Receiver$ repeatability measure, however, only in the vicinity of the channel. Errors significantly decrease far away from the Mio-Pliocene channel, even though there is the same degree of poor source and receiver positioning (Figure 3.29(a)). Moreover, there is some extension of the errors in saturation change estimates to the right hand side of the channel area, which is probably caused by the streamer gradually overlapping with the channel with each successive shot position. In addition to the $\Delta Source + \Delta Receiver$ measure, the NRMS measure is also compared with the estimation errors. There is some degree of spatial correlation between highs in the NRMS measure caused by overburden channel and the error in the oil saturation change estimation (Figure 3.29(e) and 3.29(c)). However, the saturation change error is not strictly related to the increase of NRMS measure. This increase is obtained by calculating the NRMS measure in a 600ms window above the reservoir separately for the model without the channel in the overburden and with the channel in the overburden, then subtracting both measures (Figure 3.29(e)). Hence, this NRMS difference measures the increase caused by the Mio-Pliocene

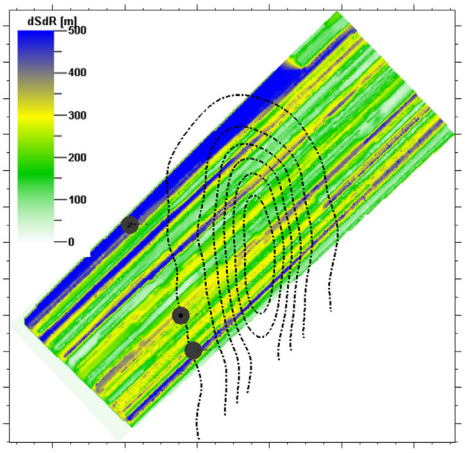

(a) $\Delta Source + \Delta Receiver$ poor case

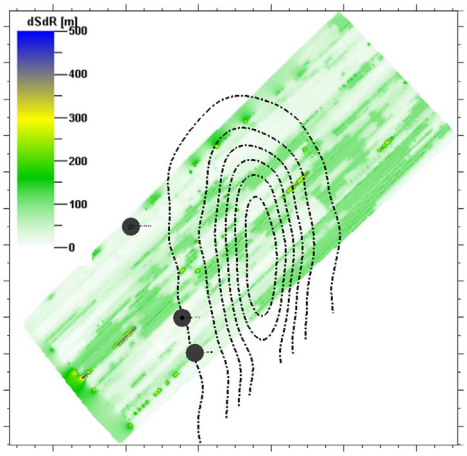

(b) $\Delta Source + \Delta Receiver$ good case

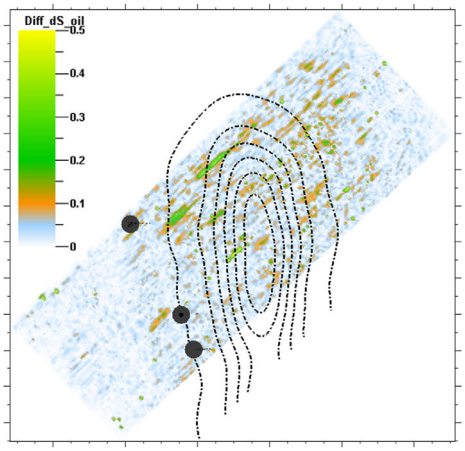

(c) Saturation change estimate error-poor case

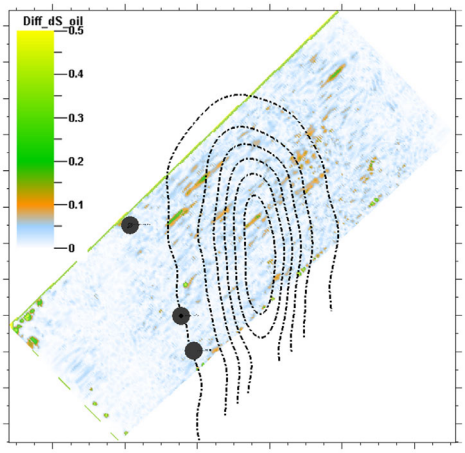

(d) Saturation change estimate error-good case

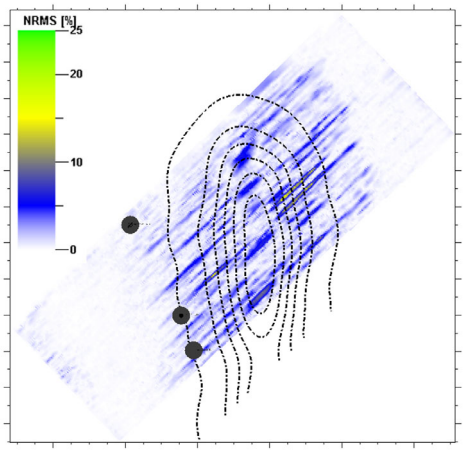

(e) NRMS difference poor case

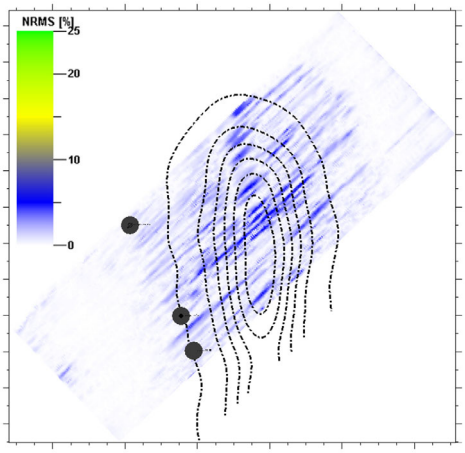

(f) NRMS difference good case

Figure 3.29: Saturation change estimation error caused by the Mio-Pliocene channel for the poor repeat case (a), (c), (e) and the good repeat case (b), (d), (f).

channel in case of the poor repeat survey. The maximum increase of the NRMS measure caused by the Mio-Pliocene channel is 16%. No change is evident away from the channel, indicating the excellent repeatability between the two models, with and without the channel, as they are the same in this region.

The maximum absolute saturation change estimation error decreases to 0.22 saturation units for the good repeat case and forms only a few clusters of localised error (Figure 3.29(d)), predominantly around the channel margins. The mean of all errors is reduced to 0.02 saturation units. This is a 27% reduction in the maximum error and a 33% reduction in the mean error compared to the poor repeat case. The standard deviation is 0.03 saturation units, thus the coefficient of variation is 1.5. This increase in the coefficient of variation over the poor repeat case is caused by the more localised clusters of error for this good repeat case. In addition, the errors are significantly less outside the channel area, although there the same degree of non-repeatability exists (Figure 3.29(b)). The mean $\Delta Source + \Delta Receiver$ measure for 1500m offset traces is reduced by 64% in the good repeat case, compared to the poor repeat case, which evidently has a large impact on the error in saturation change inversion. The influence of the Mio-Pliocene channel on the NRMS measure decreases to 7% (Figure 3.29(f)), with the largest impact on the NRMS measure beneath the thickest parts of the channel. However, there is only a weak correlation between the saturation change estimation error and the NRMS measure (Figure 3.29(d) and 3.29(f)), similar to the poor repeat Mio-Pliocene channel case.

Quaternary channel

The major differences of the Quaternary channel, compared to the Mio-Pliocene channel, is that it is very shallow, much thinner and of lower velocity compared to the the surrounding rock. Whether this changes the oil saturation change inversion error is in turn discussed. The workflow for estimating the oil saturation change is the same as for the Mio-Pliocene channel case, using data derived from ray-tracing model with and without the Quaternary channel. Furthermore, the same RMS amplitude attributes as well as the same well data are used to invert for the oil

saturation change. The maximum absolute oil saturation change error for the Quaternary channel and the poor repeat survey is 0.25 saturation units (Figure 3.30(c)) and the mean error for the entire study area is 0.02 saturation units. The errors are predominantly confined to the steeply dipping channel margins perpendicular to the seismic shooting direction, whereby errors beneath the thickest part of the Quaternary channel are negligible. The contour lines of the Quaternary channel indicate a thickness increase of 15m between each line and are overlain on the saturation change error in Figure 3.30. The standard deviation of the errors is 0.03 saturation units, thus the coefficient of variation is 1.5. In contrast to the poor Mio-Pliocene channel case, the high non-repeatability of source and receiver position does not match well with these localised errors of saturation change estimates, neither inside nor outside the channel area (Figure 3.30(a) and 3.30(c)). The maximum increase of the NRMS repeatability measure caused by the Quaternary channel and the poor repeat survey is 15% (Figure 3.30(e)), similar in magnitude compared to the Mio-Pliocene channel case. However, this increase in NRMS measure caused by the Quaternary channel does not correlate well with the channel thickness as it is observed for the previous Mio-Pliocene case, nor does it match with the observed saturation change estimate errors. The absolute error reduces by 16% to 0.21 saturation units if the good repeat case is used to model the seismic data (Figure 3.30(d)). However, the mean error stays constant at 0.02 saturation units compared to the poor repeat Quaternary channel case, but the standard deviation decreases to 0.02 saturation units. Hence, the coefficient of variation equates to 1.0 for the good repeat Quaternary channel case. Overall, the saturation change inversion error is noticeably isolated in just a few areas below the steep dipping channel margin in case of the Quaternary overburden channel affecting the wavefield. No significant errors are observed beneath channel areas that exhibit only gradually varying thickness changes. Moreover, the $\Delta Source + \Delta Receiver$ measure cannot be used to indicate possible areas of oil saturation inversion error, as the same magnitude of non-repeatability is observed across the whole survey without having significant correlation with the saturation change estimation error (Figure 3.30(b)). The same holds true for the increase of NRMS measure caused by the channel (Figure 3.30(f)). Increases of NRMS measures of up to 10% are observed, but there is no correlation

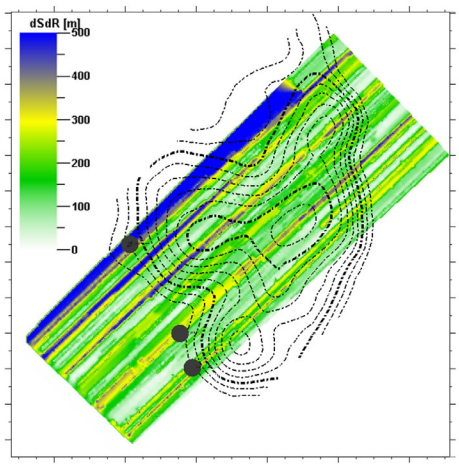

(a) $\Delta Source + \Delta Receiver$ poor case

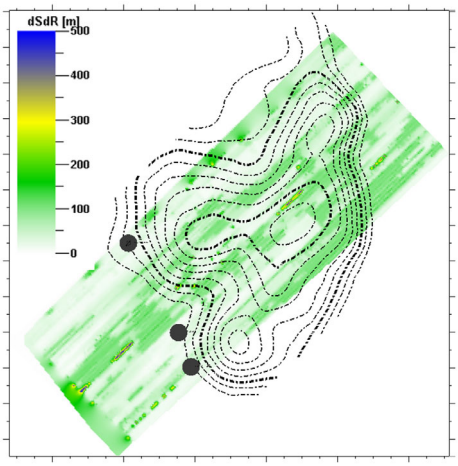

(b) $\Delta Source + \Delta Receiver$ good case

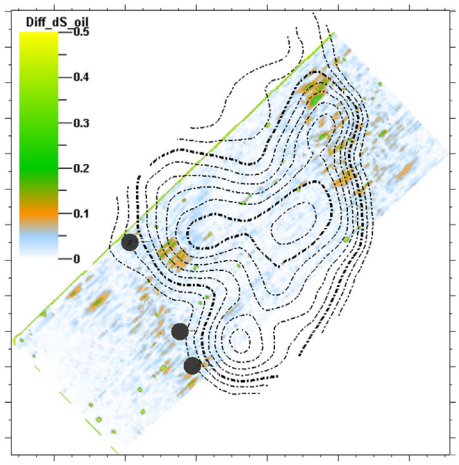

(c) Saturation change estimate error-poor case

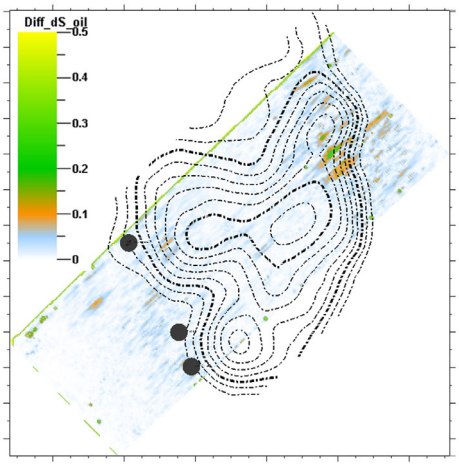

(d) Saturation change estimate error-good case

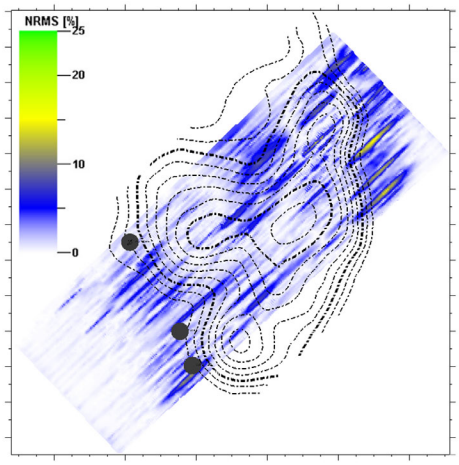

(e) NRMS difference poor case

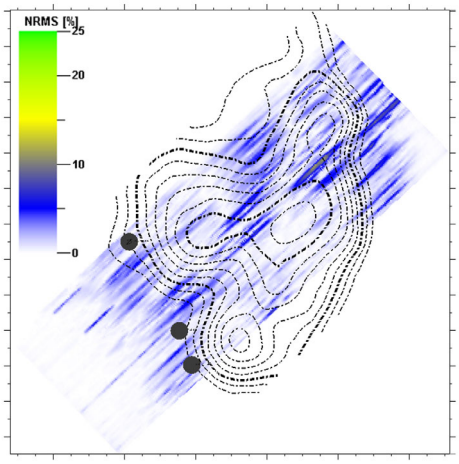

(f) NRMS difference good case

Figure 3.30: Saturation change estimation error caused by the Quaternary channel for the poor repeat case (a), (c), (e) and the good repeat case (b), (d), (f).

with the oil saturation change estimation errors. Therefore, the NRMS measure cannot be used to identify areas of increased inversion error, at least not in the case where amplitude errors only affect the seismic time-lapse data.

The maximum errors in estimating the oil saturation change from amplitude effects only are plotted against the coefficient of variation in Figure 3.31. The maximum error caused by the Quaternary channel is 16% and 5% less than the error caused by the Mio-Pliocene channel, for the poor and good repeat case, respectively. The

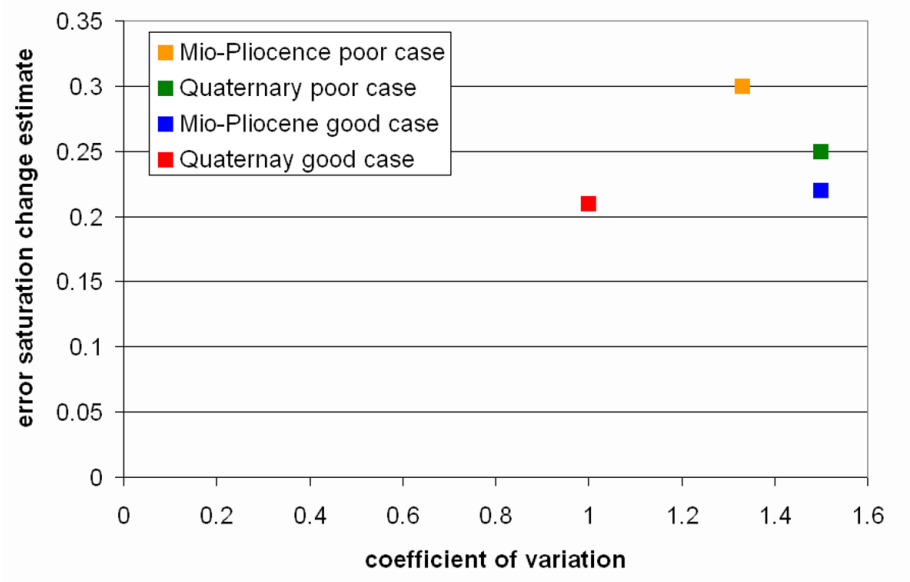

Figure 3.31: Error in estimating the oil saturation change from amplitude changes only in presence of overburden channels.

coefficient of variation indicates a narrow spread of the error across the study area, which outlines that these errors are mainly localised. The maximum errors in oil saturation change inversion are between 0.21 saturation units to 0.3 saturation units, thus between 46% to 67% of the maximum absolute oil saturation change in the model (0.45 saturation units). However, the mean errors are only between 4% to 7% of the model's maximum absolute oil saturation change.

3.7.2 Error caused by amplitude and time shift effects

In contrast to the previous section, oil saturation changes are now estimated using the RMS amplitudes extracted from the time-lapse difference data, thus they are

affected by both the amplitude and time shift effects (compare Section 3.4.1). However, the wells used for the calibration process as well as the attribute combination are kept the same, to allow for comparison between these cases.

Mio-Pliocene channel

The last section shows that the saturation change estimation errors caused by amplitude effects only do not correlate well with the increase of NRMS measure. However, when the saturation change is estimated from time-lapse difference attributes, which include amplitude as well as time shifts effects, the error caused by the overburden channel shows a better correlation to the NRMS measure (Figure 3.32(a) and 3.32(e)). The absolute error in the oil saturation change estimate increases to 0.68 saturation units (Figure 3.32(a)), the mean error increases to 0.05 saturation units and the standard deviation of the error is 0.06 saturation units. The most significant difference to the error caused by amplitude effects only is the increased error beneath the thickest part of the channel, which correlates with large residual time shifts in this area (Figure 3.32(c)). The saturation change estimation error is cross-plotted against the time shifts for each CMP bin (Figure 3.32(b)) to underline this correlation. These time shifts are extracted at the top reservoir horizon and are within the limit of ±1.5ms, but commonly in the range of ±0.5ms. Apparently, these time shifts are caused by an improper migration velocity (neglected overburden channel) and the poor repeat monitor survey, as the acquisition footprint is inherent in the time shift pattern.

In general, the saturation change inversion error increases with rising residual time shifts, however, the error is considerably spread out. Therefore, subsets of points are extracted from this cross-plot (Figure 3.32(b), dashed red lines). These subsets are regularly spaced along the time shift axis and have a width of ±0.02ms. The mean and the standard deviation are calculated for each of the subset data points and subsequently normalised by the maximum absolute oil saturation change occurring in the simulation model. Therefore, the relative increase of the mean saturation change estimation error with rising time shifts is plotted in Figure 3.32(d) (blue

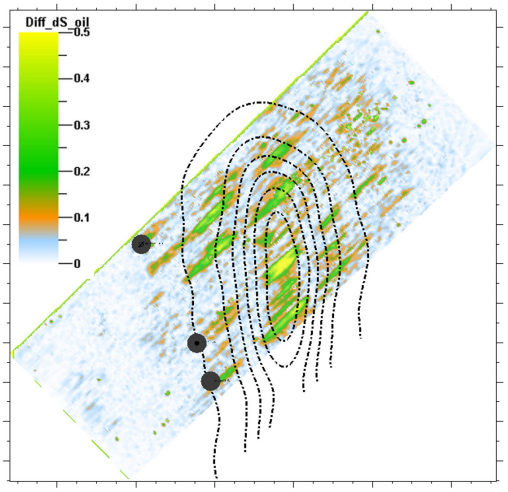

(a) Saturation change estimate error - poor case

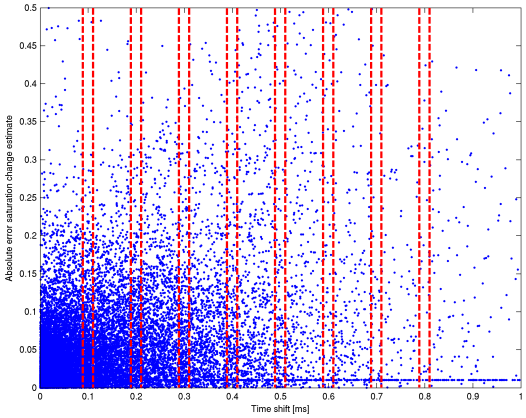

(b) Saturation change estimate error versus time shift

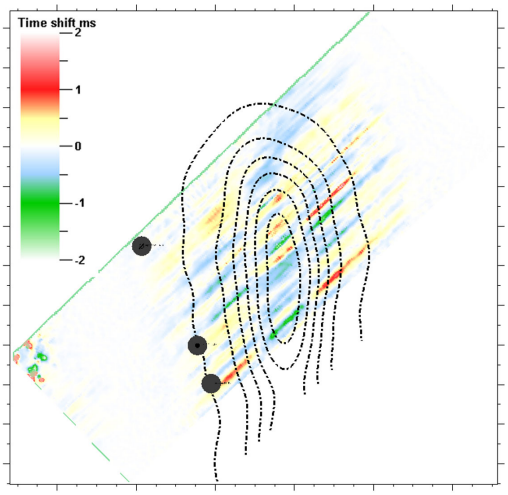

(c) Time shifts caused by the Mio-Pliocene channel

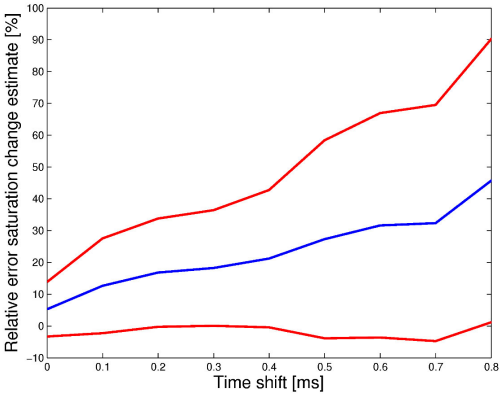

(d) Mean saturation change inversion error versus time shift

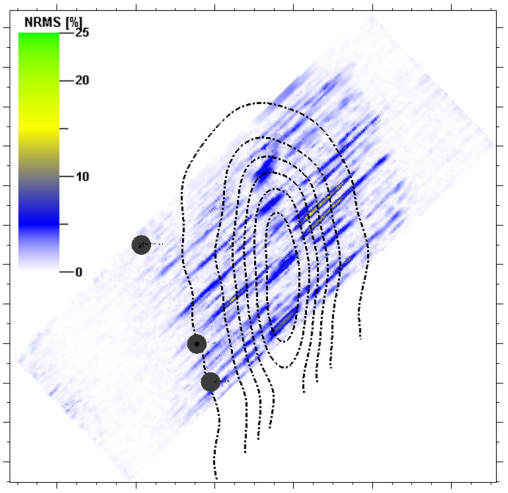

(e) NRMS difference poor case

Figure 3.32: Saturation change estimation error caused by the Mio-Pliocene channel for the poor repeat case and in case of amplitude as well as time shift effects.

line). The red lines in Figure 3.32(d) indicate the upper and lower error limit defined by one standard deviation. It is acknowledged that the lower limit cannot be negative for a relative error, however, it is still plotted for the sake of clarity. A clear and almost linear trend is observed for the increase of the mean saturation change inversion error with increasing time shift. There are not enough data points for time shifts greater than 0.8ms in order to represent an unbiased distribution, thus no data are selected in this range. Nevertheless, the trend indicates that there is a better correlation between the NRMS measure and the saturation change inversion error, in case that time shift effects impact the time-lapse data. Such small residual time shifts are known to have a large effect on the NRMS measure (Kragh and Christie, 2002) and, as shown, a significant effect on the time-lapse amplitude, thus the inversion error. However, data analysis in Section 3.7.2 shows that there is still a considerable mismatch between the NRMS measure and the inversion error, even in case when time shifts are taken into consideration.

The same study is undertaken with the Mio-Pliocene channel and the good repeat time-lapse data. In this case, the maximum saturation change estimation error decreases to 0.62 saturation units, which is a 8.80% reduction compared to the previously discussed poor repeat case (Figure 3.33(a)). The mean error, however, stays at the same level of 0.05 saturation units. The largest inversion errors are still below the thickest part of the channel, but are rapidly decreasing if far away from it. Furthermore, the residual time shifts caused by the overburden channel are significantly reduced compared to the poor repeat case (Figure 3.33(c)). Time shifts are mainly in the range of $\pm$0.5ms and compare favourably with the saturation change estimation error, as the cross-plot in Figure 3.33(b) highlights. This correlation becomes even more evident when the mean of the error is calculated for selected subsets extracted from this cross-plot and plotted against the time shift (Figure 3.33(d)). The mean oil saturation change error increases almost linearly with rising residual time shifts (Figure 3.33(d), blue line). The red line in Figure 3.33(d) is the upper and lower bound indicated by one standard deviation.

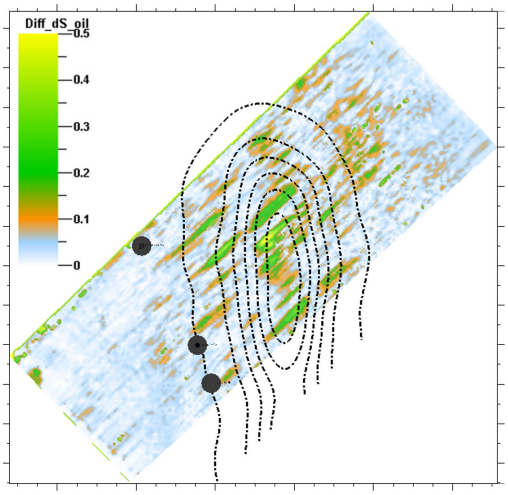

(a) Saturation change estimate error - good case

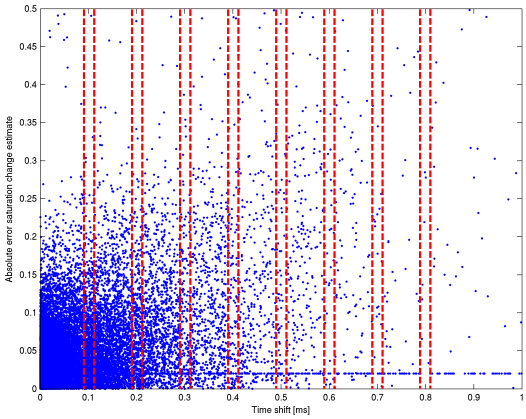

(b) Saturation change estimate error versus time shift

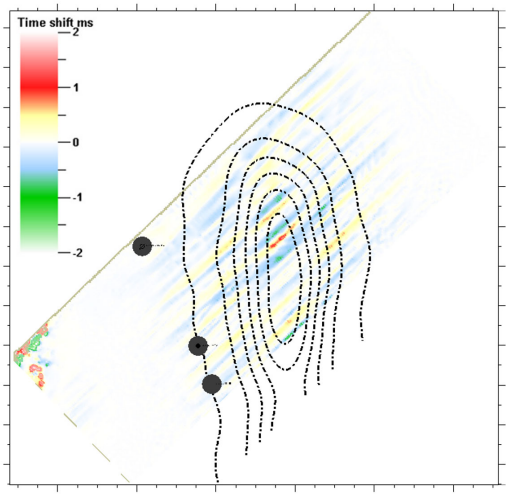

(c) Time shifts caused by the Mio-Pliocene channel

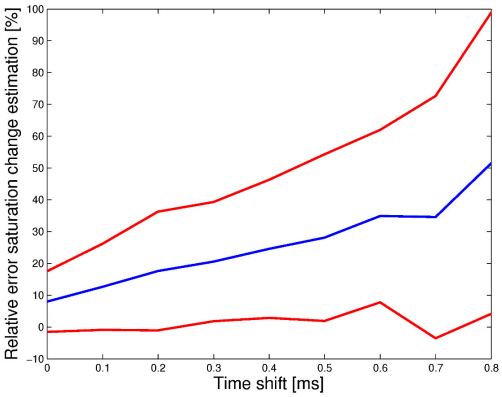

(d) Mean saturation change inversion error versus time shift

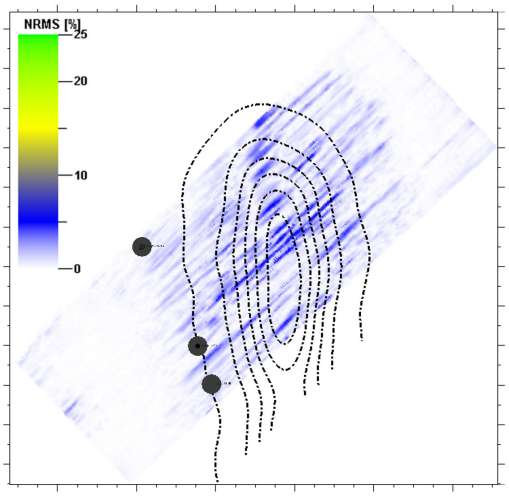

(e) NRMS difference good case

Figure 3.33: Saturation change estimation error caused by the Mio-Pliocene channel for the good repeat case and in case of amplitude as well as time shift effects.

Quaternary channel

The effect of time shifts caused by the Quaternary channel on the saturation change estimation is finally investigated for the poor and good repeat case.

Figure 3.34(a) shows the absolute saturation change inversion error caused by the Quaternary channel and the poor repeat survey. The maximum error is 0.60 saturation units and the mean error of the whole map is 0.04 saturation units. The errors are still localised beneath the steep dipping channel margin but are larger than in the case of inversion errors solely due to amplitude effects. Moreover, the correlation between the saturation change inversion error and the increase in NRMS measure as well as the residual time shifts, caused by the channel, is favourable (Figures 3.34(a), 3.34(c) and 3.34(e)). However, there are no significant errors beneath the thickest parts of the channel, although there are residual time shifts in the range of $\pm$0.5ms which are caused by the Quaternary channel and the poor repeat survey (Figure 3.34(c)). These areas which exhibit a high degree of mismatch between the saturation change estimation error and the NRMS measure as well as time shifts are marked by red arrows. This mismatch is apparent when the error in oil saturation change estimate is cross-plotted against the time shifts (Figure 3.34(b)). There are many data points with low saturation error at high time shift values. However, a weak trend of increasing saturation change inversion errors with rising time shift can be identified in the cross-plot. This trend is more visible when the mean and the standard deviation are calculated for data subsets of the cross-plot and plotted against the respective time shift (Figure 3.34(d), blue line). The linear trend confirms the assumption that the increase in saturation change error is linked to the rising time shifts. The red lines mark the upper and lower error limits within one standard deviation. Comparison of these results to the Mio-Pliocene channel poor repeat case reveals that the increase in the mean saturation change estimation error is slightly less (Figures 3.34(d) and 3.32(d)). It is also apparent that the time shifts beneath the thickest part of the Quaternary channel do not cause the largest error, which is in contrast to the previously discussed Mio-Pliocene channel case. However, the thickest part of the Quaternary channel extends over a large area where thickness changes are small. On the other hand, the thickest part of

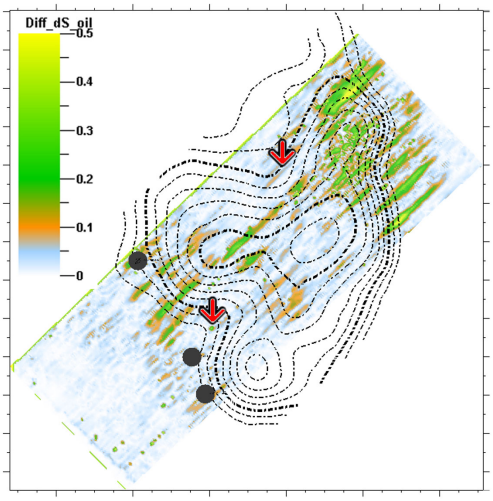

(a) Saturation change estimate error - poor case

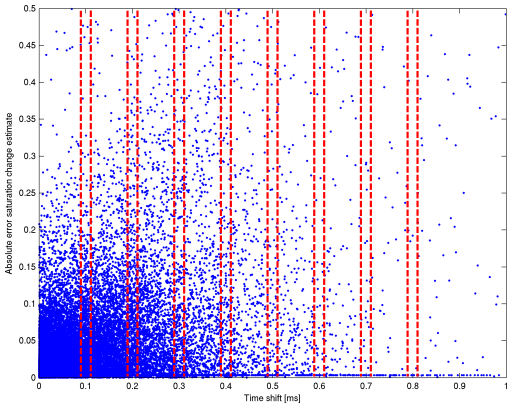

(b) Saturation change estimate error versus time shift

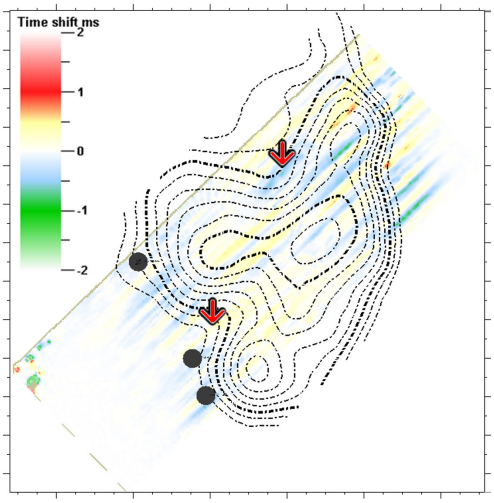

(c) Time shifts caused by the Mio-Pliocene channel

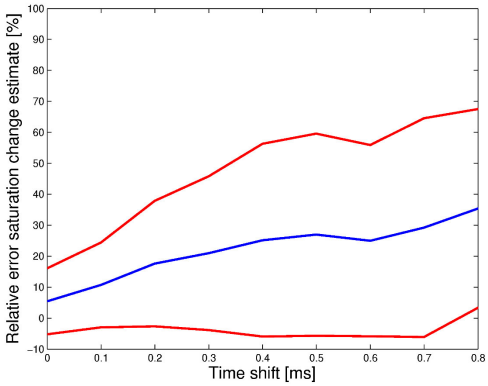

(d) Mean saturation change inversion error versus time shift

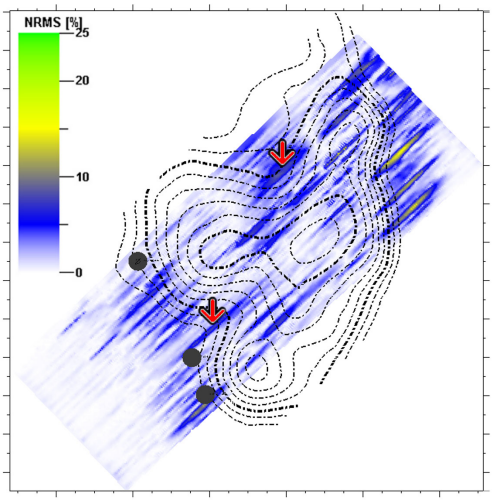

(e) NRMS difference poor case

Figure 3.34: Saturation change estimation error caused by the Quaternary channel for the poor repeat case and in case of amplitude as well as time shift effects. Red arrows indicate areas of large time shifts as well as NRMS measure that show no effect on the inversion error.

the Mio-Pliocene channel extends over a small area and is enclosed by the steeply dipping channel margins. Hence, the gradient of the Mio-Pliocene channel bottom is rapidly changing in this area, which is opposite to the slowly varying gradient at the thickest part of the Quaternary channel. Therefore, this rapid gradient change of Mio-Pliocene channel's surface, which just coincides with the thickest part of the channel, causes the large errors.

The last case discussed is the Quaternary channel and the good repeat survey. There, the maximum saturation change error decreases only slightly to 0.59 saturation units compared to the poor repeat case. Most of the errors are still below the steep dipping channel margin to the right hand side of the channel (Figure 3.35(a)). The mean error for the whole maps stays at 0.04 saturation units. The residual time shifts reduce to values well below $\pm$0.5ms and an overall satisfying correlation is found with the inversion error (Figure 3.35(c)). This correlation is further confirmed when cross potting the time-shifts and the inversion error (Figure 3.35(b)). Moreover, it is obvious that there are no usable data points for time shift values greater 0.4ms. Hence, the mean and the standard deviation are only calculated for data point subsets up to 0.4ms and plotted once more against the respective time shift (Figure 3.35(d)). The dashed line segments are derived from data subsets which do not have a significant number of samples in order to be statistically representative, thus not valid. However, the mean values for time shifts up to 0.4ms show a clear linear trend of increasing mean saturation change inversion error with increasing residual time shift (blue line). The error limits of one standard deviation are again marked by the red lines in Figure 3.35(d). Besides the favourable match between time shifts or NRMS measure and the saturation change inversion error, there are also areas with a poor correlation between these measures (Figures 3.35(a), 3.35(c) and 3.35(e), red arrow).

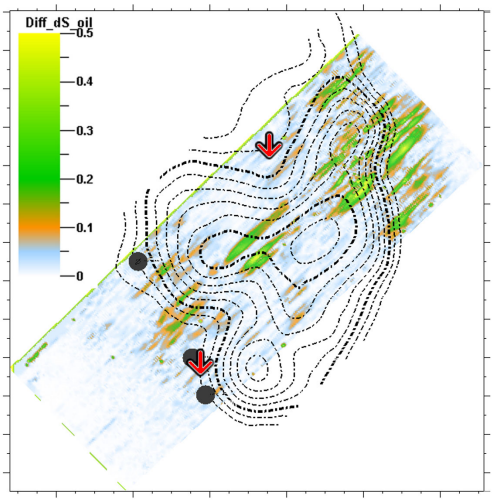

(a) Saturation change estimate error - good case

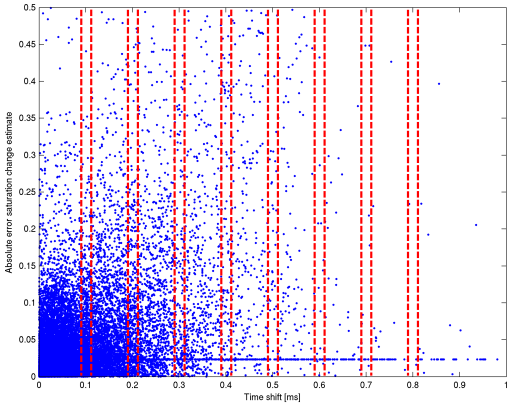

(b) Saturation change estimate error versus time shift

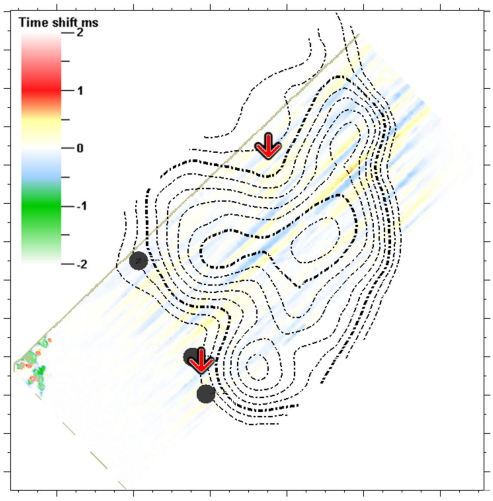

(c) Time shifts caused by the Mio-Pliocene channel

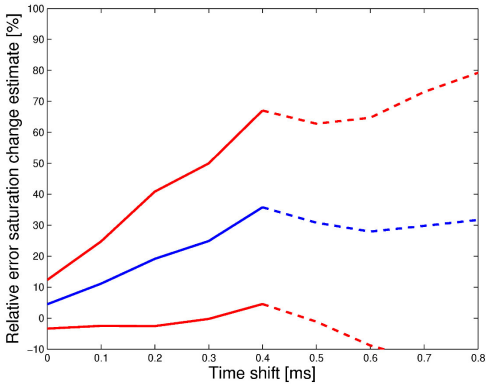

(d) Mean saturation change inversion error versus time shift

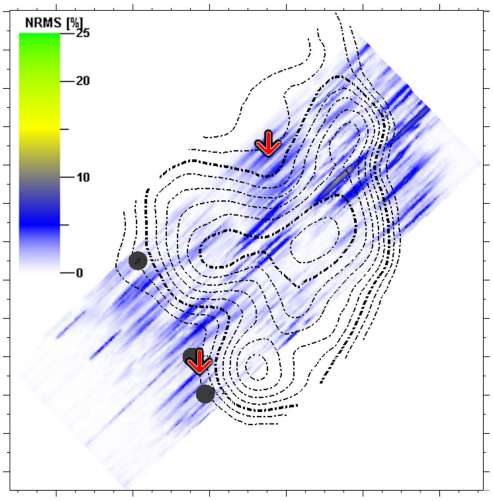

(e) NRMS difference good case

Figure 3.35: Saturation change estimation error caused by the Quaternary channel for the good repeat case and in case of amplitude as well as time shift effects. Red arrows indicate areas of large time shifts as well as NRMS measure that show no effect on the inversion error.

3.8 Discussion and implications of overburden channel effects on saturation change estimates

The previous sections show that the Mio-Pliocene and the Quaternary channel cause saturation change inversion errors if the acquisition geometry is not exactly repeated. Furthermore, the largest errors occur when the time-lapse attributes that are used for the inversion are affected by residual time shifts. The pink, orange, black and turquoise curves in Figure 3.36 show the increase in the mean saturation change estimation error with rising residual time shifts, caused by the Mio-Pliocene as well as the Quaternary channel for the good and poor repeat case. The data are extracted

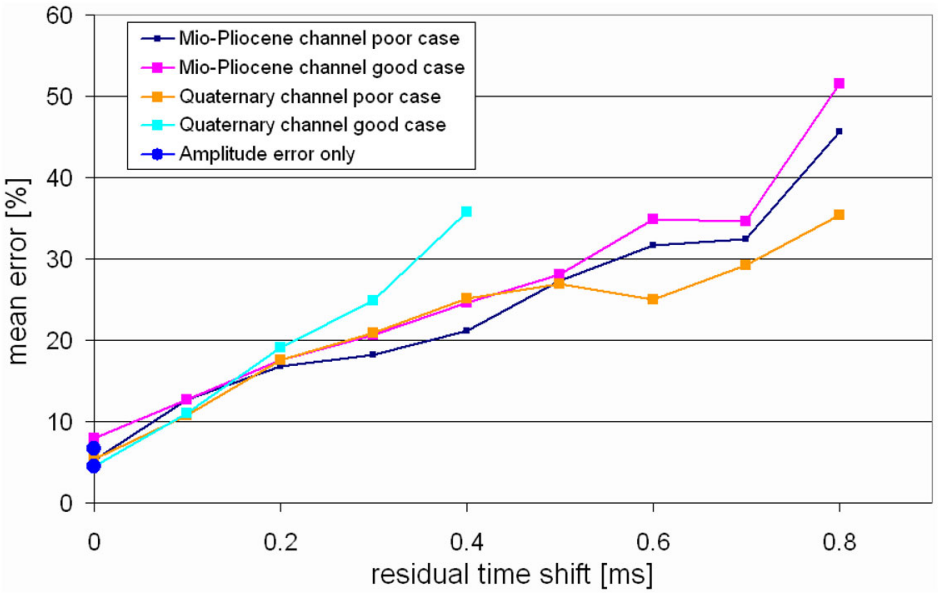

Figure 3.36: The mean saturation change inversion error plotted against the residual time shifts. The error is set relative to the maximum oil saturation change in data.

from previously discussed figures and compiled into this chart. It is observed that the error is almost independent of the type of overburden channel and also independent of whether the good or poor repeat survey is used, hence only dependent on the time shift. Moreover, the linear trend in the mean saturation change error compares favourably with the linear increase of the RMS amplitude error with increasing time shifts, observed in the simple Ricker wavelet example (Figure 3.16).

In addition, the two blue circles (at zero time) mark the mean error of saturation change inversion if the time-lapse attribute is calculated from the difference of the RMS amplitudes. These errors correlate well with the mean errors observed for zero time shifts, thus there is a strong indication that by taking the difference of the RMS amplitude, time shift effects are effectively removed from the saturation change estimates. The inversion error range can be specified when the standard deviation is taken into account for the various cases: the error is between 0% and 15% for amplitude effects only, increases to 10% to 35% for time shifts up to 0.4ms and further rises to 35% to 55% for time shifts as large as 0.8ms. These errors are relative to the absolute oil saturation change of 0.45 saturation units occurring in the model. Hence, even small residual time shifts of up to $\pm$0.4ms significantly impact the ability to quantitatively estimate and interpret the oil saturation change. On the other hand, the processing of time-lapse seismic data aims to reduce time shifts as much as possible. Therefore, cross-correlation and local as well as global matching filters are commonly applied to the baseline and monitor data (for example, Magesan et al. (2005), Kristiansen et al. (2000) and Rickett and Lumley (2001)). Nevertheless, time shifts cannot be completely removed. Østmo et al. (2007) report on estimating time shifts from repeat seismic data (Kristin field, offshore Norway) that are recorded within 24 hours, thus are not affected by production-induced reservoir changes. They state that time shifts between the baseline and monitor seismic data can be estimated with an accuracy of $\pm$0.4ms and 95% confidence, however, they also mention that additional error sources can possibly occur when the baseline and monitor data are recorded several years apart. This is certainly the case for residual time shifts observed above the Curlew D field, Central North Sea, which are in the range of $\pm$1.0ms. Fehmers et al. (2007) suspect that these residual time shifts are caused by the differences in source and receiver positioning between the surveys, but cannot be removed during processing. Moreover, residual time shifts within the range of $\pm$0.5ms are observed predominantly below overburden channels at the Nelson Field (Jon Brain, Shell UK, personal communication), which is in line with the results of this study.

Hence, it is shown in this chapter, that the Mio-Pliocene as well as the Quaternary overburden channel in conjunction with a non-repeat acquisition geometry cause residual time shifts of a magnitude commonly observed in time-lapse data, but difficult to remove. Therefore, it is concluded that these overburden channels severely increase the overall time-lapse time shift noise level, and the resulting mean oil saturation change inversion errors commonly exceed 25% compared to the maximum saturation change. The quantitative interpretability is significantly reduced by this increase of the mean inversion error as well as by smaller patches of oil saturation inversion error up to 55% (compare Figures 3.32 to 3.35). It is advisable to mark areas of increased residual time shifts as they will have a higher uncertainty in the oil saturation inversion results and quantitative interpretation of reservoir changes should be done carefully in these areas.

It is also shown that the time alignment of the baseline and monitor survey is very important if the time-lapse attributes are extracted from the difference data. Indeed, Bertrand et al. (2005) outline the importance in decoupling the effects of traveltime and amplitudes differences which are otherwise combined and impede the quantitative interpretation. They state that regular cross-correlation techniques are limited when it comes to resolving strong time shifts of opposite sign within narrow time windows and consequently present a morphing process that better resolves these shifts. However, the study presented in this chapter shows that time shifts are effectively mitigated by simply taking the difference of the RMS amplitude, which significantly reduces the oil saturation change estimate errors to the ones caused by amplitude effects of the overburden channel only. Therefore, it is strongly suggested to take the difference of the RMS amplitude to estimate the oil saturation change and consequently eliminating large inversion errors caused by time shifts. In this case the mean error reduces to less than 10% and the few very localised patches with errors up to 50% do not severely affect the quantitative interpretation (compare Figure 3.29 and 3.30), at least for the good repeat case. The errors that originate from amplitude effects in the poor repeat case, however, are of larger magnitude and also are distributed over a larger area, thus increase the mean error by one third. Therefore, the ability to quantitatively interpret the time-lapse changes is considerably affected.

Furthermore, this study shows that the position of these patches of increased (above the mean error) oil saturation inversion error cannot be accurately derived from common repeatability measures, such as the NRMS or $\Delta Source + \Delta Receiver$ measure. Therefore, these repeatability measures are only a loose guide to identify errors in the inversion results. This is most evident when the increase in NRMS measure, which is caused by the overburden channel, is plotted against the absolute oil saturation change inversion error (Figure 3.37). The correlation between the inversion

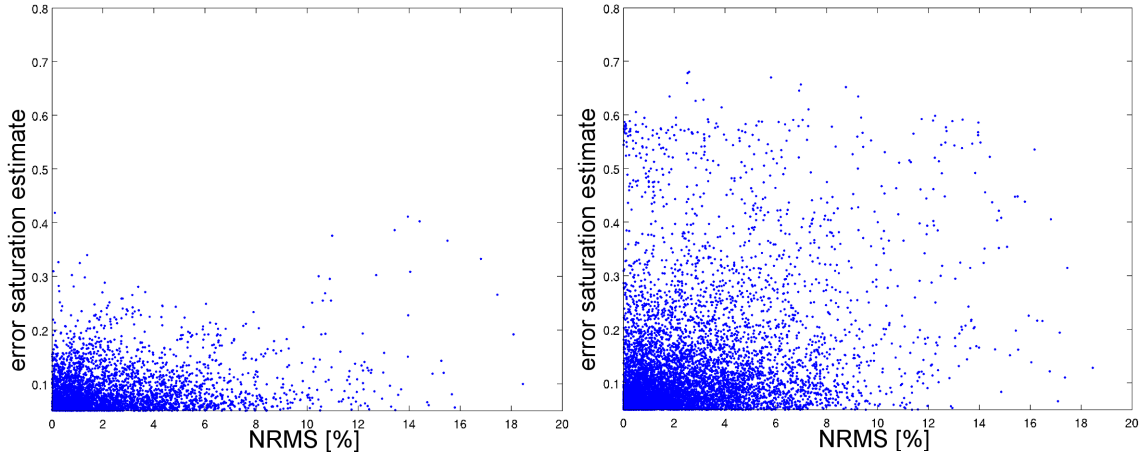

(a) Amplitude effect poor repeat case

(b) Time shifts effect poor repeat case

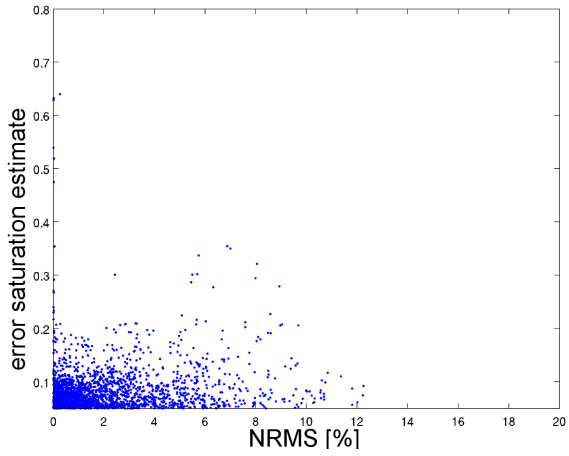

(c) Amplitude effect good repeat case

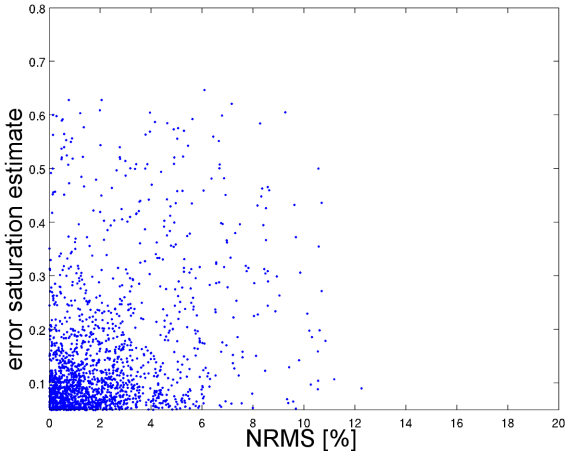

(d) Time shifts effect good repeat case

Figure 3.37: The increase of NRMS caused by the Quaternary channel is plotted against the oil saturation inversion error in case of: (a), (c) amplitude effects only; (b), (d) amplitude and time shift effects.

error and the NRMS measure is very poor if the oil saturation change is estimated from time-lapse attributes that are only affected by amplitude changes, regardless of the poor or good repeat case (Figures 3.37(a) and 3.37(c)). The correlation improves if the inversion errors are caused by time shifts (Figures 3.37(b) and 3.37(d)),

however, is far from an excellent fit. There is no clear trend that can be used to relate the increase of the NRMS measure to an increased error in saturation change inversion. Areas of higher NRMS measure than the average do not automatically exhibit a large error when inverting for the oil saturation change, thus the NRMS measure is not well suited to reliably indicate locations with increased saturation change inversion errors.

One implication for quantitative interpretation is that overburden channels cause errors in the oil saturation estimates which can obscure production-induced changes in the reservoir. This holds true especially if the time-lapse survey is intended to delineate the waterfront advancing with time to predict early water breakthrough at the producers. However, this depends on the lateral extent of the transition zone which is different for specific fields, thus the uncertainty of the exact position of the waterfront will vary. Figure 3.38 highlights two simple lateral water drive cases where the water saturation, S_w, decreases from 0.8 saturation units to 0.2 saturation units over a narrow and a wide transition zone. The blue indicates the

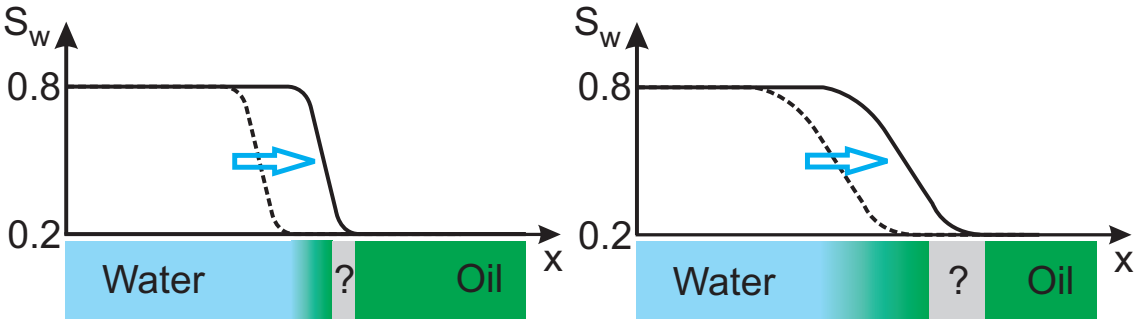

(a) Narrow transition zone (b) Wide transition zone

Figure 3.38: Schematic sketch of the uncertainty in estimating the waterfront for (a) a narrow saturation transition zone and (b) a wide transition zone. The water saturation along the x-axis inside the reservoir is plotted by the dashed and solid line for the baseline and monitor time, respectively. The grey area outlines the uncertainty in the position position of the waterfront for a 25% mean saturation inversion error.

water swept area, whereas the green indicates the unswept area of the reservoir and gradient colour marks the transition zone. The water saturation along the x-direction inside the reservoir is plotted above the reservoir, with the dashed line indicating the old position of the transition zone (baseline survey) and the solid line the new position (monitor survey). Assuming a 25% mean error in estimating the

saturation change, the grey area indicates the uncertainty in estimating the new position of the waterfront. For the Nelson Field, for example, a mean error of 25% in the oil saturation change inversion could misplace predictions of the onset of the waterfront by up to 150m. Moreover, this uncertainty might also be considered when extracting geobodies in order to estimate the remaining reserves in the reservoir.

Finally, the error in the oil saturation change inversion caused by the Quaternary channel and the poor repeat survey is imposed on the oil saturation change extracted from the simulator to give an impression of how such errors can affect the quantitative interpretation.

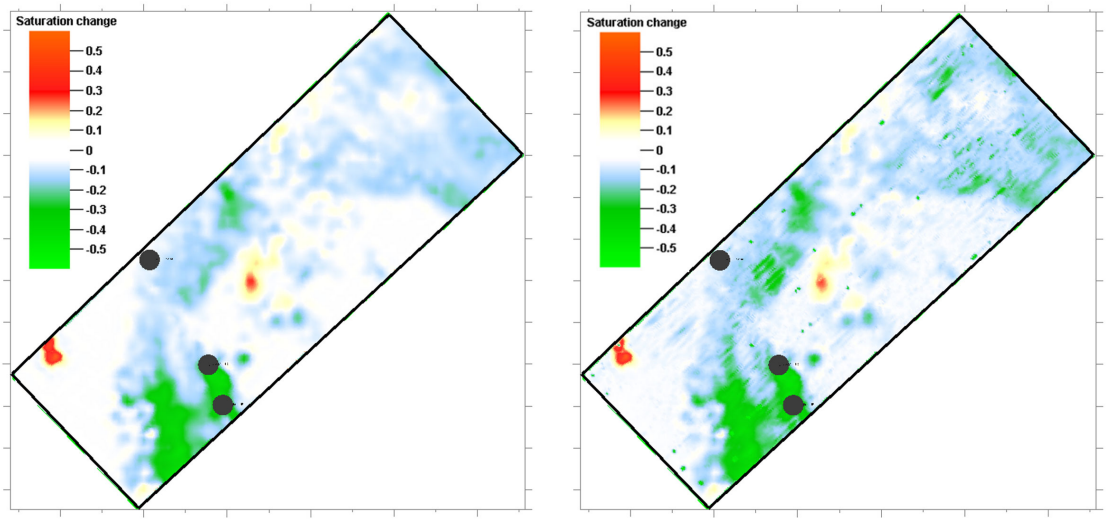

(a) Oil saturation change from simulation model (b) Errors caused by amplitude effects overlain

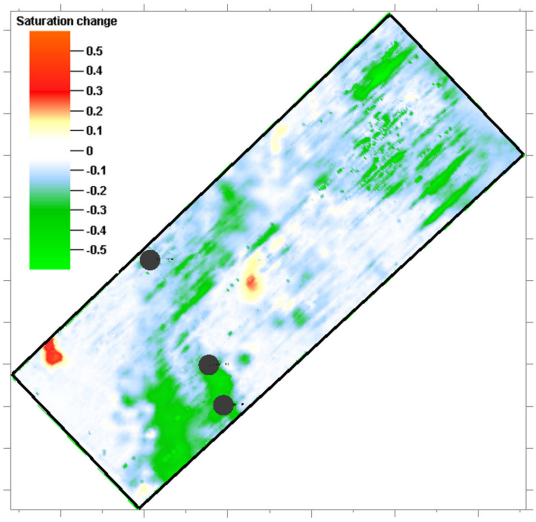

(c) Errors caused by time shift effects overlain

Figure 3.39: Overburden channel impact (poor repeat case) on the oil saturation change inversion superimposed on the simulation saturation change. (a) Change from the simulation model. (b) Change with Mio-Pliocene channel errors and (c) Change with Quaternary channel error overlain.

The errors caused by amplitude effects (Figure 3.39(b)) are less severe than the errors caused by time shifts effects (Figure 3.39(c)). Nevertheless, the main character of the saturation change is still preserved, especially in case of the errors caused by amplitude effects only. Eliminating these errors from the time-lapse data using the workflow as outlined in this chapter is difficult, because the model without the overburden channel as reference does not exist. Therefore, the next chapter discusses one possible approach to cancelling out overburden errors caused by amplitude effects using a layer stripping approach.

3.9 Summary of overburden channel effects on oil saturation change inversion

The effect of overburden channels on the time-lapse saturation change inversion is investigated. It is observed that non-repeatability of source and receiver positions during marine seismic data acquisition in conjunction with such overburden heterogeneity significantly impedes the quantitative interpretation of oil saturation changes. The absolute error in the saturation change estimation is as high as 0.68 saturation units if the amplitude attributes are affected by residual time shifts. In this case, localised errors are greater than the actual absolute oil saturation change of 0.45 saturation units. On the other hand, the saturation change inversion error reduces significantly to less than 0.30 saturation units if it is solely caused by amplitude errors originating from the overburden channel. It is thus suggested that it is best to work with the difference of the RMS amplitude attributes in order to reduce the effect of time shifts during the inversion process.

Moreover, the study shows that the shape of the channel significantly affects the spatial distribution of the saturation change inversion error at the reservoir level. This behaviour is summarised in Figure 3.40. V-shape channels (Mio-Pliocene channel) cause errors beneath the entire channel width due to the dipping channel margins (Figure 3.40(a)). On the other hand, the errors are marginal beneath the flat channel base for U-shape channels, such as the Quaternary channel (Figure 3.40(b)). In

the latter case, the errors are concentrated beneath the dipping channel margins. The acquisition direction is perpendicular to the channel axis in both cases. Furthermore, a preliminary study shows that the errors reduce significantly for both channel types in case that the acquisition direction is parallel to the channel axis.

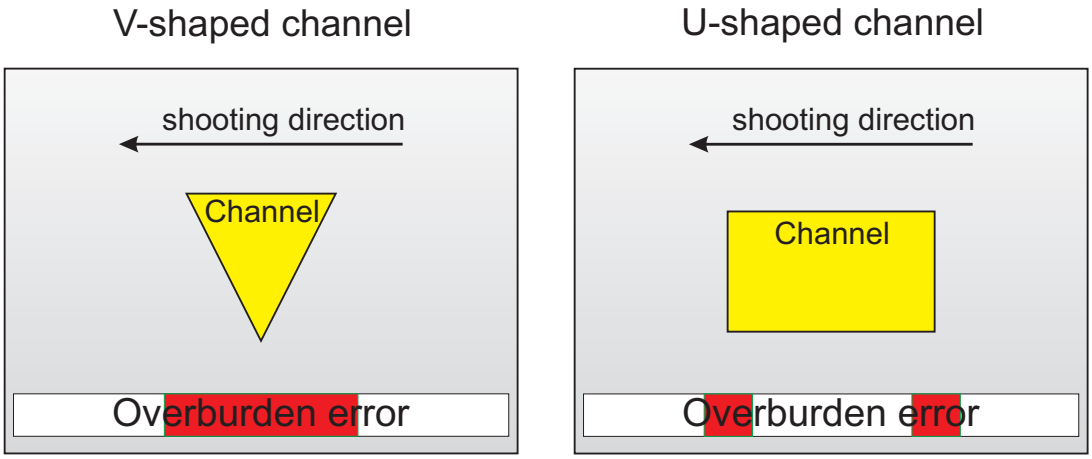

(a) (b)

Figure 3.40: Channels with different profiles cause errors at different spatial locations at the reservoir. The channel axis in both figures is perpendicular to the paper plane and the shooting direction of the seismic survey is perpendicular to the channel axis. (a) A V-shaped channel generates errors across the entire channel width. The red rectangle marks the spatial extend of the error at the reservoir level. (b) A U-shaped channel generates errors only beneath the steeply dipping channel margins, not beneath the flat channel base. The spatial extend of the error at the reservoir level is marked by the two red rectangles.

Chapter 4

Separating overburden, production and acquisition effects at the Nelson Field

This chapter first discusses the propagation of plane waves in stratified media, which is in turn used to derive a general framework that allows one to extract the time-lapse reservoir reflectivity change from the seismic data. The assumptions needed to perform this analysis in the post-stack domain are specified. Consequently, the reservoir reflectivity analysis tool is tested on the Nelson synthetic time-lapse data in order to evaluate its performance in predicting the change of the reservoir reflectivity independently of the overburden channel effects. Finally, the change in oil saturation is estimated from this new set of attributes and compared to former inversion results.

4.1 Seismic waves in stratified media

When seismic waves travel through stratified media, they are reflected and transmitted at interfaces where there is a change in elastic properties. The simple case of two homogenous half spaces bound by an interface at depth z_I (Figure 4.1) is considered first. Both half spaces have different elastic parameters, α_-, β_-, ρ_-, α_+,

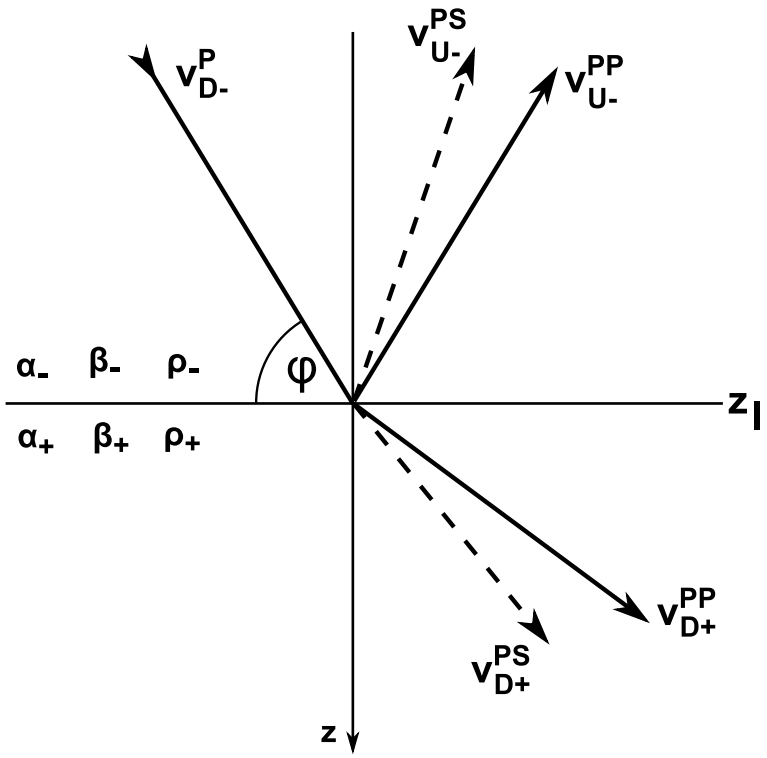

Figure 4.1: Reflected and transmitted waves in two half spaces bound at the interface at depth z.

β_+, ρ_+ and are in welded contact at the interface. Therefore, the stress displacements are continuous across the interface. The parameters α, β and ρ represent the P-wave velocity, S-wave velocity and density, respectively. Four possible types of wave conversion exist for each case, reflection or transmission. An incidence P-wave is reflected into a P-wave (P-P conversion) and an SV-wave (P-SV conversion). The same applies for an incidence SV-wave, which is converted into a P-wave (SV-P conversion) and an SV-wave (SV-SV conversion). Wave type conversions for the transmitted waves are analogous. To maintain readability, conversion types are denoted with PP, PS, SP and SS for the P-P, P-SV, SV-P and SV-SV conversion, respectively. Hence, the incidence, downgoing P-wave, $\boldsymbol{\nu}^{\mathrm{P}}_{\mathrm{D}-}$, gives rise to the reflected

upgoing P- and SV-waves, $\boldsymbol{\nu}^{\mathrm{PP}}_{\mathrm{U\text{-}}}$ and $\boldsymbol{\nu}^{\mathrm{PS}}_{\mathrm{U\text{-}}}$, as well as to the transmitted downgoing P- and SV-waves, $\boldsymbol{\nu}^{\mathrm{PP}}_{\mathrm{D+}}$ and $\boldsymbol{\nu}^{\mathrm{PS}}_{\mathrm{D+}}$. The amplitudes of the reflected and transmitted waves depend on the angle of the incidence wave, φ, and can be derived by the Zoeppritz equations (Zoeppritz, 1919). However, these equations are highly non-linear and simplified versions are used in practice (for example, the ones presented by Aki and Richards (2002)). The incidence downgoing P-wave, $\boldsymbol{\nu}^{\mathrm{P}}_{\mathrm{D\text{-}}}$, and S-wave, $\boldsymbol{\nu}^{\mathrm{S}}_{\mathrm{D\text{-}}}$, are now combined into an incidence downgoing wavefield, $\boldsymbol{\nu}_{\mathrm{D\text{-}}}$, containing both wave types. Subsequently, a reflection matrix, $\mathbf{R}^{\mathrm{I}}_{\mathrm{D}}$, is defined that connects the incidence downgoing wavefield, $\boldsymbol{\nu}_{\mathrm{D\text{-}}}$, with the upgoing reflected wavefield, $\boldsymbol{\nu}_{\mathrm{U\text{-}}}$, at one specific point along the interface:

$$\boldsymbol{\nu}_{\mathrm{U\text{-}}} = \mathbf{R}^{\mathrm{I}}_{\mathrm{D}}\, \boldsymbol{\nu}_{\mathrm{D\text{-}}} \tag{4.1}$$

This reflection matrix combines the different reflection coefficients for the different P- and S-wave conversions. Hence, the reflected upgoing wavefield, $\boldsymbol{\nu}_{\mathrm{U\text{-}}}$, can be written in terms of a wave vector, which yields (after Kennett (1983), pp.104):

$$\begin{bmatrix} \boldsymbol{\nu}^{\mathrm{P}}_{\mathrm{U\text{-}}} \\ \boldsymbol{\nu}^{\mathrm{S}}_{\mathrm{U\text{-}}} \end{bmatrix} = \begin{bmatrix} R^{PP}_{D} & R^{PS}_{D} \\ R^{SP}_{D} & R^{SS}_{D} \end{bmatrix} \begin{bmatrix} \boldsymbol{\nu}^{\mathrm{P}}_{\mathrm{D\text{-}}} \\ \boldsymbol{\nu}^{\mathrm{S}}_{\mathrm{D\text{-}}} \end{bmatrix} \tag{4.2}$$

The same applies for the transmitted downgoing wavefield, $\boldsymbol{\nu}_{\mathrm{D+}}$:

$$\boldsymbol{\nu}_{\mathrm{D+}} = \mathbf{T}^{\mathrm{I}}_{\mathrm{D}}\, \boldsymbol{\nu}_{\mathrm{D\text{-}}} \tag{4.3}$$

and

$$\begin{bmatrix} \boldsymbol{\nu}^{\mathrm{P}}_{\mathrm{D+}} \\ \boldsymbol{\nu}^{\mathrm{S}}_{\mathrm{D+}} \end{bmatrix} = \begin{bmatrix} T^{PP}_{D} & T^{PS}_{D} \\ T^{SP}_{D} & T^{SS}_{D} \end{bmatrix} \begin{bmatrix} \boldsymbol{\nu}^{\mathrm{P}}_{\mathrm{D\text{-}}} \\ \boldsymbol{\nu}^{\mathrm{S}}_{\mathrm{D\text{-}}} \end{bmatrix} \tag{4.4}$$

These reflection and transmission matrices are defined at local coordinates, x, y, along the interface intersecting the two media. These locally defined reflection and transmission matrices can in turn be expanded into a generalised reflection and transmission coefficient in case of a stratified media, bound by two half spaces. Figure 4.2 illustrates an example of a stratified media where two layers are bound between two half spaces and for which the generalised reflectivity is derived. The following problem is to be solved: the incidence downgoing wavefield, $\boldsymbol{\nu}_{\mathrm{D\text{-}}}$, is reflected and transmitted at interface B and C, thus the total upgoing wavefield, $\boldsymbol{\nu}_{\mathrm{U\text{-}}}$,

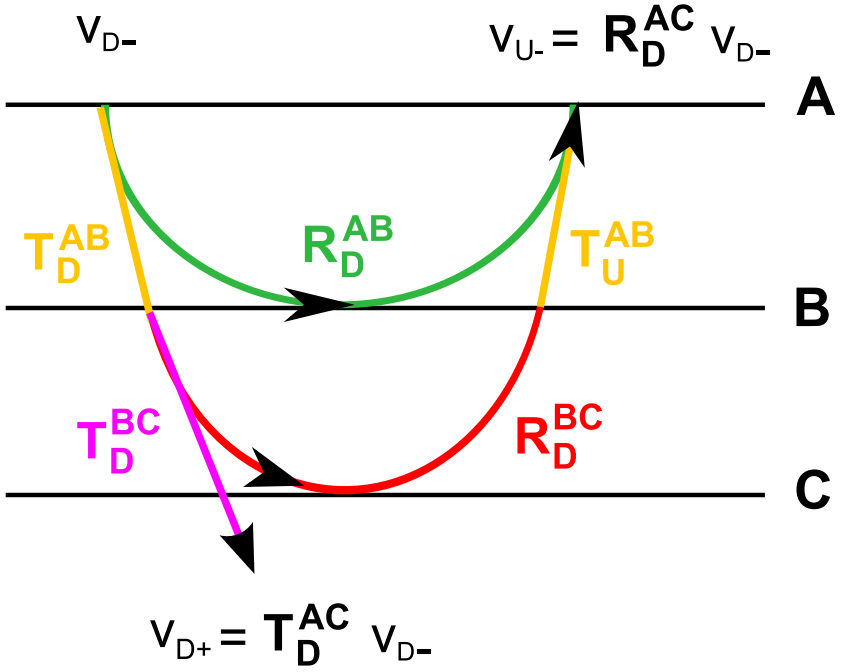

Figure 4.2: Schematic representation of the generalised reflectivity of a stratified media.

is to be constructed. The wavefield also propagates between each of the interfaces, in addition to local reflection and transmission. Hence, the traveltime between interfaces A and B as well as B and C, in both the downward and upward direction, is equivalent to a phase shift in the frequency domain. Therefore, the frequency dependent wave propagator term, $\mathbf{P}(A, B)$, is introduced, which in this case accounts for the wave propagation between interfaces A and B. Consequently, the generalised reflectivity, $\mathbf{R}_{\mathrm{D}}^{\mathrm{AB}}$, of the layer AB which describes the wave propagation from interface A down to interface B, the reflection at interface B and in turn the propagation from interface B to A, is written as follows:

$$\mathbf{R}_{\mathrm{D}}^{\mathrm{AB}}(\mathbf{x}, \omega, \mathbf{p}) = \mathbf{P}(B, A)\, \mathbf{R}_{\mathrm{D}}^{\mathrm{B}}(\mathbf{x}, \omega, \mathbf{p})\, \mathbf{P}(A, B) \tag{4.5}$$

Equation 4.5 is a plane wave formula in the frequency domain, thus the individual terms can be multiplied. Moreover, the reflectivity matrix depends on the frequency, ω, and the x- and y-position along the interface, $\mathbf{x}$. Furthermore, the reflectivity matrix, $\mathbf{R}_{\mathrm{D}}^{\mathrm{B}}$, depends on the angle of the incidence wavefield, which can also be expressed in terms of the slowness, $\mathbf{p}$. The generalised reflectivity of the stack of layers between interface A and C, $\mathbf{R}_{\mathrm{D}}^{\mathrm{AC}}$, is thus obtained by adding the wavefield

that is reflected at interface C to the generalised reflectivity, $\mathbf{R}_{\mathrm{D}}^{\mathrm{AB}}$. Intra-interface multiples can also be taken into account, and are discussed in due course. Therefore, the generalised reflectivity of the layer BC, $\mathbf{R}_{\mathrm{D}}^{\mathrm{BC}}$, is connected to the down- and upgoing wavefield by the propagator terms, $\mathbf{P}(A,B)$ and $\mathbf{P}(B,A)$, as well as the downwards and upwards transmission matrix at the interface B, $\mathbf{T}_{\mathrm{D}}^{\mathrm{B}}$ and $\mathbf{T}_{\mathrm{U}}^{\mathrm{B}}$, respectively. Consequently, the generalised reflectivity of the layers between interfaces A and C, $\mathbf{R}_{\mathrm{D}}^{\mathrm{AC}}$, equates to:

$$\begin{aligned}\mathbf{R}_{\mathrm{D}}^{\mathrm{AC}}(\mathbf{x},\omega,\mathbf{p}) = \mathbf{P}(B,A)\,\mathbf{R}_{\mathrm{D}}^{\mathrm{B}}\,\mathbf{P}(A,B) \\ + \mathbf{P}(B,A)\mathbf{T}_{\mathrm{U}}^{\mathrm{B}}\mathbf{P}(C,B)\mathbf{R}_{\mathrm{D}}^{\mathrm{C}}\mathbf{P}(B,C)\,\mathbf{T}_{\mathrm{D}}^{\mathrm{B}}\,\mathbf{P}(A,B)\end{aligned} \tag{4.6}$$

The upgoing wavefield, $\boldsymbol{\nu}_{\mathrm{U}\text{-}}$, is thus calculated from the downgoing, $\boldsymbol{\nu}_{\mathrm{D}\text{-}}$, wavefield by using the generalised reflectivity of the stack of layers:

$$\boldsymbol{\nu}_{\mathrm{U}\text{-}} = \mathbf{R}_{\mathrm{D}}^{\mathrm{AC}}(\mathbf{x},\omega,\mathbf{p})\,\boldsymbol{\nu}_{\mathrm{D}\text{-}} \tag{4.7}$$

The generalised transmissibility, $\mathbf{T}_{\mathrm{D}}^{\mathrm{AC}}$, can be derived in a similar manner to the generalised reflectivity by using wave propagator terms and local transmission matrices. The downgoing wavefield, $\boldsymbol{\nu}_{\mathrm{D}+}$, in the half space below interface C is therefore calculated using the generalised transmissibility, $\mathbf{T}_{\mathrm{D}}^{\mathrm{AC}}$:

$$\boldsymbol{\nu}_{\mathrm{D}+} = \mathbf{T}_{\mathrm{D}}^{\mathrm{AC}}(\mathbf{x},\omega,\mathbf{p})\,\boldsymbol{\nu}_{\mathrm{D}\text{-}} \tag{4.8}$$

Again, the generalised transmissibility of the stack of layers, $\mathbf{T}_{\mathrm{D}}^{\mathrm{AC}}(\mathbf{x},\omega,\mathbf{p})$, depends on the frequency, ω, the slowness of the incoming wave, $\mathbf{p}$, and the x- and y-location, $\mathbf{x}$. The former equations are correct using the plane wave assumption, that is, the distance from the source, r, is considerably larger than the wavelength, λ: $r \gg \lambda$. Therefore, Equations 4.7 and 4.8 represent an addition rule for forward modelling the seismic response from a given set of local reflection and transmission matrices at each interface in a stratified media. A complete stack of layers can thus be generalised and represented by one reflection and transmission matrix, $\mathbf{R}_{\mathrm{D}}^{\mathrm{AC}}$ and $\mathbf{T}_{\mathrm{D}}^{\mathrm{AC}}$, respectively. It is shown, in due course, how these forward modelling equations can be turned backwards and be of use in the overburden problem.

The generalised reflectivity and transmissibility as previously discussed are defined for pre-stack seismic data and account for all kind of layering and weak scatterers inside the layers. However, the following discussion is solely focused on the generalised reflectivity, as this is the property which is measured during surface seismic experiments. The generalised transmissibility, on the other hand, is only measured in rare cases, such as VSP seismic experiments or cross well seismic tomography. Consequently, the generalised reflectivity of a stack of layers is furthermore adapted to include reverberations (Figure 4.3). These multiples are labelled as $\mathbf{R}_{\mathrm{U}}$, indi-

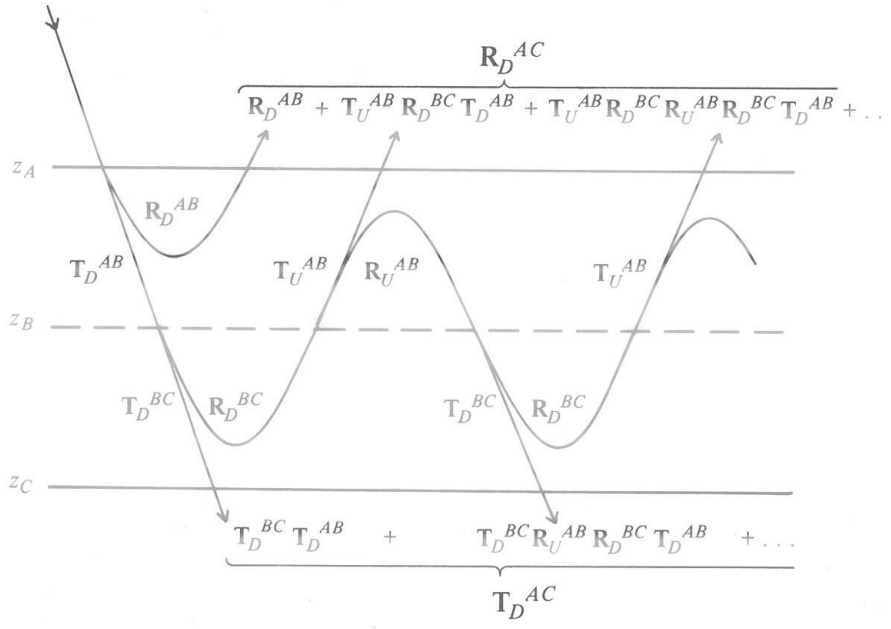

Figure 4.3: Schematic representation of the first terms of the generalised reflection and transmission matrices for stratified media (from Kennett (1983)).

cating that it is the generalised reflectivity of the upgoing wavefield being reflected back downwards. Moreover, the number of multiples which are included in the generalised reflectivity is not limited. Therefore, the generalised reflectivity of a stratified medium between interfaces A and C, including all reverberations, can be written as follows (Kennett (1983), pp.129):

$$\mathbf{R}_{\mathrm{D}}^{\mathrm{AC}} = \mathbf{R}_{\mathrm{D}}^{\mathrm{AB}} + \mathbf{T}_{\mathrm{U}}^{\mathrm{AB}}\mathbf{R}_{\mathrm{D}}^{\mathrm{BC}}[\mathbf{I} - \mathbf{R}_{\mathrm{U}}^{\mathrm{AB}}\mathbf{R}_{\mathrm{D}}^{\mathrm{BC}}]^{-1}\mathbf{T}_{\mathrm{D}}^{\mathrm{AB}} \tag{4.9}$$

The reverberation operator, $[\mathbf{I} - \mathbf{R}_{\mathrm{U}}^{\mathrm{AB}}\mathbf{R}_{\mathrm{D}}^{\mathrm{BC}}]^{-1}$, couples the regions AB and BC, with $\mathbf{I}$ being the identity matrix. All reverberations in the stack are recovered by a series

expansion of the matrix inverse:

$$[\mathbf{I} - \mathbf{R}_{\mathrm{U}}^{\mathrm{AB}}\mathbf{R}_{\mathrm{D}}^{\mathrm{BC}}]^{-1} = \mathbf{I} + \mathbf{R}_{\mathrm{U}}^{\mathrm{AB}}\mathbf{R}_{\mathrm{D}}^{\mathrm{BC}} + \mathbf{R}_{\mathrm{U}}^{\mathrm{AB}}\mathbf{R}_{\mathrm{D}}^{\mathrm{BC}}\mathbf{R}_{\mathrm{U}}^{\mathrm{AB}}\mathbf{R}_{\mathrm{D}}^{\mathrm{BC}} + \dots \tag{4.10}$$

Equation 4.10 is easily expanded to cases with more than two layers, as the addition rule applies, thus any number of layers are wrapped up into a single generalised reflectivity again. However, the limiting assumptions are that the properties such as the velocity, v(x,y), and the density, ρ(x,y), are gently varying laterally. These properties, however, should be discrete in the z direction. Up to now, only a delta pulse is considered as input to the system. This is overcome by defining a source function, $\mathbf{S}(\mathbf{x}, \omega)$, which takes the x- and y-source position, the directivity, the coupling, as well as the source signature into account. Furthermore, the receiver function, $\mathbf{D}(\mathbf{x}, \omega)$, accumulates the receiver position and the receiver coupling. Multiplying both functions to the generalised reflectivity returns the pre-stack seismic response of the stratified medium honouring the acquisition geometry, the spatial distribution of sources and receivers, as well as the input wavelet:

$$\mathbf{D}\mathbf{R}_{\mathrm{D}}^{\mathrm{AC}}\mathbf{S} = \mathbf{D}\left[\mathbf{R}_{\mathrm{D}}^{\mathrm{AB}} + \mathbf{T}_{\mathrm{U}}^{\mathrm{AB}}\mathbf{R}_{\mathrm{D}}^{\mathrm{BC}}[\mathbf{I} - \mathbf{R}_{\mathrm{U}}^{\mathrm{AB}}\mathbf{R}_{\mathrm{D}}^{\mathrm{BC}}]^{-1}\mathbf{T}_{\mathrm{D}}^{\mathrm{AB}}\right]\mathbf{S} \tag{4.11}$$

The idea now is to drive this forward modelling formula backwards in the post-stack domain, in order to extract the reflectivity change at a chosen interface. The next section explains the assumptions which are made in order to work in the post-stack domain and how to transform recorded reflection events from the baseline and monitor seismic data into reflectivity changes along a selected reflector.

4.1.1 Post-stack assumptions

In order to make use of the previously discussed wave propagation in stratified media for post-stack data, some limiting assumptions have to be made. The first simplification is to assume that only P-waves propagate in the medium. Therefore, no wave conversion from P- to SV-waves or vice versa occurs. This assumption simplifies the interface reflection and transmission matrices, $\mathbf{R}_{\mathrm{D}}^{\mathrm{I}}$ and $\mathbf{T}_{\mathrm{D}}^{\mathrm{I}}$, respectively (compare

Equations 4.2 and 4.4):

$$\mathbf{R}_{\mathrm{D}}^{\mathrm{I}} = \begin{bmatrix} R_D^{PP} & 0 \\ 0 & 0 \end{bmatrix} \quad \text{and} \quad \mathbf{T}_{\mathrm{D}}^{\mathrm{I}} = \begin{bmatrix} T_D^{PP} & 0 \\ 0 & 0 \end{bmatrix}$$

The same simplifications apply to the reflection and transmission matrices, $\mathbf{R}_{\mathrm{U}}^{\mathrm{I}}$ and $\mathbf{T}_{\mathrm{U}}^{\mathrm{I}}$. Hence, these matrices become scalars, which makes them commutative and decouples the matrix equations. In the next step multiples are excluded by setting the reverberation operator equal to the identity matrix:

$$[\mathbf{I} - \mathbf{R}_{\mathrm{U}}^{\mathrm{AB}}\mathbf{R}_{\mathrm{D}}^{\mathrm{BC}}]^{-1} = \mathbf{I} \tag{4.12}$$

Equation 4.9 can thus be written in scalar form:

$$D\, r_{\mathrm{D}}^{\mathrm{AC}}\, S = D\, r_{\mathrm{D}}^{\mathrm{AB}}\, S + D\, t_{\mathrm{U}}^{\mathrm{AB}} r_{\mathrm{D}}^{\mathrm{BC}} t_{\mathrm{D}}^{\mathrm{AB}}\, S \tag{4.13}$$

Lower case letters for the generalised reflectivity and transmissibility indicate that these are now scalar operators. However, they still depend on the spatial x- and y-location, $\mathbf{x}$, the frequency, ω, as well as the slowness, $\mathbf{p}$, of the plane wave:

$$r = r(\mathbf{x}, \omega, \mathbf{p}) \quad \textit{and} \quad t = t(\mathbf{x}, \omega, \mathbf{p})$$

When transforming pre-stack seismic data into post-stack data, some sort of NMO correction is generally applied before stacking. Therefore, the range of slowness values which are collapsed into the post-stack trace depends on the input pre-stack offset range. The offset range over which the pre-stack data is stacked thus has to be narrow, for example only nears, mids or fars, in order to assume a narrow limited slowness range, $\Delta\mathbf{p}$, for the pre-stack data. Therefore, the dependency of the pre-stack generalised reflectivity on the slowness, $\mathbf{p}$, is honoured. The post-stack generalised reflectivity, $r_{\mathrm{D}}^{\mathrm{AC}}$(post-stack), is thus approximated as the mean value of pre-stack generalised reflectivities within a limited range of slowness:

$$r_{\mathrm{D}}^{\mathrm{AC}}(\text{post-stack}) \approx \left\langle \sum_{\mathbf{p}=\mathbf{p}_0}^{\mathbf{p}=\mathbf{p}_0+\Delta\mathbf{p}} r_{\mathrm{D}}^{\mathrm{AC}}(\text{pre-stack}) \right\rangle \tag{4.14}$$

To summarise the previous discussion, the scalar Equation 4.13 is approximated for post-stack data if it is free of multiples and stacked within limited offset ranges. The equation still depends on the frequency and is still complex valued to account for phase. All equations discussed so far describe the forward modelling step. Therefore, the next section explains how to drive them backwards and use reflection events recorded in the baseline and monitor seismic post-stack data in order to derive the reservoir reflectivity change.

4.1.2 Reservoir reflectivity analysis using the spectral ratio

Figure 4.4 sketches a schematic example of a distortion in the overburden, OB, embedded in a layered medium, above a producing reservoir, which is used to explain how the generalised reflectivity is used to form the spectral ratio and thus derive the reflectivity at the top reservoir. The reflection events in the stratified medium are

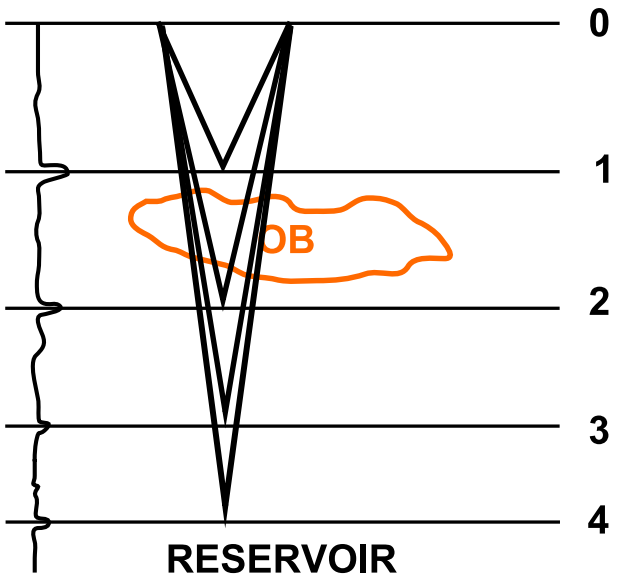

Figure 4.4: Schematic view of an overburden distortion in a stratified medium.

labelled B_1, B_2, B_3, B_4, M_1, M_2, M_3, M_4, in case they are recorded in the baseline or monitor seismic data, respectively. Therefore, each of the events can be written in terms of the generalised reflectivity as described previously, for example $B_2(\omega)$

and $M_2(\omega)$ are:

$$B_2(\omega) = D_{(B)}\, t^{01}_{U(B)} r^{12}_{\mathrm{D(B)}} t^{01}_{D(B)}\, S_{(B)}$$
$$M_2(\omega) = D_{(M)}\, t^{01}_{U(M)} r^{12}_{\mathrm{D(M)}} t^{01}_{D(M)}\, S_{(M)}$$

The subscripts (B) and (M) distinguish between the baseline and monitor data, respectively. These reflections events are described in the frequency domain, thus spectral ratios can be formed by multiplication and division of these events. For example, the ratio of the baseline and monitor reflection events B_2 and M_2:

$$\frac{B_2}{M_2} = \frac{D_{(B)}\, t^{01}_{U(B)} r^{12}_{\mathrm{D(B)}} t^{01}_{D(B)}\, S_{(B)}}{D_{(M)}\, t^{01}_{U(M)} r^{12}_{\mathrm{D(M)}} t^{01}_{D(M)}\, S_{(M)}} = \frac{D_{(B)} S_{(B)}}{D_{(M)} S_{(M)}} \tag{4.15}$$

It is assumed that the transmission through interface 1 (t^{01}_{D} and t^{01}_{U}) and the reflection at interface 2 (r^{12}_{D}) does not change between the baseline and monitor survey. Hence, these terms cancel out and only the source and the receiver terms remain. As mentioned earlier, these source and receiver terms describe the coupling, the source signature and the spatial position of the source and receiver in each survey. Therefore, the resultant complex valued ratio of Equation 4.15 represents the differences between the baseline and monitor acquisition configuration and deviates from unity if the surveys are not exactly repeated. The analysis of this ratio is performed by calculating the modulus and the phase component, φ, for each frequency, respectively:

$$\left|\frac{B_2}{M_2}\right| = \left|\frac{D_{(B)} S_{(B)}}{D_{(M)} S_{(M)}}\right| \tag{4.16}$$

$$\varphi\left(\frac{B_2}{M_2}\right) = \varphi\left(\frac{D_{(B)} S_{(B)}}{D_{(M)} S_{(M)}}\right) \tag{4.17}$$

However, this ratio does not provide information about the production-induced changes in the reservoir. Therefore, the reservoir reflectivity is studied by forming a spectral ratio that uses the following reflection events from each of the baseline

and monitor survey: B_3, B_4, M_3 and M_4 (Equation 4.18).

$$\begin{aligned}\frac{B_3M_4}{B_4M_3} &= \frac{D_{(B)}\, t^{01}_{U(B)} t^{12}_{U(B)} r^{23}_{D(B)} t^{12}_{D(B)} t^{01}_{D(B)}\, S_{(B)}}{D_{(B)}\, t^{01}_{U(B)} t^{12}_{U(B)} t^{23}_{U(B)} r^{34}_{D(B)} t^{23}_{(B)} t^{12}_{(B)} t^{01}_{D(B)}\, S_{(B)}} \\ &\cdot \frac{D_{(M)}\, t^{01}_{U(M)} t^{12}_{U(M)} t^{23}_{U(M)} r^{34}_{D(M)} t^{23}_{(M)} t^{12}_{(M)} t^{01}_{D(M)}\, S_{(M)}}{D_{(M)}\, t^{01}_{U(M)} t^{12}_{U(M)} r^{23}_{D(M)} t^{12}_{D(M)} t^{01}_{D(M)}\, S_{(M)}} \\ &= \frac{r^{23}_{D(B)} r^{34}_{D(M)}}{r^{34}_{D(B)} r^{23}_{D(M)}}\end{aligned} \tag{4.18}$$

The following assumptions are made: The transmission coefficients of interfaces above the reservoir do not change between the baseline and monitor survey, but the reflection event 4 (top reservoir reflection) changes between the baseline and the monitor survey due to production. Therefore, the generalised reflectivity r^{34}_D changes due to production. On the other hand, the generalised reflectivity r^{23}_D does not change between the two time-lapse surveys (compare Figure 4.4), as there is no production-induced change at reflection event 3. The latter assumption explicitly excludes any changes caused by a geomechanical active reservoir, thus the overburden is not compacting. Consequently, the modulus of this spectral ratio is taken to assess the production-induced change of the reservoir reflectivity change, Δr_4. Moreover, this reflectivity change is free of acquisition or overburden effects, as they cancel out (Equation 4.19):

$$\begin{aligned}\left|\frac{B_3M_4}{B_4M_3}\right| &= \left|\frac{r^{23}_{D(B)} r^{34}_{D(M)}}{r^{34}_{D(B)} r^{23}_{D(M)}}\right| \\ &= \left|\frac{r^{34}_{D(M)}}{r^{34}_{D(B)}}\right| = \frac{r_{4(M)}}{r_{4(B)}} \\ &= \frac{r_{4(B)} + \Delta r_4}{r_{4(B)}} = 1 + \frac{\Delta r_4}{r_{4(B)}}\end{aligned} \tag{4.19}$$

Therefore, the reflectivity change along the top reservoir horizon is calculated by applying the spectral ratio to time-lapse data in the frequency domain and consequently using an overburden reflection event as the reference. However, as the spectral ratio is formed in the frequency domain, it is is advisable to calculate the mean reservoir reflectivity change over a narrow frequency band centred around the central frequency. That way instabilities due to some abnormal responses at individual frequencies are reduced.

The next section tests the application of the spectral ratio to the synthetic Nelson data. It is to be seen if the method is robust enough to enhance the time-lapse seismic interpretation. Moreover, it is tested whether this new reservoir reflectivity attribute can be employed to estimate the change in oil saturation more accurately than before and also reduce the errors caused by the overburden channels and the acquisition non-repeatability.

4.2 Reservoir reflectivity analysis for the Nelson synthetic data

The Nelson synthetic seismic data, which are used to investigate amplitude and saturation change errors in the previous chapter, are now used to compute the spectral ratios and to study whether removing the overburden effects is feasible or not. Therefore, reflection events are extracted from the near, mid and far offset seismic data and the spectral ratio is calculated. A practical description of this workflow is found in Appendix B. These limited offset stacks represent a limited range of slowness values each which is needed to decouple the matrix equations (Equation 4.14). In addition, full offset stack seismic data are also used to test whether or not the method could be applied in case of a summation over all slowness values. The following analysis is divided into three parts: First, the reservoir reflectivity change is investigated in the case of the Mio-Pliocene channel in the overburden and secondly for the case of the Quaternary overburden channel. Finally, the change in reservoir reflectivity is used to estimate the oil saturation change and the result is in turn discussed.

4.2.1 Mio-Pliocene channel poor repeat case

The reservoir reflectivity change at the top reservoir horizon, T80, (Figure 4.5) is studied first for the Mio-Pliocene channel and the poor repeat case. In order to benchmark the performance of the spectral ratio, the theoretical normal incidence

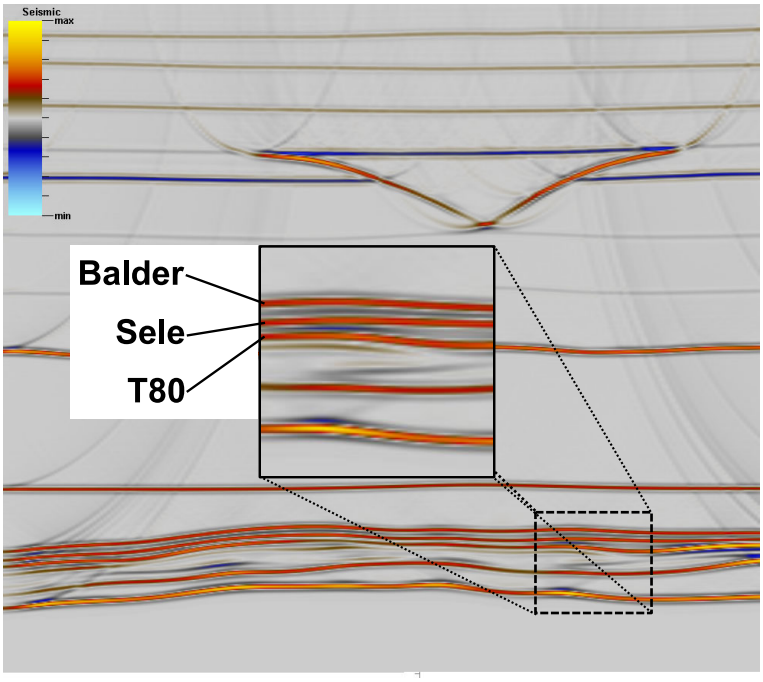

Figure 4.5: Seismic cross section through the full offset time migrated seismic data cube. The inset diagram highlights the top reservoir reflection events, T80, as well as the Sele and Balder overburden reflections events.

reflectivity change at the T80 horizon is calculated from the elastic data that are used to assemble the ray-tracing model. Hence, the impedance Z_1 and Z_2 in the layer above and below the top reservoir horizon, respectively, are calculated using the P-wave velocity and the density of each layer ($Z = v_p \cdot \rho$). Subsequently, the P-wave reflectivity, R_P, is calculated for the baseline and the monitor case:

$$R_{P(Base)} = \frac{Z_{2(Base)} - Z_{1(Base)}}{Z_{2(Base)} + Z_{1(Base)}} \quad ; R_{P(Monitor)} = \frac{Z_{2(Monitor)} - Z_{1(Monitor)}}{Z_{2(Monitor)} + Z_{1(Monitor)}}. \tag{4.20}$$

The above equation for the reflection coefficient is a simplified version of the Zoeppritz equation and valid for a zero degree incidence angle and P-waves only (Sheriff and Geldart, 1995). Next, the reflectivity change between monitor and baseline survey, $\Delta R_P = R_{P(Monitor)} - R_{P(Base)}$, is calculated and divided by the baseline reflectivity. A factor of one is added to obtain the same expression as in Equation 4.19. Figure 4.6(e) shows the production-induced normal incidence reflectivity change at the T80 horizon. A value of 1.0 indicates no reflectivity change, whereas a value above or below unity indicates production-induced changes. The top reservoir reflectivity change, ΔR(T80), is thus calculated with the spectral ratio and by using

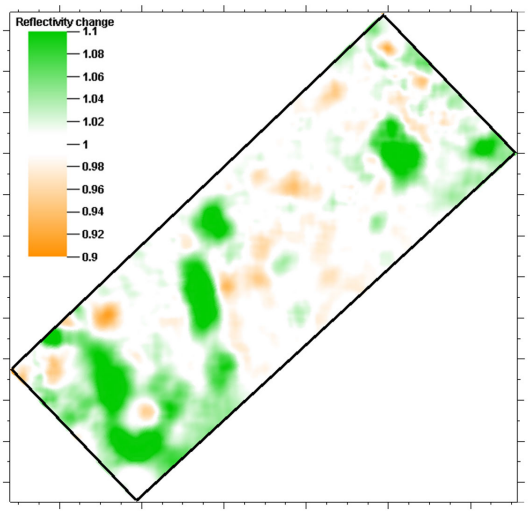

(a) Reflectivity change near offset stack

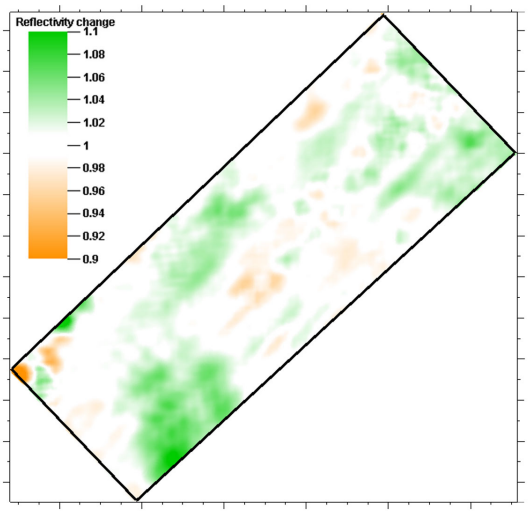

(b) Reflectivity change mid offset stack

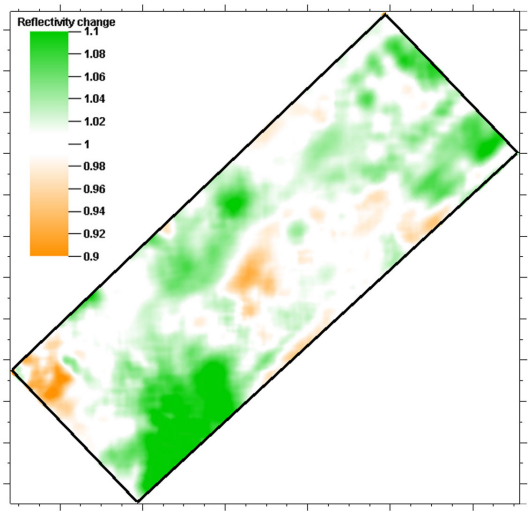

(c) Reflectivity change far offset stack

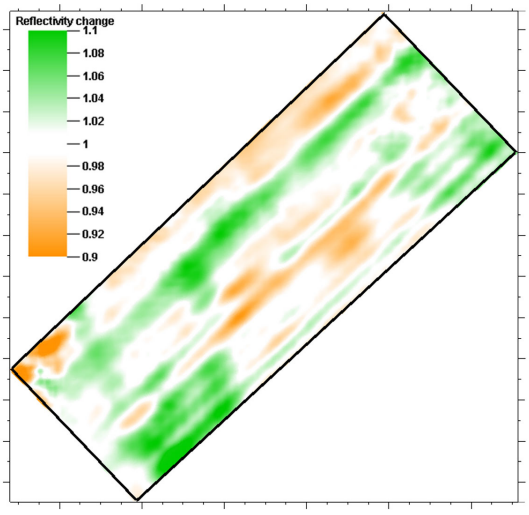

(d) Reflectivity change full offset stack

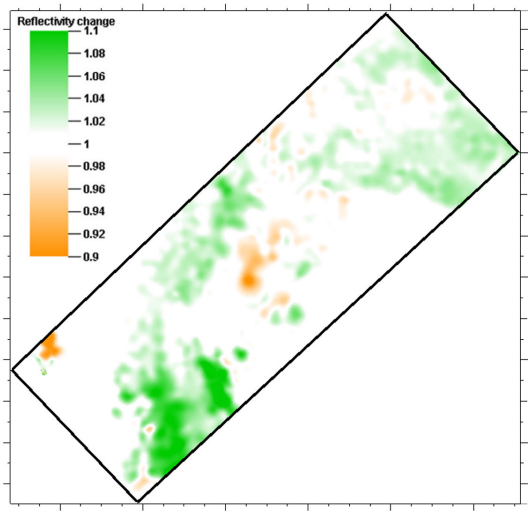

(e) Normal incidence reflectivity change

Figure 4.6: Mio-Pliocene channel poor repeat case. Modulus of the spectral ratio for: (a) near offset, (b) mid offset, (c) far offset and (d) full offset stack seismic data. A mean smoothing filter of 100m width is applied to the data in (a) to (d). The full offset stack data (d) violate the initial assumption of a limited slowness range stack and are therefore not useable. (e) Normal incidence reflectivity change calculated from the ray-tracing model input parameters.

the Sele and T80 reflection events:

$$\Delta R(\text{T80}) = \left| \frac{B_{Sele} M_{T80}}{B_{T80} M_{Sele}} \right| . \tag{4.21}$$

The reservoir reflectivity change is averaged over frequencies between 15Hz to 45Hz, thus taken around the central frequency of the wavelet. The reflectivity change estimates of the top reservoir layer are calculated from the near, mid, far and full offset stack seismic data (Figures 4.6(a) to 4.6(d)). Moreover, a mean filter of 100m width is applied to the reflectivity change maps to suppress high frequency noise which originates from division in the frequency domain. For reference, Figure 4.6(e) shows the normal incidence reflectivity change at the top reservoir horizon, T80, estimated from the model's input parameters.

The most obvious observation is that the reservoir reflectivity change calculated from the near (Figures 4.6(a)) and full stack seismic data (Figures 4.6(d)) does not correlate with the normal incidence reflectivity change calculated from the model input data (Figures 4.6(e)). Moreover, severe striping similar to the acquisition footprint is observed in the reflectivity change estimate from the full offset stack data. This lack of correlation between the estimated and the theoretical normal incidence reflectivity change is furthermore evident when both data sets are cross plotted (Figure 4.7(a) and 4.7(d)). The correlation coefficients are 0.352 and 0.566 for the near and full stack data, respectively. Such low coefficients indicate a very poor match of the data sets. On the other hand, the correlation improves considerably when the mid offset stack data are used to estimate the reservoir reflectivity change at the T80 horizon (Figure 4.6(b)). Some minor striping is still evident in the data, but the reflectivity change compares favourably to the normal incidence reflectivity change (Figure 4.6(e)). The main areas of reflectivity change are well resolved and the good correlation is evident when the estimated change in reflectivity and the model's normal incidence reflectivity change are plotted against each other (Figure 4.7(b)). The correlation coefficient increases by a factor of two compared to the near offset stack case, now reading 0.795. Moreover, the magnitude of the reflectivity change derived from the mid offset stack data is roughly twice as big as the normal incidence reflectivity change calculated from the model's input

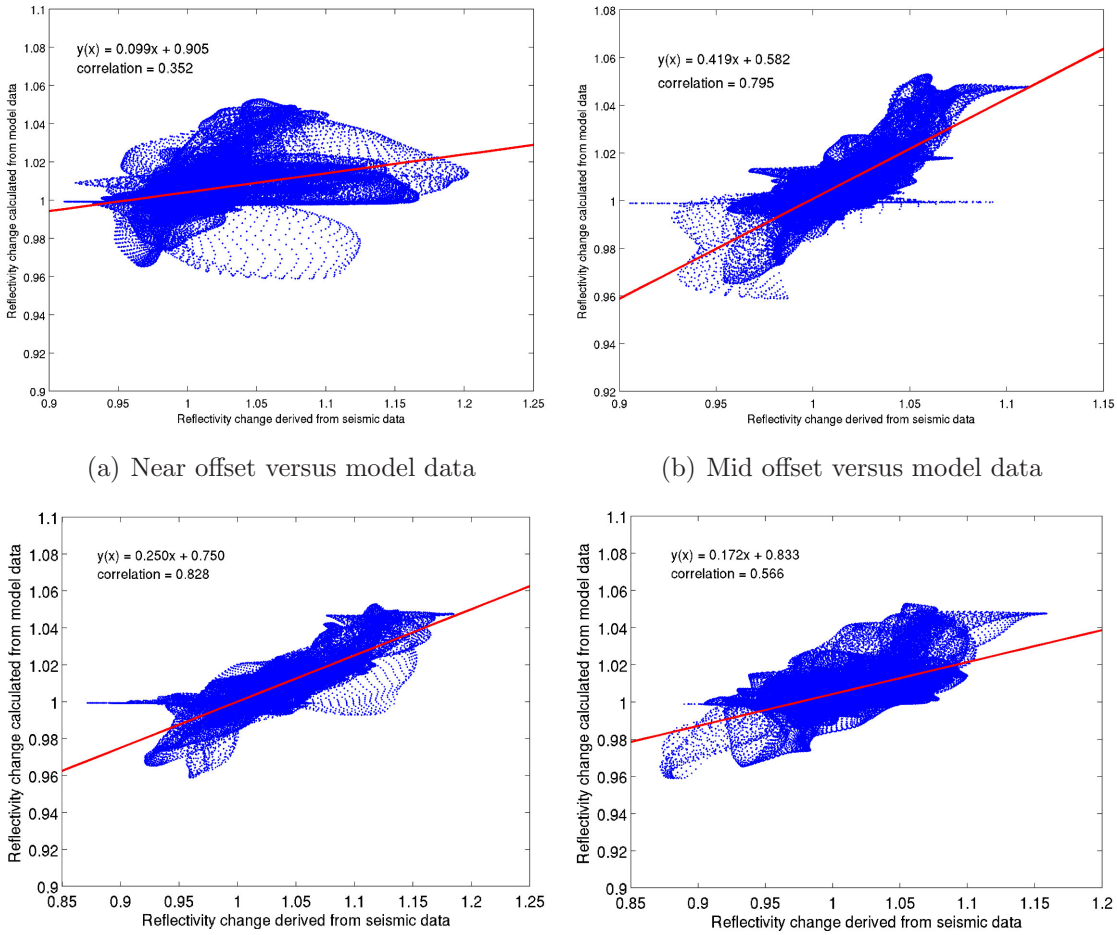

(a) Near offset versus model data

(b) Mid offset versus model data

(c) Far offset versus model data

(d) Full offset versus normal incidence

Figure 4.7: Mio-Pliocene channel poor repeat case. Cross-plot of the estimated against the normal incidence reflectivity change, derived from the model parameters. The reflectivity change is derived from the spectral ratio calculated with: (a) near offset, (b) mid offset, (c) far offset and (d) full offset stack seismic data.

data. This is indicated by the slope of the linear regression curve (0.42) of the cross plotted data (Figure 4.7(b)). The reflectivity change further increases if it is estimated from the far offset stack data (Figure 4.6(c)). However, the correlation to the normal incidence reflectivity change is very good, with a correlation coefficient of 0.828 when both data sets are cross plotted (Figure 4.7(c)). The slope of the linear regression reduces to 0.250, which represents a four times average increase of the far offset reflectivity change compared to the normal incidence case.

Two questions remain open after this overview of the different reflectivity changes: Why is the spectral ratio not working for the near and full stack data, and furthermore, can the increase in the magnitude of the reflectivity change with rising offset

be derived from the model data as well? The latter is discussed first. The increasing reflectivity change with increasing offset is assumed to be related to the AVO effect at the top reservoir horizon and not related to any seismic modelling or processing errors. Consequently, the reflection coefficients are calculated at two locations on the T80 horizon (Figure 4.8). Therefore, the approximated Zoeppritz equations as

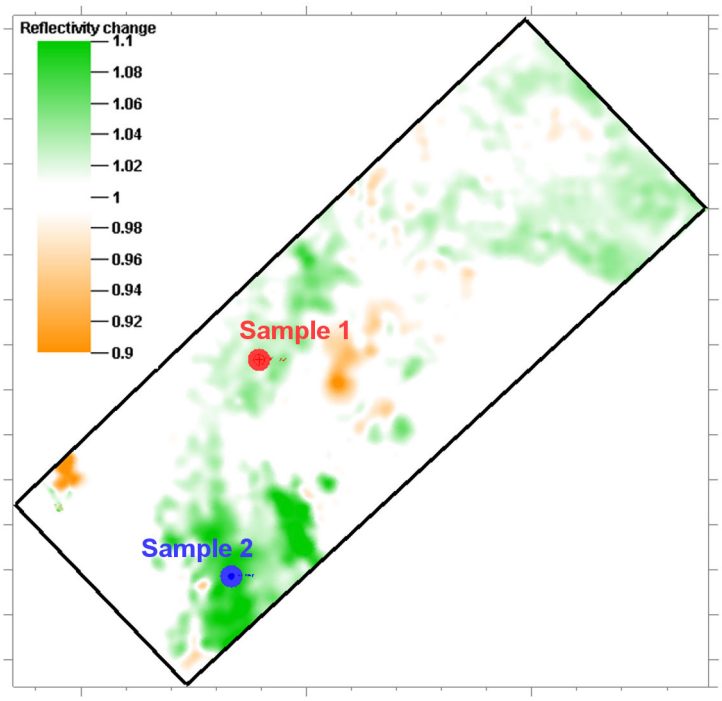

Figure 4.8: The red and blue circles, Sample 1 and Sample 2, respectively, indicate the two locations where elastic parameters are extracted in order to calculate the reflectivity change in relation to the incidence angle.

described by Aki and Richards (2002) are used to calculate the P-wave reflection coefficient in relation to the incidence angle, using the elastic properties, V_p, V_s and ρ, from the baseline and monitor ray-tracing model at these two locations. The reflection coefficients are calculated for a set of incidence angles between zero and forty degrees for the baseline and the monitor data and are in turn subtracted. This change of the reflection coefficient is normalised by the baseline reflection coefficient and plotted against the incidence angle in Figure 4.9. The reflectivity change increases for increasing incidence angle at both sample locations. The red and blue curves in Figure 4.9 display the reflectivity change at the location of Sample 1 and Sample 2, respectively. A rough estimate of the mean incidence angle for mid and far offset stack data at the Nelson Field is 25° and 35°, respectively, assuming

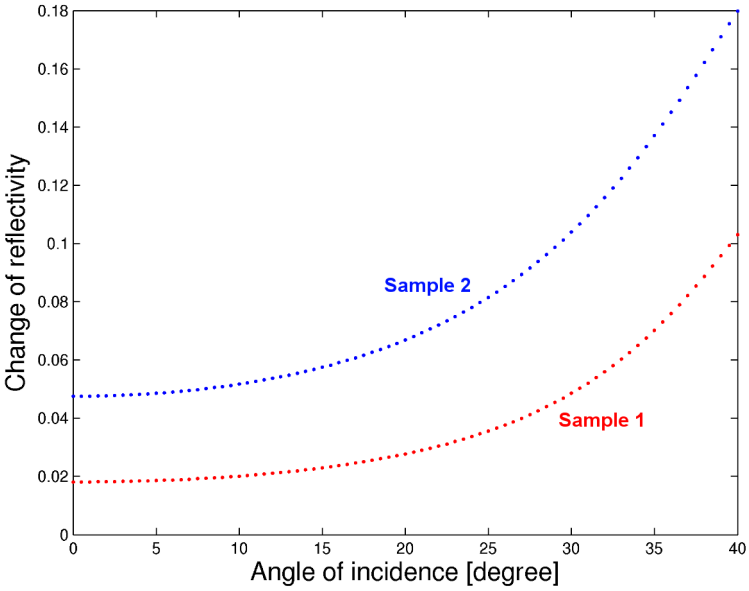

Figure 4.9: The blue and red curves show the change in reflectivity in relation to the incidence angle, based on the elastic parameters extracted at the two locations shown in Figure 4.8.

straight rays in the overburden. Therefore, the change in reflectivity at 25° divided by the normal incidence change is 0.510 and 0.630 for Samples 1 and 2, respectively. This compares favourably with the average ratio of 0.419 for the mid offset stack data, indicated by the slope of the linear regression in Figure 4.7(b). Similarly, the change in reflectivity at 35° divided by the normal incidence change is 0.260 and 0.360 for Samples 1 and 2, respectively. Both values compare well to the slope of the linear regression in Figure 4.7(c), which is 0.250. However, data with a wide range of incidence angles are stacked in the mid and far offset data, thus the linear regression curves in the cross-plots have to be considered as an average value over many angles. Nevertheless, the reflectivity changes derived from the poor repeat mid and far offset post-stack data, using the spectral ratio, compare very favourably with the changes directly derived from the model's input parameters.

The poor result when using the full offset stacked data is assumed to be caused by the summation over a very large range of slowness values, which violates the assumption made to decouple the general reflectivity (Equation 4.14). In addition, a violation of these assumptions is most probably the cause of the spectral ratio applied on the near offset stack (200m to 1000m) data not performing well. Large azimuth variations occur between the baseline and the poor repeat monitor survey

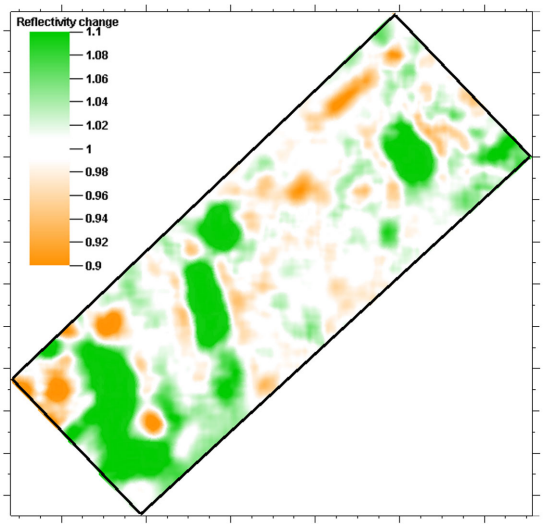

(a) 200m - 400m offset

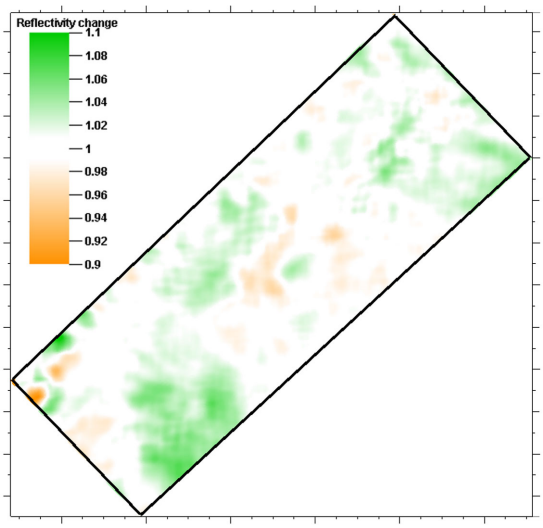

(b) 400m - 800m offset

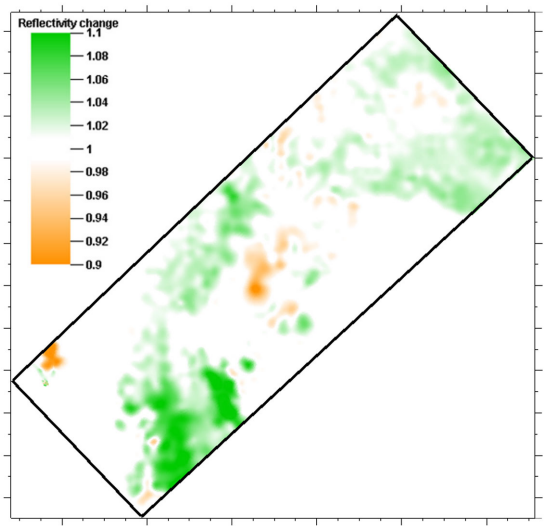

(c) Normal incidence reflectivity change

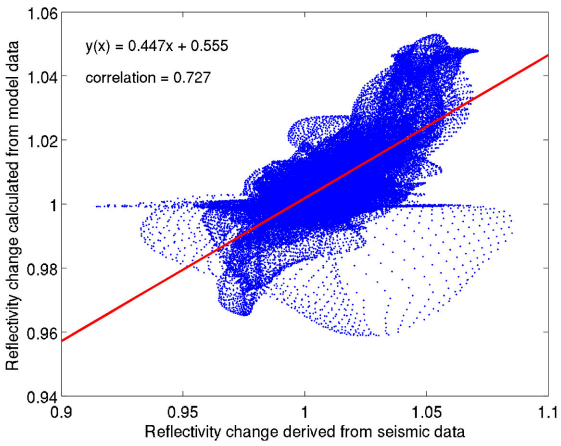

(d) Cross-plot of (b) and (c)

Figure 4.10: Reflectivity analysis for the Mio-Pliocene poor repeat near offset data: (a) Estimated reflectivity change from limited 200m-400m offset stacked data. (b) Estimated reflectivity change from limited 400m-800m offset stacked data. (c) Normal incidence reflectivity change calculated from the ray-tracing model input parameters. (d) Cross-plot of the normal incidence and the 400m-800m limited offset stack derived reflectivity change.

at near offsets, which cause the slowness value to vary considerably. Therefore, these near offset stack poor repeat data are divided into two limited offset stacks: Seismic traces are stacked for offsets between 200m to 400m and 400m to 800m. The smoothed reflectivity change derived from the 200m-400m offset stack data (Figure 4.10(a)) exhibits the same pattern as the estimate from the near (200m-1000m) offset stack (Figure 4.6(a)) and does not correlate with the normal incidence reflectivity

change calculated from the model data (Figure 4.10(c)). In contrast, the reservoir reflectivity change estimated from the 400m-800m limited offset stack data (Figure 4.10(b)) correlates favourably with the normal incidence change. Cross plotting the reflectivity change estimate from the 400m-800m offset stack data against the normal incidence data affirms that the changes are sufficiently determined (Figure 4.10(d)). The correlation coefficient increases to 0.727 and matches well with the correlation coefficients for the mid and far offset stack estimates. However, the correlation coefficient for the 200m-400m offset stack reflectivity change estimates decreases to 0.216. These results are in line with the assumption that the azimuth differences are too large for these very near offset stack data, thus no valid result can be expected. It is to be seen whether such near offset stack data can be used in the case of the good repeat survey, which is discussed in due course.

Estimating the reflectivity change at the top reservoir horizon and comparing it with the normal incidence reflectivity change is one way to validate the spectral ratio results. However, there are no changes in elastic parameters outside the reservoir layers in the ray-tracing model, thus there is no reflectivity change at any of the non-reservoir horizons. The reflectivity change is therefore calculated for the Sele horizon, using the Balder and Sele reflection event (Figures 4.11(a) to 4.11(d)). In this case, the estimated reflectivity change should be unity for all offsets. An excellent agreement with the theoretical value of unity is found for the estimates from the mid, far and full offset stacked data. The mean reflectivity changes of these estimates are 1.000, 0.996 and 0.999, respectively. However, the reflectivity change calculated from the near stack data exhibits some rather large areas of apparent mismatch, which is caused by the large azimuth differences for such data as discussed previously. Nevertheless, the mean estimated reflectivity change for the near offset stack is 1.004, close to the theoretical value of unity.

To summarise, the results from the Mio-Pliocene channel and the poor repeat case, the reservoir reflectivity change derived from the near, mid and far offset stacks, is free of any strong residual acquisition footprint. However, there is a considerable lack in correlation with the normal incidence reflectivity change if the spectral ratio is formed from very near offset data. The large azimuth variations for these near

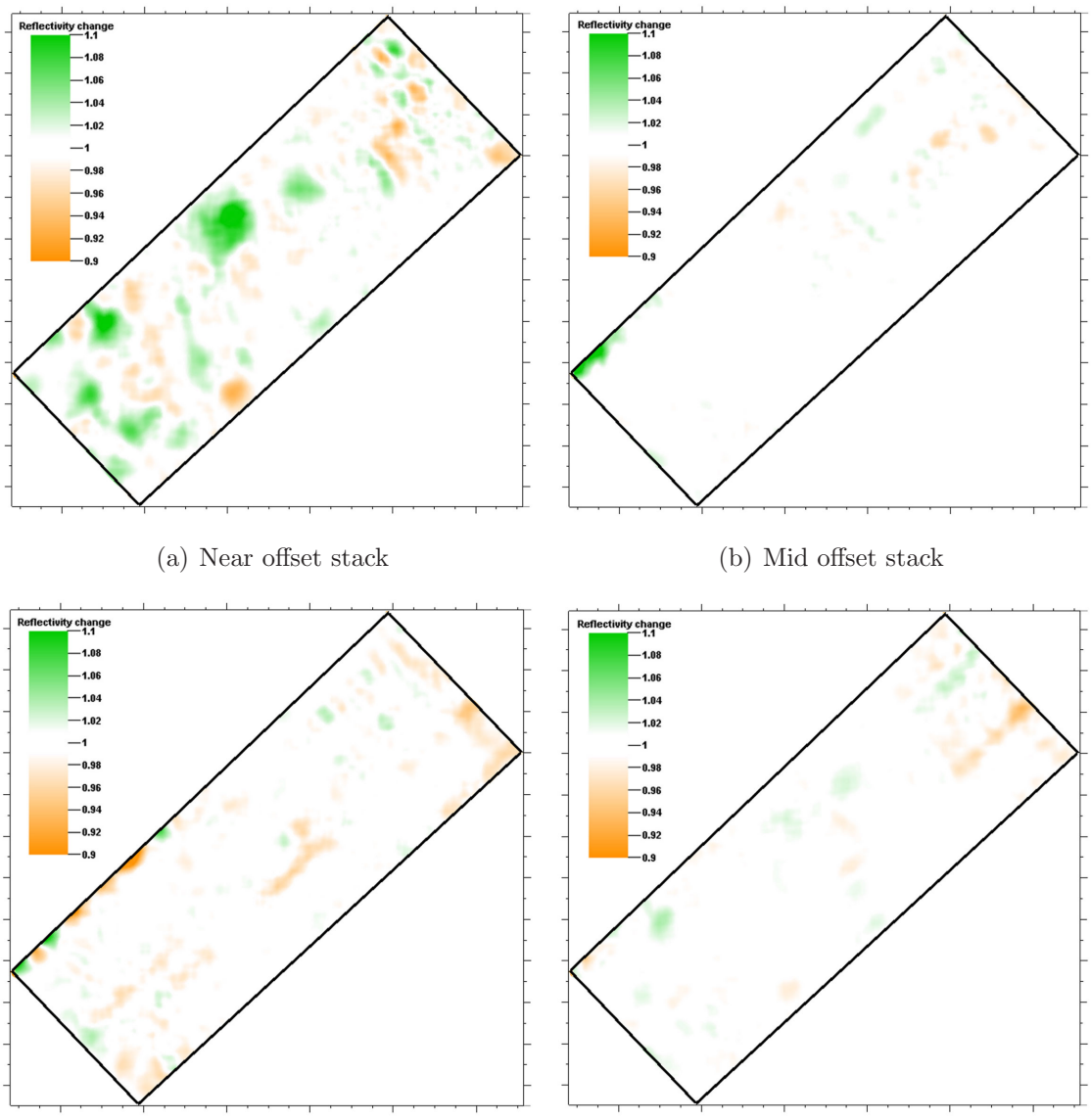

(a) Near offset stack

(b) Mid offset stack

(c) Far offset stack

(d) Full offset stack

Figure 4.11: Reflectivity change between baseline and monitor survey at the top Sele horizon calculated by taking the spectral ratio of the poor repeat seismic data with the Mio-Pliocene channel in the overburden for the following offsets: (a) near offsets, (b) mid offsets, (c) far offsets and (d) full offsets. A mean filter of 100m width is applied to all data. The model reflectivity change is unity at this interface.

offset stacked data invalidate the initial assumption of a narrow slowness range. This is also the case if the reflectivity change is estimated from the full stack data.

4.2.2 Mio-Pliocene channel good repeat case

The reservoir reflectivity change is now estimated using seismic data from the good repeat case. The top reservoir reflectivity change extracted from the near offset stack data is shown in Figure 4.12(a). The correlation with the normal incidence reflectivity change calculated from the model data is very good (Figures 4.12(e) and 4.13(a)), with an overall correlation coefficient of 0.751. This is in strong contrast to the poor correlation of the reflectivity change estimated from the poor repeat near offset stack (Figure 4.6(a)). Hence, the improved source and receiver positioning in the good repeat case significantly reduces the azimuth difference so that the spectral ratio becomes applicable to the near offset data. All major changes compared to the normal incidence case are well resolved, however, one has to bear in mind that the near offset stack is not strictly a normal incidence case, but rather an approximation for that case.

Consequently, the correlation of the reflectivity change estimated from the mid offset good repeat data with the normal incidence change improves as well (Figure 4.12(b) and 4.13(b)). The correlation coefficient increases to 0.900, which is significantly better compared to the poor repeat case (0.795). Moreover, the slope of the linear regression is 0.521, which is an improved match with the theoretical reflectivity change for mid offsets at Samples 1 and 2 (0.510 and 0.630), as outlined in Figure 4.9. Therefore, the AVO effect at the top reservoir horizon is well captured in the reflectivity change estimate. Overall, the acquisition related striping is further reduced in the reflectivity change estimates using the good repeat data (compare Figure 4.12(b) with 4.6(b)).

A similar decrease of noise and acquisition footprint is also observed when the reflectivity change is calculated from the far offset stack, good repeat data (Figure 4.12(c)). The spatial correlation to the normal incidence reflectivity change is very good, with a correlation coefficient of 0.904 if both data sets are cross-plotted (Figure 4.13(c)). In addition, the slope of the linear regression curve (0.304) is between the calculated values at sample locations 1 and 2 (0.260 and 0.360), which indicates that the characteristic AVO behaviour at the top reservoir horizon is resolved.

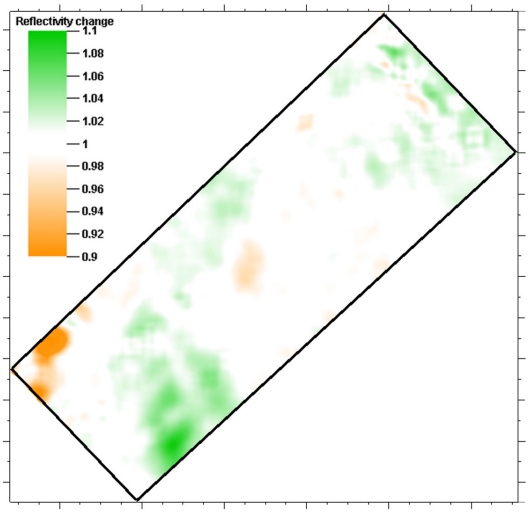

(a) Reflectivity change near offset stack

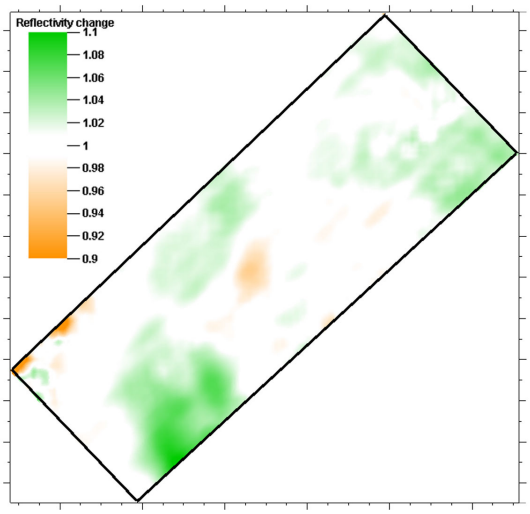

(b) Reflectivity change mid offset stack

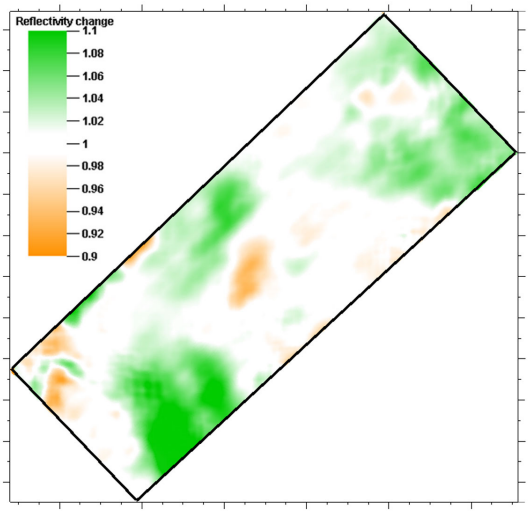

(c) Reflectivity change far offset stack

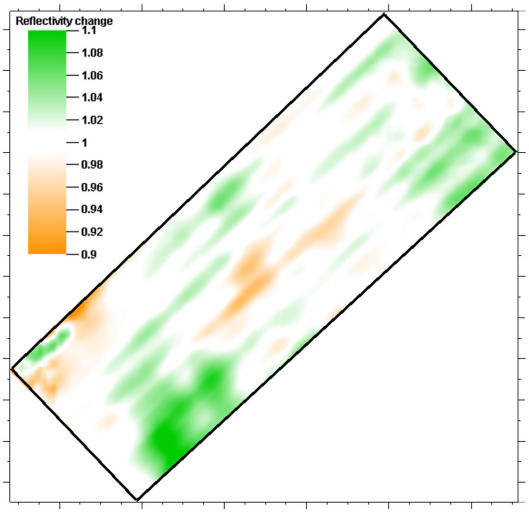

(d) Reflectivity change full offset stack

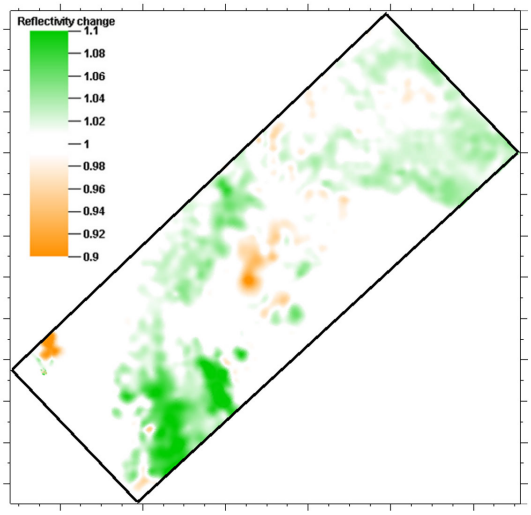

(e) Normal incidence reflectivity change

Figure 4.12: Mio-Pliocene channel good repeat case. Modulus of the spectral ratio for: (a) near offset, (b) mid offset, (c) far offset and (d) full offset stack seismic data. A mean smoothing filter of 100m width is applied to the data in (a) to (d). The full offset stack data (d) violate the initial assumption of a limited slowness range stack and are therefore not useable. (e) Normal incidence reflectivity change calculated from the ray-tracing model input parameters.

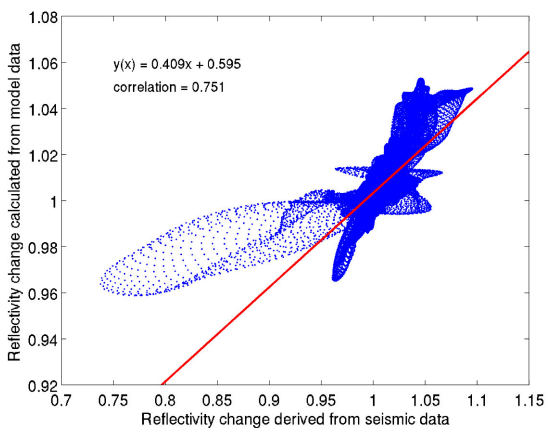

(a) Near offset versus model data

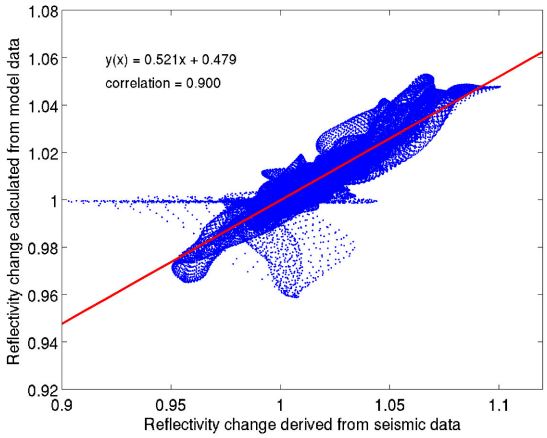

(b) Mid offset versus model data

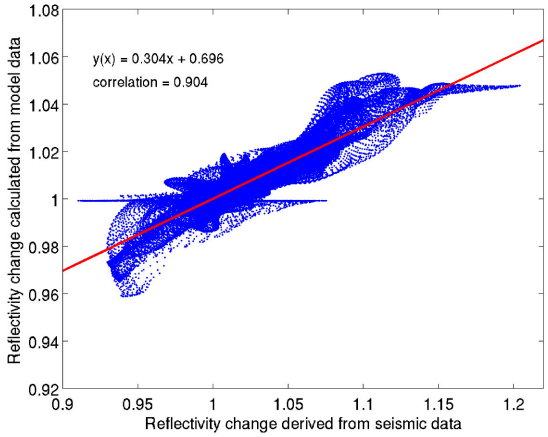

(c) Far offset versus model data

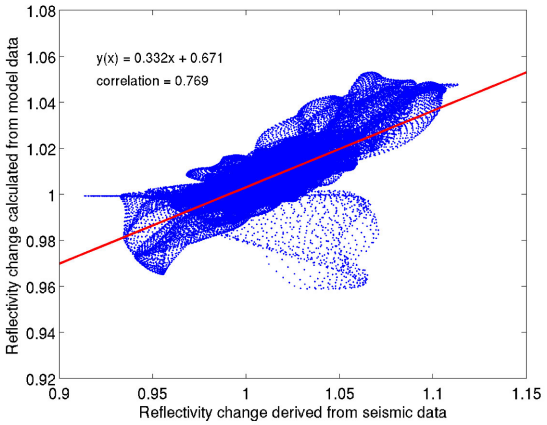

(d) Full offset versus normal incidence

Figure 4.13: Mio-Pliocene channel good repeat case. Cross-plot of the estimated against the normal incidence reflectivity change, derived from the model parameters. The reflectivity change is derived from the spectral ratio calculated with: (a) near offset, (b) mid offset, (c) far offset and (d) full offset stack seismic data.

However, the reflectivity change calculated from the full stack data (Figure 4.12(d)) is still poor and does not spatially correlate with the normal incidence change (Figure 4.13(d)). The areas of the largest changes can be identified, but their interpretation would be extremely uncertain without having the normal incidence reflectivity change for comparison. The correlation coefficient of the cross plot between the estimate from the full stack data and the normal incidence change is 0.769, however, the persistent striping in the data impedes a reliable interpretation of the production-induced reflectivity changes. There is some improvement over the poor repeat case, but not enough in order to consider these reflectivity estimates as an interpretable time-lapse attribute. Hence, full stack data are once again not suited

to be input into the spectral ratio.

The various results for the poor and good repeat Mio-Pliocene channel data are summarised in Figure 4.14. The correlation coefficients of the reflectivity change

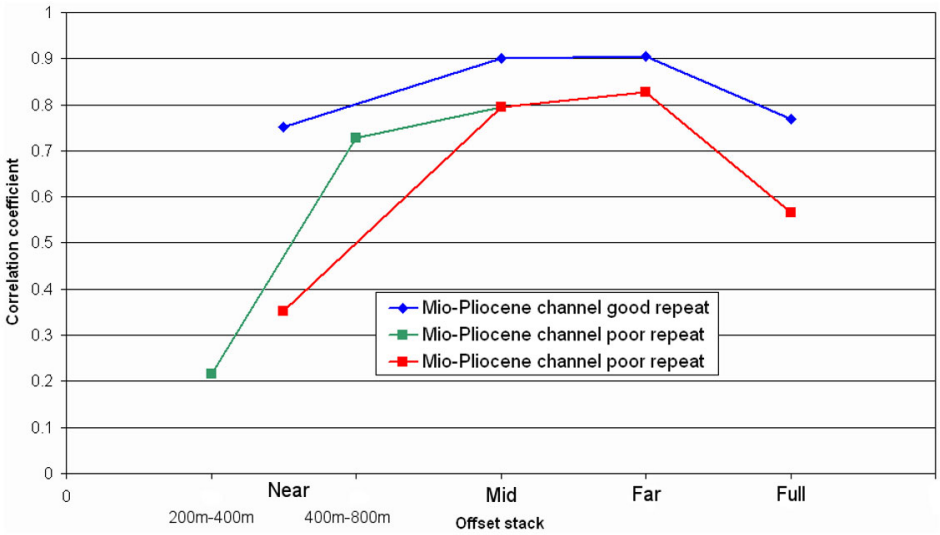

Figure 4.14: Comparison of the reflectivity change estimated from the near, mid and far offset stack poor as well as good repeat data by their respective correlation to the normal incidence reflectivity change.

estimates are plotted against the respective offset, from which the change is calculated. The correlation coefficients for the near, mid, far and full offset stack and the poor repeat case are connected by the red line. As discussed earlier, the performance of the spectral ratio for the near and full offset data is poor. The green line outlines the improvement in estimating the reflectivity change when the near offset data are split into two groups, 200m-400m and 400m-800m. The reflectivity changes from the very near offset (200m-400m) correlate poorly with the normal incidence change, due to large azimuth differences. On the other hand, the estimates from the 400m-800m offset stacked data show a dramatic increase in correlation to the normal incidence reflectivity change. The correlation coefficients further improve if the reflectivity change is estimated using the good repeat data (Figure 4.14, blue line). There is a consistently better performance of the spatial ratio for the good repeat data and the results from the near, mid and far offset stack data are usable. Only the estimates from the full stack data are not good for time-lapse interpretation, despite having a good correlation coefficient.

This consistently good performance of the spatial ratio on the good repeat data is also observed when the reflectivity change is estimated for the top Sele horizon (Figure 4.15). All estimates agree very well with the theoretical reflectivity change

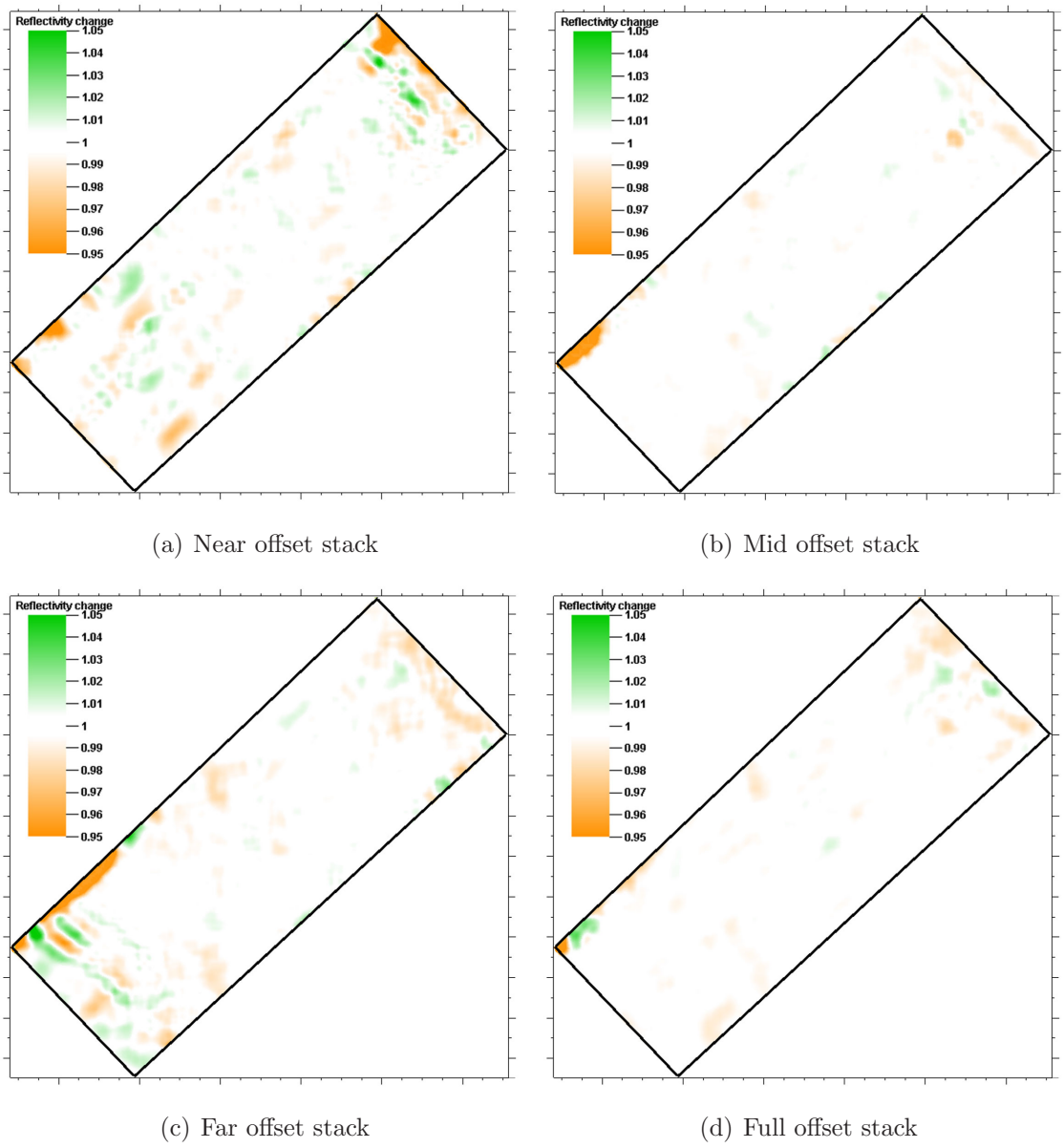

(a) Near offset stack

(b) Mid offset stack

(c) Far offset stack

(d) Full offset stack

Figure 4.15: Reflectivity change between baseline and monitor survey at the top Sele horizon calculated by taking the spectral ratio of the good repeat seismic data with the Mio-Pliocene channel in the overburden for the following offsets: (a) near offset stack, (b) mid offset stack, (c) far offset stack and (d) full offset stack. A mean filter of 100m width is applied to all data. The model reflectivity change is unity at this interface.

of unity at this horizon, with estimates derived from the mid and full offset stack showing the best agreement. It is also important to note that a different colour bar with lower minimum and maximum values is used in order to reveal these subtle

errors. The mean value of the estimates from the near, mid and far offset data is 0.998, whereas the mean value for the estimated change using the full offset data is 0.999. No striping is apparent in the reflectivity estimate calculated from the full offset stacked data, as compared to the spectral ratio taken for the top reservoir reflectivity change estimate, even though the degree of non-repeatability is unchanged.

4.2.3 Quaternary channel poor repeat case

The previous sections show that the reservoir reflectivity change can be accurately estimated from the time-lapse seismic data, even though the Mio-Pliocene channel in conjunction with a non-repeated acquisition geometry affects the wavefield. This section carries out the same study, but using time-lapse seismic data that is affected by the Quaternary channel.

Figure 4.16(a) shows the reservoir reflectivity change calculated from the 400m - 800m offset stack data. The smoothed reflectivity change correlates favourably with the normal incidence change (Figure 4.16(e)) and the correlation coefficient is 0.697 when both data sets are cross-plotted (Figure 4.17(a)). Not shown is that the reflectivity changes estimated from the 200m - 400m offset stacked data, as well as the near offset (200m - 1000m) stacked data, correlate poorly with the normal incidence reflectivity change, as these estimates are very similar to the ones presented for the Mio-Pliocene poor repeat data (Figures 4.6 and 4.10). The correlation coefficients for these two cases when plotted against the normal incidence reflectivity change are 0.199 and 0.282, respectively.

The reflectivity change estimated from the Quaternary channel poor repeat mid offset stacked data (Figure 4.16(b)) correlates well with the normal incidence reflectivity change. The main areas of production-induced change are recovered, despite the fact that some striping from the non-repeat acquisition is visible. The correlation coefficient equates to 0.786 (Figure 4.17(b)), which matches the correlation coefficient of 0.795 for the mid offset Mio-Pliocene poor repeat data quite well (compare Figure 4.7(b)). The reservoir reflectivity change increases in magnitude when

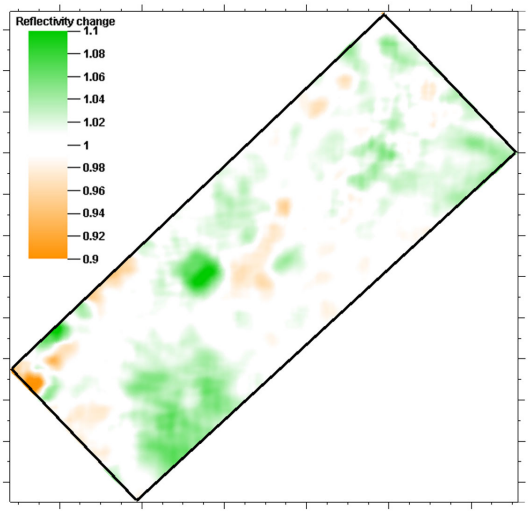

(a) Reflectivity change 400m - 800m offset

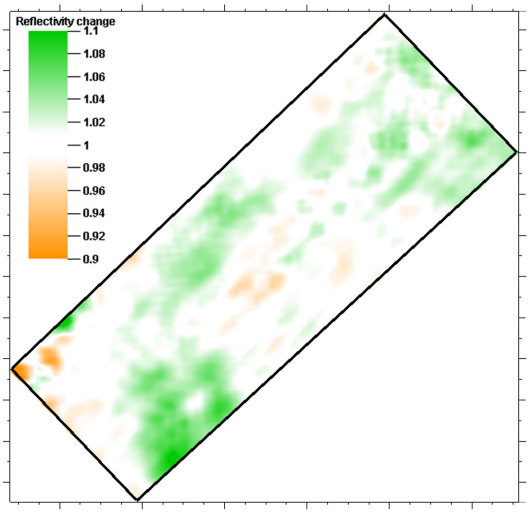

(b) Reflectivity change mid offset

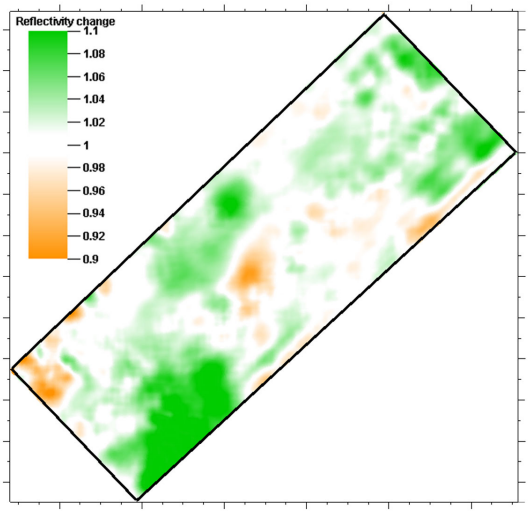

(c) Reflectivity change far offset

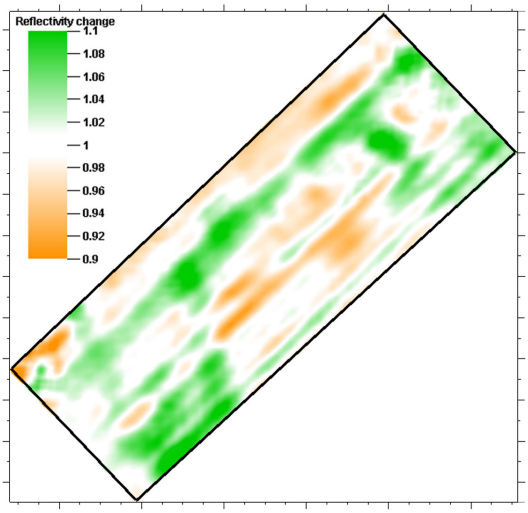

(d) Reflectivity change full offset

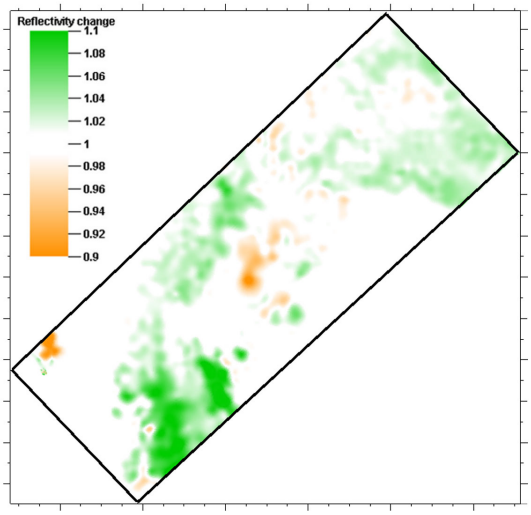

(e) Normal incidence reflectivity change

Figure 4.16: Quaternary channel poor repeat case. Modulus of the spectral ratio for: (a) 400m - 800m offset stack, (b) mid offset stack, (c) far offset stack and (d) full offset stack seismic data. A mean smoothing filter of 100m width is applied to the data in (a) to (d). The full offset stack data (d) violate the initial assumption of a limited slowness range stack and are therefore not useable. (e) Normal incidence reflectivity change calculated from the ray-tracing model input parameters.

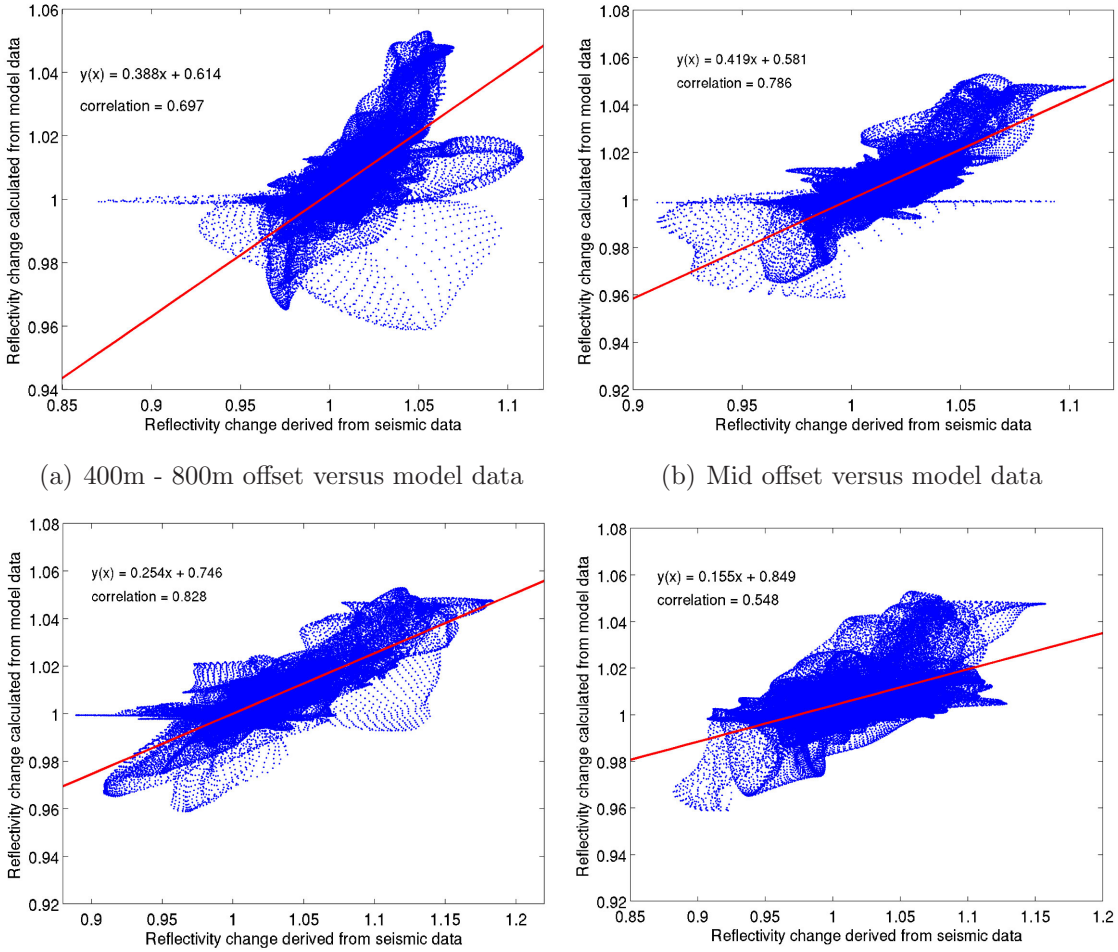

(a) 400m - 800m offset versus model data

(b) Mid offset versus model data

(c) Far offset versus model data

(d) Full offset versus normal incidence

Figure 4.17: Quaternary channel poor repeat case. Cross-plot of the estimated against the normal incidence reflectivity change, derived from the model parameters. The reflectivity change is derived from the spectral ratio calculated with: (a) 400m - 800m offset stack, (b) mid offset stack, (c) far offset stack and (d) full offset stack seismic data.

extracted from the far offset stack data (Figure 4.16(c)), which outlines the AVO effect at the top of the reservoir. The correlation to the normal incidence model reflectivity change is good and most of the changes are spatially resolved, however, some minor striping is still visible. The correlation coefficient is 0.828 (Figure 4.17(c)). Again, the reflectivity change is very similar to the one estimated from the Mio-Pliocene far offset data. This is also true for the reflectivity change calculated from the full offset stack data (Figure 4.16(d)). However, there is severe striping in the data and no spatial correlation with the normal incidence change (Figure 4.17(d)), also indicated by the correlation coefficient of 0.548. It is thus concluded that the full stack reflectivity change estimate is not suitable for time-lapse inter-

pretation. Moreover, it indicates that the initial assumption of using only a limited slowness range is violated for these full offset stack data.

The above discussion shows that the reservoir reflectivity changes are similar whether they are calculated with data from the Mio-Pliocene or the Quaternary channel model. Figure 4.18 shows that the correlation coefficients are almost identical for the Mio-Pliocene (blue line) or the Quaternary channel (red line) poor repeat case. It is evident that the major source of mismatch between the estimated reflectivity

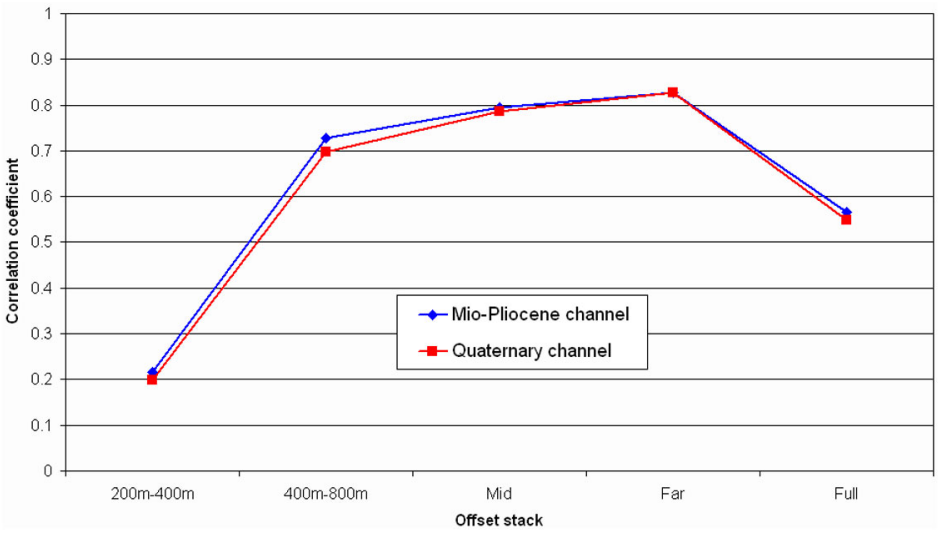

Figure 4.18: Correlation coefficients for the reflectivity change estimates from the poor repeat Mio-Pliocene and Quaternary channel data.

changes and the model's normal incidence changes is the 200m - 400m offset stack data for the Mio-Pliocene as well as the Quaternary channel model. On the other hand, the change in the reservoir reflectivity estimated from the 400m - 800m offset data as well as the mid and far offset stacks correlates well with the normal incidence change. Moreover, the similarity of these correlation coefficients suggest that the spectral ratio resolves the reservoir time-lapse change equally well for both overburden channel models. This consistent performance independent of the type of overburden channel is most evident when the reflectivity change estimates from the Mio-Pliocene and the Quaternary channel model are cross plotted (Figure 4.19). The differences between the estimates are small, whether the wavefield is affected by the Quaternary or the Mio-Pliocene channel. The correlation coefficients for the mid, far and full offset data are 0.953, 0.968 and 0.947, respectively. Only the reser-

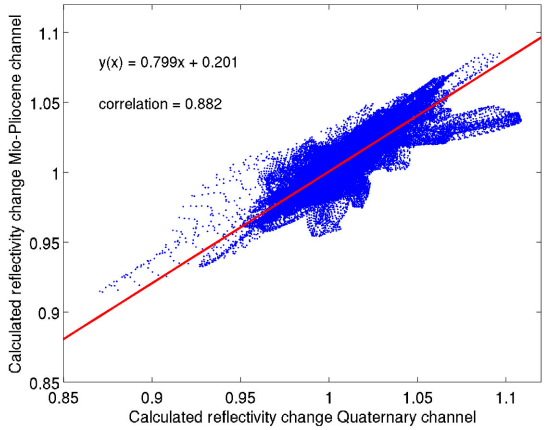

(a) 400m - 800m offset data

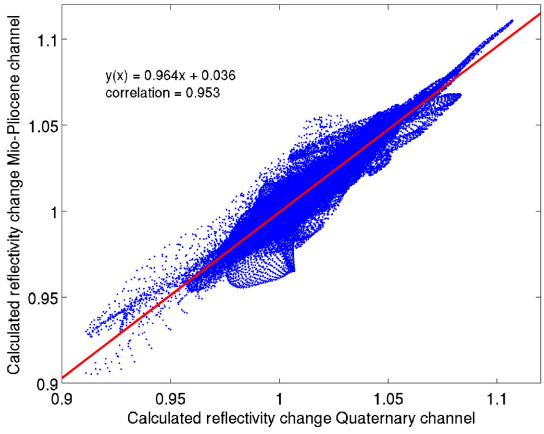

(b) Mid offset data

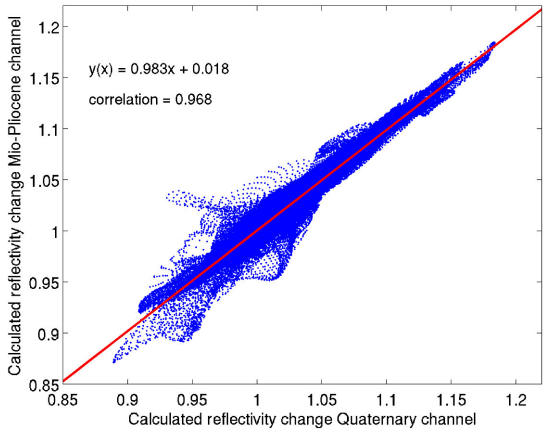

(c) Far offset data

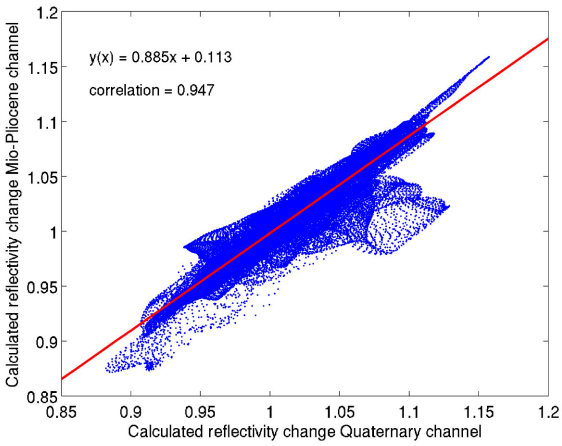

(d) Full offset data

Figure 4.19: Poor repeat case: Cross plots of the reservoir reflectivity change estimated from the Mio-Pliocene channel data versus the Quaternary channel data for: (a) 400m - 800m offset stack, (b) mid offset stack, (c) far offset stack, (d) full offset stack.

voir reflectivity change calculated from the 400m - 800m offset stack data exhibits differences, with a wider spread of data points and a lower correlation coefficient of 0.882. It is thought that the large azimuthal differences in these very near offset data are the cause of these slight differences, when the waves travel through the overburden channel.

As discussed in the previous cases, the reflectivity change at the top Sele horizon is calculated in order to further assess the accuracy of the spectral ratio. The results are all very similar to the ones extracted from the Mio-Pliocene channel poor repeat data. Figure 4.20 shows the reflectivity change calculated from the near and mid offset stacked data. Similar to the Mio-Pliocene channel data (Figure

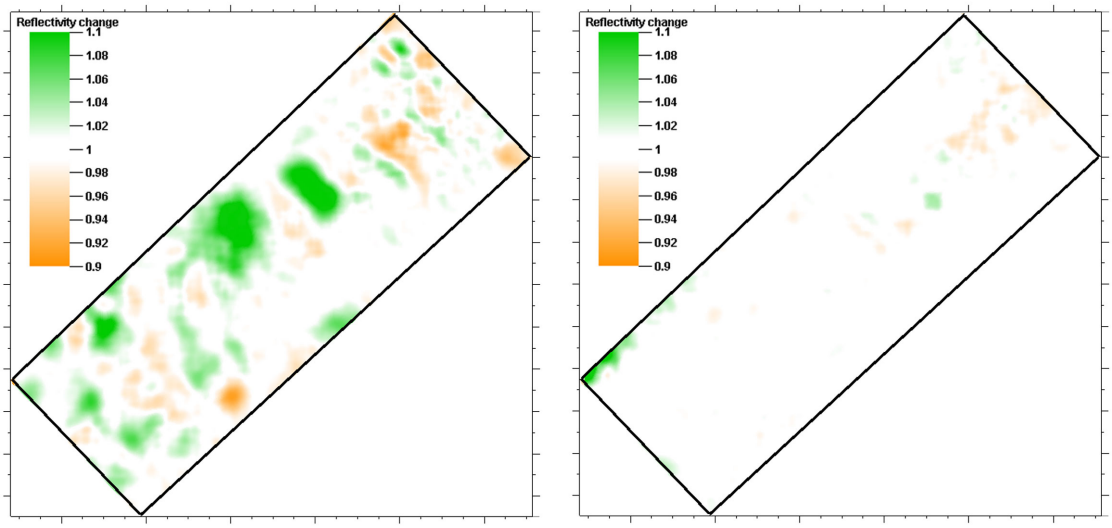

(a) Near offset stack (b) Mid offset stack

Figure 4.20: Quaternary channel poor repeat case: Reflectivity change at the top Sele horizon calculated from the (a) near offset stacked and (b) mid offset stacked seismic data. A mean filter of 100m width is applied to all data and the theoretical reflectivity change is unity.

4.11), the change is close to unity when estimated from the mid offset stack. This also holds true for the far and full offset stack data (not shown). Only the reflectivity change calculated from the near offset stack data exhibits larger errors, however, it matches the reflectivity change calculated from the Mio-Pliocene near offset data well. Hence, the reflectivity changes at the top Sele horizon furthermore show the consistent performance of the spectral ratio results, regardless of the type of overburden channel.

4.2.4 Quaternary channel good repeat case

The reservoir reflectivity changes estimated from the good repeat time-lapse data with the Quaternary channel in the overburden are discussed in this section and consequently compared to the reflectivity change estimates calculated from the Mio-Pliocene good repeat data. First, the near offset stacked seismic data are used to determine the change in reflectivity at the T80 horizon (Figure 4.21(a)). The spatial match of the smoothed data to the normal incidence change (Figure 4.21(e)) is good and the major reflectivity changes are recovered. A correlation coefficient of 0.755

is obtained when the normal incidence and the reservoir reflectivity change data are cross-plotted (not shown). Overall, this is a good match, but leaves room for improvement.

However, the reservoir reflectivity change estimated is not significantly different for the Quaternary channel in comparison to the Mio-Pliocene channel good repeat estimate (Figure 4.22(a)). The correlation coefficient of this cross-plot is high (0.967), which furthermore affirms the excellent performance of the spectral ratio to determine the reflectivity change independently of the overburden channel effects. Moreover, both reflectivity change estimates are of the same magnitude indicated by the slope of the linear regression being close to unity (0.955).

The reflectivity change using the mid and far offset stack data correlates very well with the normal incidence change (Figures 4.21(b), 4.21(c) and 4.21(e)). The correlation coefficients are 0.900 and 0.891, respectively, when the reflectivity change estimates are plotted against the normal incidence change (not shown). In addition, the AVO effect is clearly seen in the increased amplitude of the reflectivity change. Furthermore, the resolution of detailed changes is superior over the near offset stack estimates. However, the most important observation is that the estimates from the mid and far offset stack Quaternary channel data exhibit an excellent match to the reflectivity change calculated from the mid and far offset stacked Mio-Pliocene channel data (Figures 4.22(b) and 4.22(c)). There are only few scattered data points and the correlation coefficients are 0.976 and 0.985, respectively. Moreover, the slope of the linear regression is 0.991 and 0.988 for the mid and far offset data, which indicates that the amplitude of the reflectivity change estimates is unaffected regardless of whether the Quaternary or the Mio-Pliocene channel affects the wave propagation.

The same consistency is found when the reflectivity change is estimated from the full offset stack data. The estimated reservoir reflectivity change is almost identical when data from the Quaternary channel or Mio-Pliocene channel model are used (Figure 4.22(d)). The correlation coefficient of this cross-plot is 0.990 and the slope of the linear regression is 0.977, again indicating that the amplitude of the reflectivity change is nearly the same for both data sets. However, this correlation

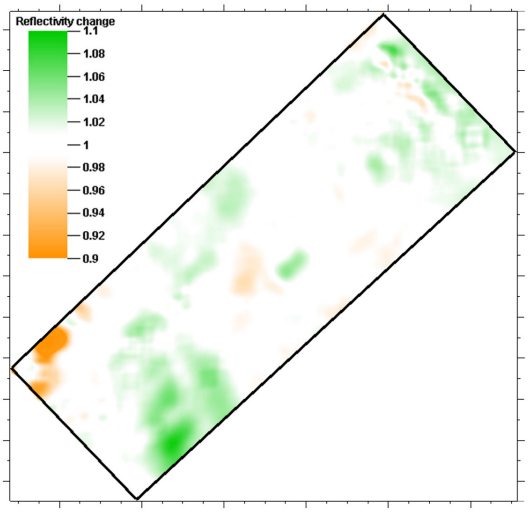

(a) Reflectivity change near offset stack

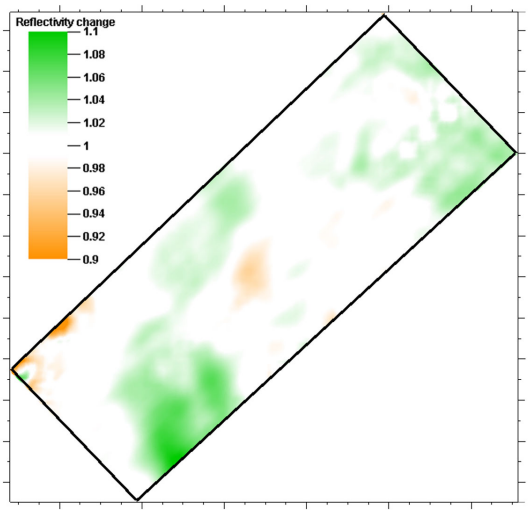

(b) Reflectivity change mid offset stack

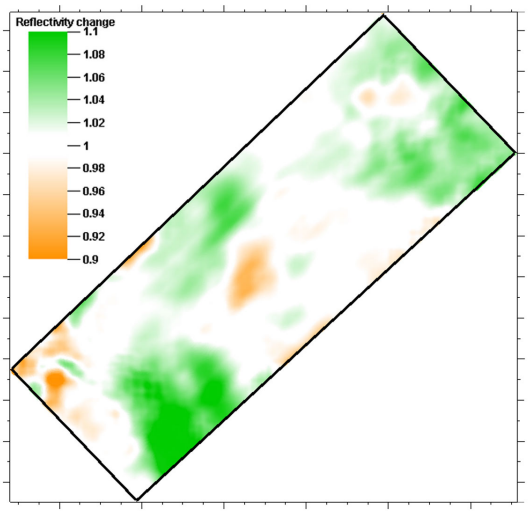

(c) Reflectivity change far offset stack

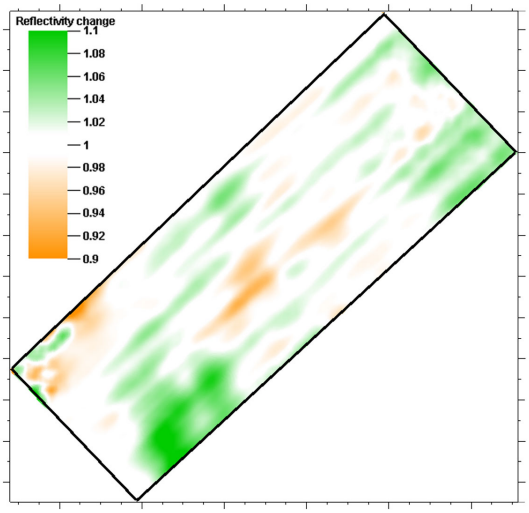

(d) Reflectivity change full offset stack

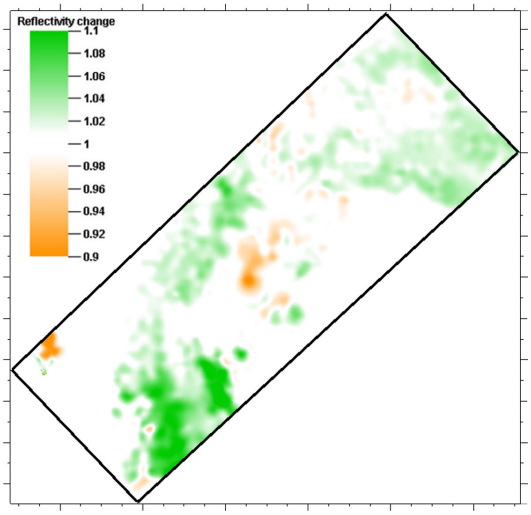

(e) Normal incidence reflectivity change

Figure 4.21: Quaternary channel good repeat case: Displayed is the modulus of the spectral ratio for: (a) near offset stack, (b) mid offset stack, (c) far offset stack and (d) full offset stack seismic data. A mean smoothing filter of 100m width is applied to the data in (a) to (d). The full offset stack data (d) violate the initial assumption of a limited slowness range stack and are therefore not useable. (e) Normal incidence reflectivity change calculated from the ray-tracing model input parameters.

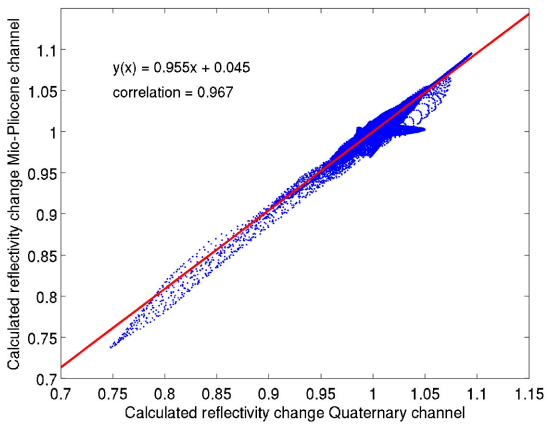

(a) Near offset stack

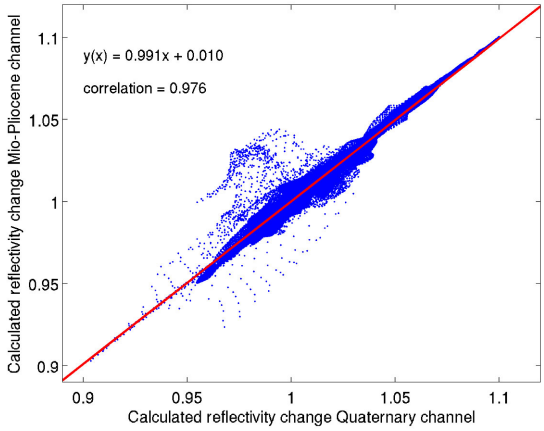

(b) Mid offset stack

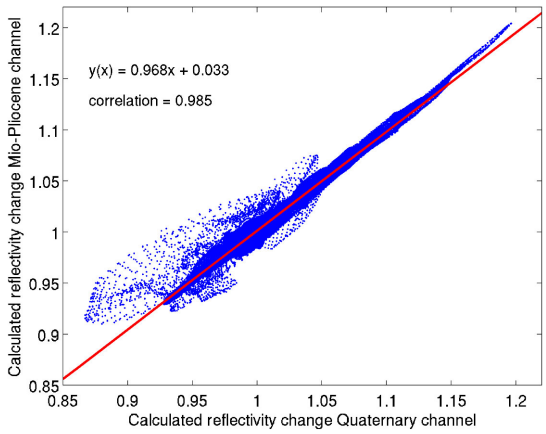

(c) Far offset stack

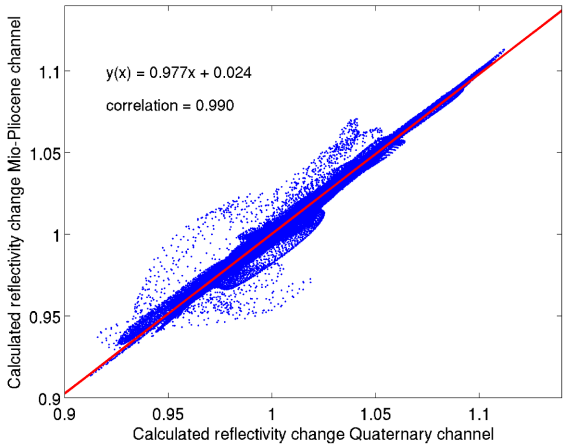

(d) Full offset stack

Figure 4.22: Quaternary channel good repeat case: Cross plots of the reservoir reflectivity change estimated from the Mio-Pliocene channel data versus the Quaternary channel data for: (a) near offset stack, (b) mid offset stack, (c) far offset stack, (d) full offset stack.

only shows that the reflectivity change estimates are the same, but the actual spatial correlation with the normal incidence reflectivity change is still poor (Figures 4.21(d) and 4.21(e)). Severe striping dominates the result and makes an interpretation meaningless. The correlation coefficient is 0.764 when the normal incidence and the reservoir reflectivity change are cross-plotted (not shown). Again, calculating the reflectivity change from the full offset stack data is violating the assumption of a narrow slowness range to be input to the spectral ratio.

On the other hand, excellent results showing the good performance of the spectral ratio are obtained when the reflectivity change is calculated at the top Sele horizon using the near, mid, far and full offset stack data. The minimum of the mean value

for the estimates is 0.997 and the maximum standard deviation of those four cases is 0.016. These values indeed match very well with the theoretical reflectivity change of unity at this interface.

The previous examples indicate that the spectral ratio performs well and independently of different overburden heterogeneities affecting the wavefield. As shown in this section, the spatial correlation of the reservoir reflectivity change to the normal incidence change is independent of the type of overburden channel. The correlation coefficients for the cross-plots between the reservoir reflectivity change and the normal incidence change using the good repeat data are summarised in Figure 4.23. The data points are almost identical and consistently high for the limited offset

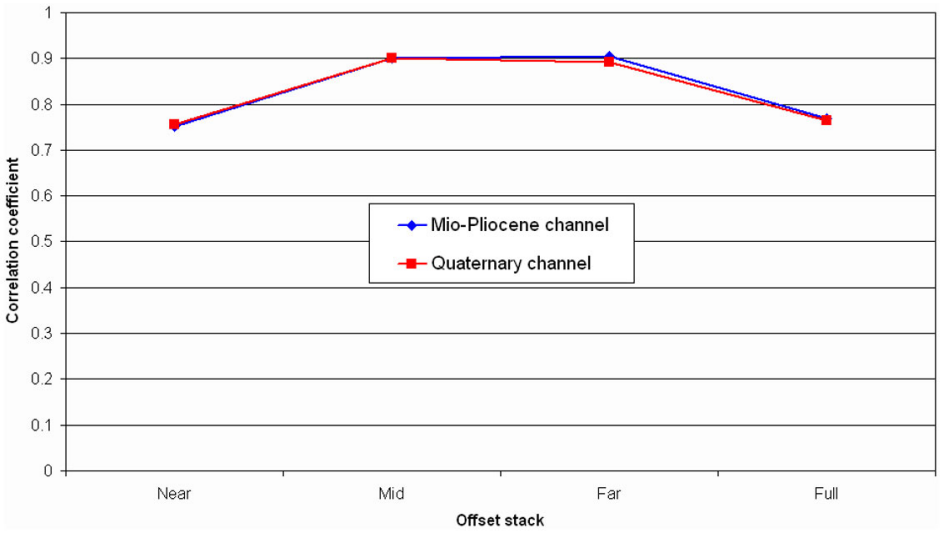

Figure 4.23: Good repeat data: correlation coefficients for the cross-plots of the reservoir reflectivity change against the normal incidence reflectivity change calculated from the Mio-Pliocene channel data and the Quaternary channel data.

stack data of the Mio-Pliocene or Quaternary channel model. Even the near offset stack data of the good repeat case deliver usable results for the reservoir reflectivity change. This is in contrast to the near offset stack data of the poor repeat case, which spectral ratios remain critical due to the large azimuth variations caused by the significant non-repeatability (compare Figure 4.18). Consequently, these near offset stack poor repeat data are split into two smaller offset stacks in order to obtain acceptable reflectivity change estimates. A clear outcome of the study is also that very limited offset stacks should be used to compute the spectral ratio in the case of a highly non-repeated monitor survey. Furthermore, it is thought

that calculating the spectral ratio pre-stack will improve the results for such poor repeated near offset data. Full offset stack data, moreover, should not be used to estimate the reservoir reflectivity change with the spectral ratio. The division of the post-stack data into three groups (near, mid and far) is very suitable if the data is well repeated, as seen in the results for the good repeat case.

The previous discussion shows that the reservoir reflectivity change estimates differ slightly with varying acquisition non-repeatability, although, in theory, the non-repeatability as well as the overburden effects should cancel out. Nevertheless, the reservoir reflectivity change estimated from the poor repeat data is accurately resolved in comparison to the normal incidence change and the acquisition footprint is significantly reduced. Therefore, it is investigated whether using these reservoir reflectivity change estimates improves the oil saturation change inversion and thus the quantitative time-lapse interpretation.

After this discussion of the spectral ratio, it has to be mentioned that the use of this method in a time-lapse sense has been reported by Korneev et al. (2004). However, it is considered that the implementation of the spectral ratio, as presented in this chapter, is an improvement over the application described in the literature, as this earlier implementation shows large errors and is only tested on two-dimensional data. Moreover, there is no statement as to whether the extracted reflectivity change improves the quantitative time-lapse interpretation or not. A more detailed discussion is found in Appendix B.

4.3 Oil saturation change estimation using spectral ratio attributes

The previous section shows that the reservoir reflectivity change can be estimated from limited offset stacked time-lapse data with a significantly reduced acquisition and overburden imprint when using the spectral ratio. Consequently, these new attributes are used to invert for the oil saturation change in the synthetic Nelson data. First, the reservoir reflectivity changes estimated from the 400m-800m, mid

and far offset stack poor repeat seismic data are input into the multi-attribute inversion. The attributes are extracted from the model with the Mio-Pliocene overburden channel. Moreover, the pressure change is set to be zero for the inversion, which is in line with the small pressure changes occurring in the data. Figure 4.24(a) shows the oil saturation change estimated from the reservoir reflectivity change attributes (poor repeat case).

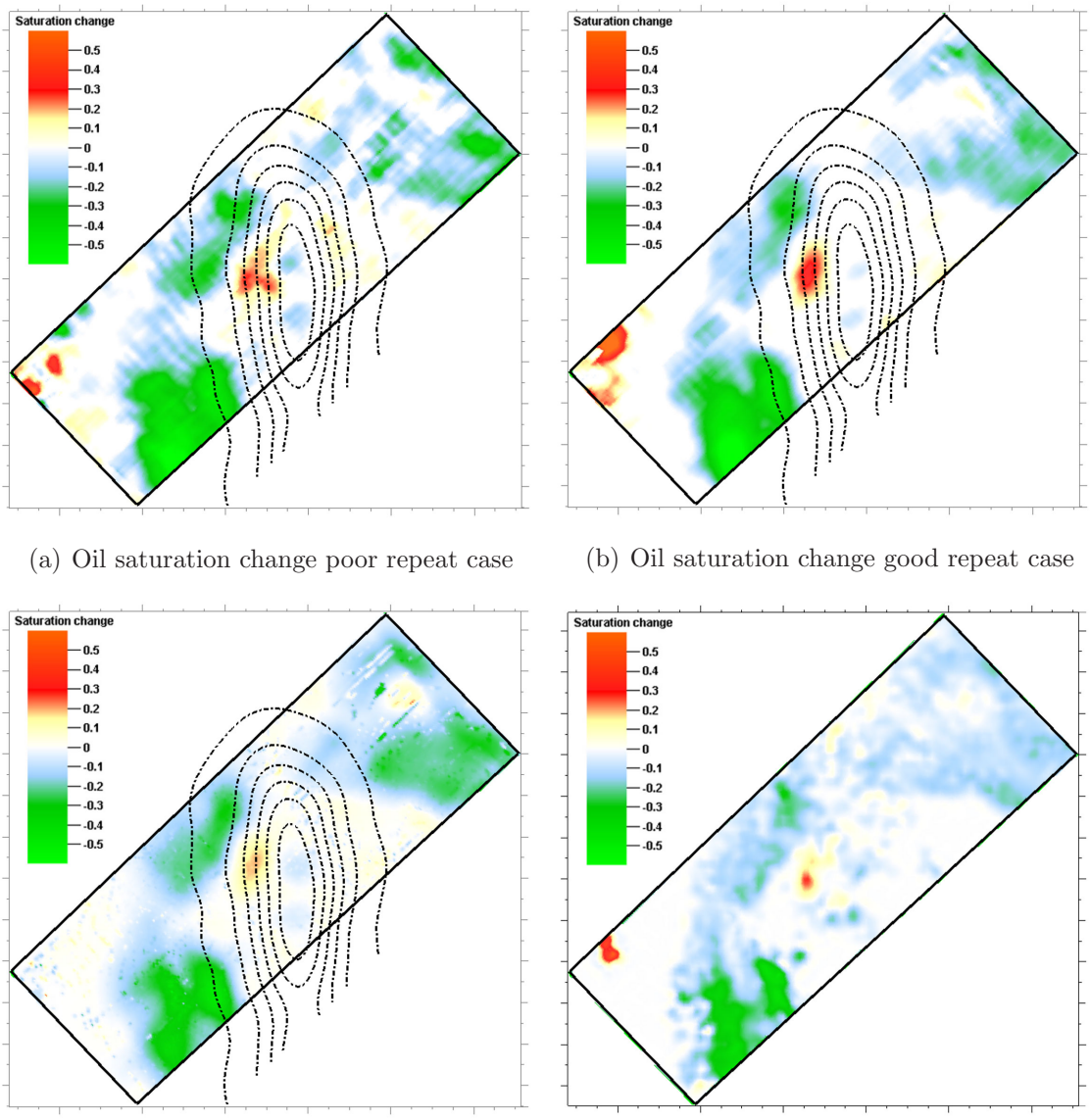

(a) Oil saturation change poor repeat case

(b) Oil saturation change good repeat case

(c) Oil saturation change ideal repeat case

(d) Oil saturation change simulator

Figure 4.24: Oil saturation change estimated from (a) the reflectivity change attribute of the poor repeat data, (b) the reflectivity change attribute of the good repeat data and (c) the amplitude attribute of the ideal repeat data. (d) The oil saturation change from the simulation model.

The oil saturation change is well resolved, but slightly overestimated compared to the oil saturation change extracted from the simulation model (Figure 4.24(d)). Some minor striping is also visible in the data. In addition, the saturation change estimate using RMS amplitude attributes from the Mio-Pliocene channel seismic data modelled with an ideal repeated monitor survey (same acquisition geometry for the baseline and monitor survey) is shown in Figure 4.24(c). The saturation change estimated from the reflectivity change matches closely with this ideal repeat case. An even better match to the oil saturation change of the simulation model and thus the ideal survey case is obtained when the reflectivity change attributes from the good repeat case are employed (Figure 4.24(b)). The saturation change estimated from the reflectivity change attribute (good repeat case) correlates well with the normal incidence change from the simulation model. Moreover, it is less over-predicted than the saturation change estimate using the ideal repeat amplitude data (Figure 4.24(b), right-hand side of the channel and Table 4.1). The contour lines of the Mio-Pliocene channel are overlain on the inversion results to emphasise that the overburden channel is included in the ray-tracing model and thus affects the wave propagation and the seismic data.

Furthermore, the oil saturation change is estimated from the reservoir reflectivity changes of the Quaternary channel model and the poor, as well as good repeat case. The correlation to the true saturation change of the simulation model improves similar to the previously presented Mio-Pliocene results. To highlight these improvements, the difference between the true and the estimated saturation change is calculated. The mean errors and the standard deviations of the absolute difference are in turn calculated for the ideal repeat case, as well as the poor and good repeat case (Table 4.1). These are the average values of the respective Mio-Pliocene and Quaternary channel cases. The lowest errors are obtained with the ideal repeat survey, however, the mean inversion errors are reduced if the oil saturation change is estimated from the reflectivity change derived by the spectral ratio. In addition, the standard deviation is very comparable to the ideal repeat case. On the other hand, the standard deviation is high if the oil saturation change is estimated from the RMS amplitude attribute, thus influenced by the overburden channel and the non-repeated monitor survey.

	Mean error	Standard deviation
Ideal repeat case	0.02 saturation units	0.06 saturation units
Spectral ratio - good repeat case	0.01 saturation units	0.08 saturation units
Spectral ratio - poor repeat case	0.01 saturation units	0.08 saturation units
Good repeat case	0.02 saturation units	0.11 saturation units
Poor repeat case	0.02 saturation units	0.13 saturation units

Table 4.1: Mean error and standard deviation of the difference between the true and the estimated oil saturation change. RMS amplitudes are used for the inversion in the case of the ideal, good and poor repeat case. The spectral ratio derived reservoir reflectivity change is used for the accordingly named good and poor repeat cases. The maximum absolute oil saturation change in the data is 0.45 saturation units.

The spectral ratio is also calculated for the poor and good repeat case without an overburden channel and the derived reservoir reflectivity change is in turn used to estimate the oil saturation change (not shown). Then, both oil saturation estimates, with and without the overburden channel, are subtracted in order to highlight the error caused by the overburden channel, as done in the previous studies. The oil saturation change inversion error caused by the Mio-Pliocene channel and the poor repeat survey is reduced when the reservoir reflectivity change attribute is used (Figure 4.25(a)). The error in saturation change inversion when using RMS amplitude attributes from the poor repeat data is displayed in Figure 4.25(b). The arrows in both figures mark large inversion errors which are caused by the Mio-Pliocene channel when using horizon based amplitude attributes, but eliminated when using the spectral ratio method. Nevertheless, not all errors caused by the overburden channel are removed by the spectral ratio, but at least their magnitude is lowered. The maximum absolute inversion error in the vicinity beneath the channel reduces from 0.30 (Figure 4.25(b)) to 0.18 (Figure 4.25(a)). The extensive errors at the edge of the map, however, are caused by horizon picking problems. There is clearly room for improvement, as the spectral ratio does not remove all overburden and acquisition related errors. However, this would certainly require the ratio to be calculated

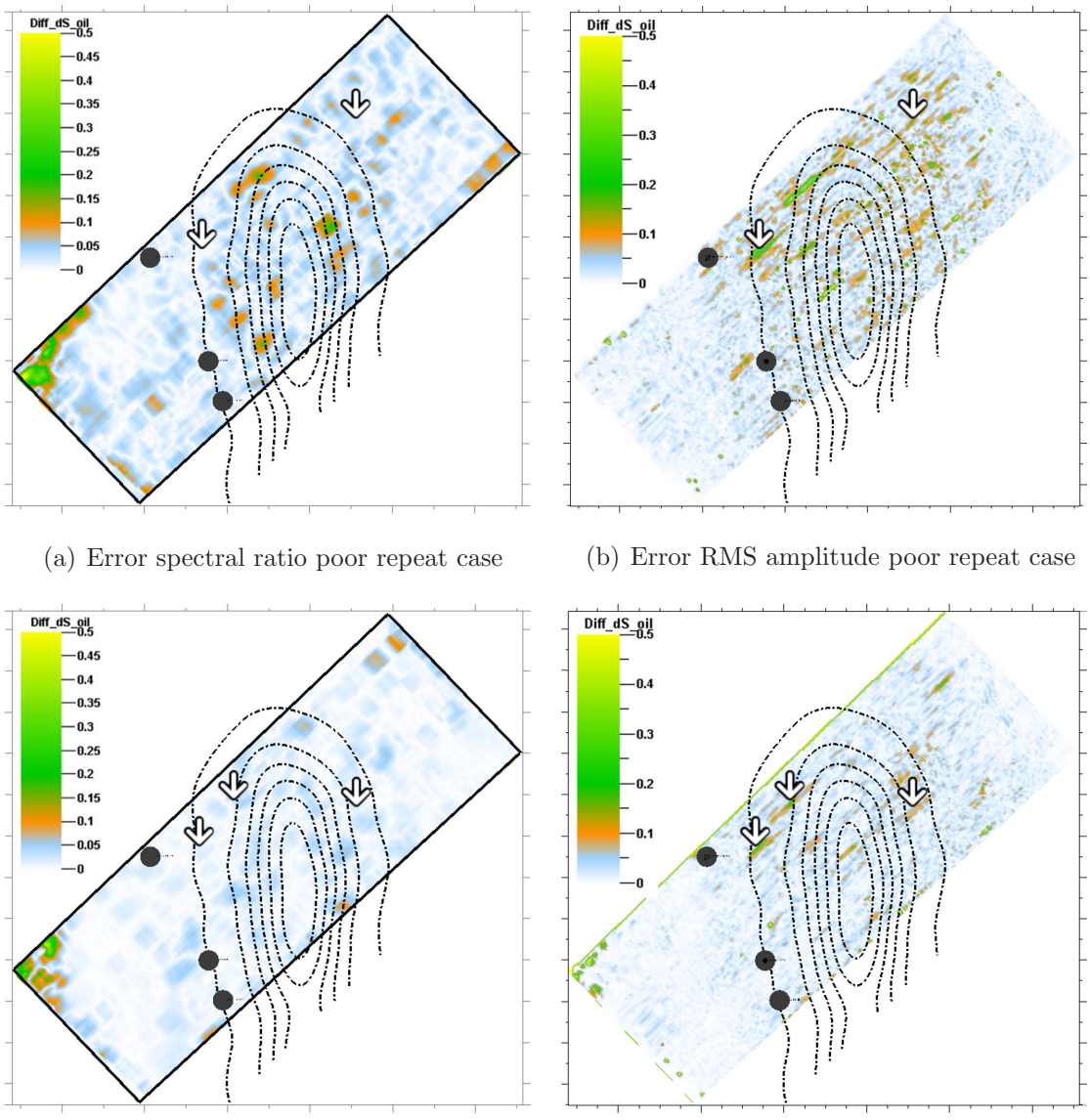

(a) Error spectral ratio poor repeat case

(b) Error RMS amplitude poor repeat case

(c) Error spectral ratio good repeat case

(d) Error RMS amplitude good repeat case

Figure 4.25: Eliminating acquisition and overburden errors by usage of the spectral ratio. (a) and (c): Oil saturation change inversion errors caused by the Mio-Pliocene channel when using the reservoir reflectivity attribute. (b) and (d): Errors in the saturation change inversion when using horizon based RMS amplitude attributes.

pre-stack in order to follow the assumption that the ratio is defined for small slowness variation in the input seismic data. Therefore, using just three limited offset stacks (400m-800m, mid and far) is barely sufficient in order to leverage the full potential of the spectral ratio method when using poor repeat time-lapse data.

On the other hand, the oil saturation inversion error caused by the Mio-Pliocene channel is significantly reduced by the use of the spectral ratio for the good repeat

case (Figure 4.25(c)). The errors caused by the overburden channel when using RMS amplitude attributes are shown in Figure 4.25(d). Arrows indicate that most of these errors are eliminated by the spectral ratio. Moreover, the maximum absolute saturation change error reduces from 0.22 saturation units to 0.09 saturation units in the area beneath the Mio-Pliocene channel, which is a reduction by a factor of more than two. Some larger errors at the edge of the study area are again caused by picking uncertainty in the data. Working with the near, mid and far limited offset stacks in the post-stack domain appears to be sufficient to eliminate most of the overburden as well as acquisition related errors for the good repeat data. Nevertheless, it remains a topic of future research whether these good results might further improve when calculating the spectral ratio pre-stack. Another parameter that should be considered in future studies is the frequency range over which the modulus of the spectral ratio is averaged. All previous examples use a rather broad range around the central frequency of the wavelet. However, the reflectivity change in different frequency bands might provide additional information about reservoir changes which can be of use for refining the quantitative interpretation. The oil saturation change estimated from the reflectivity change attributes and the Quaternary channel in the overburden improve similar to the presented Mio-Pliocene channel data. Therefore, they are not explicitly shown.

It is thus concluded that the reservoir reflectivity change attribute which is calculated with the spectral ratio significantly improves the saturation change inversion result. The acquisition footprint is considerably reduced and the saturation change estimate now better matches the input saturation change. Furthermore, the mean error is reduced by a factor of two and the standard deviation of the saturation change estimation error is lowered by as much as 60% when using the layer stripping approach. In case that the reflectivity change attribute is calculated from the good repeat data, inversion results are directly comparable to the saturation change estimated with RMS amplitude attributes from ideal repeat data. Therefore, time-lapse attributes calculated with the spectral ratio improve the quantitative interpretation. These are promising results, but more work has to be done on calculating the spectral ratio pre-stack, as the assumption of narrow slowness range limits the use of post-stack data. Using the layer stripping approach on post-stack partial stacks is

considered to be a quick tool to assess the reservoir changes. However, these results imply that there are significant limitations when using post-stack seismic attributes for time-lapse inversion and using pre-stack data should be considered.

4.4 Summary

Removing the overburden and acquisition effect by using the spectral ratio is successfully demonstrated in this chapter. The reservoir reflectivity changes estimated from limited offset stack seismic data correlate spatially well with the model's normal incidence reflectivity change. Moreover, AVO effects are also satisfactorily recovered. Only the reflectivity change estimates from near offset stacks of the poor repeat seismic data do not perform well. These estimates are improved by dividing the near offset stack range into two narrow offset classes, but this indicates the limitations of the technique when applied to post-stack data. The estimated reservoir reflectivity change attributes are input into a multi-attribute saturation inversion method to demonstrate that the inversion results are superior to the ones that use RMS amplitude attributes. Subtle changes in the reservoir are better resolved and less overestimated. In addition, the error in estimating the saturation change, which is caused by the overburden channel, is reduced by a factor of two.

Chapter 5

Overburden effects of stacked reservoirs, West of Africa

This chapter investigates the effect of stacked reservoirs on the time-lapse seismic amplitude attribute. The study is based on an offshore West of Africa deepwater oil field. Multiple stacked reservoirs are present; consequently, a ray-tracing model is built to investigate and quantify how the time-lapse signal of the deepest reservoir is distorted by the production imprint from the overlying reservoir. Moreover, amplitude effects that are caused by migrating the monitor seismic data with the baseline velocity model are highlighted.

5.1 Introduction

The Nelson study which is presented in Chapter 3 and 4 demonstrates that an overburden channel, if not well resolved in the migration velocity model and in conjunction with a non-repeat monitor survey, causes errors in the time-lapse interpretation. In this chapter, the effect of stacked reservoir channels on the time-lapse amplitude is studied in case of a non-repeated acquisition geometry and an inaccurate migration velocity model. Figure 5.1 illustrates the situation where two reservoir units lie above each other in space. The proceeding study refers to these two reservoirs as Channel 1 and Channel 2 for the upper and lower reservoir, respectively. Depending on the thickness of these two channels, it is difficult to resolve

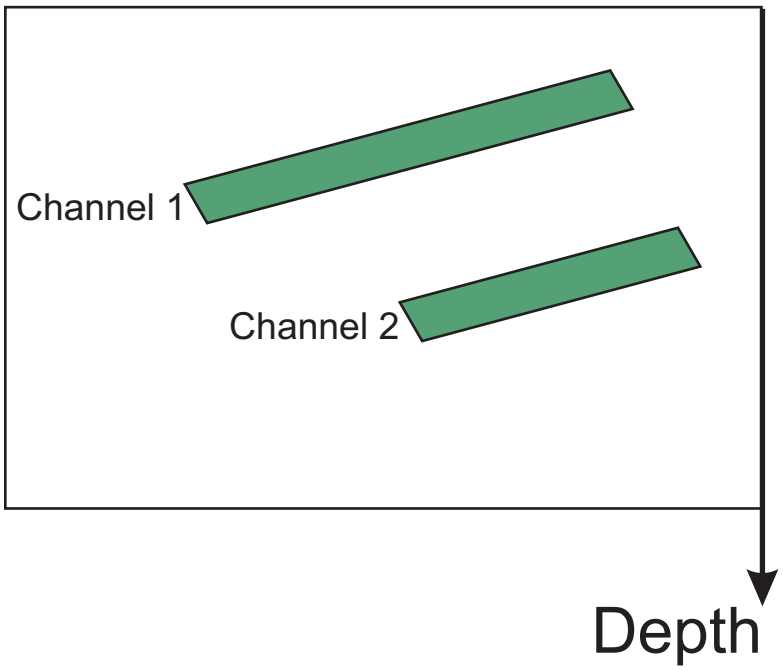

Figure 5.1: Schematic cross section of two stacked reservoir units, Channel 1 and Channel 2, respectively.

their velocity adequately in the migration velocity model. The commonly used velocity building workflows employ traveltime tomography to obtain the migration velocities on a coarse grid, for example, 500m x 500m x 100m. Full wavefield inversion techniques might be the tool to use. However, they are also restricted to match only the low spatial wavelengths in the seismic data and thus resolve large-scale velocity heterogeneities with a wavelength greater than 200m. Therefore, a rather

smooth velocity model is commonly used for migration purposes.

Moreover, the baseline velocity model is used to migrate the monitor data, although the velocity inside Channel 1 and 2 changes due to production. Figure 5.2 outlines this common practice. Channel 1 and Channel 2 are not produced at the time of the baseline survey, indicated by no colour fill of the reservoir. At the time of the monitor survey, however, both channels are produced (green fill). Therefore, migrating the monitor seismic data with the baseline velocity model, which does not include these velocity changes, might cause errors in the monitor seismic data. These errors could in turn impact the ability to accurately interpret the time-lapse difference data, especially in case of a non-repeat monitor survey geometry. Furthermore, the

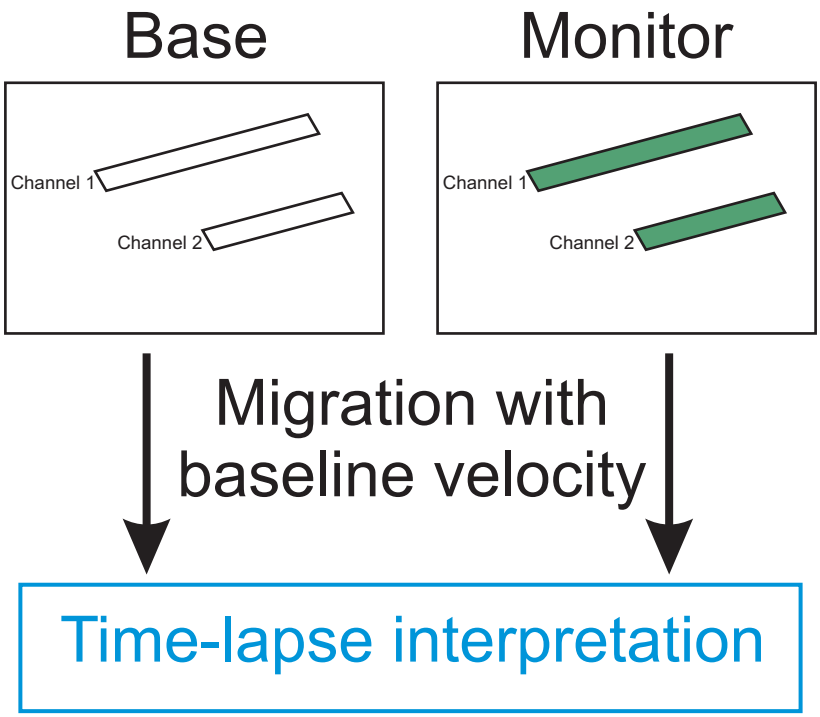

Figure 5.2: Common time-lapse workflow for stacked reservoir data processing. No colour fill in the channel indicates a pre-production reservoir state, whereas a green colour fill indicates the reservoir state after production.

interpretation of the time-lapse amplitude changes at Channel 2 might be particularly affected by the changes inside Channel 1 which imprint on Channel 2. This chapter therefore addresses these two problems of stacked reservoirs by building a synthetic ray-tracing model using data from a West of Africa field, which is further described in the proceeding sections.

5.2 Field description

The input data for this study are taken from a West of Africa field, which is located in the Congo Basin (Figure 5.3). The dominant sediment fill of the Congo Basin

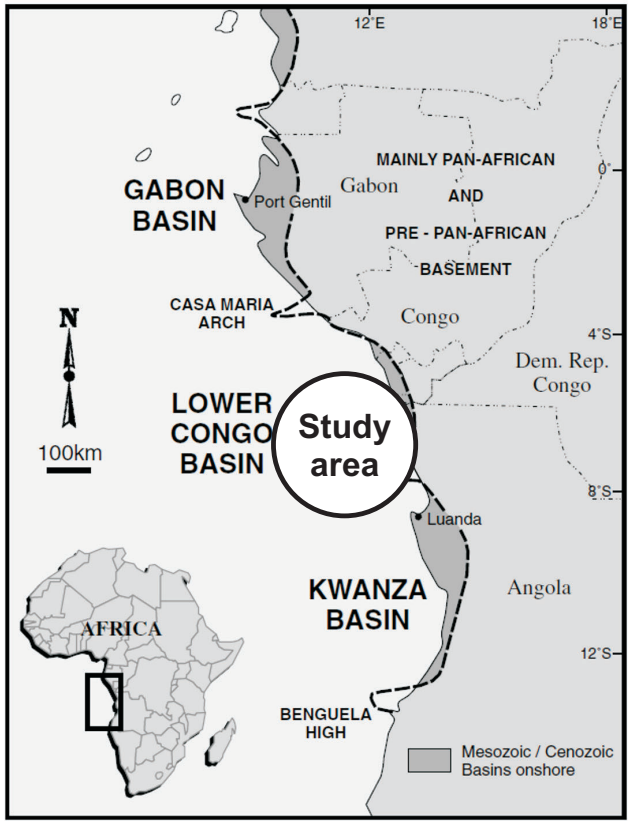

Figure 5.3: Location map showing the study area offshore Angola, in the Congo Basin (modified from Anderson et al. (2000)).

consists of as much as 6000m of Cenozoic clastics of the Malembo formation with the principal reservoir rocks being turbidites and debris flow deposits. The deposition occurs in channel complexes on the slope of the West African passive margin during the Miocene (Beaubouef et al., 1998). These channel complexes generally trend from East to West. The field segments are combined structural stratigraphic traps cut at right angles by normal faults. The seismic cross section through a part of the Congo Basin highlights the characteristic stacked multistory reservoirs of Miocene Age embedded in the Malembo formation (Figure 5.4). The regional tectonic setting of this area is controlled by salt related deformation in a gravitationally driven, linked extensional contractional system (Reeckmann et al., 2003). Therefore, these

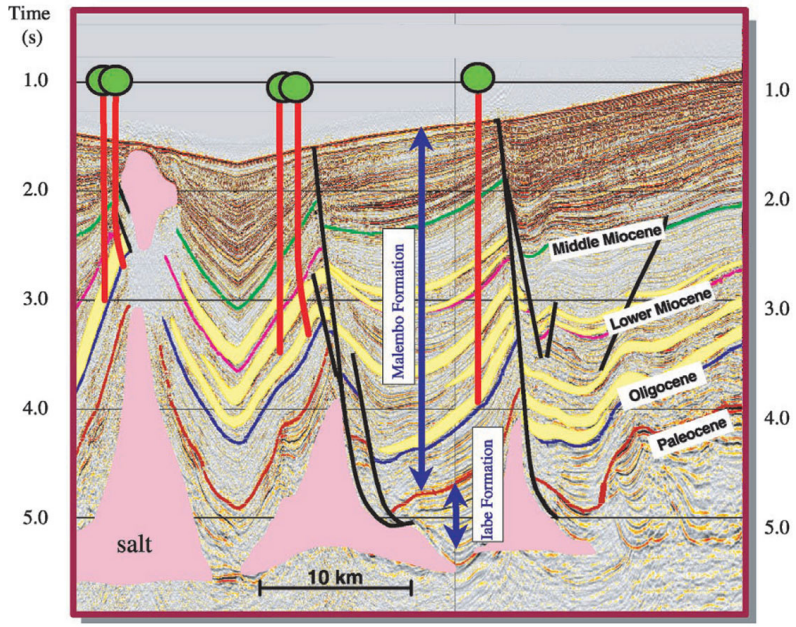

Figure 5.4: Example of stacked reservoirs (yellow), West of Africa. Black lines indicate major faults (modified from Reeckmann et al. (2003)).

reservoir channels are draped and faulted over large salt cored structures. The reservoirs are at depths between 500m and 1900m below mud line, which is about 2000ms to 3400ms TWT below mean sea level. Water depth is approximately 1200m. The oil column height ranges between 400m to 1000m, depending on the reservoir seal capacity.

Most of the Miocene Age reservoirs are multi-cycle depositional units with a total thickness ranging between 50m and 400m and a width of 1500m to 6000m. Figure 5.5 shows a depositional model of one such a multistory reservoir in more detail. The various intra-reservoir, multi-cycle channels are clearly seen. Porosity varies between 15% and 35% and permeability is between 1000mD and 5000mD for the hydrocarbon bearing sands. The two reservoirs under investigation in this study are made up of multi-cycle depositional intra-reservoir channels a few tens of metres in thickness and a few hundred metres' width, similar to the depositional model in Figure 5.5. The production of both reservoirs is by down flank water injection to maintain the pressure and support the natural aquifer to drive the oil up dip. Gas coming out of solution is detected in the up dip wells of Channel 1, in addition to the reinjected associated gas at the top. The gas oil ratio (GOR) varies between 450

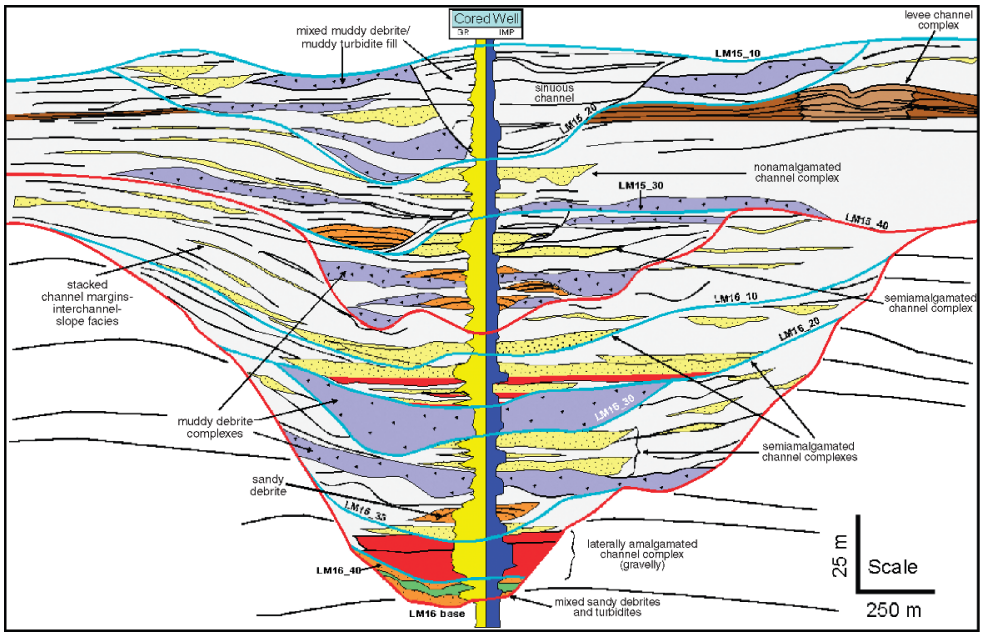

Figure 5.5: Depositional model for a multistory reservoir channel in the Congo Basin (modified from Porter et al. (2006)).

and 800 with oil gravity being between 24-35° API. Water breakthrough is observed at some intra-reservoir layers at Channel 2. Hence, the presence of free gas, as well as water replacing the oil, results in significant changes of the elastic parameters, velocity and density, in both Channels 1 and 2.

Two high-resolution 3D surveys capture the time-lapse changes in the reservoirs. The baseline survey is shot pre-production, followed by a monitor survey shot two years after the first production of oil. The basic acquisition parameters are outlined in Table 5.1. Both surveys are acquired on the same bin size which is also used for time-lapse binning purposes.

	Shot interval		Streamers		
	Inline	Xline	Spacing	Towed	Steered
Base	25m	25m	50m	10	8
Monitor	25m	25m	50m	12	8

Table 5.1: Acquisition parameters for the baseline and monitor survey. The receiver group interval is 12.5m for both surveys, thus the natural bin grid is 12.5m x 6.25m.

Unlike other areas such as the North Sea or the Gulf of Mexico, streamer feathering in the Congo Basin is not caused by predictable water currents. The feathering in the Congo Basin is mainly influenced by fresh water turbulences caused by the Congo River flowing into the Atlantic Ocean. Therefore, the variation in the streamer feathering angle is unpredictable for successive shooting lines of the same survey.

It is possible to shoot the monitor survey to match the baseline acquisition geometry in such conditions, but the fundamental question is whether this is necessary. Steering the streamers for coverage and not try to repeat shot and receiver positions from the baseline survey does result in a good mean positioning error under these unpredictable and almost random feathering conditions. Additional acquisition non-repeatability during the monitor survey is caused by the field facilities. No production facilities are installed at the field at the time the baseline survey is acquired. However, subsequent development employs a tension-leg platform (TLP) as well as a floating production storage and offloading (FPSO) vessel which is offloaded to tankers via a catenary anchor-leg mooring buoy (CALM). These facilities obstruct the central part of the field above the reservoir channels, resulting in an undershoot area in the monitor survey, which in turn affects the time-lapse data quality. Consequently, the NRMS measure increases in the undershoot area to 40% from a mean value of 25% for the whole field. A further increase to 50% is observed over faults between salt cored anticlines. The data quality around salt diapirs is worst, with NRMS values as high as 70%. All measures are calculated in a 200ms window above the reservoir channels. These high noise levels indicate that acquisition non-repeatability as well as overburden complexities have a detrimental effect on the time-lapse NRMS attribute. Therefore, it is to be seen if production from stacked reservoir units does also affect the time-lapse interpretation.

5.3 Stacked reservoir study - model building

The former section generally describes the production in Channels 1 and 2, the monitor and baseline survey, as well as the observed time-lapse data quality. Consequently, a ray-tracing model is built that contains these two channels embedded in

the surrounding rock, as well as real survey acquisition parameters. The intention is to model synthetic pre-stack shot gathers in order to investigate how the production in Channel 1 affects the time-lapse amplitude interpretation at Channel 2. The NORSAR3D^{TM} software package is chosen for the seismic modelling, thus all constraints discussed in Chapter 2 apply. The following input data are needed for the model building stage:

- Interpreted depth horizons
- Velocity and density information for Channels 1 and 2, as well as for the surrounding rock
- Source and receiver positions for the baseline and monitor survey as P1/90 navigation data files

First, the following horizons are extracted from seismic interpretation projects and imported into the ray-tracing subsurface model:

- Sea floor, also called mud line
- Top and base of Channel 1 and Channel 2, respectively
- Chattian sequence boundary (Oligocene age) as bottom layer of the ray-tracing model

Figure 5.1 schematically outlines the position of Channels 1 and 2 in the subsurface, whereas Figure 5.6 shows the top and base horizon of each channel as it is input into the ray-tracing model. Moreover, the top and base of Channels 1 and 2 (Figure 5.6) are smoothed using a 100m Hamming filter. The sea floor is input into the model by smoothing (250m Hamming filter width) the bathymetry data. Finally, the base horizon for the model is imported into the ray-tracing model after smoothing with a 250m Hamming filter. Subsequently, the elastic parameters for the overburden rock as well as for both reserviors are imported. The velocity and density parameters between top and base of Channels 1 and 2 are obtained by applying a petro-elastic transformation to the reservoir simulation data taken at two time steps: before production and two years after the start of production. Figure 5.7 shows one cross

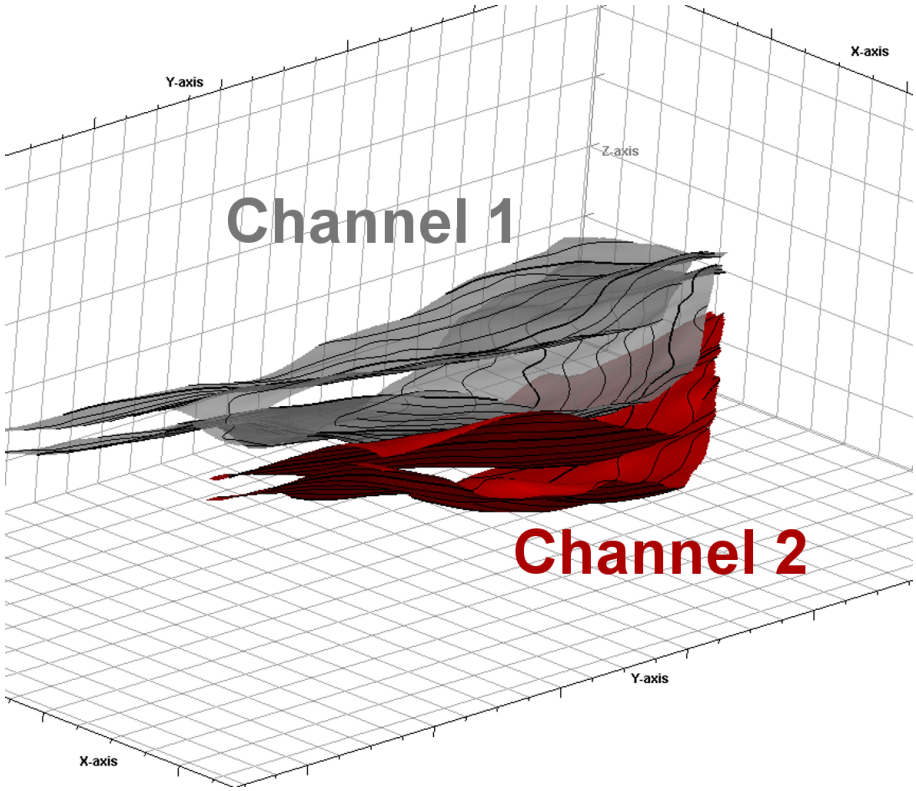

Figure 5.6: Top and base of Channel 1 (grey) above top and base horizon of Channel 2 (red).

section through the pre-production P-wave velocities inside Channel 1. The base horizon for Channel 1 is plotted as well, in order to outline the good alignment between the elastic parameters obtained from the reservoir simulation model and the imported surfaces in the subsurface model. The difference in velocity corresponds to the intra-reservoir multi-cycle channels, which are partly shown in Figure 5.8. These channels are heavily intersected with varying erosional contact surfaces, thus the top and base horizons of these intra-reservoir channels are not explicitly input into the ray-tracing model. Extracting each of the individual depositional units in order to be include separately in the model would have been too time consuming. However, all production related changes which affect the velocity and density change inside Channels 1 and 2 and thus the wave propagation, are captured between top and base of Channels 1 and 2. Only intra-channel reflections are not modelled. The velocity (V_p and V_s) and density parameters of Channels 1 and 2 are further smoothed by a running Hamming filter of 50m x 50m in the lateral direction and by 12m in the vertical direction to ensure the stability of the ray-tracing process. Additional resampling to 25m x 25m x 4m is necessary in order to reduce the memory

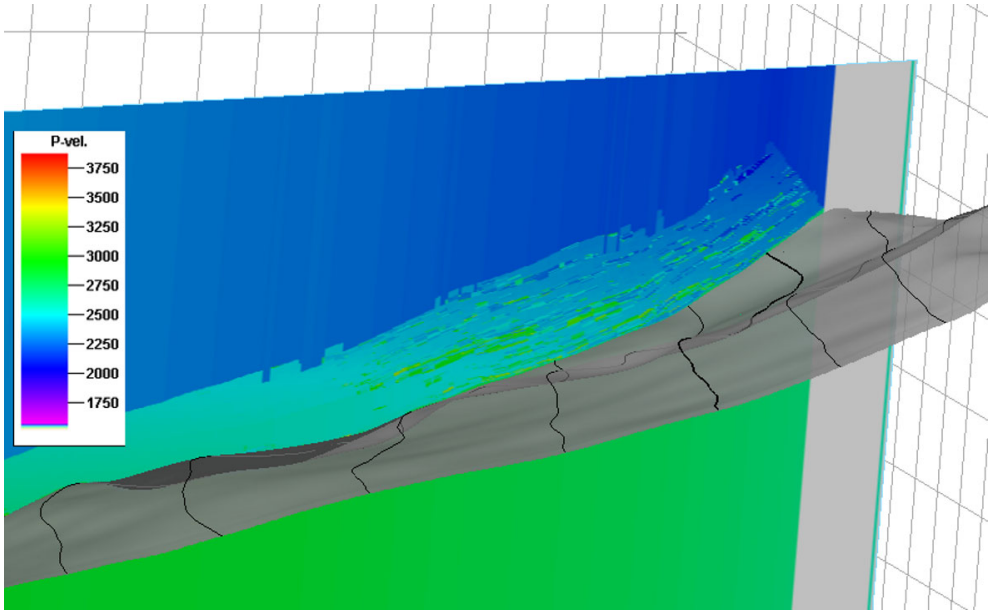

Figure 5.7: The P-wave velocity is displayed on one cross section through the velocity volume of Channel 1. The base horizon of the channel complex is shown as well. Constant velocity is assigned outside the reservoir simulation grid.

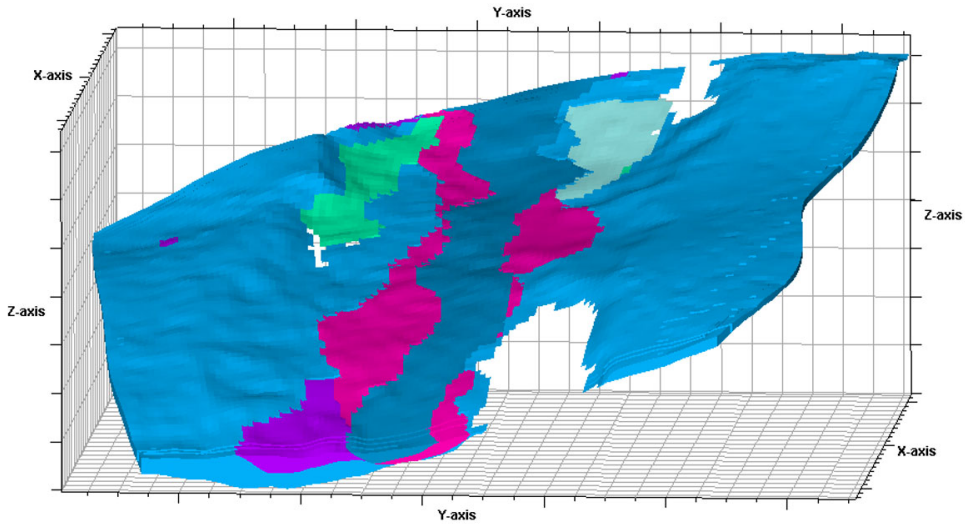

Figure 5.8: Internal structure of the Channel 1 multistory reservoir unit. Different multi-cycle depositional units are colour coded.

requirement of the final ray-tracing model. Production induced acoustic impedance changes in Channel 1 are negative in the study area due to gas coming out of solution and the reinjection of gas at the top (Figure 5.9). The impedance change in

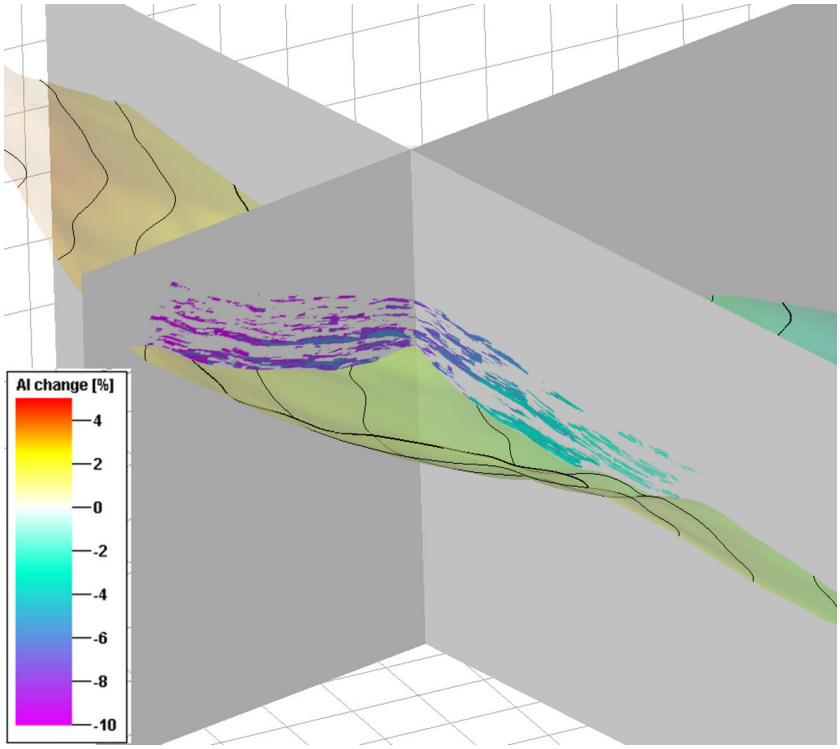

Figure 5.9: Two sections showing the acoustic impedance change in Channel 1 due to reservoir production. The base horizon for Channel 1 is also plotted.

Channel 2 is in the range of ±3%. Furthermore, the change of density in Channel 1 and Channel 2 is in the order of ±2%.

The P-wave velocity for the background rock in which Channels 1 and 2 are embedded is taken from an interval depth velocity model and further smoothed using a 500m filter width. The shear wave velocity is calculated from the P-wave velocity using the following depth dependent V_p/V_s ratio:

$$V_p/V_s = 2.9 - 0.0004 \cdot Zbml \quad . \tag{5.1}$$

The ratio decreases with the depth below mud line, Zbml. Conversely, the density for the surrounding rocks, $\rho(z)$, increases with depth and is calculated using an empirical trend adequate for the study area:

$$\rho(z) = \rho_{Shale} \cdot (1 - \phi(z)) + \rho_{Brine} \cdot \phi(z) \quad , \phi(z) = 0.525 \cdot e^{(-0.0006 \cdot Zbml)} \tag{5.2}$$

where a shale density, ρ_{Shale}, of 2.65kg/m^3 and a brine porefill density, ρ_{Brine}, of 1.05kg/m^3 is used. A constant velocity and density is assumed for the sea water layer.

Finally, source and receiver positions from the baseline and the monitor survey are input to the ray-tracing model. Unfortunately, Channel 1 and Channel 2 are located directly beneath the undershoot area. It is known that the time-lapse data quality is severely affected in this area, thus investigating the stacked reservoir case under such poor repeatability conditions is not considered as a worthwhile test. Therefore, the source and receiver positions that are used to represent the baseline as well as the monitor acquisition geometry in the ray-tracing model are extracted in a zone outside the undershoot area and subsequently moved over the study area to replace the undershoot acquisition geometry. Hence, a "regular" instead of an undershoot acquisition non-repeatability is modelled, but the general character of the non-repeatability over this reservoir is maintained. The shot and receiver locations chosen for the pre-stack modelling extend over an area of 3500m x 7000m, which translates into a fully illuminated post-stack area that expands 3000m x 5000m in the crossline and inline direction, respectively. A large number of 22000 shots are modelled pre-stack due to the high resolution baseline and monitor survey acquisition geometry.

Before processing the seismic data, traces from the baseline and monitor survey are selected to minimise their respective difference between source and receiver positions. The $\Delta Source + \Delta Receiver$ repeatability measure for all traces with 1500m offset is plotted in Figure 5.10. An overall good match between the baseline and monitor survey is observed with a mean $\Delta Source + \Delta Receiver$ measure of 76m. Some lines, however, exhibit large mispositioning errors exceeding 400m. Source and receiver reciprocity is assumed for sail lines which are shot in the opposite direction.

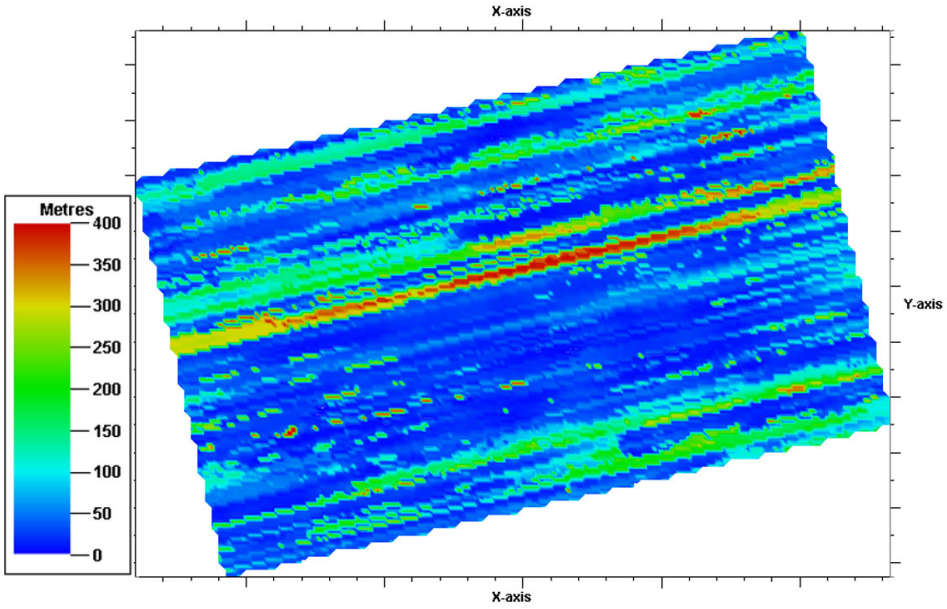

Figure 5.10: Stacked reservoir study: $\Delta Source + \Delta Receiver$ repeatability measure for traces at 1500m offset.

5.4 Seismic modelling and data processing

The seismic modelling is performed after building the ray-tracing model, which is described in the previous section. Traces for 12,000,000 shot and receiver pairs are generated and in turn processed to stacked volumes. This section first describes the methodology used to isolate time-lapse amplitude effects in this stacked reservoir study, then presents the seismic processing sequence applied to the data.

The question to address in this study is whether the production-induced changes in Channel 1 imprint on Channel 2, and whether using the baseline velocity model to migrate the monitor seismic data causes additional error. Figure 5.11 outlines the methodology used to assess possible time-lapse amplitude interpretation errors.

Left-hand side of Figure 5.11:

> Two ray-tracing models are set up. The baseline data are modelled before oil is produced from Channels 1 and 2, indicated by no colour fill in the channels. The monitor seismic data are modelled after both channels produced oil for 2 years (green fill). In turn, both seismic data sets are migrated with the baseline velocity model, which is the common

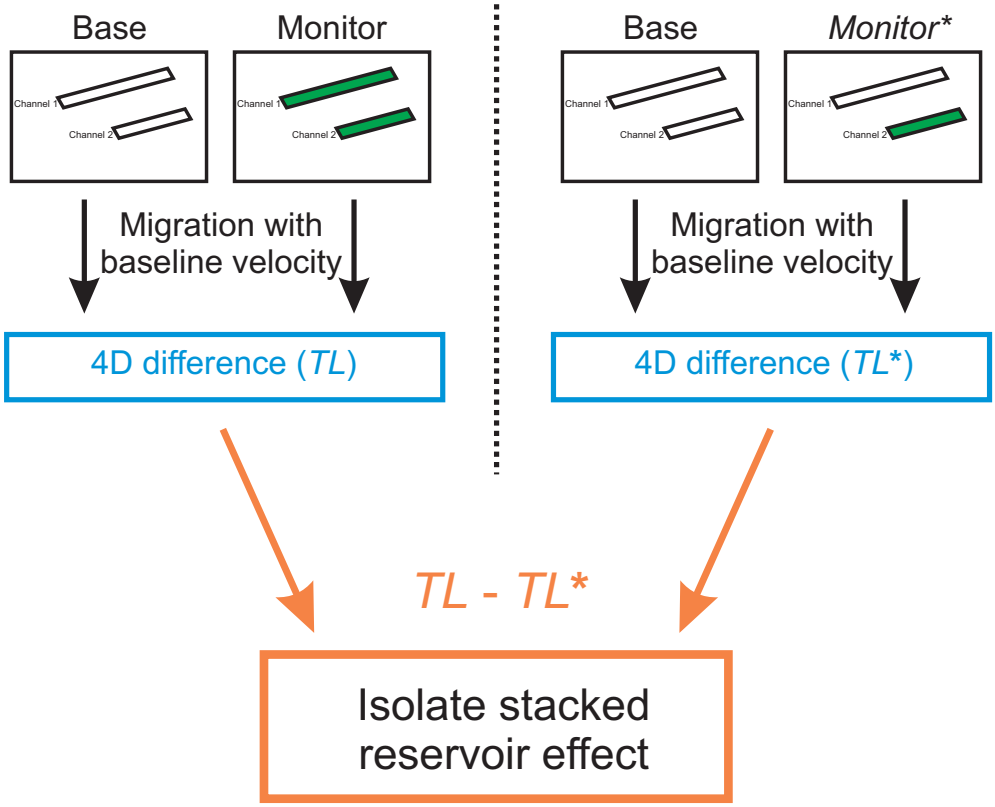

Figure 5.11: Methodology to assess the impact of stacked reservoirs on time-lapse seismic interpretation. No colour fill in Channel 1 or 2 indicates no production; whereas a green fill indicates 2 years of production.

practice in time-lapse processing. Therefore, the baseline seismic data are accurately imaged, but the monitor seismic data are migrated with an incorrect velocity model, one that does not account for the change in velocity in Channels 1 and 2 at the time of the acquisition. The time-lapse difference data, *TL*, are thus possibly affected by the changes in Channel 1, imprinting on Channel 2 and additional errors caused by using the baseline velocity model to migrate the monitor seismic data.

Right-hand side of Figure 5.11:

Again, two ray-tracing models are set up. The baseline seismic data are modelled before oil is produced from Channels 1 and 2 (no colour fill). However, the monitor data are modelled for the case that only Channel 2 is produced (green fill), whereas Channel 1 is not produced. In turn, both data sets are migrated with the baseline velocity model. Hence, the migration is accurate for the baseline seismic data and moreover, the monitor seismic data are correctly migrated up to the top of Channel 2. Therefore, no imprint of Channel 1 is expected to impede the time-lapse interpretation of amplitude changes at Channel 2, as there are no production-induced changes inside Channel 1.

The amplitude imprint of Channel 1 onto Channel 2 is assessed by taking the difference of the two time-lapse differences, TL - TL^*, extracted at Channel 2 (Figure 5.11). These residual amplitudes thus possibly prevent quantitative interpretation of time-lapse changes at Channel 2.

The amplitude error which is caused by using the incorrect migration velocity when imaging the monitor seismic data in the *TL* case can be quantified after migrating the monitor data with the correct (monitor) velocity (Figure 5.12). The left-hand side of Figure 5.12 outlines that the monitor seismic data are migrated with the baseline velocity. On the right-hand side of Figure 5.12, the monitor data are migrated with the monitor velocity, which includes the production-induced velocity changes. Hence, the difference of both migrated seismic cubes isolates the amplitude error caused by the incorrect baseline migration velocity model.

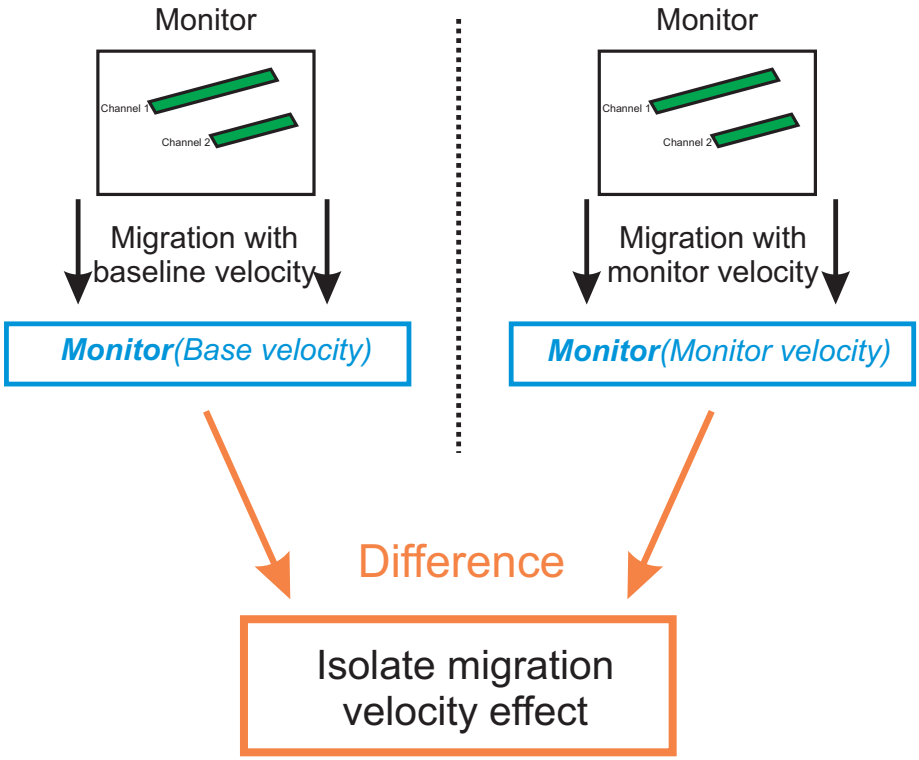

Figure 5.12: Methodology to assess the impact of the migration velocity used during processing the monitor seismic data. Production induced changes in Channels 1 and 2 are indicated by the green fill.

Consequently, three different ray-tracing models are set up for this study:

1. Baseline: No production from Channel 1 and Channel 2
2. Monitor: Production from Channel 1 and Channel 2
3. *Monitor**: No production from Channel 1; production from Channel 2

The same acquisition geometry is used for both monitor surveys, Monitor and *Monitor**; thus both exhibit the same acquisition non-repeatability. Moreover, use is made of the ray-tracing model to obtain the migration velocity. The P-wave velocity is extracted from the baseline and monitor ray-tracing model on a fine grid (100m x 100m x 10m) in the depth domain and in turn converted into a RMS time domain velocity cube via Dix's conversion formula (Equation 2.5). Smoothing the RMS velocity model by 500m x 500m x 100ms ensures that the migration operator is numerically stable. The main steps of the seismic processing sequence are summarised in Table 5.2. The combination of DMO (dip moveout) correction followed by post-stack extended Stolt migration is a good and fast approximation for a full

pre-stack seismic time migration (Bancroft, 2007) in case that the structures are simple and the dips are moderate. Full offset stacked time migrated seismic vol-

Read SEGY data

⇓

Assign geometry and CMP binning

⇓

DMO correction

⇓

NMO correction

⇓

CMP stack to full offset

⇓

Extended Stolt post-stack migration

⇓

SEGY output

Table 5.2: Seismic processing sequence applied to the pre-stack seismic data.

umes are written to the disk for further time-lapse interpretation at the end of the processing sequence. This workflow is initially chosen due to its speed in processing the data. However, it is shown that the Stolt migration approach is limited when applied to the West of Africa seismic data and a full pre-stack Kirchhoff time migration algorithm is thus needed to overcome the problem. The next section discusses the time-lapse amplitude effects in detail.

5.5 Amplitude effects of the stacked reservoirs

The initial interpretation of the seismic data reveals some inconsistency between observed and expected changes, thus leading to re-processing and re-interpretation. Nevertheless, these initial interpretation results are briefly presented to highlight the importance of working with the data carefully.

After applying the processing sequence as outlined in Table 5.2 to each of the seismic data volumes, it is found that the data contain a considerable amount of noise and migration artefacts. However, reflection events of Channels 1 and 2 are believed to be identifiable in the data, although difficult to trace throughout the volume (Figure 5.13). Hence, the RMS amplitude attribute is calculated from the TL and TL^*

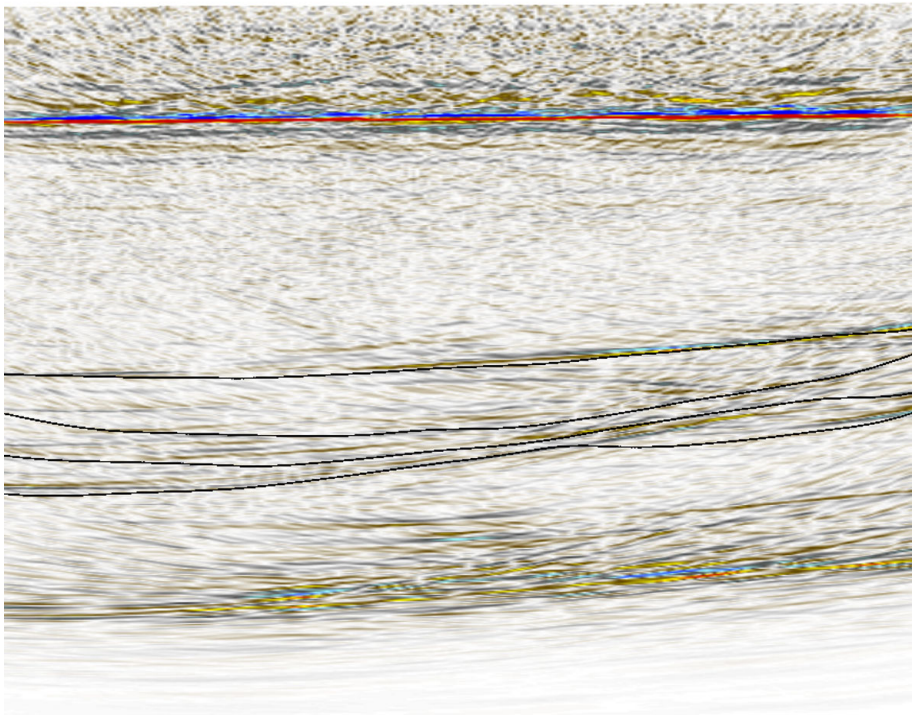

Figure 5.13: Cross-section through post-stack Stolt migrated seismic data. Black lines mark the two channels in the following order from top to bottom: top and base Channel 1; top and base Channel 2.

difference data, in a window that includes the top and the base of Channel 1. Both amplitude maps are in turn subtracted (TL - TL^*), which should resolve the amplitude change caused by the production-induced changes inside Channel 1 (compare Figure 5.11).

The expected amplitude changes at the top and base horizon of Channel 1 are proportional to the impedance change across these interfaces. However, the impedance of the surrounding rock does not change, thus the spatial distribution of the expected amplitude changes coincides with the change of acoustic impedance inside Channel 1, which can be extracted at the top and the base horizon (also compare Figure 5.9). Hence, the impedance change at the bottom of Channel 1 is extracted

from the ray-tracing model's input parameters (Figure 5.14(b)) in order to compare its spatial pattern to the residual amplitudes at Channel 1. The residual amplitudes of the TL -TL^* difference data (Figure 5.14(a)) do not correlate with the impedance changes along the base horizon of Channel 1, extracted from the model. Instead, a weak circular pattern of noise is visible, which is not anticipated. Calculating

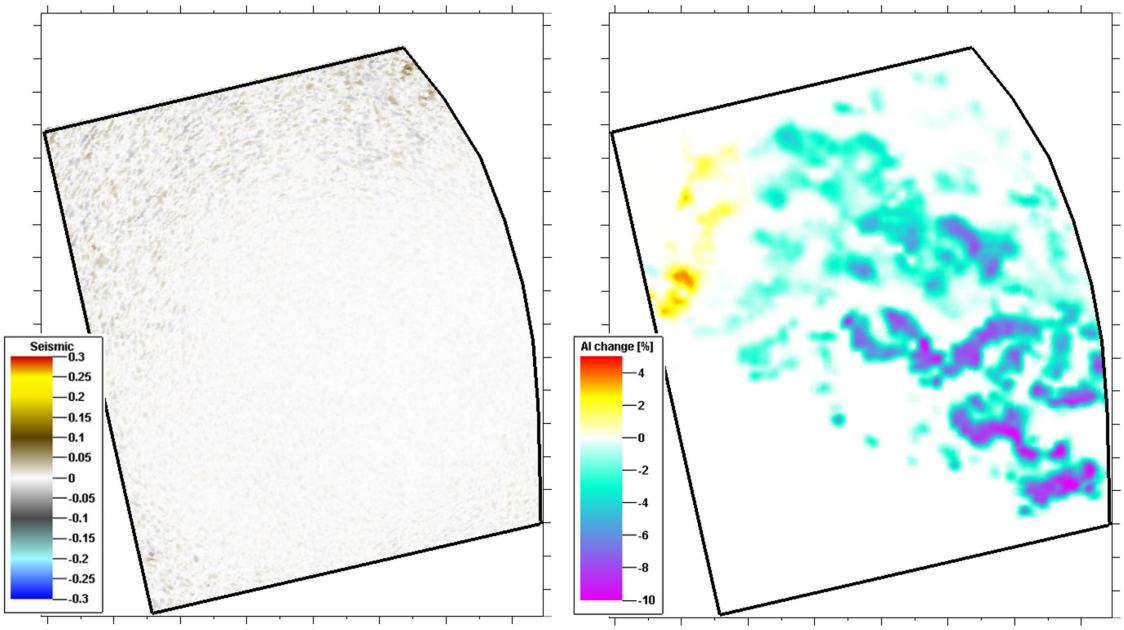

(a) Channel 1: TL -TL^* (b) Base Channel 1: impedance change

Figure 5.14: (a) The TL -TL^* difference of RMS amplitudes extracted at Channel 1. (b) Acoustic impedance change, extracted from the model along the base horizon of Channel 1, caused by the reservoir production.

the RMS amplitude individually in a window centred around the base horizon of Channel 1 in each of the Base, Monitor and $Monitor^*$ data sets, then subtracting, does not resolve the expected amplitude change in the TL -TL^* difference data either.

In addition to the uncertain results from the amplitude analysis at Channel 1, the amplitude analysis at Channel 2 is also not consistent with what is expected. According to the workflow outlined in Figure 5.11, any amplitude changes caused by the production inside Channel 2 or by the acquisition non-repeatability should cancel each other for the TL -TL^* difference. The only residual amplitude imprint that is expected is the one caused by the production changes inside of Channel 1. Hence, the RMS amplitude is extracted for the TL and TL^* difference data in a

window containing top and base of Channel 2 to test this assumption. The residual amplitudes, TL -TL^*, are clearly divided into two distinct regions, A and B (Figure 5.15(a)). However, there is no correlation with the model's impedance change extracted at the base of Channel 1 (Figure 5.15(b)) and thus no correlation with possible amplitude imprints from Channel 1 onto Channel 2. An initial interpretation suggests that the increased $\Delta Source + \Delta Receiver$ positioning error in region A causes the increased residual amplitude. However, a weak circular pattern is again observed in the residual amplitude data, which is interpreted as migration artefacts or general noise. Therefore, it is concluded that the DMO followed by the extended Stolt post-stack migration is not the best processing sequence for those data sets. A substantial amount of consistency and correlation between the residual amplitudes at Channel 1 and Channel 2 as well as the expected amplitude effects at these channels are missing.

A pre-stack Kirchhoff time migration is run on the data (Table 5.3), in order to resolve the question of whether a full pre-stack migration is able to better image the data and improve the amplitude interpretation. However, the CMP bin size is reduced to 25m x 25m to keep the computation time within an acceptable range of less than 24 hours for each data set. The seismic data quality improves significantly when using the PSTM (compare Figure 5.16 with Figure 5.13). The noise is considerably reduced, although migration artefacts are still present (Figure 5.16, orange arrow). The reflection events are much better focused and now align well with the top and base horizons of Channels 1 and 2. Despite the fact that the ray-tracing model is conditioned to have a non-zero impedance contrast at the top and base of the channels, these reflection events are still not continuous. The zone of high noise in the middle of the cross section is marked by the white arrow (Figure 5.16). Nevertheless, the increased data quality provides confidence to reinterpret the amplitude changes, using RMS amplitudes extracted in a 20ms window centred around the base horizon of Channel 1 in the Base, Monitor and $Monitor^*$ data sets. The TL -TL^* difference shows areas of increased residual amplitude marked by arrows in Figure 5.17(a). These areas correlate favourably with the extracted impedance changes at the base of Channel 1 (Figure 5.17(b)), thus outlining the production-induced amplitude change, as expected. The correlation is fair, but there are also

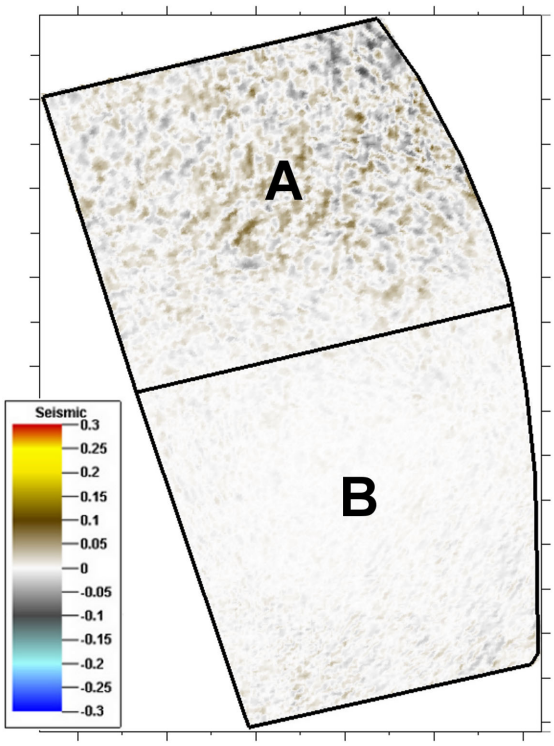

(a) Channel 2: TL -TL^*

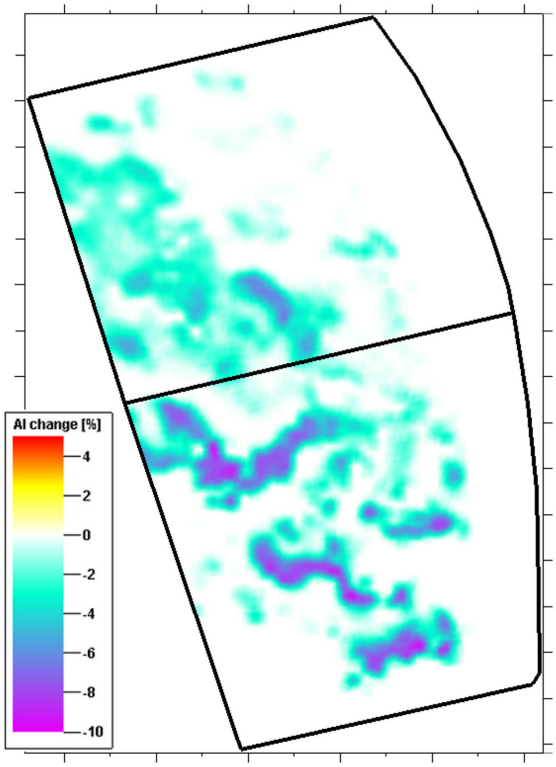

(b) Base Channel 1: impedance change

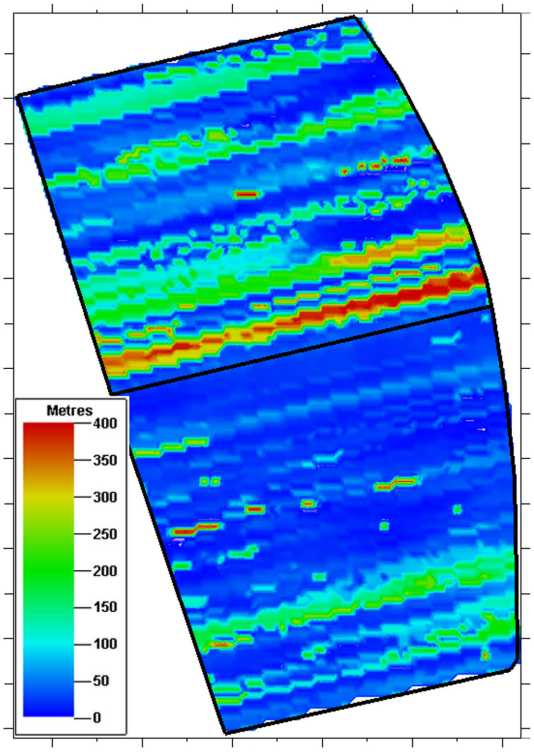

(c) $\Delta Source + \Delta Receiver$

Figure 5.15: (a) The TL -TL^* difference of RMS amplitudes extracted at Channel 2. (b) Acoustic impedance change extracted from the ray-tracing model at the base of Channel 1. (c) $\Delta Source + \Delta Receiver$ measurement overlain on Channel 2. The mean $\Delta Source + \Delta Receiver$ of region A and B is 100m and 50m, respectively.

Read SEGY data

⇓

CMP re-binning to 25m x 25m

⇓

Assign geometry

⇓

4D trace selection

⇓

pre-stack Kirchhoff time migration

⇓

CMP stack to full offset

⇓

SEGY output

Table 5.3: Re-processing sequence using a full Kirchhoff pre-stack time migration approach.

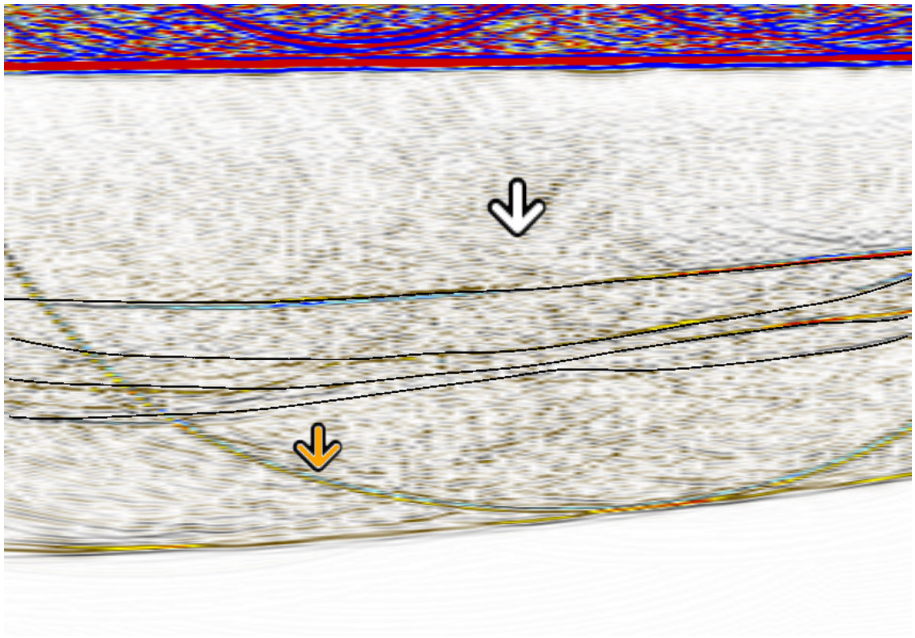

Figure 5.16: Cross-section through the pre-stack Kirchhoff time migrated seismic data. The top and base of Channels 1 and 2 are marked with black lines. The white arrow marks a zone of increased noise, whereas the orange arrow marks strong migration artefacts.

areas where the impedance changes but no residual amplitude is observed. Some prominent migration artefacts are still present in the data (Figure 5.17(a), orange arrow). The absolute maximum residual amplitude is 0.26, whereas the standard deviation of the map is 0.05.

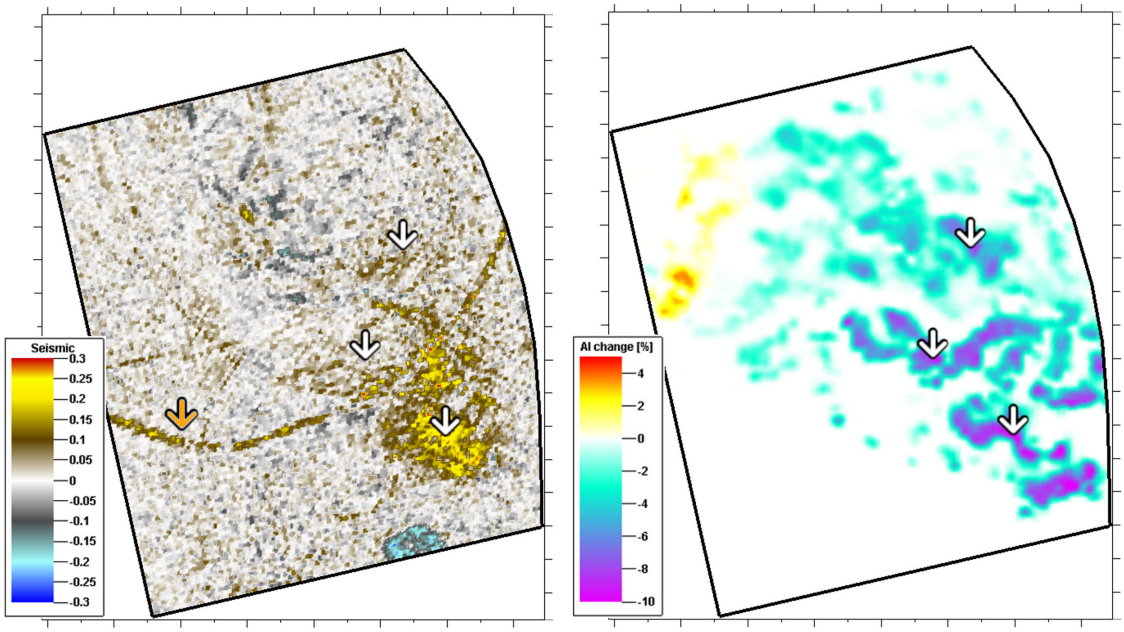

(a) Base Channel 1: TL -TL^* (b) Base Channel 1: impedance change

Figure 5.17: (a) The TL -TL^* difference of the RMS amplitudes extracted from the PSTM seismic data at the base of Channel 1. (b) Acoustic impedance change along the base horizon of Channel 1 caused by the reservoir production. The white arrows show matching areas between amplitude change and production-induced impedance change. The orange arrow marks a strong migration artefact.

This good match between the expected and the observed amplitude changes at the base of Channel 1 assures that the data quality is suitable to further interpret the residual amplitudes at the top and base of Channel 2. Therefore, the RMS amplitudes are extracted in a 20ms window centred around the respective horizon. Consequently, the TL -TL^* differences are calculated for the top and base of Channel 2 (Figure 5.18(a) and 5.18(c)). The residual amplitudes along the top of Channel 2 show two distinct areas of decreased amplitude marked with arrows. These areas correlate with the impedance change and thus with the amplitude changes at the base of Channel 1 (Figure 5.18(b) and 5.18(d)). However, these residual amplitude imprints differ slightly in their spatial position when extracted at the top or the base of Channel 2. Moreover, the amplitude imprint decreases slightly in magnitude at

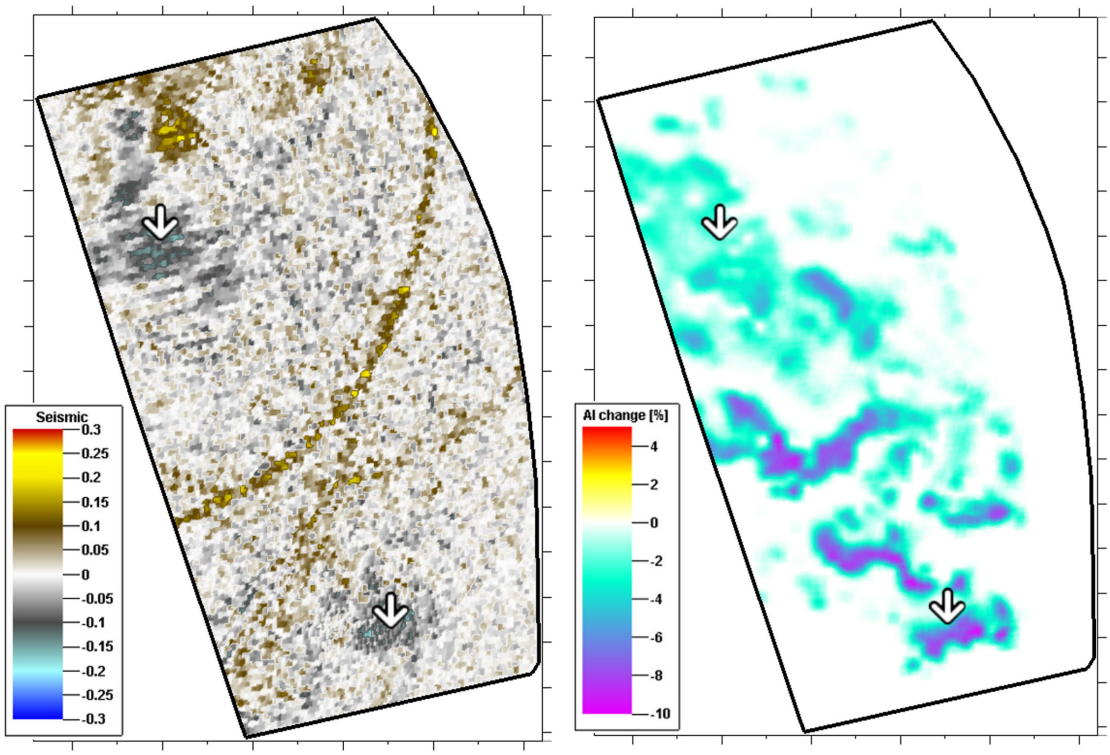

(a) Top Channel 2: TL -TL^*

(b) Base Channel 1: impedance change

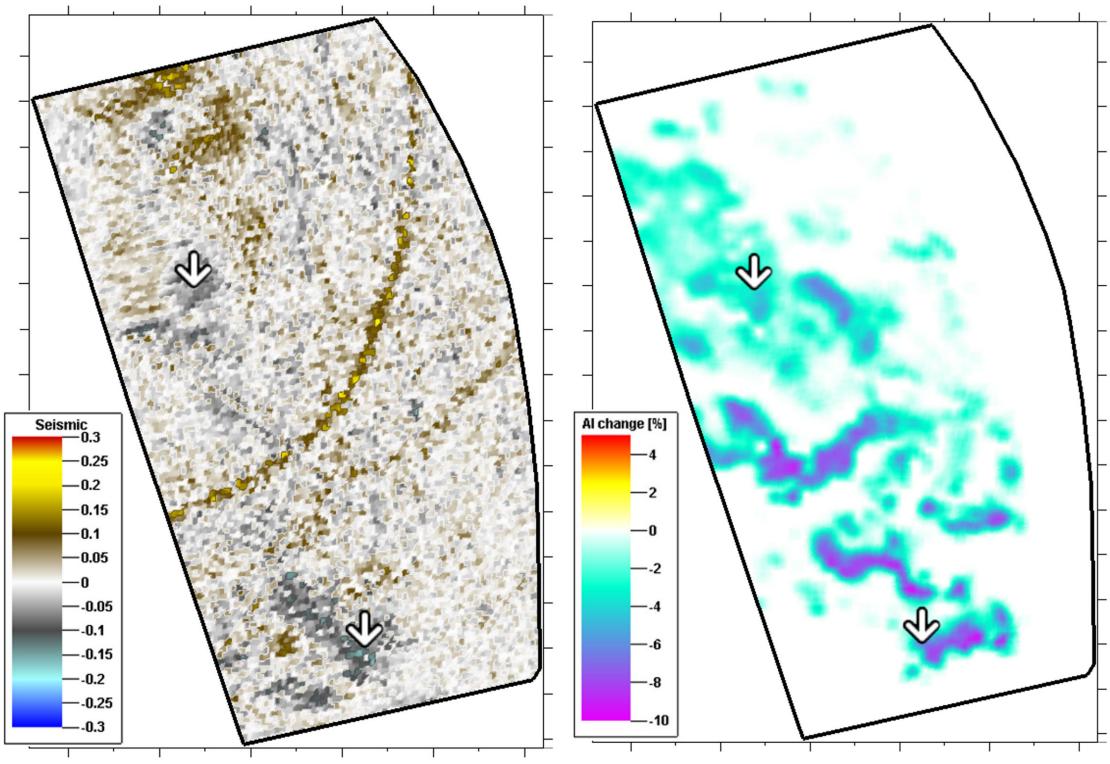

(c) Base Channel 2: TL -TL^*

(d) Base Channel 1: impedance change

Figure 5.18: (a) The TL -TL^* difference of the RMS amplitudes extracted from the PSTM seismic data at the base of Channel 1. (b) Acoustic impedance change along the base horizon of Channel 1 caused by the reservoir production. The white arrows show matching areas between amplitude change and production-induced impedance change.

the base of Channel 2, compared to the imprint at the top of the channel. The absolute maximum of the residual amplitude is 0.11 and 0.10 for the top and the base of Channel 2, respectively. The standard deviation is 0.040 and 0.039 for the top and the base, respectively. The spatial positions of both imprints at the top and base of Channel 2 correlate well with the x- and y-location of the strong residual amplitude observed at the base of Channel 1. However, the residual amplitudes show a substantial amount of noise as well as migration artefacts.
The previous observations are focused on amplitude changes caused by production and leave aside the effects caused by acquisition non-repeatability. As outlined earlier, all acquisition related effects are suppressed by taking the TL - TL^* difference, which is further proven by the amplitude study at Channel 2. No correlation is found between the residual amplitudes at top and base of Channel 2 and the $\Delta Source + \Delta Receiver$ measurement (Figure 5.10). Hence, the production in Channel 1, whether included in the migration velocity model or not, does not significantly change the acquisition footprint and indeed the footprint cancels out in the TL - TL^* difference data.

Finally, it is tested whether the choice of the migration velocity alters the amplitude response at Channels 1 or 2. Therefore, RMS amplitudes are extracted from the ***Monitor****(Base velocity)* and ***Monitor****(Monitor velocity)* data which are migrated with the baseline and monitor velocity, respectively (compare Figure 5.12). The residual amplitude imprint at Channel 1 and Channel 2 caused by using the baseline velocity instead of the accurate monitor velocity is shown in Figure 5.19 and 5.20, respectively. The residual amplitude error is confined to a distinct zone at the base of Channel 1, which matches well with the impedance change inside Channel 1 (Figure 5.19, red polygon). However, this time the impedance change is calculated by taking the RMS of the change between the top and base of Channel 1, then multiplying by a factor of -1. This volume attribute is used because the wave propagation is affected everywhere inside Channel 1 and not only at the top and base horizon. The maximum absolute amplitude error is 0.11 and the standard deviation is 0.011. Noise is still present in the data; however, no severe migration artefacts are observed. Moreover, the residual amplitudes outside the red polygon are close to zero, which indicates the excellent repeatability of the migration process if the same velocity is

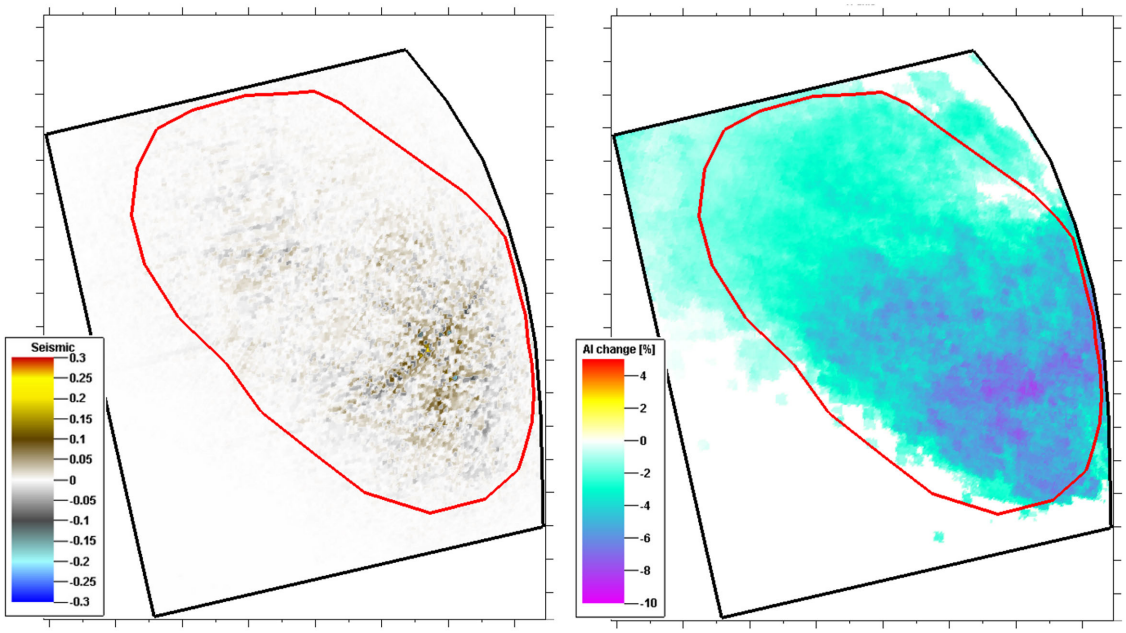

(a) Base Channel 1 (b) Channel 1: impedance change

Figure 5.19: (a) Residual amplitude caused by the choice of the migration velocity model for imaging the monitor data. (b) RMS impedance change between top and base of Channel 1 multiplied by -1.

used (the velocities outside the channel are the same for the baseline and monitor model).

The absolute maximum of the amplitude imprint at the top of Channel 2 (Figure 5.20(a)) decreases to 0.05. The red line defines the same area as for Channel 1 and the RMS impedance change inside Channel 1 is overlain on Channel 2 (Figure 5.20(c)). These residual amplitudes are further dimmed at the base of Channel 2 (Figure 5.20(b)), so that the maximum absolute amplitude error reduces to 0.02 and migration artefacts now become dominant (Figure 5.20(b), orange arrow). The standard deviation of the amplitude error at the top and base of Channel 2 is 0.009. Moreover, the residual amplitudes at the top and base of Channel 2 are quite noisy and vary around a mean value of zero. Therefore, no clear statement can be made as to whether using the monitor migration velocity increases or decreases the amplitudes at these horizons. On the other hand, the residual amplitudes at the base of Channel 1 are positive in the area of the largest amplitude error. This leads to the conclusion that the RMS amplitude at the base of Channel 1 is larger in the ***Monitor****(Monitor velocity)* seismic data than in the ***Monitor****(Base velocity)* data,

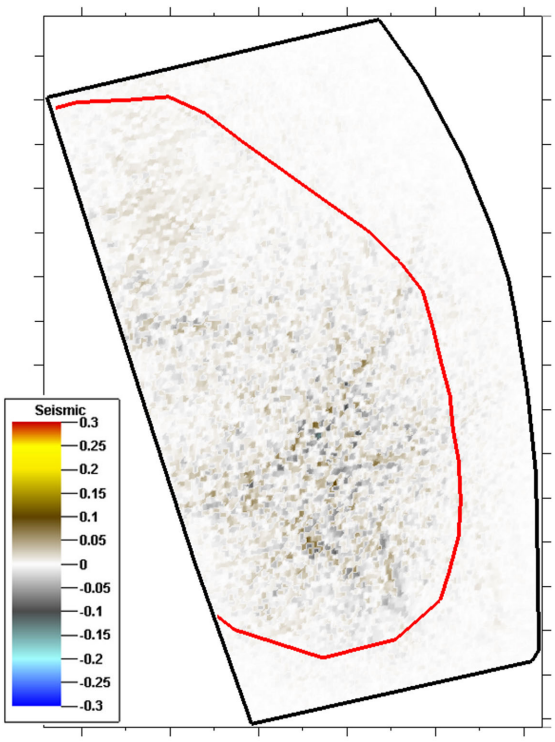

(a) Top Channel 2

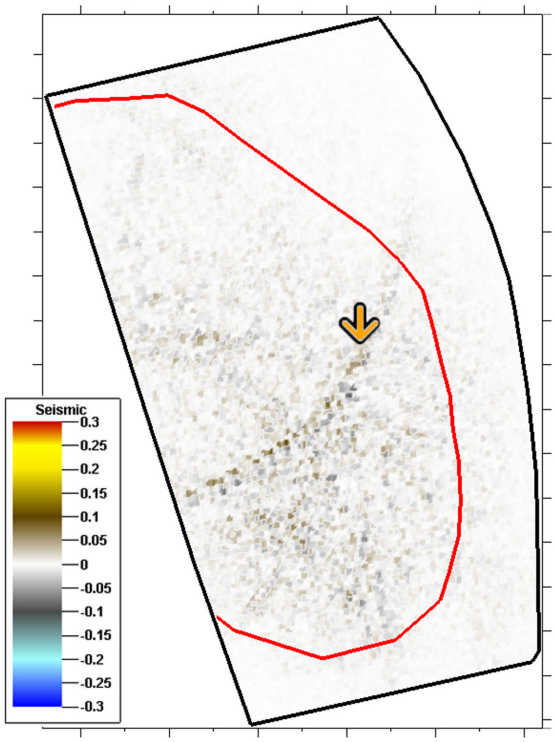

(b) Base Channel 2

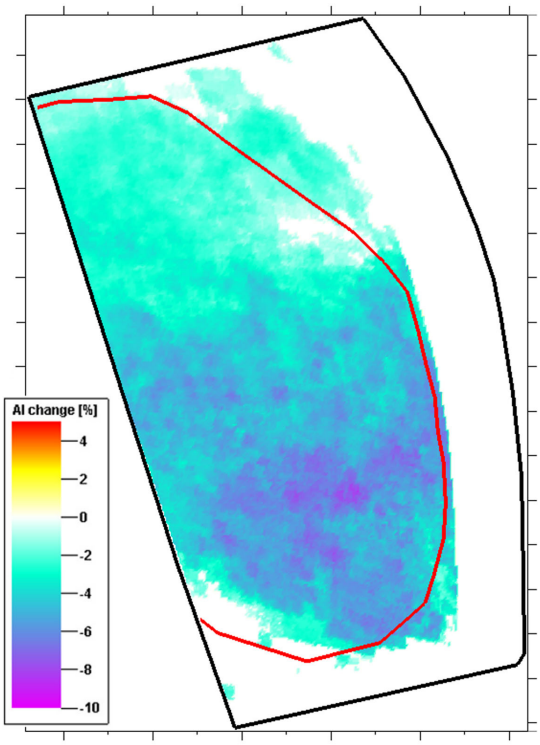

(c) Channel 1: impedance change

Figure 5.20: Residual amplitudes at the top (a) and base (b) of Channel 2, caused by the choice of the migration velocity model. (c) RMS impedance change between the top and base of Channel 1 multiplied by -1 and overlain on Channel 2. The orange arrow marks migration artefacts.

which is probably due to a better focusing of the energy when the velocity changes inside Channel 1 are included in the migration velocity. Further discussion on the overall data quality and the seismic modelling is provided in the following section.

5.6 Discussion

The presentation of the various residual amplitude maps in the previous section provides a good overview of the magnitude of the stacked reservoir effects. The residual amplitudes, although noisy and certainly not of the best quality, are consistent throughout the interpretation, when using the Kirchhoff pre-stack time migrated data. The migration artefacts do not randomly change in-between different maps, which provides confidence to quantitatively compare the observed errors to each other and rank the impact of each effect (Figure 5.21).

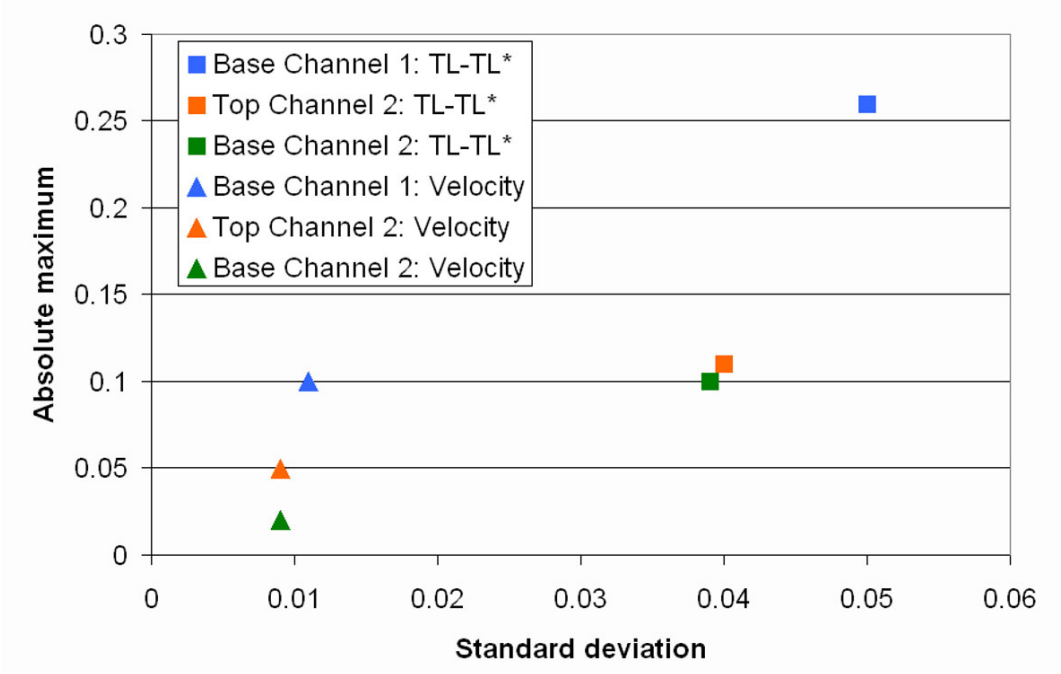

Figure 5.21: Amplitude errors which are caused by production in stacked reservoirs are extracted at the top and base of channels 1 and 2. The maximum amplitude error of each map is plotted against the standard deviation. Squares indicates the amplitude error caused by the production in Channel 1, whereas triangles indicate the amplitude error caused by using the incorrect migration velocity for the monitor data.

The production-induced time-lapse amplitude changes extracted at the base horizon of Channel 1 are the largest in this study. Therefore, this time-lapse signal is used as a reference to compare with the residual amplitude errors. The maximum magnitude of the amplitude imprint at the top and base of Channel 2 is 42% and 38% of the time-lapse amplitude change at Channel 1, respectively (Figure 5.21, orange and green rectangle). Moreover, the residual amplitudes at Channel 2 exhibit a much higher noise content, evident from the high standard deviation of 0.04 in comparison to the maximum error of 0.10. However, both of these amplitude imprints are clearly above the noise level. The amplitude error which is caused by migrating the monitor seismic data with the baseline velocity is most prominent at the base of Channel 1. There the maximum absolute error is 0.10, which is 38% of the maximum time-lapse signal (Figure 5.21, blue triangle). This amplitude effect is well above the standard deviation of the respective amplitude map (Figure 5.17(a)) and thus considered a genuine signal. Hence, it is concluded that the amplitude error caused by using the baseline migration velocity model significantly reduces the quantitative interpretation at the base of Channel 1. It is advisable to use an updated velocity model to migrate the monitor data, however, it remains questionable if the production-induced changes can be resolved by current velocity modelling techniques.

On the other hand, the maximum RMS amplitude errors at the top and base of Channel 2, caused by using the baseline migration velocity, are significantly less: 0.05 and 0.02, respectively. Furthermore, the interpretation of these amplitude errors is probably biased by the high noise content in the data. Unfortunately, the production-induced amplitude change at the top and base of Channel 2 are not discussed due to their very limited effect. The impedance change at the top and base of this channel barely exceeds -2% and is also confined to a small area. For comparison, the largest impedance change at the base of Channel 1 is -12%, which induces a maximum absolute amplitude change of 0.26. Hence, a maximum absolute RMS amplitude change in the range of 0.04 is expected for changes at the top and the base of Channel 2. In this context, the fractional amplitude errors at the top and base of Channel 2, caused by the wrong migration velocity model, amount to 125% and 50% of the expected time-lapse signal at Channel 2, although

with narrow spatial extend (compare Figure 5.18). These large fractional errors are due to the weak reflection strength at the top and base of Channel 2. Therefore, quantitative interpretation of time-lapse changes at Channel 2 should be done with care. Extracted attribute maps should be compared to extracted attributes at Channel 1 in order to identify areas where changes inside Channel 1 imprint on Channel 2. In addition, it is found that the residual amplitudes do not show any sign of a strong acquisition footprint and it is concluded that the acquisition non-repeatability has no effect on the residual amplitudes caused either by the shadowing effect due to production inside Channel 1 or by the use of the incorrect baseline migration velocity model.

Similar amplitude dimming is observed at the Foinaven field, West of Shetland (Al-Maskeri, 2005), which consists of stacked turbidite channels. Therefore a wedge model is set up where gas saturated sands overlie oil saturated rocks. The author consequently demonstrates that the observed dimming is caused by interference effects when the vertical distance of the lower channel to the upper channel is less then 15m. The application of a high-cut frequency filter to the individual seismic vintages drastically decreases the dimming effect. However, this approach is not appropriate for the current West of Africa study, as the minimum vertical distance between the base of Channel 1 and the top of Channel 2 is 50m and the maximum distance is 160m. Hence, interference effects are not considered to cause the observed residual amplitudes. In addition, the dominant frequency of the high resolution baseline and monitor survey in this West of Africa example is considerably higher than the dominant frequency of the Foinaven data (45Hz versus 30Hz). This further increases the vertical resolution and reducing a possible interference effect between stacked reservoir channels.

It turns out that the high level of migration noise and the non-continuous reflection events cause the most uncertainty in this interpretation. The following section shows that even synthetic data are not straightforward to process and interpret. Using the DMO plus post-stack extended Stolt migration has a severe effect on the data, which results in non-focused reflection events. There is not a clear answer yet as to why this happens. This migration scheme should be a good approximation for

the PSTM, at least in the constant velocity case. However, the dipping horizons of Channels 1 and 2 (approximately 13 °), the spatially as well as vertically varying velocity and an insufficiently tuned stretch factor for the extended Stolt migration might have a combined negative impact on the migration result. It is not possible to test if further changes in the parameters would improve the migration when using the DMO/Stolt approach.

On the other hand, the Kirchhoff pre-stack time migration naturally handles steep dips and focuses the reflection energy well, even in case of the velocity model being not exact (Bancroft, 2007). Nevertheless, the reflection events from the top and base of Channel 1 and Channel 2 are still not continuous throughout the stacked seismic cube (Figure 5.16). Strong migration noise from the base reflector sweeps upwards and contaminates the seismic data at earlier times. Hence, several possible causes are discussed in turn.

The migration noise might be caused by the coarse bin grid (25m x 25m) used in the PSTM. In addition, the data is binned in 100m offset classes for the PSTM versus 50m offset classes for the DMO/Stolt approach. However, reducing the grid size to 12.5m x 6.25m, the grid that is used for the DMO plus Stolt migration, would increase the processing time of the PSTM to five days for a single data set and thus is not done due to time restrictions. Computing times are based on eight CPUs (2.5GHz) with a shared RAM of 64GB.

Moreover, the PSTM uses a migration velocity field that only varies vertically but is constant laterally across the migration aperture. On the other hand, the production induced velocity changes inside the channels considerably vary in the lateral direction within the migration aperture. This violates the PSTM assumption of a laterally constant velocity field and might thus contribute to the migration noise. Employing a pre-stack depth migration algorithm would overcome this problem by taking into account the vertical as well as lateral variations in the velocity field. It is assumed that this also reduces the migration noise. However, when using such an advanced imaging algorithm, it is advisable to employ full wavefield forward modelling techniques in order to eliminate the smoothness constrains of the ray-tracing modelling, too. Furthermore, it is assumed that the migration noise as seen in the

current data is not caused by a rugose channel surface. All surfaces are smoothed before being input into the ray-tracing model. Seismic data quality issues, caused by rough and unsmoothed surfaces, are mainly identified by large and unreasonable amplitude variations in the common shot gathers, but not by missing reflection events which are discussed in the remainder of this section.

Another explanation for the lack of continuous reflection events is the lack of impedance contrast across the interface in the ray-tracing model, which might be a systematic error during the model building stage. Figure 5.9 shows that the top and base horizon of each channel is used to enclose the velocity and density changes inside the channel. The change in elastic parameters inside the channel affects the wave propagation; however, the ray-tracing algorithm only calculates reflection events at the top and base channel interfaces. Therefore, only the impedance difference across these interfaces causes a reflection event that is recorded in the synthetic seismic data. The grey areas in Figure 5.9 which make up the non-reservoir rock between the top and base of Channel 1 are thus inspected more closely. The velocity and density of these areas is similar to the rock properties outside Channel 1 and thus have only a small impedance contrast, which might lead to the break up of the continuous reflection event in some areas. However, a simple calculation does not reveal any large area of low impedance contrast across the base of Channel 1.

The last possibility is that the ray-tracing itself is erroneous and reflection events are not traced in some parts of the model. Figure 5.22(a) shows five pre-stack shot gathers. The reflection events from both channels are clearly visible in most of these gathers. The red arrow indicates a small area where reflection events from Channels 1 and 2 are missing. A small number of these ”holes” in the pre-stack data do not cause major problems during migration. However, a closer look at shot gathers recorded in the area of high noise and non-continuous reflection events (Figure 5.16) reveals that only the sea floor reflection event is recorded in many shot gathers. Reflection events from the tops and bases of Channels 1 and 2 as well as the base interface of the ray-tracing model are absent (Figure 5.22(b), red arrow).

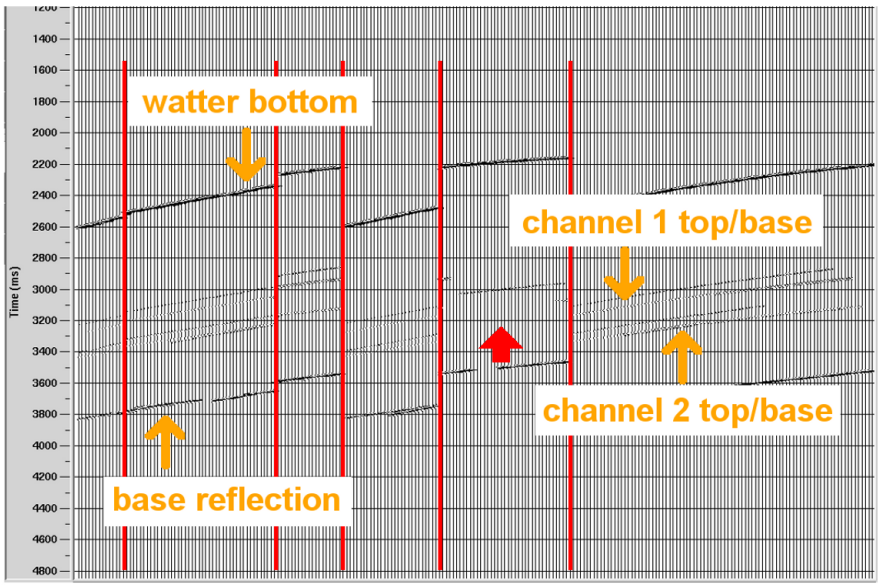

(a) Common shot gathers

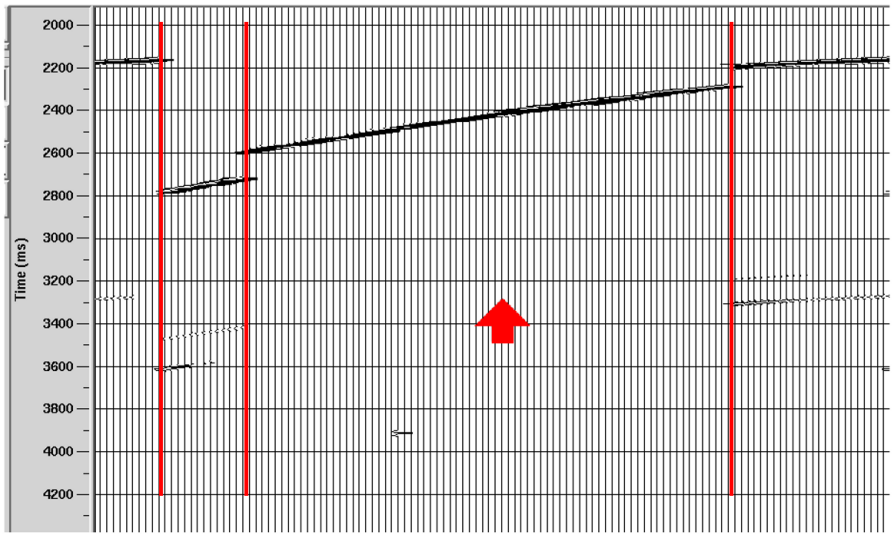

(b) Common shot gathers

Figure 5.22: (a) Pre-stack common shot gathers showing the reflection events from the water bottom, Channels 1 and 2 as well as the base horizon of the model. Red lines separate individual gathers. The red arrow indicates a small area of missing reflections events. (b) Pre-stack common shot gathers where multiple reflection events are missing (red arrow). Red lines again separate individual gathers. Trace numbers vary across the gathers due to the time-lapse binning applied to the data.

This observation indicates that the ray-tracing itself causes the break up of reflection events in the pre-stack data. In turn, these data gaps most probably cause the strong migration artefacts in the post-stack data.

Moreover, these missing reflection events are possibly the explanation as to why the DMO plus Stolt migration approach fails. After Bancroft (2007), the DMO kinematic operator has just a small spatial extent over which data is actually added and moved (Figure 5.23). This summation process might break down if the narrow operator is not equally populated with seismic reflection energy when successively moving through the data. Severe artefacts after DMO are thus believed to cause further problems during the post-stack Stolt migration. On the other hand, the

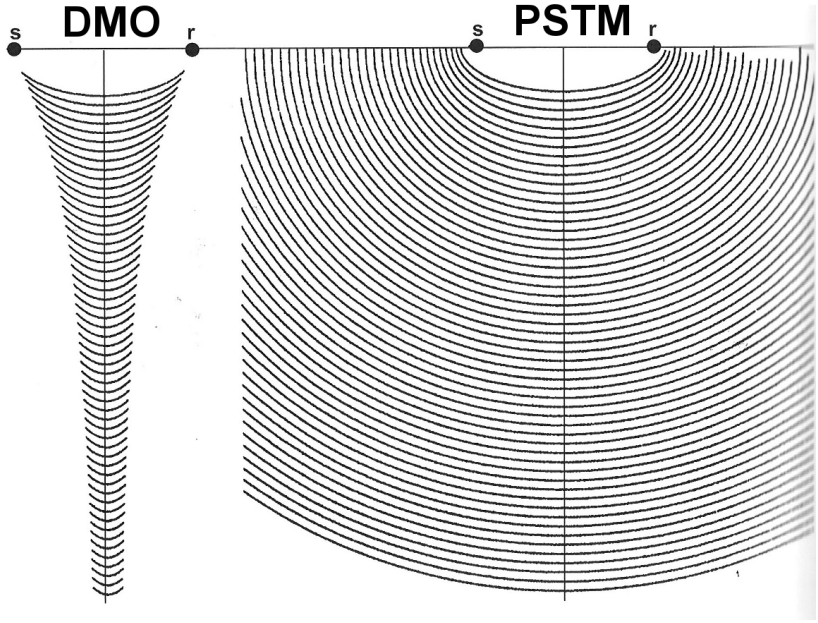

Figure 5.23: Comparison of DMO and PSTM kinematic operators. Source and receiver positions are denoted by s and r, respectively (modified from Bancroft (2007)).

PSTM kinematic operator extends over a larger area, and therefore is less sensitive to missing seismic energy, if the data gaps are not too large. The PSTM is thus able to smooth out small-scale errors caused by missing data. It is concluded that the seismic modelling does not perform well in certain areas and improving the pre-stack data quality requires rebuilding the ray-tracing model. Rerunning the model is not an appropriate option as the same errors are reproduced.

It is thus outlined how the increased knowledge about the current limitations and errors of these data could be used to modify the model in a way that the pre-stack seismic data quality improves.

The first improvement would be to set up the largest of the multi-cycle, intra-reservoir channels inside Channel 1 (compare Figure 5.8) separately. It is previously argued that doing so is very time-consuming, however, the quality control of the parameters inside the ray-tracing model becomes much easier. Furthermore, velocity and density parameters that vary only laterally to the channel axis, but are constant vertically to the axis should be assigned to each of these intra-reservoir channels. Therefore, a well defined impedance contrast is set up for each unit, which is also more convenient to QC in a map view at later stage. Moreover, there is greater control over the elastic properties when assigned to each intra-reservoir channel separately, instead of assigning one property field in-between the top and base of Channel 1. Vertically varying elastic parameters are only used for the background model, if necessary. However, the downside is that not only the model building takes considerably longer, but also interpreting changes at each of these intra-reservoir channels is a time intensive task, as many small surfaces have to be picked, attributes generated and subsequently interpreted.

Furthermore, Channel 2 should be radically altered that it is replaced by a plane with approximately the same dip as the channel (13°). A large impedance contrast across this plane, which is constant in the baseline and the monitor model, ensures that observed changes are not influenced by any changes at the plane itself. Moreover, the large impedance contrast ensures that this ”reference” horizon is clearly imaged in the data and easy to pick. Deviations from its planar shape would assist in the identification of time shift effects caused by the production-induced changes in Channel 1 above.
Simplifying the ray-tracing model, thus breaking down volumes with highly variable parameters into smaller volumes with possibly constant parameters is a lot of work in the first instance, but will prove helpful to ensure good pre-stack data quality.

In addition to the changes of the subsurface model, input parameters of the NORSAR3D^{TM} software package that control the computation of the wave front

inside the model should be adjusted as well. For example, the ”two way shot similarity” is an option that improves the runtime of the calculations considerably by a factor of five to ten. The concept is that two closely separated shots are traced through the model and in turn the information about these two calculated wave fronts is used to construct the wave fronts of intermediate shots in a fraction of time. This is a well tested feature with very accurate results. However, if one of these two initially traced shots has an error, it affects the intermediate shots as well. In the unlikely event that both initial shots are severely damaged, a poor result can be expected for the shots subsequently traced in-between. Therefore, this option should be used with care, however, it might be a necessity if tens of thousands of shots are traced through the model.

Finally, the seismic processing applied to the data turned out to be critical as well. It is still believed that a DMO followed by post-stack migration is suited for the data processing workflow. However, the pre-stack data quality has to be good enough to ensure numerical stability. Test runs are probably still necessary in order to find the most suitable set of parameters to use, but require more time to be spent on evaluating input parameters than interpreting the data. In summary, it can be said that even synthetic seismic data, which are well controlled, need a considerable investment of time until they can be used for time-lapse studies. Three-dimensional seismic modelling is an absolute necessity for such studies in order to accurately capture the non-repeatability problem in the time-lapse seismic data. Furthermore, it is concluded that investigating complex geological settings like in the West of Africa study requires the use of full wave equation seismic modelling techniques to overcome the smoothness constrains of the ray-tracing approach. The use of finite-difference seismic modelling workflows would be well suited to capture the important small scale effects in cellular models like the one used for the West of Africa study. The accuracy of ray-tracing methods and pre-stack time migration imaging is clearly limited in this case.

5.7 Summary

The time-lapse amplitude effects of two stacked reservoir channels are studied in this chapter. Therefore, synthetic seismic data are generated using a ray-tracing model which is assembled from realistic input data. Initial interpretation of the data is inconclusive. However, the data quality improves after reprocessing the shot gathers with a full Kirchhoff pre-stack time migration algorithm. The imprint of production-induced amplitude changes on the deeper reservoir turns out to be the major cause for amplitude distortions. This imprint diminishes with increasing separation from the overburden channel. The amplitude error caused by using the baseline velocity to migrate the monitor seismic data is observable and significant. Overall, the interpretation results are consistent throughout, but suffer from a high noise content due to migration artefacts and thus poor pre-stack data quality. Therefore, a key rule is that a three-dimensional ray-tracing model used in such studies should be as simple as possible, in order to retain greater control over its input parameters. However, the latter constraints for this ray-tracing based modelling approach are a clear limitation when a complex geology is modelled. In case of the presented West of Africa stacked reservoir study, the use of three-dimensional finite-difference seismic modelling is strongly advised, in order to fully capture the time-lapse seismic changes of the structurally complex reservoir channels.

Chapter 6

Ekofisk field - Overburden velocity changes over a compacting reservoir

This chapter evaluates time-lapse amplitude errors for the case of a geomechanically active reservoir. The compaction of the reservoir and thus the elongation of the overburden rock are first modelled using a three-dimensional geomechanical simulation model. Subsequently, ray-tracing models are assembled from which synthetic pre-stack baseline and monitor seismic data are generated. The pre-stack seismic shot gathers are in turn processed to limited offset stacked cubes. Further amplitude analysis of these post-stack seismic data sets investigates the amplitude effects when using the baseline velocity model to migrate the monitor seismic data, instead of the correct monitor velocities. These amplitude errors are compared for different limited offset stacks and the time-lapse amplitude error caused by a non-repeated monitor acquisition geometry.

6.1 Ekofisk field description

The aim of the study is to investigate time-lapse amplitude errors over a compacting reservoir. The Ekofisk field is chosen due to its extensive compaction caused by reservoir production. The field is an elongated anticline structure of high porosity chalk located in the central graben in the southern part of the Norwegian sector of the North Sea (Figure 6.1). It was discovered in 1969 and initial test production

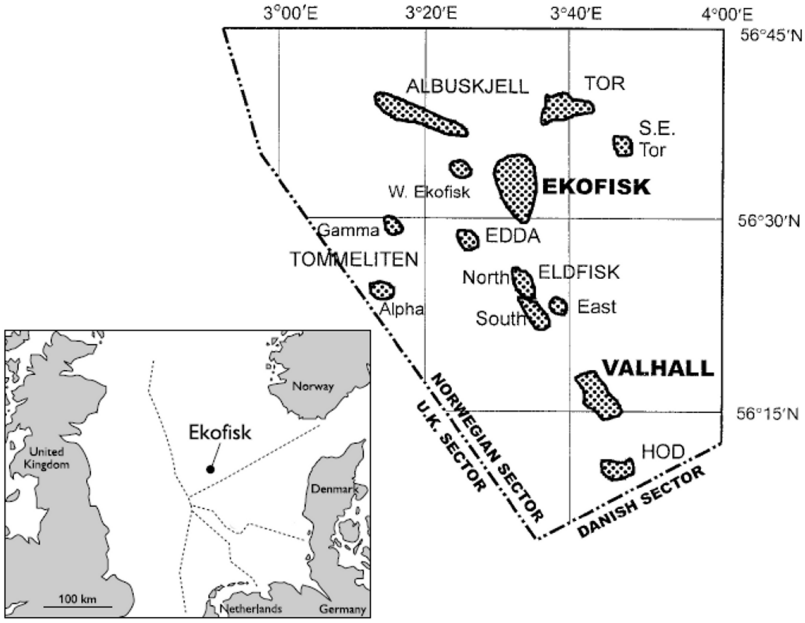

Figure 6.1: Location map of the Ekofisk chalk field (from Goulty (2003) and Japsen et al. (2004)).

started in 1971 (Hermansen et al., 1997). The reservoir is produced from two chalk layers, the Ekofisk Formation and the Tor Formation, which are overlain by sediments of mainly shales and clay. The Ekofisk Formation is of Danian Age and at a depth of 2840m at the crest, with thickness varying between 100m to 150m, and a porosity of up to 48%. The Tor Formation is of Maastrichtian Age and consists of high porosity chalk with porosities ranging from less than 30% to 40%. The Tor Formation varies in thickness between 80m and 150m (Hermansen et al., 1997; Sulak and Danielsen, 1989). Both reservoir zones are separated by a thin (less than 15m) low porosity zone, called tight zone (Figure 6.2). The initial oil production drive of the overpressured reservoir was by pressure depletion which resulted in the increase of effective stress in the reservoir and thus compaction due to pore col-

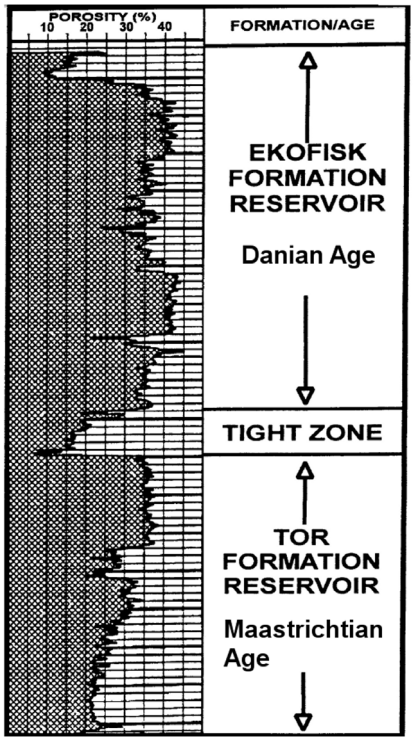

Figure 6.2: Typical lithologic column showing the two reservoir formations as well as the non-reservoir tight zone of the Ekofisk field. (modified from Rhett (1998)).

lapse (Chin and Nagel, 2004). The reservoir pressure drops from an initial value of 7120psi (49MPa) to below 3500psi (24MPa) in large parts of the field. This pressure decrease and the resulting compaction leads to a porosity loss of as much as 10% (Gauer et al., 2002). Hence, a field wide water flood is first initiated in 1987 for the Tor Formation to counteract the compaction and to increase the oil recovery factor, as laboratory studies show a favourable water imbibition into the reservoir formation. Furthermore, water is injected into the Ekofisk Formation from 1990 onwards to not only increase the oil recovery rate, but also stabilise the reservoir pressure, thus preventing further compaction. However, the injected sea water weakens the chalk matrix and compaction continues despite the increase in pore pressure due to water injection (Rhett (1998) and Sylte et al. (1999)). Nevertheless, the subsidence rate stabilises at 10cm/year, significantly less than the initial rate of 40cm/year during the pressure depletion phase (Gauer et al., 2002). The observed total reservoir compaction, that is the compaction of the Ekofisk and the Tor layer as well as the tight zone, at the top of the Ekofisk Formation is up to 11 metres (Figure 6.3(a)) in the year 2000 (Chin and Nagel, 2004). This compaction propagates partially up

to the sea floor where a subsidence of a maximum of 8 metres is measured (Figure 6.3(b)). Consequently, the compaction of the reservoir, thus the subsidence of the

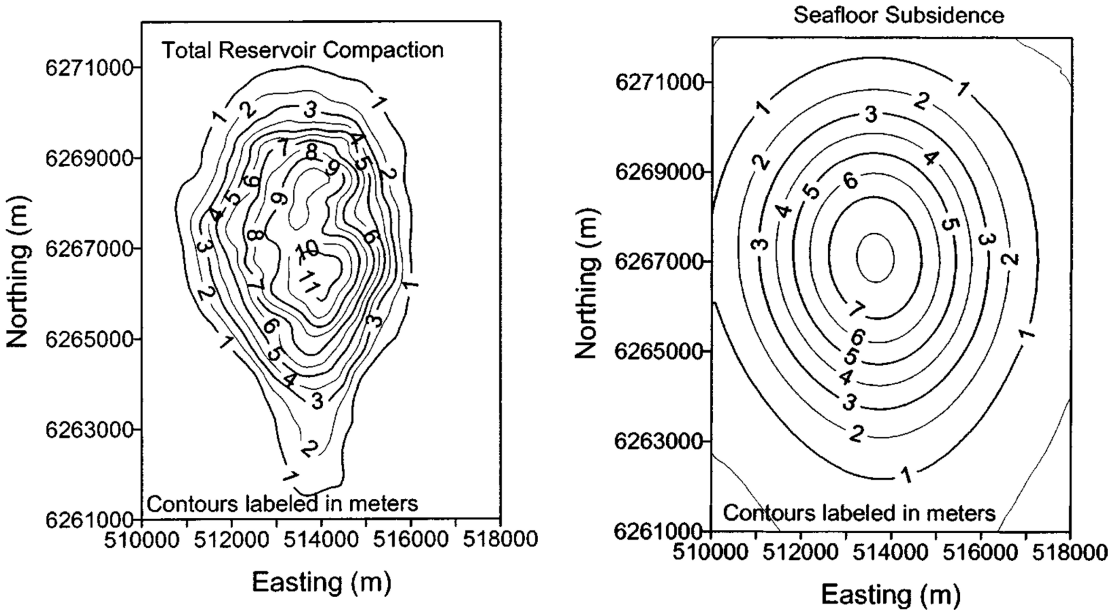

(a) Reservoir compaction

(b) sea floor subsidence

Figure 6.3: Cumulative compaction over the Ekofisk field in the year 2000: (a) contour map of the total reservoir compaction measured at the top of the Ekofisk Formation and (b) contour map of the sea floor subsidence (from Chin and Nagel (2004)).

seabed causes a variety of problems:

- Well failure and casing failure either inside the reservoir zone or in the overburden is first discovered in 1978 at the Ekofisk field (Yudovich et al., 1989) and since then intensively studied and documented (Anvik and Gibson, 1987).

- The sea floor subsidence induced by the reservoir compaction poses a severe threat to the production facilities as their minimum height above the sea level is significantly reduced. Therefore, the steel platform at the Ekofisk field needed to be jacked up in 1987 (Holhjem, 1998).

- Well log measurements change over time due to the compacting reservoir, for example, the depth to the formation top changes and the pore volume is not constant in time. Therefore, the well measurements need to be corrected for such dynamic effects in order to use the complete well database to build consistent geological models or estimate the original oil in place, even after

several years of production. Consequently, Gauer et al. (2002) introduce a well decompaction process and validate corrected well log data with, for example, time-lapse derived compaction maps.

These above mentioned problems are mainly related to the engineering and the geological interpretation domain. However, the reservoir compaction also causes severe errors in the seismic domain, for example, when seismic post-stack data are converted from time to depth. The volumetric strain changes inside the reservoir and the overburden subsequently alter the elastic parameters, such as the velocity. Guilbot and Smith (2002) report that the initial attempt to depth convert the first monitor survey shot over the Ekofisk field failed. The magnitude of the compaction derived from the depth converted seismic data is reported too large by a factor of two to four compared to the reservoir model, if only the time shifts at the top reservoir are used in combination with the baseline velocity model. Therefore, the authors conclude that the changes in the overburden velocity have to be considered, because much of the time shifts are indeed accumulated by a longer traveltime through the overburden layers and not due to the physical movement of the top reservoir horizon. They consequently set up a synthetic model to study the effect of velocity changes in the overburden on the depth conversion. Indeed, they find that a subtle overburden RMS velocity decrease from 1986m/s to 1984m/s, at the top reservoir positions the horizon at 2989m instead of 2992m. This is a marginal error for structural interpretation purposes, but these three metres of misplacement are a 75% error when estimating the correct compaction of four metres. However, Guilbot and Smith (2002) realise that such small velocity changes in the overburden cannot be updated using regular stacking velocity analysis. Consequently, they use well tops and general relationships between the thickness-, porosity- and thus velocity change derived at the well locations to update the depth conversion interval velocity model. Figure 6.4(a) displays the compaction derived from the time shifts at the top reservoir when only using the baseline velocity model. On the other hand, Figure 6.4(b) shows the correction term, and thus the apparent compaction, that is caused by the velocity slowdown and which needs to be subtracted from the compaction in Figure 6.4(a). However, this approach solely focuses on correctly positioning the post-stack reflection events in space, thus adjusting the vertical position of the

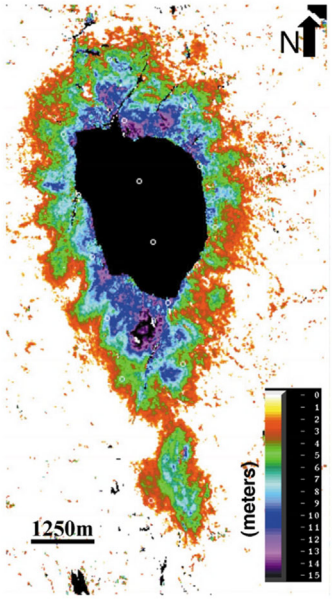

(a) Compaction estimate from time shift

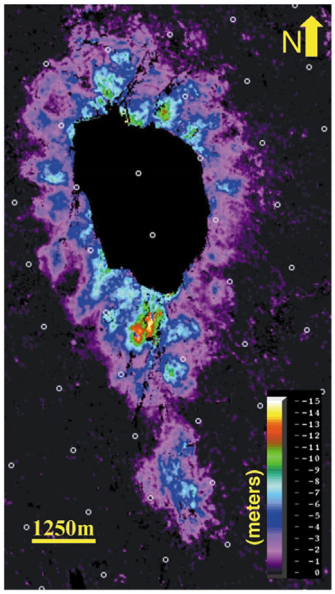

(b) Apparent compaction caused by velocity change

Figure 6.4: (a) The compaction derived from depth converted time-lapse seismic data is overestimated if the baseline velocity model is used. (b) The apparent compaction caused by velocity changes in the overburden needs to be considered during the depth conversion. The large hole in the middle of the field is caused by a gas cloud, thus there is no reliable seismic data (from Guilbot and Smith (2002)).

horizon in the repeat survey. There is no change to the seismic amplitude or phase information. Nevertheless, the study by Guilbot and Smith (2002) shows clearly that even small velocity changes have a significant impact on the interpretation of time-lapse attributes, in this case the estimate of reservoir compaction from time-lapse data.

Beyond this time-depth conversion problem, several authors believe that such subtle velocity changes in the overburden also affect the amplitude information of the repeat seismic data if not migrated with the correct velocity (compare Sections 1.4.5 and 1.7). Consequently, this chapter addresses the question to what extent the reservoir compaction induced overburden velocity change affects the time-lapse seismic amplitude attribute at the top reservoir. Seismic energy is added and moved spatially during the migration process, thus amplitude effects may contaminate the production-induced time-lapse signal if the baseline velocity model is used to migrate the monitor seismic data. This study thus looks at the dynamic time-lapse attributes beyond the static time-depth conversion problem.

In order to study the effect of overburden velocity changes on the time-lapse amplitude attribute, a three-dimensional geomechanical model is set up which is based on data from the Ekofisk field. The production-induced stress and strain change is thus modelled for the reservoir and overburden layers and is in turn used to alter the elastic parameters inside a ray-tracing model. Therefore, pre-stack shot gathers, modelled at two distinct times (baseline and monitor), adequately capture the three-dimensional overburden effects caused by the reservoir compaction. These pre-stack shot gathers are processed to limited offset stacks and time-lapse amplitude errors are discussed. Furthermore, the impact of source and receiver non-repeatability on the time-lapse amplitude attribute is investigated. The next section thus describes the geomechanical model in more detail.

6.2 The Ekofisk geomechanical model

Before describing the geomechanical model setup for this study, I would like to acknowledge the work of Alejandro Garcia, a PhD student with the ETLP group. He built, conditioned and ran the geomechanical model and without his expertise this study would not have been possible.

A geomechanical model is needed in order to adequately calculate the production-induced compaction in the reservoir as well as the resulting deformation of the overburden, which are in turn used to update the ray-tracing model (discussed in due course). The GEOSIM finite-element geomechanical simulator is used for this study, which runs in direct coupling with a reservoir simulator. Table 6.1 outlines the steps for this geomechanics part along with the input data needed. The geomechanical as well as the ray-tracing model are assembled from the same set of subsurface layers: five overburden, two reservoir and two underburden layers (Figure 6.5). The horizons which enclose these layers are extracted from the baseline seismic interpretation project and further smoothed before they are input to the geomechanical model. Subsequently, the grid for this subsurface model is defined. The lateral size of the cells is 200m x 200m and the vertical dimension is defined by the distance between the top and base horizon enclosing the respective layer. To

1. Set up layers in the geomechanical model and define the grid for the over-, under- and sideburden.
2. Populate the grid with static elastic moduli of the rock: Young's modulus (E) and Poisson's ratio (ν).
3. Set the initial state of stress in the geomechanical model.
4. Initialise the reservoir simulation model with well locations and production rates.
5. Start the reservoir simulation model and commit the pressure every 50 days to the geomechanical simulator (direct coupling).
6. Export the lateral and vertical displacements for every subsurface horizons after 20 years of simulation as xyz-ascii file.

Table 6.1: Sequence of steps needed to set up and run the geomechanical simulation model for the Ekofisk compaction study.

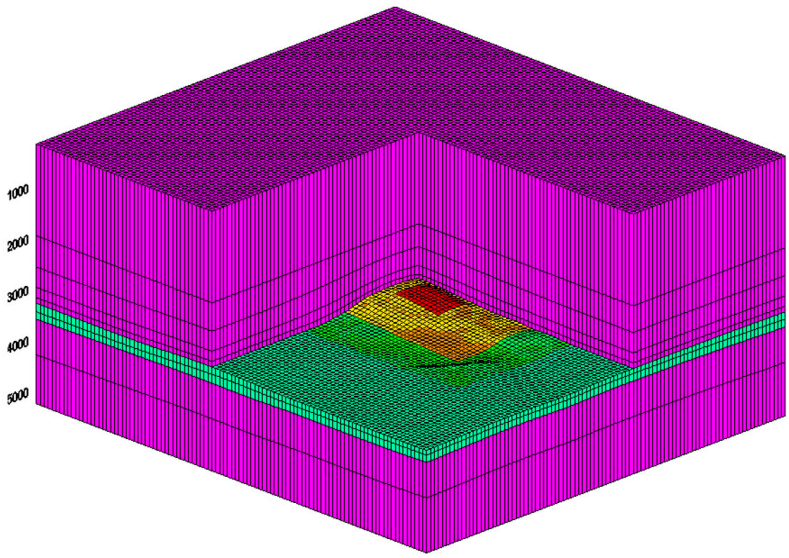

Figure 6.5: Overburden- and underburden- layers of the Ekofisk geomechanical model are pink, whereas the two reservoir layers are green. Red and orange zones indicate the varying porosity inside the reservoir.

populate this grid with the correct rock parameters (Young's modulus and Poisson's ratio) proved difficult during the model building stage. Ideally, the baseline geomechanical model, the initial model, should possess the same physical properties as the ray-tracing baseline model. However, the latter is conditioned using velocity and density as input parameters, whereas the geomechanical model is populated with the initial stress, Young's modulus and the Poisson's ratio. Hence, equations are needed to relate these parameters in order to achieve the correct physical behaviour for both models. Moreover, the static mechanical properties are needed for the geomechanical modelling. The dynamic mechanical properties, which are readily related to the P- and S-wave velocity cannot be used. Unfortunately, no single, exact relation between these parameters exists for North Sea shales. Indeed, there are many studies that measure static mechanical and acoustic properties on core samples, but the results vary considerably depending on the porosity, the temperature or the water content of the shale sample (Horsrud et al., 1998; Muniz et al., 2005; Holt et al., 1996; Manafov et al., 2007). Therefore, converting wireline log velocities into static mechanical properties yields different results depending on the publication used. Moreover, hardly any of the publications compare the measured velocity in the laboratory with the measured wireline log velocity at the location where the sample is extracted, thus being of limited use. Fortunately, Horsrud (2001) published a study on North Sea shales which uses a large data population covering a wide range of depths, porosities and clay mineral constituents. This study consequently provides empirical relations between measured wireline interval P-wave velocity, V_p, and the static Young's modulus as well as the Shear modulus, G (V_p in [m/s] and E, G in [GPa]):

$$E = 0.076 \cdot (V_P)^{3.23} \tag{6.1a}$$

$$G = 0.030 \cdot (V_P)^{3.30} \tag{6.1b}$$

The Poisson's ratio is easily derived from these static properties: $\nu = (E/2G) - 1$. Hence, it is possible to use velocity and density parameters extracted from one well log to condition the non-reservoir grid for the ray-tracing model and also derive the static mechanical shale properties to set up the geomechanical model, thus estab-

lishing a dependency between these two models. The constant static moduli which are assigned to each of the non-reservoir layers in the baseline (pre-production) geomechanical model are summarised in Table 6.2.

Model layer	E [GPa]	G [GPa]	ν	V_p [m/s]
Overburden 1	0.78	0.33	0.20	2060
Overburden 2	0.80	0.33	0.20	2070
Overburden 3	0.71	0.30	0.21	2000
Overburden 4	0.82	0.34	0.20	2090
Overburden 5	0.86	0.36	0.20	2120
Reservoir Ekofisk Fm.	0.45 - 3.35	0.19 - 1.64	0.02 - 0.20	2400
Reservoir Tor Fm.	0.78 - 7.34	0.31 - 3.56	0.03 - 0.25	2500
Underburden 1	1.56	0.66	0.19	2550
Underburden 2	1.88	0.80	0.18	2700

Table 6.2: Summary of mechanical and elastic property values used in the geomechanical and ray-tracing baseline model. V_p is extracted from one well log; the mechanical parameters for the over- and underburden are calculated with Equations 6.1a and 6.1b. The mechanical parameters for the reservoir chalk are derived by the empirical relation Equation 6.2.

As with the shale properties, assigning mechanical parameters to the reservoir chalk is not straightforward. The major concern for the rock parameters of the chalk is that the magnitude of reservoir compaction using these parameters should be comparable to the observed compaction at the Ekofisk field. Hence, the Young's modulus for the reservoir chalk is calculated from the initial reservoir porosity, ϕ, using an overall trend valid for North Sea chalk (Fjær et al., 2008):

$$E = 22.5\, e^{-11.2\,\phi} \tag{6.2}$$

The Poisson's ratio of the chalk is also guided by the porosity and taken from Fabricius et al. (2007) by means of a linear interpolation of their measurements for the Ekofisk and Tor Formation, described for the nearby South Arne chalk field.

This field is approximately at the same depth and has a very similar porosity range as the Ekofisk field, thus justifying the use of these parameters. The static mechanical parameters for the reservoir chalk are also included in Table 6.2. The mechanical parameters of the reservoir thus vary spatially with the reservoir porosity, which is upscaled into four discrete zones from the reservoir simulation model (Figure 6.6). The initial stress in the geomechanical model increases with depth and is determined from a general trend valid for the North Sea.

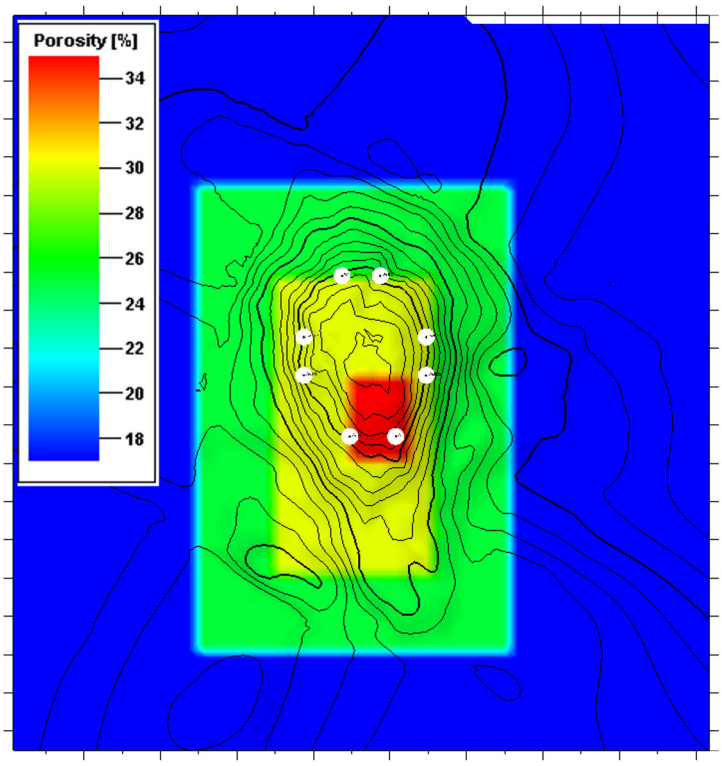

Figure 6.6: Porosity distribution of the generic geomechanical model. The distribution is a very simplified and upscaled representation of the Ekofisk Field porosities. Interpreted seismic horizons from the Ekofisk Field are input into the geomechanical model. The black contour lines indicate the subsea depth of the top reservoir horizon and increment by 20m. White circles mark the well locations in the reservoir simulation model.

In addition to the geomechanical model, the reservoir simulation model needs to be set up as well. The locations of the horizontal wells are marked with white circles in Figure 6.6, however, for the sake of clarity their well paths in the reservoir are not plotted. The simulated production is by pressure depletion only and the flow rates are adjusted to match the cumulative production of the Ekofisk field.

Moreover, the reservoir- and the geomechanical simulator are directly coupled. The change in reservoir pressure is passed to the geomechanical simulator every 50 days, which then triggers an update of the state of stress in the geomechanical model. The lateral and vertical displacements of the top Ekofisk layer after 20 years of production are shown in Figure 6.7. The maximum vertical displacement (Figure 6.7(c)) amounts to 7.75m which is in good agreement with the compaction reported in the literature. The lateral displacements are in the range of -0.9m and 0.9m. These spatial displacements are exported for every horizon in the geomechanical model and in turn used to update the horizons in the ray-tracing monitor model. Moreover, the vertical displacement is used to update the interval velocity of the ray-tracing model, which is outlined in the next section.

6.3 Ray-tracing model of the Ekofisk field

The baseline ray-tracing model is assembled from the same horizons as used for the initial geomechanical model. These horizons are smoothed with a 100m Hamming filter before being input into the model. Subsequently, the initial elastic parameters, such as P-wave velocity and density, are extracted from one well log and assigned to each layer (Table 6.3). The V_p/V_s for the shales and the chalk are taken from two publications (Holt and Fjær (2003) and Japsen et al. (2004)). The displacement vectors extracted from the geomechanical model at the end of the simulation run are in turn added to the baseline horizons in the ray-tracing model, thus creating the monitor ray-tracing model which includes the physical changes of the subsurface horizons. In addition, the velocity is adjusted as well. Therefore, use is made of the R-factor, a concept first introduced by Hatchell and Bourne (2005) and Røste et al. (2005). The authors propose a simple relation between the change in normal incidence P-wave velocity, $\Delta V_P/V_P$, and the vertical strain, ε_{zz}:

$$\frac{\Delta V_P}{V_P} = -R\,\varepsilon_{zz} \tag{6.3}$$

The dimensionless value, R, is assumed to be dependent on the type of rock, thus varying across different reservoirs. Furthermore, the sign convention follows that

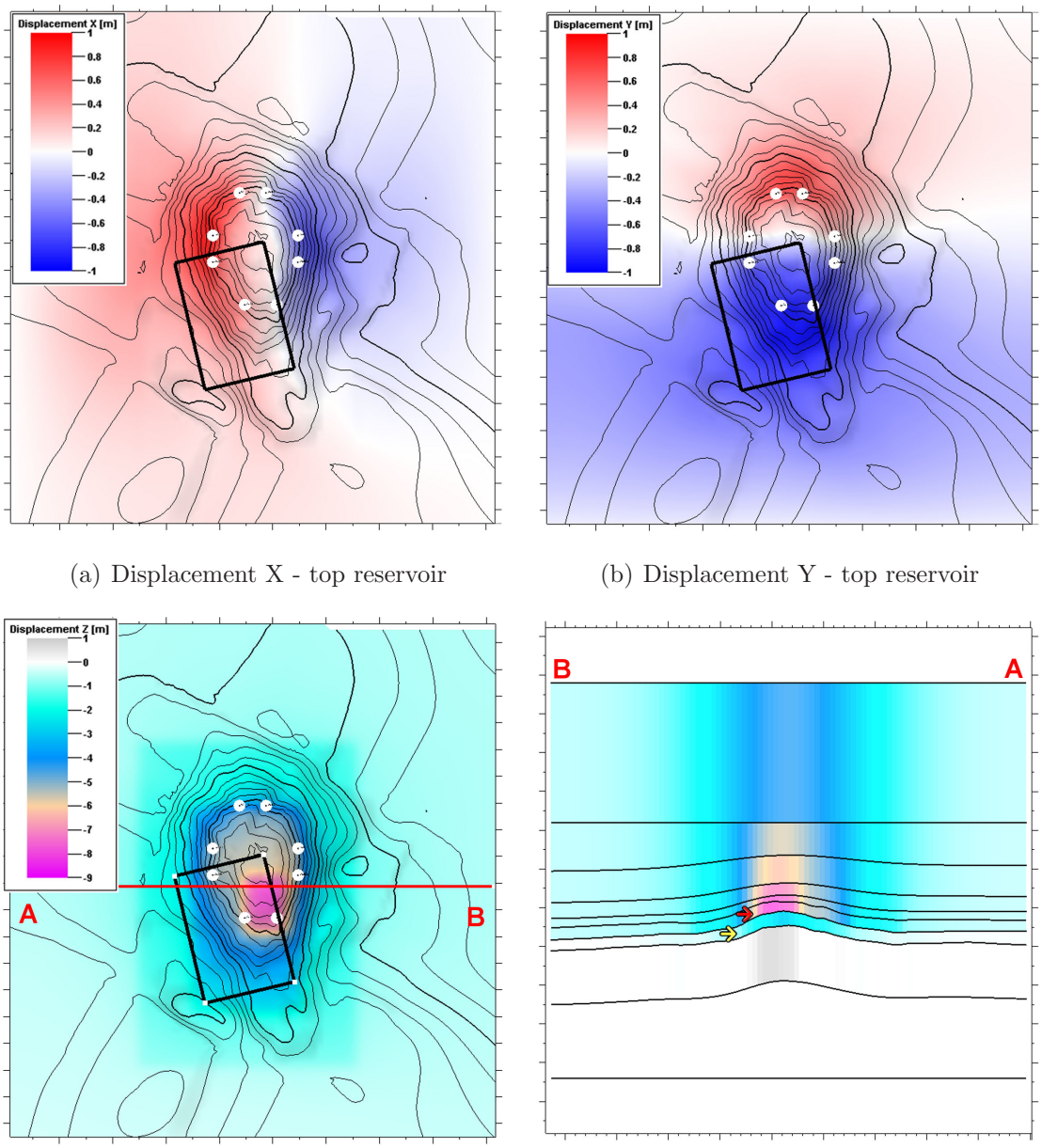

(a) Displacement X - top reservoir

(b) Displacement Y - top reservoir

(c) Displacement Z - top reservoir

(d) Cross-section of Z displacement

Figure 6.7: (a) to (c) lateral and vertical displacement of the top reservoir horizon (Ekofisk Formation) after 20 years of production. Wells are marked by white circles. The black rectangle outlines the area covered by the modelled synthetic seismic data. (d) cross-section showing the vertical displacement; the Ekofisk and Tor Formations are marked with the red and yellow arrow, respectively. The position of the cross-section is indicated by the red line in (c).

Model layer	V_p [m/s]	V_p/V_s	ρ [kg/m^3]
Sea water	1480	–	1000
Overburden 1	2060	2.1	2000
Overburden 2	2070	2.1	2090
Overburden 3	2000	2.1	2000
Overburden 4	2090	2.1	2100
Overburden 5	2120	2.1	2115
Reservoir Ekofisk Fm.	2400	1.75	2110
Reservoir Tor Fm.	2500	1.75	2180
Underburden 1	2550	2.1	2300
Underburden 2	2700	2.1	2400

Table 6.3: Summary of elastic properties used in the Ekofisk ray-tracing baseline model.

positive strains are extensional and commonly decrease the velocity. The vertical strain in the monitor ray-tracing model is calculated from the vertical positions of the upper and lower horizon and the geomechanical displacement field of each layer. Janssen et al. (2006b) observe R values between four and six for the overburden and a value of two for the reservoir rocks of the Ekofisk field. Consequently, an R-factor of five and two is used to calculate the interval velocity change in the overburden and reservoir layers, respectively. However, it has to be mentioned that the use of such a simplistic relation between vertical strain and fractional P-wave velocity change generates some controversy. A persistent mismatch is reported between the R value determined from core samples in the laboratory and the R value derived from seismic data, but the cause is not yet understood (Janssen et al., 2006b; Herwanger, 2008). Hence, R values that are observed in real seismic data are used to update the interval velocities in this study, as the forward modelling is in the seismic domain as well, thus there is a consistent approach to the problem. Figure 6.8 shows the fractional velocity change (relative to the baseline velocity) in the Ekofisk Formation and in the overburden layer adjacent to the top reservoir layer. The maximum fractional

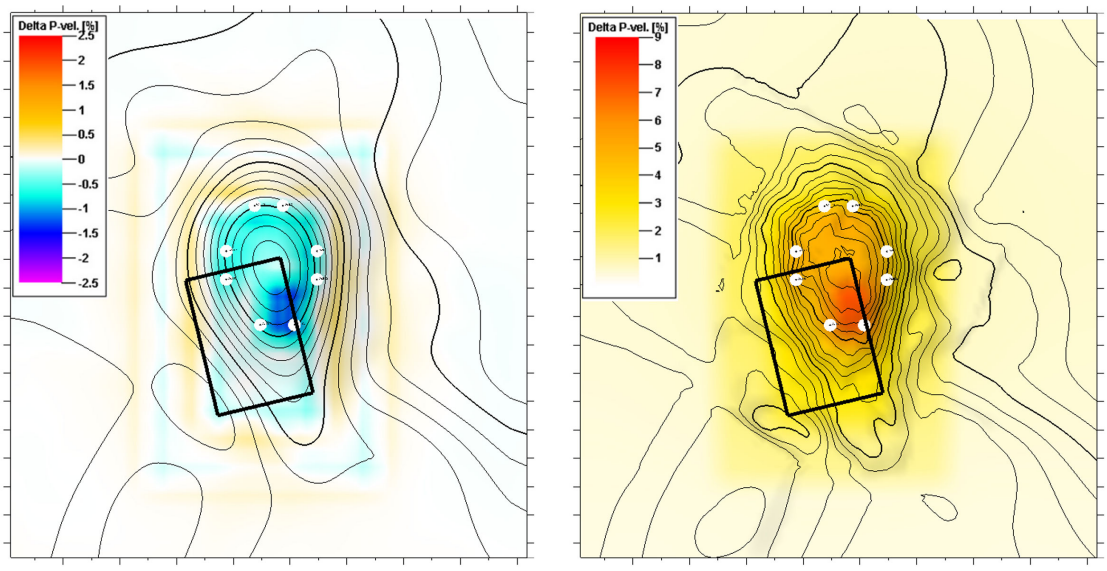

(a) Overburden layer (b) Top reservoir layer

Figure 6.8: Fractional interval velocity change in the (a) overburden layer adjacent to the reservoir and (b) in the Ekofisk Formation (top reservoir). The production wells are highlighted by white circles and the black rectangle outlines the study's seismic modelling area.

interval velocity decrease is -1.3% in the overburden layer, which is caused by the expansion of the rock. The velocity change is smoothed with a 400m Hamming filter to comply with the smoothness criterion for the ray-tracing. Nevertheless, the blocky distribution of the initial porosity in the reservoir (compare Figure 6.6), which controls the compaction, is still imprinted in the velocity change. However, the velocity change inside the seismic modelling area (Figure 6.8(a), black rectangle) is unaffected by this imprint so that these velocities are well suited to model the monitor seismic data. The smoothed (400m Hamming filter) velocity change is largest in the Ekofisk Formation, where the compaction causes a maximum increase of the interval velocity of up to 7.3% (Figure 6.8(b)). On the other hand, the density and V_p/V_s parameters remain unchanged in the monitor ray-tracing model. Furthermore, anisotropy effects of the overburden shale are not included in the ray-tracing models.

The navigation data of two seismic surveys shot over the Ekofisk field in 1999 and 2003 are used to adequately model the seismic acquisition geometry (Table 6.4). Moreover, the shot points of both surveys are shown in Figure 6.9, where the

Survey	1999	2003
Number of sources	2	1
Source separation	150m	∼135m
Shot interval	25m	25m
Active cable length	4 x 2987.5m	8 x 3587.5m
Streamer separation	75m	50m
Group interval	12.5m	12.5m
Near trace offset	∼150m	∼180m
	$\Delta Source + \Delta Receiver = 80$m	

Table 6.4: Summary of towing parameters for the two seismic surveys used in the Ekofisk study. The $\Delta Source + \Delta Receiver$ is averaged over all traces with 1550m offset traces.

undershoot zone above the crest of the reservoir which is caused by the production facilities is clearly seen. Unfortunately, the largest compaction and thus the area

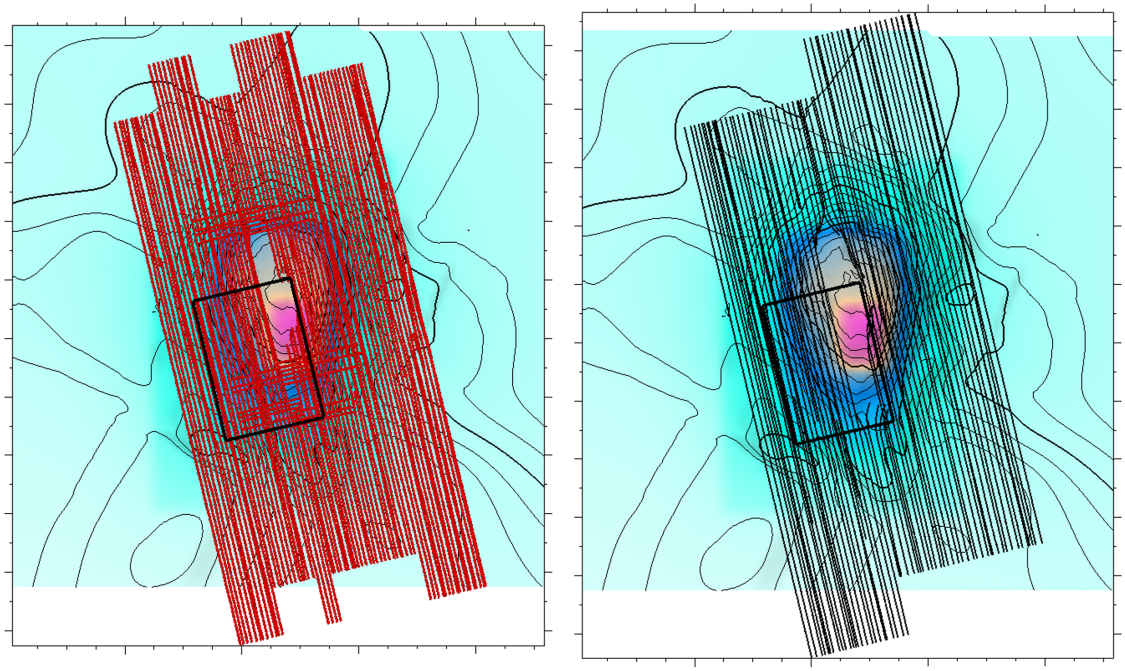

(a) 1999

(b) 2003

Figure 6.9: Shot points for the 1999 and 2003 survey overlain on the vertical displacement map of the top reservoir horizon. The black rectangle outlines the study area.

of interest coincides with this undershoot zone. Hence, shot and receiver pairs are selected outside this undershoot area and are consequently moved to obtain a regular seismic coverage above the study area (Figure 6.9, black rectangle). This approach worked well for the study in Chapter 5 and the character of the non-repeatability is preserved, but the seismic data quality problems of the undershoot area are avoided. Around 6000 shots are traced through the baseline (1999) and monitor (2003) model and a Ricker 30Hz zero phase wavelet is used to generate the pre-stack shot gathers. The seismic processing applied to the data and the methodology of how to study the error in the time-lapse amplitude attribute caused by a velocity change in the overburden are discussed in the following section.

6.4 Seismic processing of the synthetic data

The schematic workflow in Figure 6.10 outlines the chosen approach to study the impact of a changing overburden velocity that is not accounted for in the monitor migration velocity model.

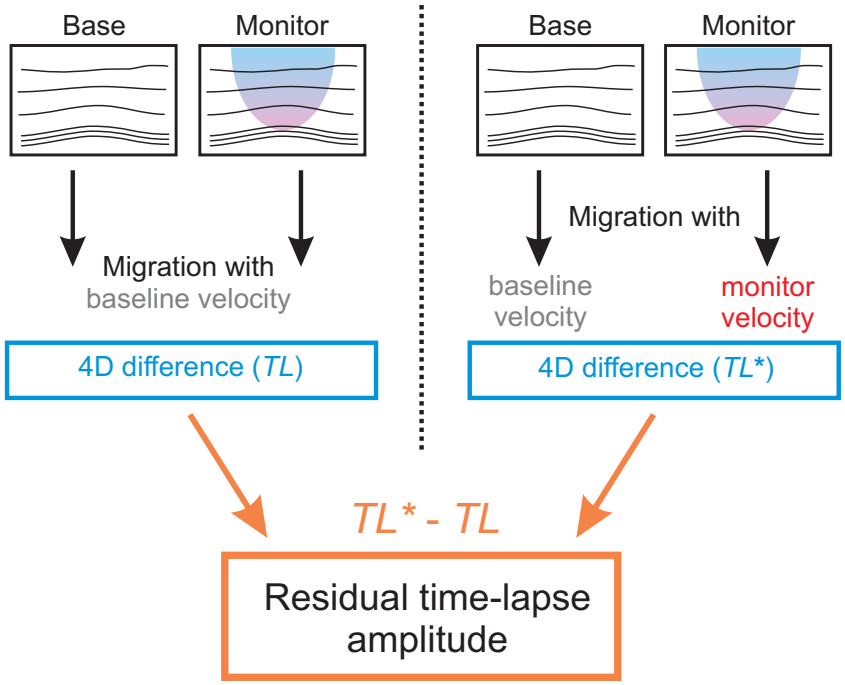

Figure 6.10: Schematic workflow to evaluate the amplitude errors caused by a change in overburden velocity above a compacting reservoir.

The left-hand side shows the regular time-lapse approach, *TL*, where the baseline and monitor seismic data are migrated with the baseline velocity model. Therefore, the velocity change in the overburden rocks which is caused by the reservoir compaction is not accounted for during the imaging process. Conversely, a second set of time-lapse data, TL^*, are obtained when the monitor data are migrated with the exact velocity model, thus accounting for the changes in the overburden (Figure 6.10, right-hand side). The amplitude error caused by migrating the monitor data with the inaccurate baseline velocity model is assessed by subtracting both time-lapse amplitude attributes: TL^* - *TL*. Furthermore, the same acquisition geometry (1999) is used to model the baseline and monitor pre-stack data in a first pass, in order to exclude errors caused by non-repeated source and receiver positions. These errors are separately studied with a second set of monitor ray-tracing models, where the 2003 acquisition parameters are used to model the pre-stack seismic data. Furthermore, Table 6.5 summarises the main seismic processing steps from reading in the pre-stack data to exporting limited offset stacks.

Read SEGY data

⇓

CMP binning by 25m x 25m

⇓

Assign geometry

⇓

4D trace selection

⇓

Pre-stack Kirchhoff time migration

⇓

Limited CMP offset stacks

⇓

SEGY output

Table 6.5: Seismic processing sequence applied to the Ekofisk synthetic data.

The migration velocity is obtained by converting the densely sampled interval depth velocities, taken from the ray-tracing model, to RMS velocities by means of the Dix's equation. The pre-stack seismic modelling area extends over 4700m x 6200m and is covered with a processing bin grid of 25m x 25m due to computational limitations when running the PSTM. Finally, near, mid, far and full offset post-stack data are exported for the full illuminated interpretation area which extends over 4500m x 5550m in the crossline and inline direction. A cross-section through the full stack baseline seismic data is shown in Figure 6.11.

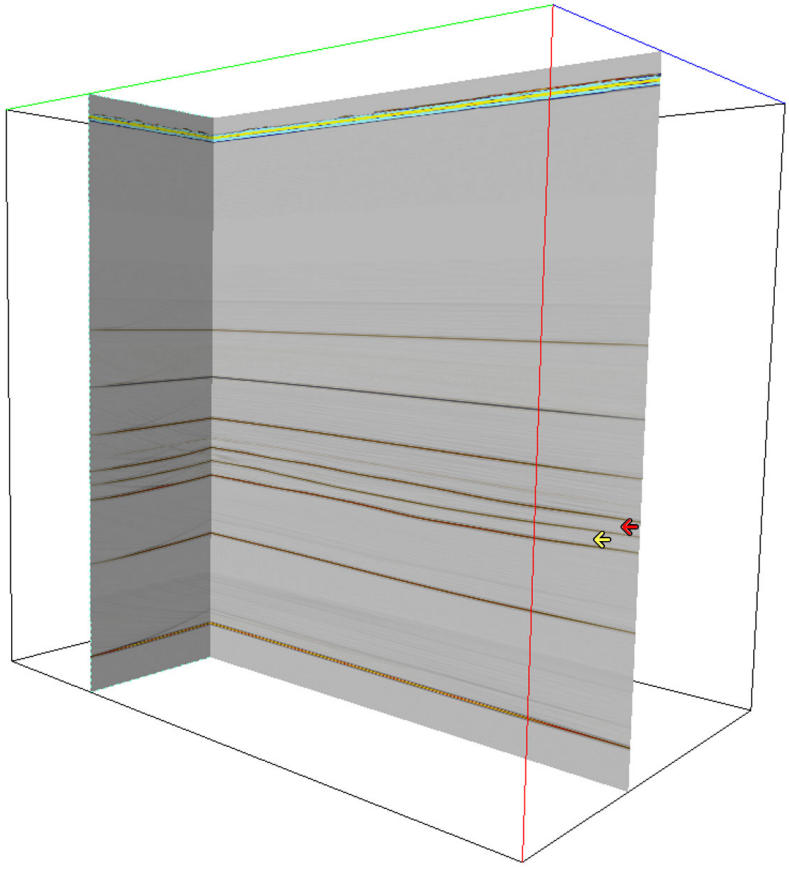

Figure 6.11: Cross-section through the full stack baseline synthetic seismic data. The red and yellow arrows indicate the Ekofisk and Tor Formations, respectively.

6.5 Amplitude changes due to an incorrect velocity model

As outlined in the previous section, the baseline and monitor seismic data are first modelled with the same acquisition parameters (1999 survey) to eliminate amplitude errors caused by non-repeated source and receiver positions. For the following analysis, RMS amplitudes are extracted in a 20ms window centred around the top reservoir horizon. The *TL* amplitude attribute extracted from the full offset stacked data shows the time-lapse amplitude change after 20 years of production (Figure 6.12(a)). This amplitude change is caused by the impedance change of the reservoir rock, as well as the impedance change of the overburden rock due to the overburden stretching. The attribute correlates spatially with the production-induced pressure change (Figure 6.12(b)), but the largest amplitude change coincides with the area of highest initial porosity (Figure 6.12(c)). This is a known behaviour, which is first described by Corzo (2009) using synthetic and real data from the Valhall chalk field:

$$\Delta A = (B\,\phi_0 + C)\Delta P \tag{6.4}$$

Where ΔA is the time-lapse amplitude attribute, ΔP the pressure change, ϕ_0 the initial porosity and B, C coefficients that need to be determined from the data. Her findings are thus qualitatively confirmed to be applicable to this study as well. However, the current study is about the time-lapse amplitude error caused by the inaccurate baseline velocity used to migrate the monitor seismic data, thus the TL^* amplitude attribute and the TL^* - TL difference are calculated (Figures 6.13(b) and 6.13(c)). The TL^* amplitudes are larger compared to the TL amplitudes, especially in the area of displacements greater than six metres (Figure 6.13(d)), which also approximately coincides with the area of highest initial porosity. Hence, using the exact monitor migration velocity focuses the seismic reflection energy better in the area of the largest vertical strain and thus velocity change. The maximum absolute error of the full offset stack TL^* - TL amplitude is 0.18 and the standard deviation 0.03. However, a more complete insight into the spatial distribution of the amplitude error is gained when the fractional error is calculated: $(TL^*$ - $TL)/TL$. Conversely,

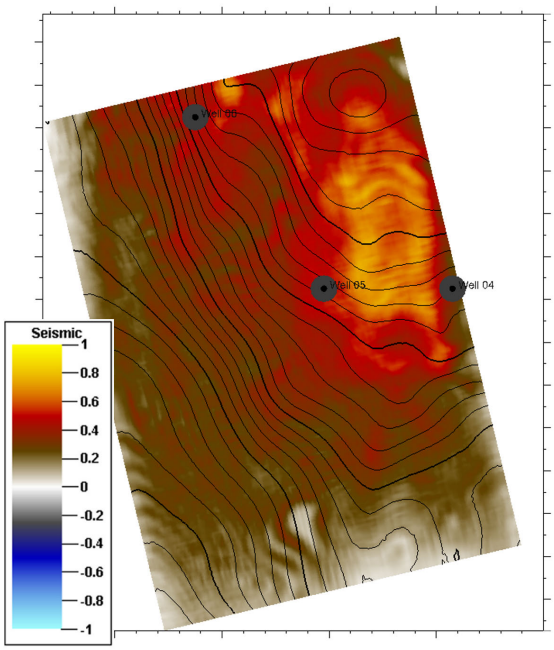

(a) RMS amplitude *TL*: full offset stack

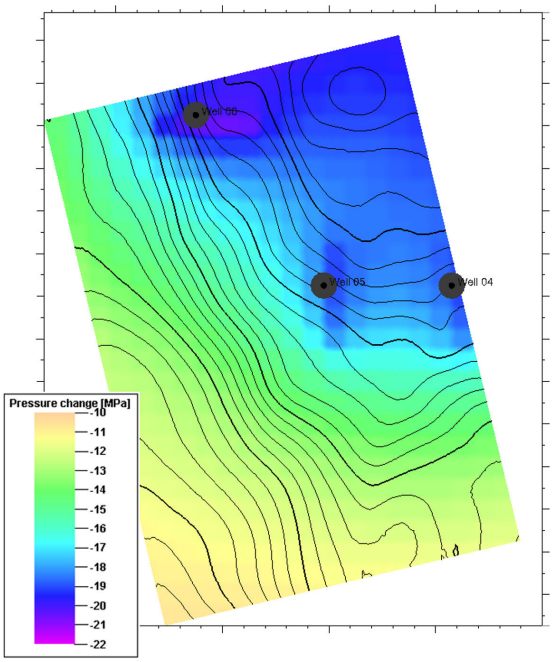

(b) Pressure change

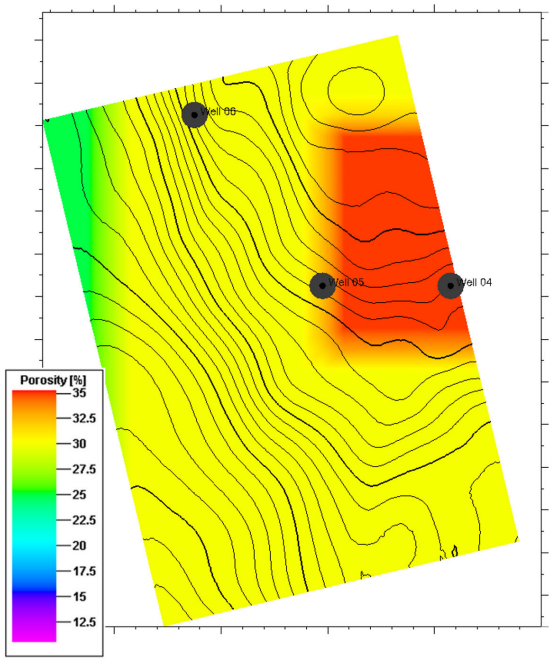

(c) Initial porosity

Figure 6.12: (a) *TL* amplitude extracted at the top reservoir horizon. The same acquisition parameters are used for the baseline and monitor seismic modelling. (b) Pressure change in the top reservoir layer after 20 years of production. (c) Initial porosity of the top reservoir layer. The black circles mark the well positions.

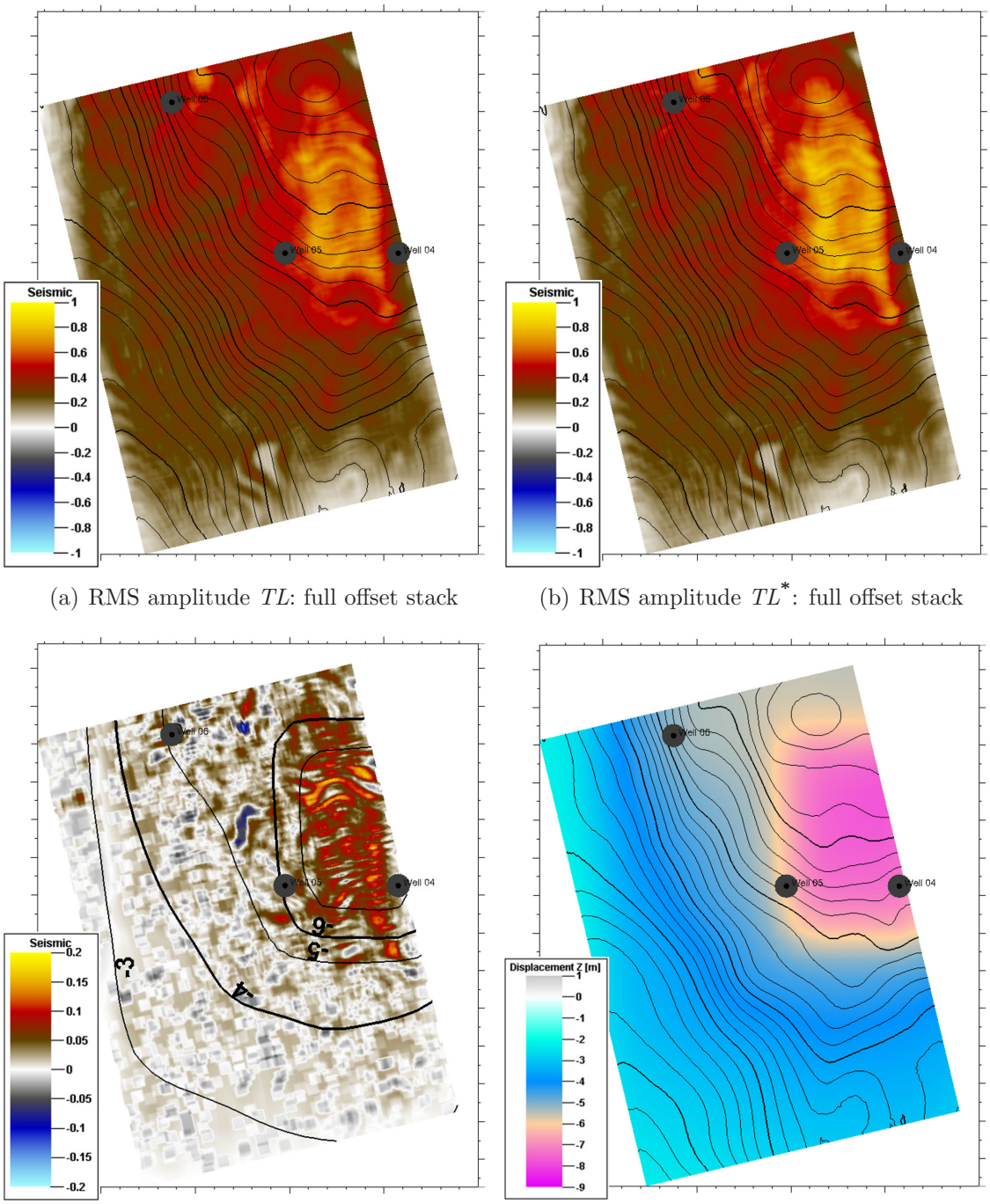

(a) RMS amplitude TL: full offset stack

(b) RMS amplitude TL^*: full offset stack

(c) TL^* - TL amplitude: full offset stack

(d) Vertical displacement

Figure 6.13: (a) TL and (b) TL^* amplitude extracted at the top reservoir horizon. The same acquisition parameters are used for the baseline and monitor seismic modelling. (c) TL^* - TL residual amplitude highlights the error caused by the incorrect migration velocity model. The contour lines outline the vertical displacemnet in metres. The amplitude artifacts (banding) in the area of highest compaction are caused by the large grid block size in the geomechanical model, which is refined when importing the layers into the ray-tracing model. (d) Vertical displacement of the top reservoir horizon. The black circles indicate well positions in all figures.

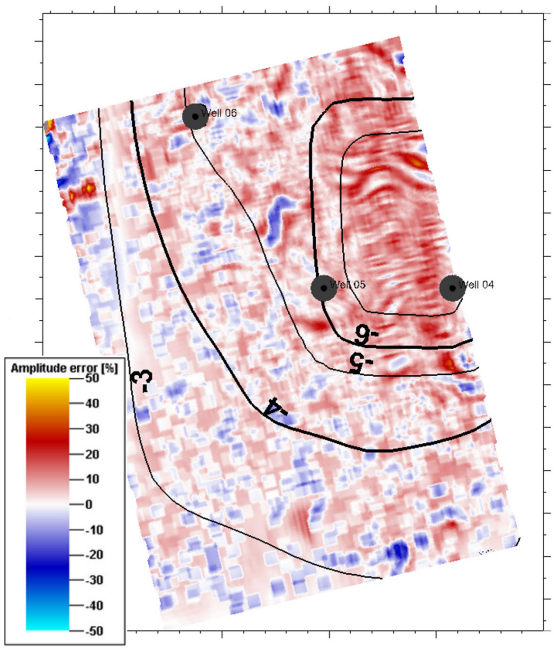

Figure 6.14: Fractional full stack amplitude error: $(TL^*$ - $TL)/TL$. The contour lines indicate the amount of vertical displacement in metres of the top reservoir horizon, caused by the production induced reservoir compaction. The amplitude artifacts (bandling) in the area of highest compaction are caused by the large grid block size in the geomechanical model, which is refined when importing the layers into the ray-tracing model.

the fractional error is measurably increased in the area of high vertical displacements greater than six metres (Figure 6.14). The mean error in this area is 9.40%, whereas the mean error outside this zone (displacement smaller than six metres) is only 2.30%. The standard deviations are 5.9 percentage units and 6.0 percentage units for the zones of displacement greater than six metres or smaller than six metres.

In addition, the near, mid and far offset stacks are generated from the pre-stack time migrated data to investigate whether the RMS amplitude attribute of these limited offset stacks is affected in a similar way to the full offset stack case. Consequently, the TL^* - TL differences are calculated for these limited offset stacks (Figure 6.15). The magnitude of the TL^* - TL amplitude in the near offset stack data (Figure 6.15(a)) is significantly less compared to the full offset stack data (Figure 6.13(c)). The residual amplitudes are slightly negative for the areas with a compaction larger than six metres, which is due to smaller amplitudes in the TL^* difference compared to the TL difference, whereas amplitude errors are close to zero outside this area. These observations become more obvious when the fractional error of these near offset stack data is calculated (Figure 6.16(a)). The mean error and the standard deviation inside the area of compaction exceeding six metres is -1.42% and 4.12 percentage units, respectively. The mean error outside this area is -0.05% with a standard deviation of 3.18 percentage units. It is not clear why the TL^* amplitudes

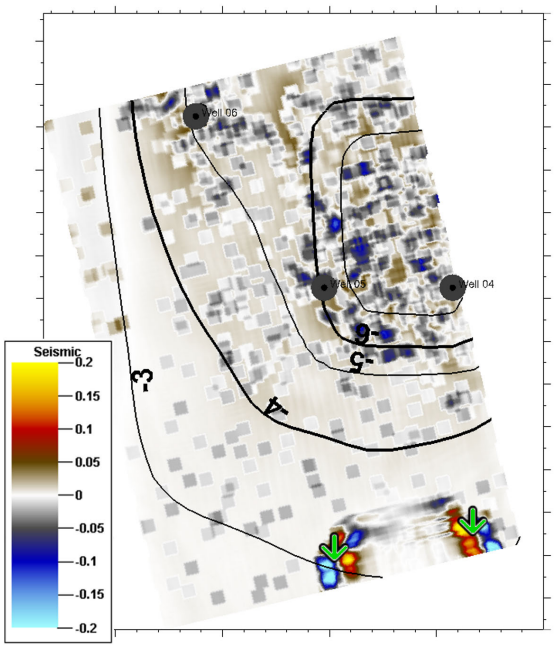

(a) TL^* - TL amplitude: near offset stack

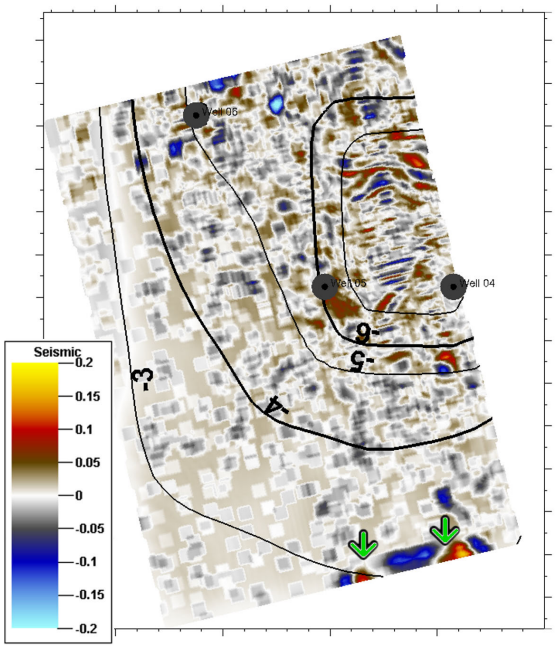

(b) TL^* - TL amplitude: mid offset stack

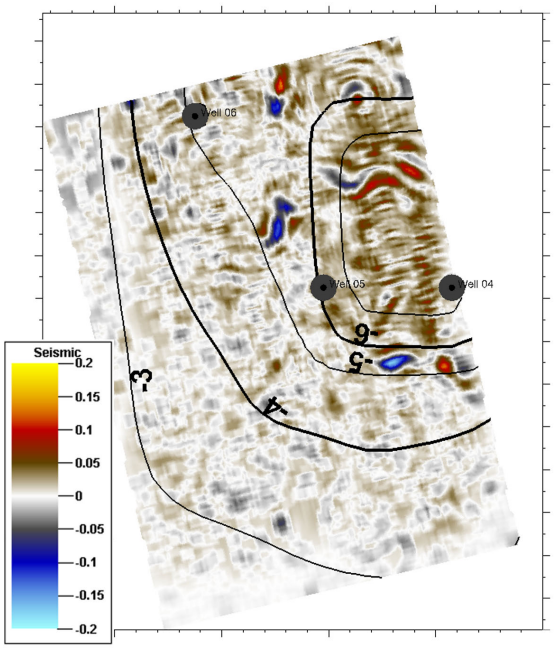

(c) TL^* - TL amplitude: far offset stack

Figure 6.15: TL^* - TL amplitudes highlight the error caused by the incorrect migration velocity model for: (a) near offset stack, (b) mid offset stack and (c) far offset stack data. The green arrows in (a) and (b) indicate areas with picking problems. The black circles mark well locations and the vertical displacement (in metres) is marked by the contour lines.

are smaller than the *TL* amplitudes in the near stack, which is also opposite to the observations made for the mid and far offset stack data described in the following paragraphs. The large amplitude errors indicated by green arrows are solely caused by picking problems in the data, because of a low near offset fold in the monitor survey as lines are shot in the opposite direction.

Next, Figure 6.15(b) shows the TL^* - *TL* amplitudes of the mid offset stacked data. No area of increased amplitude error is apparent, but a general increase of the overall noise level is observed. The amplitude error in the zone of compaction larger than six metres is 1.25%, thus marginally increased compared to the errors outside this zone, which amounts to -0.09%. The standard deviations are very similar with values of 5.18 percentage units and 5.29 percentage units in these zones (Figure 6.16(b)).

Finally, the far offset stack data are used to compute the TL^* - *TL* difference (Figure 6.15(c)). The amplitudes errors for this case are comparable to the ones initially presented in the full offset stack case (Figure 6.13(c)). Hence, the amplitude error is large in the zone of the largest vertical displacement (>6m), but noise similar to the previous mid offset stack residual amplitudes is still apparent in the data. The mean fractional amplitude error equates to 4.23% and 1.61% inside and outside the area of highest initial porosity, and the standard deviations are 4.26 percentage units and 5.36 percentage units for the respective areas. The full and far offset stack amplitudes thus show a pronounced error in the zone of largest compaction, which is measurably different to the error outside this zone, if the baseline velocity is used to migrate the monitor data.

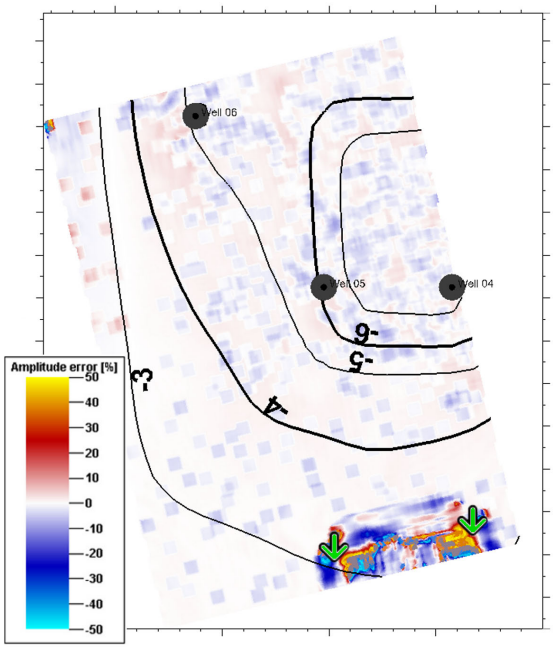

(a) Near offset stack

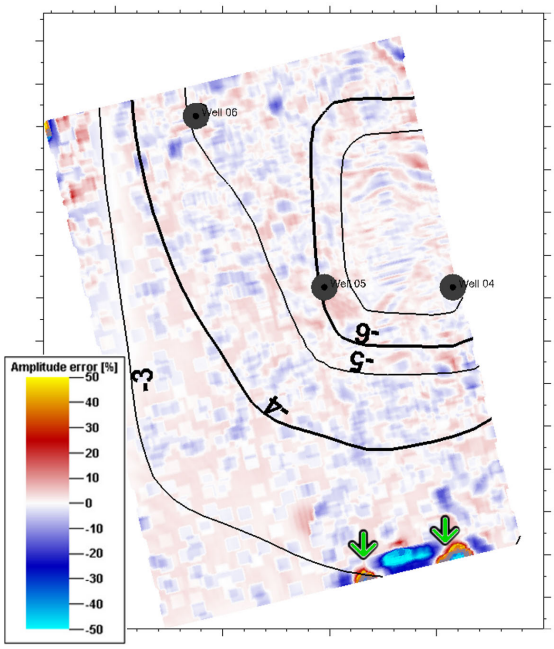

(b) Mid offset stack

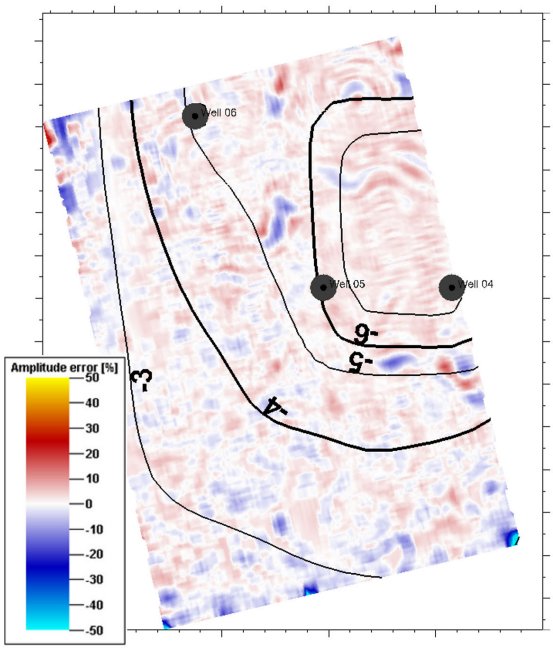

(c) Far offset stack

Figure 6.16: Fractional amplitude error, $(TL^{*} - TL)/TL$, caused by the incorrect migration velocity model for: (a) near offset stack, (b) mid offset stack and (c) far offset stack data. The green arrows in (a) and (b) indicate areas with picking problems. The black circles mark well locations and the vertical displacement (in metres) is marked by the contour lines.

The influence of structural changes

The previous section outlines that there is an increased amplitude error in the area of largest compaction for the full and far offset stack time-lapse amplitudes. However, this time-lapse amplitude error is caused by the combined effect of the velocity change and the structural change (surface displacement) in the overburden. Consequently, an additional monitor ray-tracing model is assembled that contains the velocity changes in the overburden rock caused by the reservoir compaction, however, no structural changes of the horizons. These "*no compaction*" monitor data are again migrated with the baseline and the monitor velocity model to calculate the differences: $TL_{(no\ structure)}$ and $TL^{*}_{(no\ structure)}$ (following the workflow in Figure 6.10). Hence, the amplitude error in the full offset stack data, caused solely by the velocity change in the overburden, is assessed by taking the difference: $TL^{*}_{(no\ structure)}$ - $TL_{(no\ structure)}$ (Figure 6.17(a)).

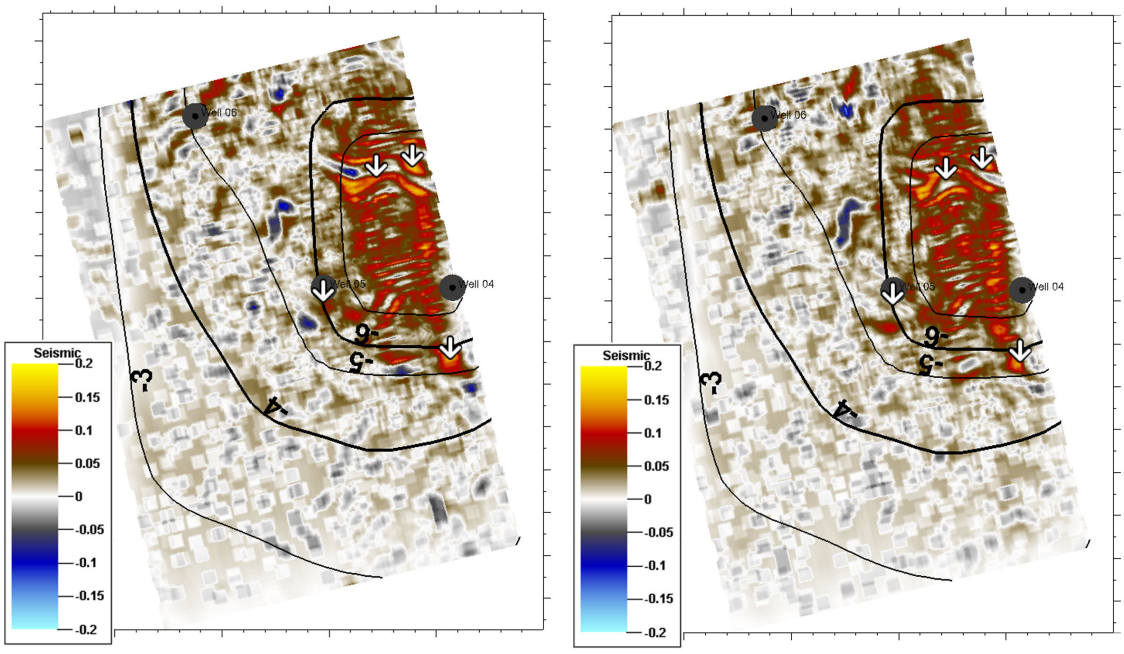

(a) $TL^{*}_{(no\ structure)}$ - $TL_{(no\ structure)}$: full stack

(b) TL^{*} - TL : full stack

Figure 6.17: (a) Full offset stack amplitude error caused by velocity changes in the overburden only. (b) Full offset stack amplitude error caused by velocity changes in the overburden and physical deformation of the overburden horizons. The white arrows are in the same place on the two figures, thus the lateral shift of the amplitude error is easy to recognise.

The fractional amplitude error, $(TL^{*}_{(no\ structure)}$ - $TL_{(no\ structure)})/TL_{(no\ structure)}$, is virtually unchanged with a mean error of 9.23% and a standard deviation of 6.33 percentage units in the zone of largest compaction (>6m). The mean error outside this zone is 2.21% with a standard deviation of 6.12 percentage units. However, the most noticeable difference to the full offset stack amplitude error, TL^{*} - TL, is that the error is shifted spatially. The arrows in Figures 6.17(a) and 6.17(b) mark the same positions in both maps. A maximum upwards shift of the amplitude error of approximately 100m is identified between the two maps. Hence, the physical displacement of the top reservoir horizon, due to the compaction in the reservoir, moves the time-lapse amplitude error spatially, but does not alter its magnitude. The fractional errors in the near, mid and far offset stack data are very similar to the previous case, including the structural changes. Hence, the errors and their respective standard deviations from inside and outside the zone of largest compaction are summarised in Table 6.6.

	Displacement > 6m	Displacement < 6m
Near offset stack	-1.67% (SD 3.96 percentage units)	-0.32% (SD 3.53 percentage units)
Mid offset stack	0.19% (SD 5.78 percentage units)	-0.23% (SD 5.75 percentage units)
Far offset stack	3.60% (SD 5.15 percentage units)	1.70% (SD 5.36 percentage units)

Table 6.6: Fractional amplitude errors for the *no compaction* case, calculated inside and outside the zone of highest initial porosity. The mean error, as well as the standard deviation (SD) are listed for the near, mid and far offset stack data.

The above presented lateral shifts are solely caused by the the structural changes in the subsurface and not by using a wrong migration velocity model. Conversely, Cox and Hatchell (2008) report on lateral shifts of up to five metres which are observed above the Shearwater Field, North Sea. The authors speculate that these shifts are caused by using the wrong migration velocity for the monitor survey and subsequently demonstrate that these shifts can be reproduced in a modelling study. Therefore, the synthetic seismic data discussed in this chapter are used by a PhD student of the ETLP group to verify the observations made by Cox and Hatchell

(2008). Preliminary results suggest that using the wrong migration velocity model causes lateral shifts of up to three metres, however, there is still much uncertainty about the concept of using a single R-factor to describe such velocity changes of the overburden and reservoir rock (Alejandro Garcia, Heriot-Watt University, personal communication).

The influence of acquisition non-repeatability

The previous amplitude analysis is based on an ideal acquisition repeatability, thus neglecting possible amplitude errors caused by a non-repeated monitor survey. Consequently, the TL^* difference data (compare Figure 6.10) is modified so that the monitor seismic data is modelled using the 2003 acquisition geometry, thus denoted with $TL^*_{(non-repeat)}$. However, the baseline velocity model is used throughout to migrate the pre-stack shot gathers. Therefore, when taking the $TL^*_{(non-repeat)}$ - TL difference, the common signal caused by the incorrect velocity model cancels out and the residual amplitudes due to the acquisition non-repeatability is obtained (Figure 6.18(a)). The fractional amplitude error is again calculated to better describe the impact of the non-repeatability in relation to the TL time-lapse data (Figure 6.18(c)). The difference in source and receiver positions between the 2003 and 1999 survey causes the amplitude error to vary around a mean value of -0.22%, but no apparent zone of increased error is identified. The standard deviation is 5.54 percentage units. These errors, however, do not correlate with the $\Delta Source + \Delta Receiver$ measure, thus it is concluded that the non-repeated monitor survey increases the general noise level of the time-lapse amplitude attribute but does not cause pronounced striping in conjunction with the unaccounted velocity change in the overburden. That is, the pre-stack reflection events are much more affected by the change of the overburden velocity than by the change in source and receiver position.

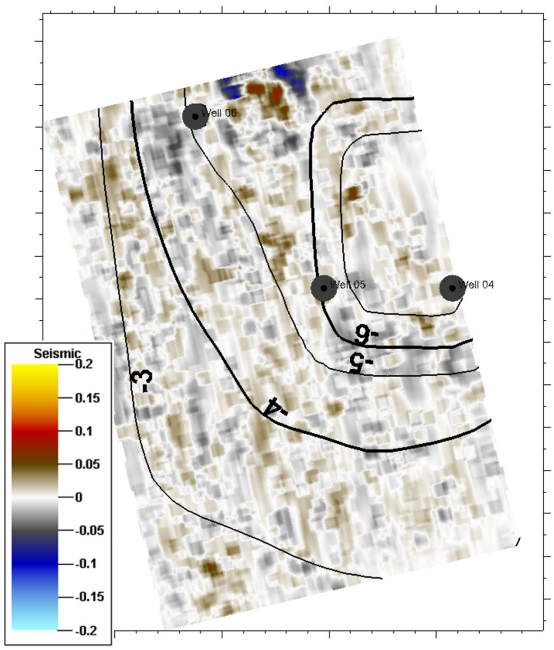

(a) $TL^*_{(non-repeat)}$ - TL : full offset

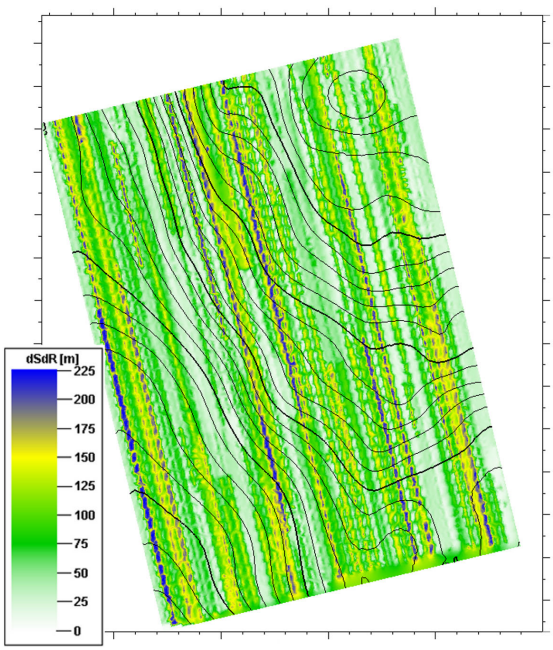

(b) $\Delta Source + \Delta Receiver$

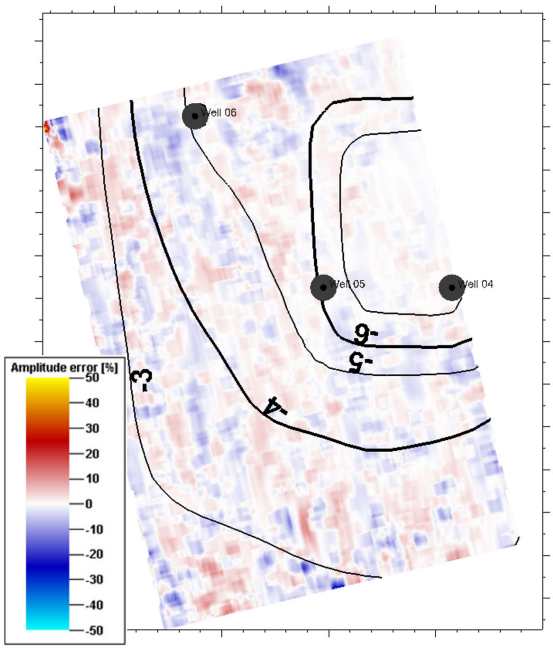

(c) Fractional amplitude error

Figure 6.18: (a) Residual amplitude caused by the non-repeatability between the 1999 and 2003 survey. (b) $\Delta Source + \Delta Receiver$ measure for traces with 1500m offset. (c) Fractional amplitude error, $(TL^*_{(non-repeat)}$ - $TL)/TL$, for the full offset stack data.

6.6 Discussion

The various offset stack dependent mean amplitude errors are consequently compared in Figure 6.19. The mean amplitude errors, extracted from the area of highest

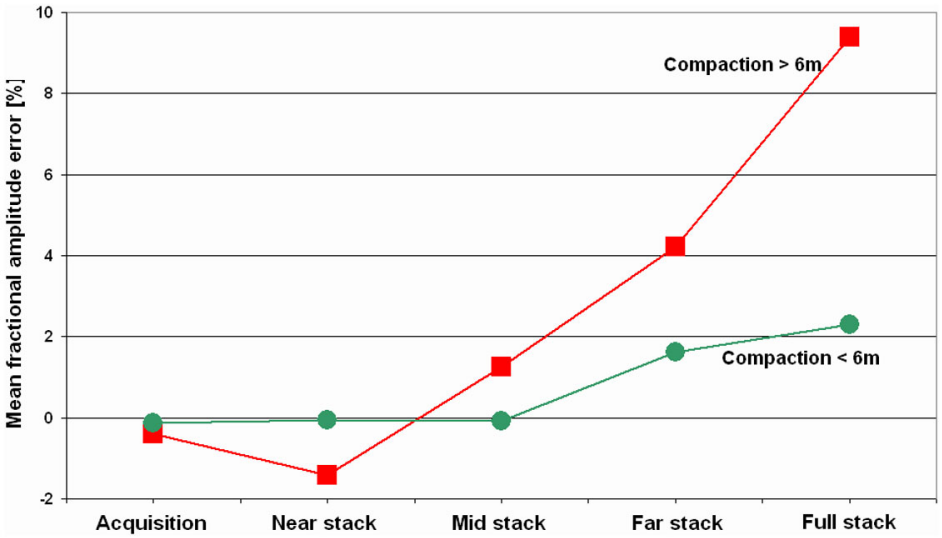

Figure 6.19: Comparison between the mean amplitude errors caused by an incorrect migration velocity in the case of a compacting reservoir for the near, mid, far and full offset stack data, as well as the mean error caused by the non-repeated acquisition geometry. Amplitude errors calculated in a zone of displacement larger than six metres are marked in red, whereas errors outside this zone are marked in green.

initial porosity (red data points) which coincides well with reservoir compactions being larger than six metres, are compared against the mean amplitude errors calculated outside this area (green data points). There is no significant difference between the amplitude errors caused by the non-repeated monitor acquisition geometry, whether measured inside or outside the high compaction zone. The differences increase slightly for the mean errors extracted from the near and mid offset stack data, however, they are less than 1.50 percentage units. On the other hand, the mean amplitude errors in the far offset stack data are increased in both zones, moreover, the difference between these errors rises to 2.63 percentage units. Finally, the mean errors of the full stack data exhibit a significant difference of 7.10 percentage units when calculated in the area of highest initial porosity, thus highest compaction, compared to the mean amplitude error measured outside this zone. Further work is needed to investigate why the error in the full stack data is greater

than any error in the partial stacks. One thought is that the full stack data picks up the artifacts caused by the grid size difference between the geomechanical and ray-tracing model. However, a refined geomechanical simulation model is necessary in order to further investigate these effects.

An important observation is that these time-lapse amplitude errors are caused by the overburden velocity change. The structural deformation of the subsurface horizons, hence the physical displacement of the horizons causes the amplitude error to move spatially. This is described in Figure 6.20 using a cartoon-like sketch and assuming

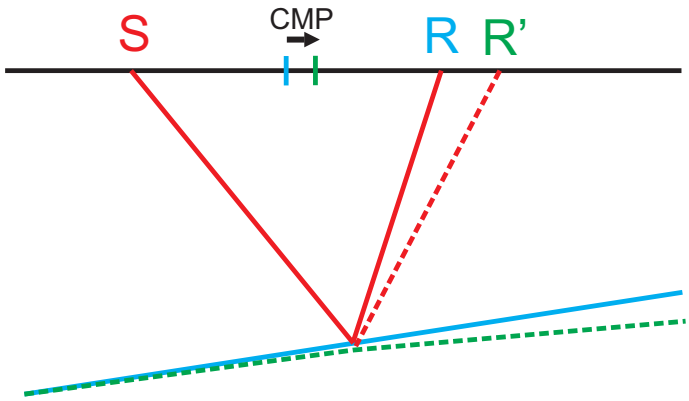

Figure 6.20: Schematic sketch showing the spatial shift of the reflection event for the case of a structural change of the top reservoir horizon. Shot and receiver positions are denoted with S, R and R', respectively. The arrow indicates the shift of the CMP position.

straight rays. In the baseline survey, the seismic wave is emitted from the source location, S, reflected at the top reservoir horizon (blue line) and recorded at the receiver R. Subsequently, the horizon moves downwards due to compaction (green dashed line) and the reflection event for waves with the same shot position as in the baseline survey is recorded at a different receiver position, R'. Therefore, the common midpoint, CMP, between S and R moves to a new position in the monitor survey (indicated by the arrow). Because the baseline velocity model is used for migrating the monitor data, the DMO operator, which is an inherent part of the Kirchhoff pre-stack time migration, cannot fully account for the locally changed reflector dip. Therefore, the magnitude of the spatial shift depends on the amount of the local dip change at the reflection point. However, these shifts of up to 100m increase location uncertainty for infill wells drilled to target unproduced reservoir zones.

The first conclusion drawn from this study is that the time-lapse amplitude attributes of the near and mid offset stack data are equally affected by the amplitude errors due to an incorrect monitor migration velocity. On average, this amplitude error is less than 1.5 percentage units of the time-lapse RMS amplitude change, regardless of whether the attribute is extracted in a zone of large overburden velocity changes or not. The time-lapse amplitude change is thus coherent across the reservoir and the quantitative interpretation of the near and mid offset stack amplitude change is not biased by the unaccounted overburden velocity change if only studying relative changes.

On the other hand, the time-lapse RMS amplitudes are affected unequally when extracted from the far and full offset stack data. The largest amplitude errors are measured at the zone of highest initial porosity and thus the zone of largest compaction in this model. The spatial time-lapse amplitude variations are up to 7.10 percentage units in the full stack data and up to 2.63 percentage units in the far offset stack data. These variations are caused by the overburden velocity change and not by production-induced reservoir changes. Hence, the extracted time-lapse amplitudes are not coherently changing across the reservoir and are not well suited for quantitative interpretation. Furthermore, the observations in this study are in line with the real Ekofisk time-lapse data, where the waveform of the far and full offset traces is reported not to match inbetween various time-lapse vintages, however, the magnitude of this mismatch has yet not been assessed (Aaron Janssen, personal communication). This study thus quantifies the magnitude of these amplitude errors compared to the time-lapse amplitude change.

Implications for quantitative reservoir change estimates - The current deterministic pressure and saturation change inversion methods rely on spatially coherent attribute changes in order to estimate the reservoir changes. Therefore, the impact of these amplitude errors on the pressure change inversion is discussed next to highlight possible problems if the far and full offset stack amplitudes are used.

The quantitative pressure and saturation change inversion method as presented and used in Chapter 3 and 4 will not perform well when far or full offset stack

amplitude attributes are employed, because the underlying assumption that the time-lapse attribute change is caused by hydrocarbon production in the reservoir only is invalid. As a consequence, the calibration coefficients, C_S and C_P, which are determined in the areas of largest amplitude error cannot be used to estimate the reservoir change in regions which are less affected by the overburden change induced amplitude error. Other amplitude attributes that are derived from the far or full offset stack data, such as the sum of negatives or the amplitude envelope, might have limited use as well. On the other hand, measured time shifts can be used as an additional attribute to condition the inversion process. Indeed, a previous study done within ETLP (unpublished) uses near and far stack RMS amplitudes as well as measured time shifts to estimate the pressure, saturation and porosity change at the Ekofisk field. Some relations are found between the estimated reservoir changes compared to the reservoir simulation model.

However, this inversion still uses the far offset stack data, which is shown to be measurably affected by the overburden velocity change. Nevertheless, amplitude attributes from the far offset stack data might be used if separate inversions are performed, each confined to an area of approximately the same amplitude error induced by the overburden. However, identifying these areas of variable amplitude error is not possible without the knowledge of the true monitor velocity model to process the monitor seismic data to a reference case, as done in this study. Hence, a first approach might be to divide the reservoir into zones based on the observed vertical displacement at the top reservoir which is readily available from repeat well logging (Menghini, 1989). Alternatively, zones can also be determined using the measured time shift at the top of the reservoir. The previous study shows that the time-lapse amplitude is affected most in the area with displacements greater than 6m (Figure 6.13). Consequently, a separate pressure change inversion in this area might be satisfactorily consistent, because the time-lapse attributes are equally affected by the overburden induced error. The same applies for estimating the reservoir changes outside this zone of largest vertical displacement. Nevertheless, there might be an increased uncertainty in the quantitative interpretation if the continuity of these separately estimated reservoir changes is poor between the individual zones. In addition, the selected areas have to be sufficiently large to contain several wells with

repeat engineering measurements to calibrate the C_S and C_P coefficients separately. Therefore, it is necessary to further study the best way to combine attributes measured in the overburden, such as time shifts or lateral shifts with attributes that are measured at the reservoir, in order to reduce the impact of geomechanical effects on the quantitative estimation of reservoir changes. Although this discussion is focused on the time-lapse interpretation, there is certainly the need to also investigate the best approach, as well as the limitations, to update the migration velocity model.

6.7 Summary

Subtle errors in the time-lapse amplitude attributes, caused by overburden changes over a compacting reservoir, have been postulated by several authors, but deemed hard to quantify. Hence, a geomechanical model is set up to simulate stress and strain changes in the overburden above a highly compacting North Sea chalk reservoir. In turn, baseline and monitor ray-tracing models are conditioned utilising these changes, and synthetic pre-stack data are generated. However, the velocity changes caused by the expansion of the overburden rocks are not included in the monitor migration velocity model and thus cause amplitude errors in the seismic time-lapse data. Consequently, the magnitude of these errors is estimated. The conclusion drawn from this study is that the far and full offset stack data should not be used for quantitative time-lapse interpretation as the amplitude error does not change coherently across the reservoir. The near and mid offset stack data are marginally affected and are recommended as data to extract time-lapse amplitude attributes from. The amplitude error caused by a non-repeated monitor survey is not increased over the zone of largest overburden velocity change.

Chapter 7

Conclusions and recommendations for future research

The influence of various overburden complexities on time-lapse seismic attributes is studied in this thesis. Seismic modelling, processing and interpretation is carried out such that the magnitude of the error in the time-lapse data is quantified. This chapter summarises the findings and provides an outlook on possible future research. Recommendations are made on how to overcome technical challenges somebody might face when continuing along a similar research pathway. It is pointed out that there are still a multiplicity of opportunities to improve the quantitative time-lapse interpretation.

The motivation for this research is to study the influence of overburden heterogeneities on the time-lapse amplitude attribute, as well as on the saturation change estimation, to test the limits of quantitative time-lapse interpretation. Three distinct overburden features are studied in this work:

Chapter 3: Overburden sand channels above the Nelson Field.

Chapter 5: Deep water stacked reservoirs West of Africa.

Chapter 6: Overburden velocity changes caused by the compacting Ekofisk chalk reservoir.

A layer stripping method is presented in Chapter 4 that reduces the overburden and acquisition imprint. This method is consequently applied to the data presented in Chapter 3 in order to demonstrate that the time-lapse interpretation results significantly improve. The layer stripping method could also be applied to the West of Africa data (Chapter 5). However, a continuous reflector needs to be present between the reservoir channels which can be used as a reference horizon when forming the spectral ratio. No such a horizon is set up in the synthetic West of Africa ray-tracing model, thus the method is not tested with this data.

In order to accurately quantify the errors in the time-lapse data, introduced by these overburden heterogeneities and acquisition non-repeatability, extensive use is made of modelling synthetic pre-stack seismic data. Chapter 2 provides an overview of current seismic modelling techniques, their advantages as well as disadvantages. It is concluded that the ray-tracing approach is best suited for this study due to its unmatched speed when it comes to modelling the wave propagation through large three-dimensional models. Reasoning is given to outline the advantages of the synthetic modelling approach, as it allows us to arbitrarily modify the models best suited to individual problems.

Channels in the overburden

The influence of two distinct overburden channels of Quaternary and Mio-Pliocene Age on the time-lapse amplitude attribute is studied in Chapter 3. Various synthetic ray-tracing models, which include or exclude these channels, are set up to separate the amplitude errors caused by the overburden channels from the amplitude errors caused by the acquisition non-repeatability and the production-induced amplitude changes. The amplitude errors caused by the Mio-Pliocene channel are largest below the thickest part of the channel, whereas the amplitude errors caused by the Quaternary channel are largest beneath the steeply dipping channel margins. It is also observed that these amplitude errors follow the non-repeatability pattern in the vicinity of the channel. On average, the maximum amplitude error, normalised by the maximum production-induced amplitude change, is 233% for the poor repeat case. The maximum error decreases to an average of 82% for the good repeat case. Figure 7.1 summarises these normalised amplitude errors caused by the Quaternary channel and the Mio-Pliocene channel using the good and poor repeated acquisition geometry, respectively. The above analysis shows that the overburden channels

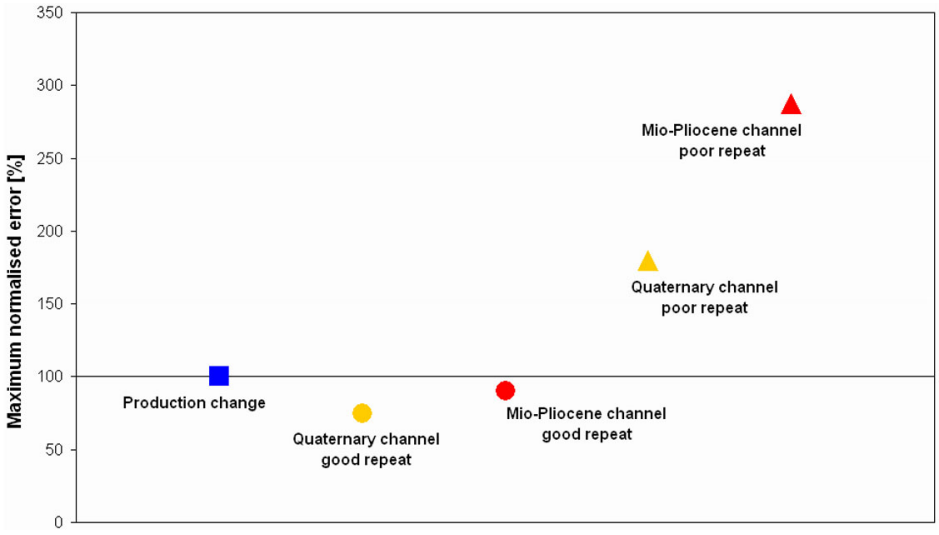

Figure 7.1: Maximum amplitude error caused by the Mio-Pliocene and Quaternary channel in conjunction with the poor and good repeat survey. Errors are normalised by the maximum production-induced amplitude change.

cause an amplitude error exceeding the magnitude of the production-induced amplitude change in case of the poor repeated monitor survey.

This amplitude study forms the basis to further investigate the accuracy of a multi-attribute oil saturation change estimation method. Indeed, Floricich (2006) stresses that one assumption for applying this multi-attribute inversion technique to time-lapse seismic data is their perfect repeatability. Further testing the limits and robustness of this technique as well as the accuracy for a given seismic repeatability (NRMS) is suggested. These questions are addressed in the second part of Chapter 3 where the time-lapse amplitude attributes are used to estimate the oil saturation change in the top reservoir layer. The maximum and mean saturation change estimation errors using the poor repeat data are 60% and 6%, respectively. These estimation errors decrease to 46% and 4% for the maximum and mean error, respectively, when the saturation change is derived from the good repeat data. The errors are normalised by the maximum saturation change. In addition, residual time shifts in the seismic data, caused by the overburden channels in conjunction with a non-repeated monitor survey, are found to severely alter the RMS amplitude attribute if calculated from the time-lapse difference data. The discussion in Chapter 3 shows that residual time shifts smaller than 0.4ms can currently not be removed from the seismic data and thus yield a saturation change estimation error of at least 20% (Figure 7.2). The error is again normalised by the maximum saturation change. It is strongly suggested to take the difference of the RMS amplitudes as this effectively removes the time shift effect and reduces the mean saturation change inversion error to less than 6%, thus improving the quantitative interpretation of the reservoir change. No correlation is found between the saturation change estimation error and the NRMS as well as $\Delta Source + \Delta Receiver$ measure, if only amplitude errors caused by the overburden channels affect the time-lapse amplitude attribute. The correlation slightly improves when residual time shifts affect the time-lapse amplitudes used to estimate the saturation change, however, there are areas of high NRMS and $\Delta Source + \Delta Receiver$ measures which do not cause large errors in the saturation change estimates. The overall conclusion is:

> *The commonly used repeatability measures, NRMS and $\Delta Source + \Delta Receiver$, do not correlate well with the error of the saturation change estimates, induced by the overburden channels. Thus, these measures have to be considered as a loose guide of the mean error only.*

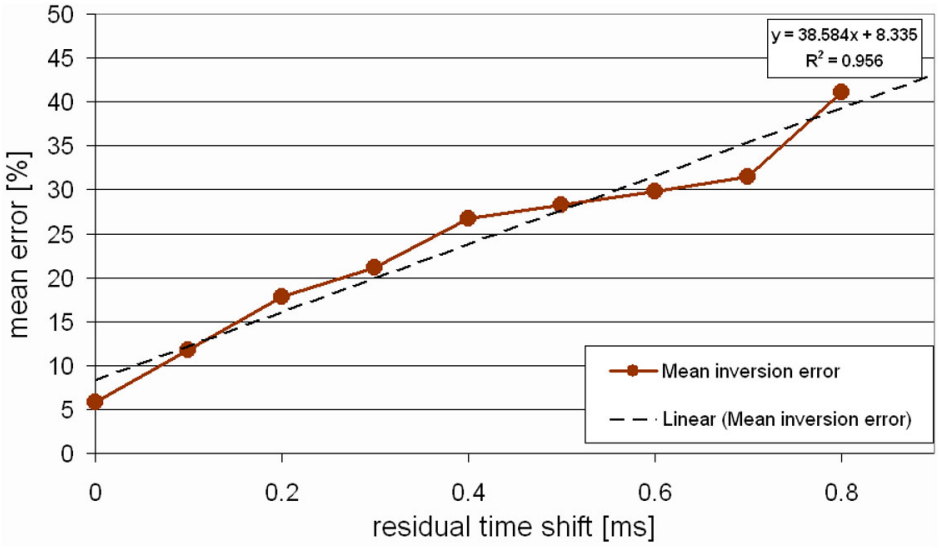

Figure 7.2: The average oil saturation change inversion error increases with rising residual time shifts (brown line), caused by the Mio-Pliocene and Quaternary channel. The error is normalised by the maximum absolute oil saturation change of 0.45 in the reservoir. The dashed line is the linear regression curve.

Besides quantifying the errors in the time-lapse interpretation, caused by overburden channels, this study also reveals problems of the current implementation of the pressure and saturation change inversion method. The calibration and selection of the correlation coefficient, C_S and C_P, is only reliable if the acquisition geometry is repeated perfectly. Small pressure changes of less than 200psi (1.38MPa) cannot be resolved with the current multi-attribute inversion method. These findings are discussed in Appendix A.

To summarise, the overburden channels cause errors in the time-lapse amplitude attribute, which affect the saturation change inversion. In addition, the accuracy of the inversion method decreases rapidly if the seismic data are not repeated perfectly. Therefore, two possible solutions could correct for that: improvement of the seismic repeatability and thus the input attribute or improvement of the inversion method. The former is investigated in Chapter 4 by means of a layer stripping method to eliminate the overburden and acquisition effects. The latter is not investigated in this thesis as it would have deviated the focus of this research too much. Suggestions for future research on the multi-attributes inversion method are made at the end of this chapter.

Layer stripping

Kennett's reflectivity method (Kennett, 1983) is simplified to be used on post-stack data in order to derive the reservoir reflectivity change from the time-lapse seismic data. However, the limitations for using this method on post-stack data are that only P-wave reflections are considered and partial stacks can only include data within a narrow slowness range. Furthermore, the method is valid under the condition that the subsurface is smoothly varying in the lateral direction. Despite these limitations, the key observations after testing this method on synthetic data are that the estimated reservoir reflectivity changes are well resolved for the mid and far offset stacked data, regardless of the acquisition non-repeatability. The spectral ratio performs well for the near offset stacks and the good repeat case, but the wide azimuth distribution at near offsets in the poor repeat data limits the layer stripping approach in the post-stack domain. It is shown that using the estimated reservoir reflectivity change attributes improves the saturation change estimates. The maximum errors of the saturation change estimates are reduced by factors of 1.6 and 2.4 for the poor and good repeat case respectively. The overall mean error of the difference between the estimated and the true saturation change, normalised by the maximum true saturation change, decreases from 4.4% to 2.1% when using the reflectivity change attributes derived by the layer stripping approach. A large improvement is made to reduce the standard deviation of the difference between the estimated and the true saturation change, which decreases from 28% to 18% for the poor repeat case and from 23% to 18% for the good repeat case (Figure 7.3). The layer stripping approach reduces the impact of the overburden channels in conjunction with a non-repeated acquisition geometry. The saturation change estimates become directly comparable to the estimates from the ideal repeated seismic data (Figure 7.3).

Stacked reservoirs

The focus shifts from overburden channels to stacked reservoirs and also away from the North Sea to a West of Africa deepwater field in Chapter 5. Time-lapse ampli-

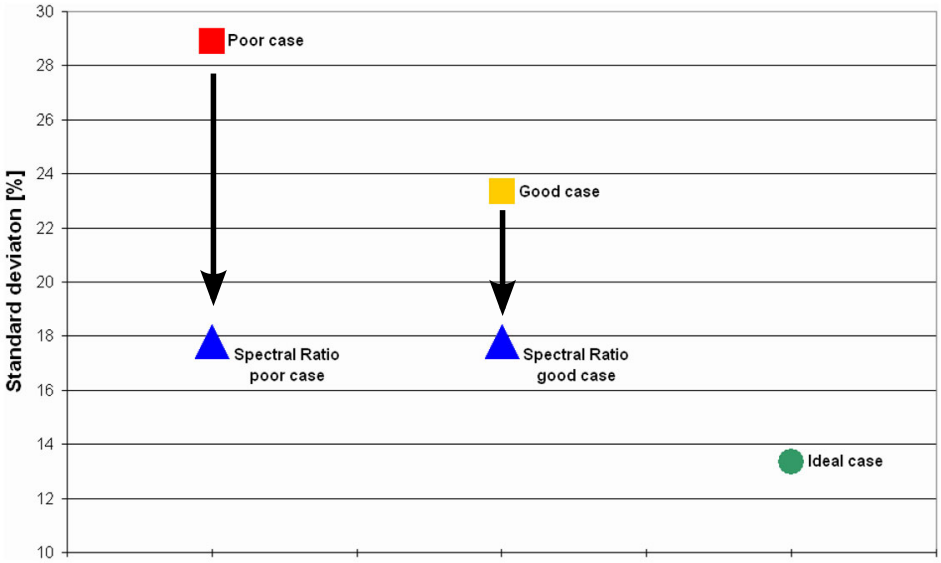

Figure 7.3: Standard deviation of the difference between the estimated and the true oil saturation change for three repeatability cases: ideal, good and poor. Values are normalised by the maximum absolute oil saturation change.

tude errors caused by a non-repeated acquisition geometry and an incorrect migration velocity model which does not include the production-induced changes in the stacked reservoir channels, Channel 1 and Channel 2, are investigated. It is found that the production-induced amplitude change at the base of Channel 1 imprints on the top and base horizon of the lower Channel 2. The magnitude of these imprints reduces to 40% at Channel 2. In addition, the study investigates the time-lapse amplitude error for the case of the production-induced P-wave velocity change inside Channel 1 not being taken into account when migrating the monitor seismic data. Neglecting the production-induced velocity change inside Channel 1 underestimates the time-lapse amplitude change by as much as 38% at the base of Channel 1. This maximum error reduces to 18% and 8% measured at the top and base of Channel 2, respectively, and thus decreases with increasing distance from Channel 1. A key finding of this study is that investigating those time-lapse attribute changes by seismic modelling is not a simple and straight forward process. Great care is needed to condition the ray-tracing model and to process the pre-stack seismic data. The most important recommendations to avoid technical problems during future seismic modelling studies are summarised later in this chapter.

Compacting reservoir and straining overburden

The impact of velocity changes in the overburden on the time-lapse amplitudes, caused by a compacting reservoir, is quantified in Chapter 6. Three domains, reservoir simulation, geomechanical modelling and seismic modelling, are linked together for this study. The integration of the geomechanical model with the ray-tracing model is difficult as there are no standard relations linking the static mechanical rock properties to the elastic properties of the ray-tracing model. The time-lapse amplitudes of the full and far offset stack data are underestimated on average by 9.4% and 4.23%, respectively, in the area of largest displacement being greater than six metres, in case the baseline velocity model is used to migrate the monitor data (Figure 7.4). The mean error is less than 2.3% in the area with a vertical displacement less than six metres. The amplitude attributes in the near and mid offset stack data are marginally affected by the overburden velocity change and show mean amplitude errors of less than 1.5% (Figure 7.4). It is thus recommended to used the near and mid offset stack amplitude attributes for quantitative amplitude studies. The full and far offset stack amplitudes should not be used to estimate the reservoir changes, as they do not coherently change across the reservoir, and amplitude effects do not solely originate from production-induced changes. The reservoir compaction leads to structural changes of the subsurface horizons. These changes do not affect the magnitude of the amplitude error, but the spatial position of the time-lapse changes. The pre-stack Kirchhoff time migration algorithm cannot fully account for these structural changes when using the baseline velocity model, and reflection events are misplaced in the monitor data. Maximum observed shifts are up to 100m after 20 years of production. This increases the location uncertainty for infill wells drilled to target unproduced reservoir zones.

Technical issues during large three-dimensional modelling studies

One key learning from conducting these seismic modelling studies is that a substantial amount of work is needed to combine data from the different domains into the ray-tracing model. Many custom scripts and tools have to been written to convert

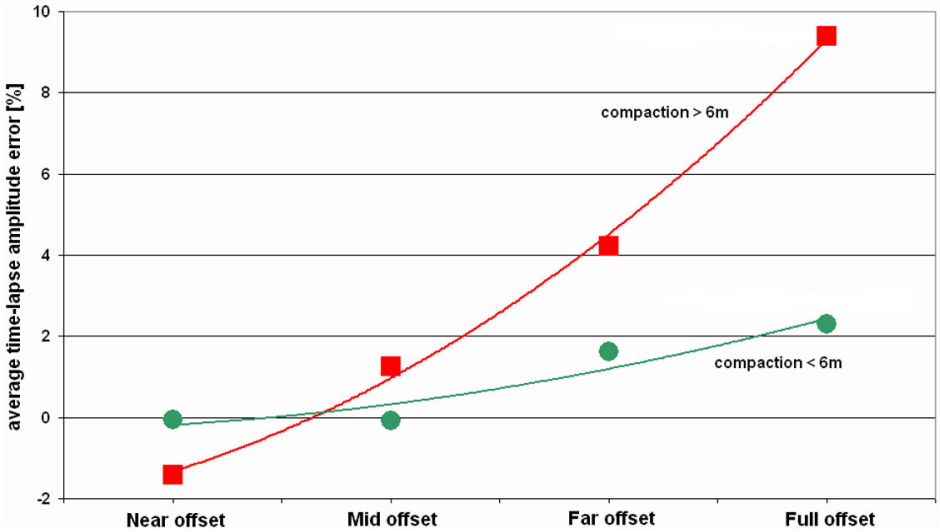

Figure 7.4: Mean time-lapse amplitude error caused by an unaccounted velocity change in the overburden for different limited offset stacks. The errors for the low initial porosity zone are marked with green circles, whereas errors at the zone of high initial porosity are marked with red squares. Simple curve fit lines (red and green) indicate the trend for each initial porosity zone.

data formats onto a common reference which are available within the ETLP group to facilitate future seismic modelling studies. Reservoir simulation data are typically on an i, j, k coordinate system, whereas the input horizons are referenced to the inlines and crosslines of the interpretation project. The navigation data on the other hand are in UTM format, however, sometimes in different projections when recorded several years apart or by different contractors. For example, the Nelson Field seismic navigation data are in two different UTM projections, depending on whether the data were acquired for Enterprise Oil or later on for Shell. Hence, it is crucial for the success of the seismic modelling and interpretation that all these data are on a common grid.

The size of the seismic modelling area is often limited by the computational facilities and the time available to build, model, process and interpret the data. Single seismic volumes are as large as 300GB for a modelling area of approximately 3km x 7km, when simulating a high resolution acquisition geometry as done in Chapter 5. The ray-tracing approach is fast and accurate as long as no fine scale heterogeneities are to be modelled and the subsurface changes are smooth. Therefore, heterogeneities which are less than one half of the dominant wave length in size are not accurately

represented in the velocity and density field. In case that many small objects need to be input into the seismic model, finite-difference seismic modelling is suggested as the model building is less labour intensive and even the smallest features of less than one metre are resolved, if the finite-difference mesh is adjusted accordingly. The trade-off is that finite-difference modelling is computational demanding.

7.1 Future research

Overburden heterogeneities

This work investigates a limited set of overburden heterogeneities, such as channels, stacked reservoirs and geomechanical active overburden. It is suggested to study additional overburden complexities, so that a database of their impact on the time-lapse interpretation can be established. Structures which could be studied next using this approach are:

- Sand channels at just above the reservoir.
- Polygonal faults above the reservoir.

Sand channels with faster seismic velocities than the surrounding rock can cause strong inter-channel multiples. If such channels are situated just above the reservoir, these multiples interfere with the reservoir reflection events, thus complicate the interpretation of reservoir changes. The Tay sand channels, for example, are just above the Nelson reservoir and are reported to be a strong source of intra-channel multiples, which are difficult to remove from the seismic data. Lateral variations of the channel thickness are reported to further distort the amplitudes at the reservoir level (Jonathan Brain, Shell, personal communication).

Polygonal faults are frequently observed in the Central North Sea (Lonergan and Cartwright, 1999; Fyfe et al., 2003), as well as in the Norwegian North Sea (Berndt et al., 2003). These faults cause focusing and defocusing effects in the seismic data, thus it is thought they potentially impede the quantitative interpretation of time-lapse attributes if the acquisition geometry is not ideally repeated. It is strongly advised to use finite-difference seismic modelling to study such overburden faults, as the ray-theory approach cannot handle the sharp discontinuities of these faults. It is furthermore suggested to study the impact of these overburden complexities on different time-lapse attributes.

Eventually, a spread sheet can be compiled that indicates the best attribute to be used for a given overburden heterogeneity and acquisition non-repeatability. In addition, seismic modelling of permanent sensor acquisition layouts, which reduces the $\Delta Source + \Delta Receiver$ non-repeatability as sensors are fixed, and increases the azimuthal coverage of the subsurface, are suggested to be incorporated in future studies. It is also suggested to perform a pre-stack depth migration on the synthetic seismic data to study whether further quantitative improvements are observed.

Pressure and saturation change inversion

An important outcome of this study is that the pressure and saturation change estimation method needs to be improved in order to perform reliably even with non-ideal repeated data. The coefficient calibration and selection process has to be refined so that noise in the seismic attribute does not result in arbitrary selections of attributes. Also, it has to be understood how the error and noise inherent in the time-lapse attributes propagates into the final reservoir change estimates. This study shows that the sensitivity to detect small reservoir changes needs to be improved. Alternatively, small changes that cannot be resolved should be effectively suppressed so they do not bias the result. Additional research needs to be done in order to understand how the seismic data processing affects the estimates, in particular with regards to using pre-stack or post-stack time-lapse attributes. Finally, studies should be carried out to investigate whether spatial filtering or smoothing of the attribute maps before the inversion improves the results.

Layer stripping

The layer stripping method presented in Chapter 4 is a promising step towards reducing the errors induced by a heterogenous overburden and acquisition non-repeatability. The performance of this method with post-stack data is good, considering that only three limited offset stacks are used. However, additional work is needed to evaluate whether the estimated reservoir reflectivity change improves if

the spectral ratio is calculated pre-stack. Future studies also need to investigate if the estimated reservoir reflectivity change varies depending on the frequency range over which the modulus of the spectral ratio is averaged. A computational efficient C++ or FORTRAN implementation is needed to cope with the increased number of discrete Fourier transforms that need to be calculated. An application to real data is necessary to confirm the good results this approach shows in the synthetic Nelson study.

Compacting reservoirs

The compacting reservoir study certainly needs additional research in order to determine the best strategy of how to estimate the pressure and saturation change in the reservoir. The initial study in Chapter 6 shows that there is need to further investigate the relation between the reservoir production, the stress and strain changes in the overburden, as well as the migration of the seismic data.

The geomechanical model should be refined and run in iterative coupling with the reservoir simulation model to best capture the production-induced changes. Water injection into the formation and especially for chalk reservoirs the associated water weakening and compaction has to be considered in the simulation model. Substantial work is needed to find accurate relations between the static mechanical rock properties and the elastic parameters. Frequently repeated surveys should be modelled to better constrain how potential time-lapse interpretation errors develop with time. Especially for this study, access to a large database of measured core data of reservoir and overburden rocks, as well as geological and reservoir simulation models will be beneficial. The amount of work spent on modelling the synthetic data is going to be extensive and should be done within a further project. In addition, it has to be investigated whether a combined inversion of time shifts and amplitude changes improves the pressure and saturation change estimation. Apparent lateral shifts, extracted from the time-lapse data, might be an additional constraint when interpreting the reservoir changes.

Finally, it is suggested that migration studies are performed to investigate whether the migration noise increases if the monitor migration velocity is updated, but still does not perfectly match the true case. This should include a study of the accuracy of current velocity modelling techniques, to determine the smallest velocity change that can be reliably resolved from the seismic data.

Appendix A

Instability of pressure and saturation inversion

A very brief summary of the main steps in estimating the saturation and pressure changes from time-lapse seismic attributes is given in Section 3.6. This appendix provides a detailed description of the actual workflow, from the seismic attribute to the final saturation change map. Limitations of the multi-attribute inversion technique are discussed to make the reader aware of the uncertainty involved in doing such inversion. The general workflow of the inversion process as outlines in Table 3.3 is thus discussed step by step.

A.1 Calibrating the time-lapse seismic attribute to the engineering data

First, the time-lapse attributes are extracted from the seismic data. These attributes do not have to be RMS amplitude. Every attribute that might be sensitive to either the saturation or the pressure change can be used. The next step is to calibrate the C_S and C_P coefficients at the selected well locations by solving Equation 3.10. The change in pressure, ΔP, and saturation, ΔS, at the well location is obtained from the reservoir simulation model in case of the formerly discussed synthetic Nelson

model. The average of the respective change is taken over 3x3 cells surrounding the well. However, downhole pressure measurements and water cut measurements will serve as input parameters in real data studies. The user also specifies uncertainties for the pressure and saturation change well measurements. Therefore, uncertainty is attached to each well measurements, which is assumed to obey a Gaussian distribution with the specified uncertainty being the standard deviation, σ, centred on the mean value of the distribution. Random values for the pressure and saturation change are then selected from this prior error distribution for each well, in order to calculate the C_S and C_P coefficients (Figure A.1). The C_S and C_P coefficients

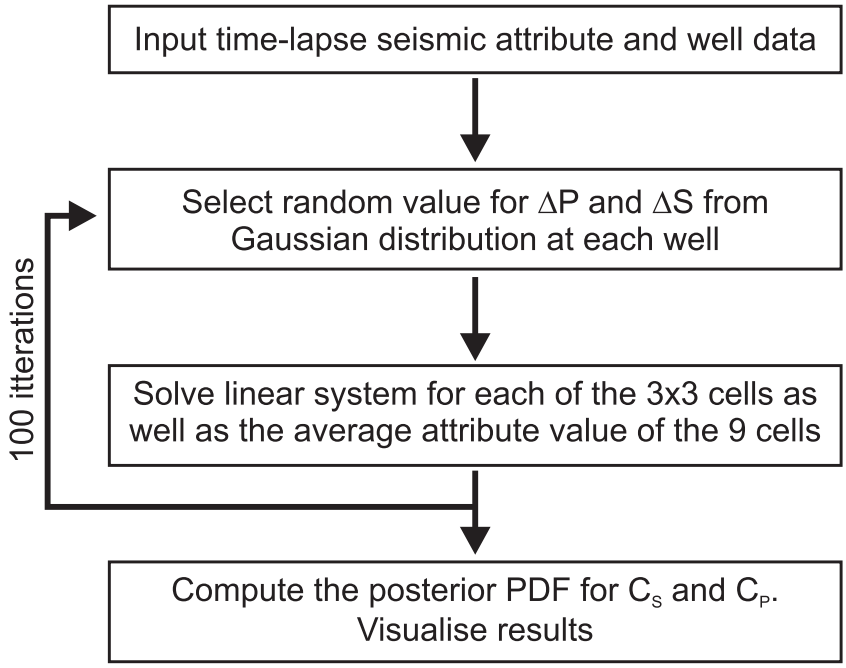

Figure A.1: Workflow for estimating the C_S and C_P coefficients from the time-lapse attributes and the well data (modified from Floricich (2006)).

are calculated using the time-lapse attributes surrounding the well location within a 3x3 cell array. In addition, the coefficients are also estimated using the average time-lapse attribute the 3x3 array at each well. The computation of the C_S and C_P coefficients is repeated one hundred times in order to obtain a posterior probability density function (PDF) for the coefficients at each well location (Figure A.2). The impact of the seismic data uncertainty on the C_S and C_P coefficients is seen in the middle row of Figure A.2. Each dot is the estimate of C_S and C_P for one time-lapse attribute from one specific cell around the well location. The horizontal error bars indicate the variability of the coefficient due to the uncertainty in the well data.

Finally, the initial time-lapse attribute is calculated at each well location by using the engineering data and the C_S and C_P coefficients and in turn compared to the actual input time-lapse attribute (Figure A.2 bottom panel).

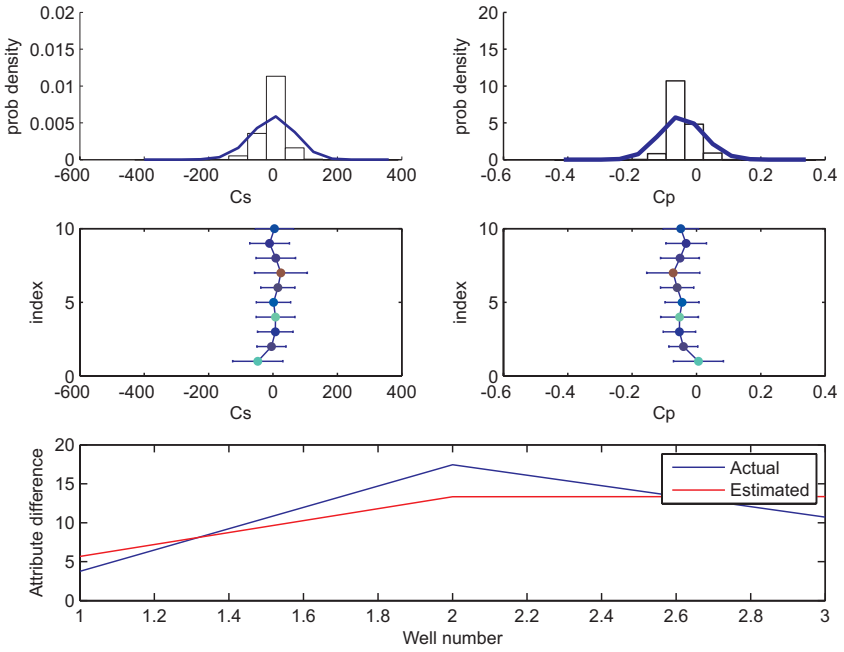

Figure A.2: Time-lapse multi-attribute calibration with well data. Top row: probability density function for the C_S and C_P coefficients. Middle row: Variability of C_S and C_P within the 3x3 attribute cell array as well as the mean attribute value over all calibration wells. Bottom row: Actual and estimated time-lapse attribute values at each well location.

A.2 Attribute selection by cross validation

The C_S and C_P coefficients could now be used to invert for the pressure and saturation change at each CMP bin across the field (Equation 3.12). However, the aim of using multiple attributes is to separate the pressure from the saturation change. Thus, the ability to separate between saturation and pressure change has to be assessed for each attribute combination. Amplitude attributes are extracted from five limited offset stacks, 1m-400m, 400m-800m, 800m-1200m, 1200m-1800m, 1800m-3000m, to be used in the following examples. These five offset stacks are roughly equivalent to the following angle stacks: 0°-6°, 6°-12°, 12°-18°, 18°-24° and 24°-32°. There are 26 combinations if five attributes are input to the inversion. An

automatic selection of the best attribute combination is thus most important. This problem is addressed by using the training wells and compute a cross-validation error for each attribute combination by using the workflow outlined in Figure A.3. The

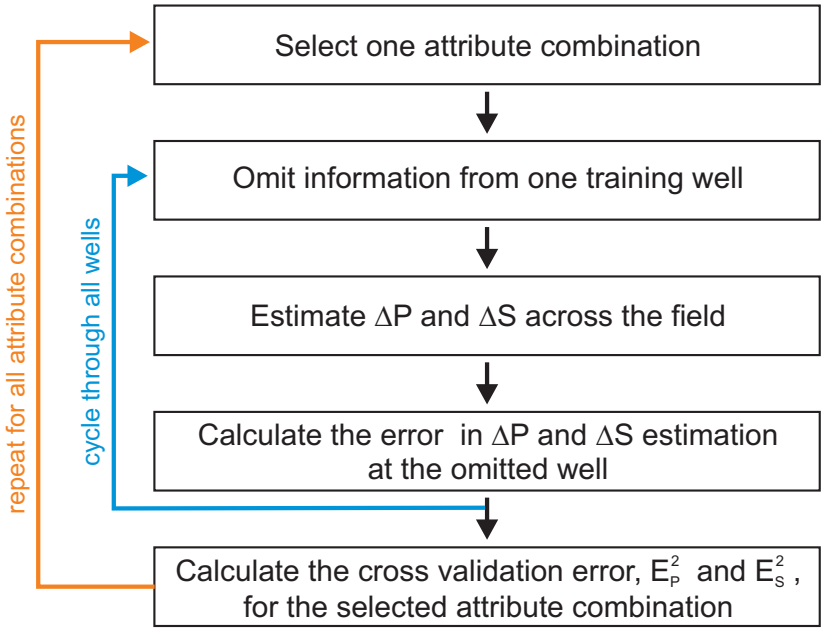

Figure A.3: Work flow diagram for the computation of the cross validation error.

pressure and saturation change is calculated for one chosen attribute combination, while omitting the information from one training well. In turn, the error between the predicted change in pressure, $\Delta P^{estimate}$, and saturation, $\Delta S^{estimate}$, and the actual change at the omitted well, ΔP^{actual} and Δs^{actual} respectively, is calculated. This step is repeated by cycling through all available training wells ($k = 1, ..., N$) and omitting one at a time. The cross validation error for the pressure and saturation change inversion, E_P^2 and E_S^2, respectively, is finally calculated for the selected attribute combination:

$$E_P^2 = \frac{1}{N}\sum_{k=1}^{N}(\Delta P_k^{actual} - \Delta P_k^{estimate})^2 \tag{A.1}$$

$$E_S^2 = \frac{1}{N}\sum_{k=1}^{N}(\Delta S_k^{actual} - \Delta S_k^{estimate})^2 \tag{A.2}$$

The final step consists of computing the cross validation error for each possible attribute combination and plotting into a diagram (Figure A.4). The top plot displays the cross validation error for the pressure change estimate, whereas the middle one shows the error for the saturation change estimate for each attribute combination.

The average cross validation error is obtained by multiplying the former two and is plotted in the bottom diagram of Figure A.4. The Nelson synthetic ray-tracing

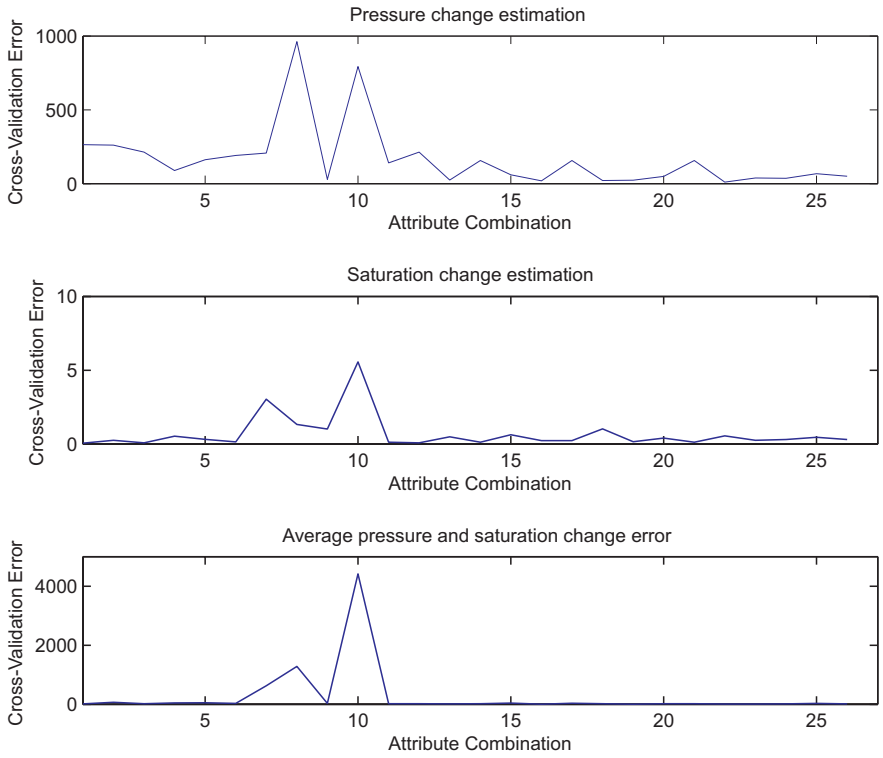

Figure A.4: Cross validation error panels calculated from the Mio-Pliocene ideal repeat time-lapse seismic data. Top: cross validation error in the pressure change estimate. Middle: cross validation error in the saturation estimate. Bottom: average cross validation error for pressure and saturation change estimate.

model with ideal repeat monitor survey is used to generate these cross validation error panels. The attribute combination with the lowest cross validation errors should provide the best estimate for the pressure and saturation change across the field. The combination with the lowest cross variation error for the ideal repeat case is number 16, which are the following offset stacks: 400m-800m, 800m-1200m and 1200m-1800m. Hence, these selected attributes are used to estimate the oil saturation change (Figure A.5). This estimate correlates well with the actual input taken from the reservoir simulation model (Figure 3.27(a)). The difference between the estimated change and the true saturation change from the simulation model is plotted in Figure A.6. The oil saturation change is slightly overestimated compared to the true case. However, the absolute estimation error is fairly constant at around ± 0.10. Other combinations with low cross validation error are also tested, however, no significant variations in the saturation change estimates are observed.

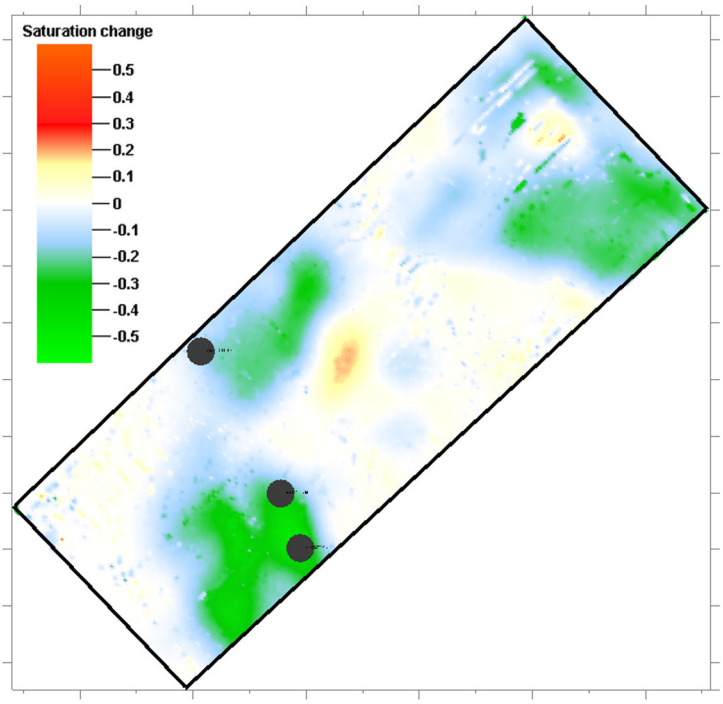

Figure A.5: Oil saturation change estimated from attribute combination number 16. The time-lapse monitor survey is acquired with the same acquisition geometry as the baseline survey. Black dots indicate the well positions.

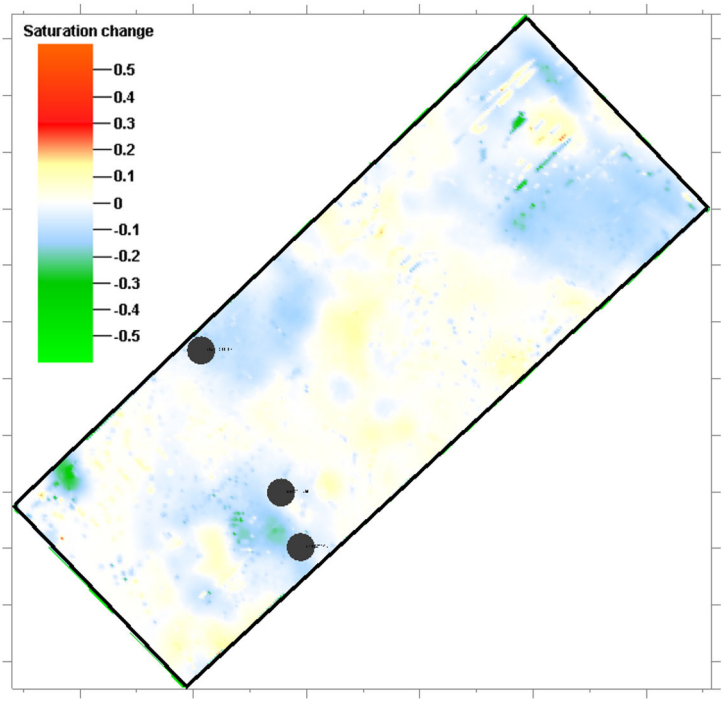

Figure A.6: Difference between the oil saturation change estimated from the ideal repeat data and the input saturation change from the simulation model. Black dots indicate the well positions.

The approach of using the training wells and consequently performing a blind test to compute an overall cross variation error is working satisfactorily for this ideal repeat synthetic time-lapse data.

The Mio-Pliocene channel poor repeat time-lapse seismic data is consequently used to repeat the calculation of the C_S and C_P coefficients (Figure A.7). The variability of the coefficients with the seismic data at different well locations is much increased over the former presented ideal repeat case. The C_S and C_P coefficients are highly variable around their mean value (Figure A.7 middle plot). However, the difference between the actual time-lapse attribute and the estimated attribute is good overall (Figure A.7 bottom diagram). The poor repeatability of the monitor survey

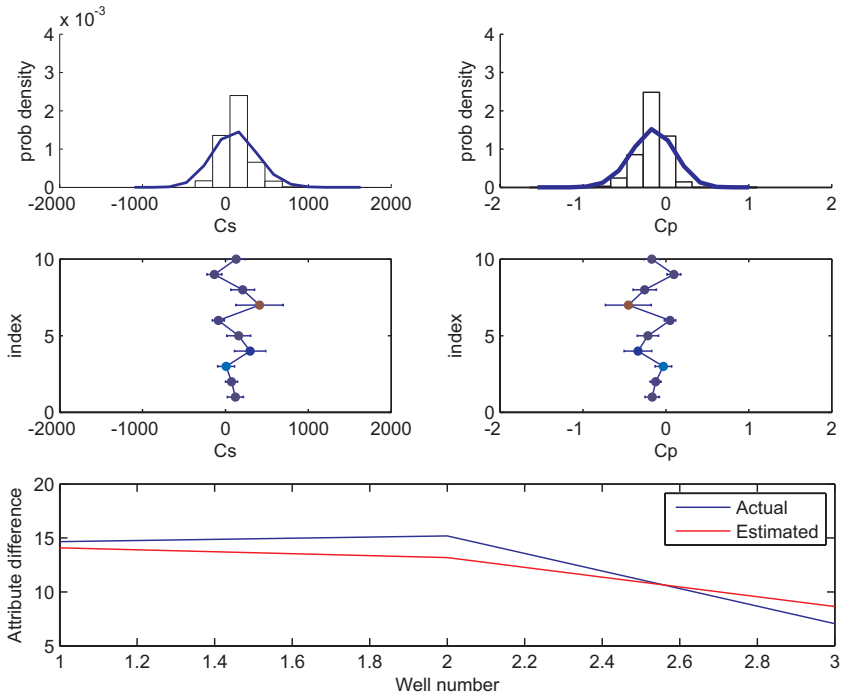

Figure A.7: Time-lapse multi-attribute calibration with well data for the Mio-Pliocene channel, poor repeat case. Top row: probability density function for the C_S and C_P coefficients. Middle row: Variability of C_S and C_P within the 3x3 attribute cell array as well as the mean attribute value over all calibration wells. Bottom row: Actual as well as estimated time-lapse attribute values at each well location.

therefore effects the estimation of the C_S and C_P coefficients at the well locations. The cross validation error is in turn calculated for the poor repeat time-lapse data (Figure A.8). The variability of the cross validation error for the poor repeat case is much increased over the ideal repeat case (compare Figure A.8 and A.4), which

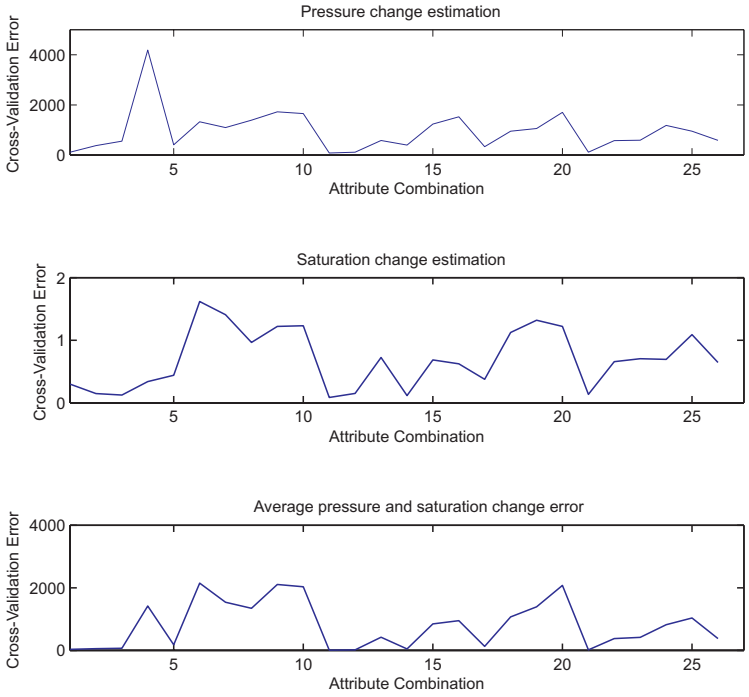

Figure A.8: Cross validation error panels calculated from the Mio-Pliocene poor repeat time-lapse seismic attributes. Top: cross validation error in the pressure change estimate. Middle: cross validation error in the saturation estimate. Bottom: average cross validation error for pressure and saturation change estimate.

indicates that the repeatability and thus the time-lapse seismic data quality have a noticeable impact on the calibration step. The attribute combination with the lowest cross validation error for the poor repeat survey is now number 11 (1m-400m, 400m-800m, 800m-1200m offset stacks) and not combination number 16 as for the ideal repeat case. The oil saturation change estimate using the suggested combination number 11 (Figure A.9(a)) does not match the change from the reservoir simulation model (Figure 3.27(a)). However, the estimate improves considerably by using the attribute combination number 16 (Figure A.9(b)). Other attribute combinations are further tested for the poor repeat time-lapse data, but rejected due to a poor match of the saturation change estimate to the model input. Indeed, the attribute combination number 16 (400m-800m, 800m-1200m, 1200m-1800m offset stacks) has the best match for the poor, the good and the ideal repeat seismic data, even though the cross validation error is not minimised. Therefore, this combination is used throughout the overburden study of the Nelson Field data.

This discussion shows that the calibration of the C_S and C_P coefficients depends on the repeatability of the time-lapse data and thus the data quality. The ability

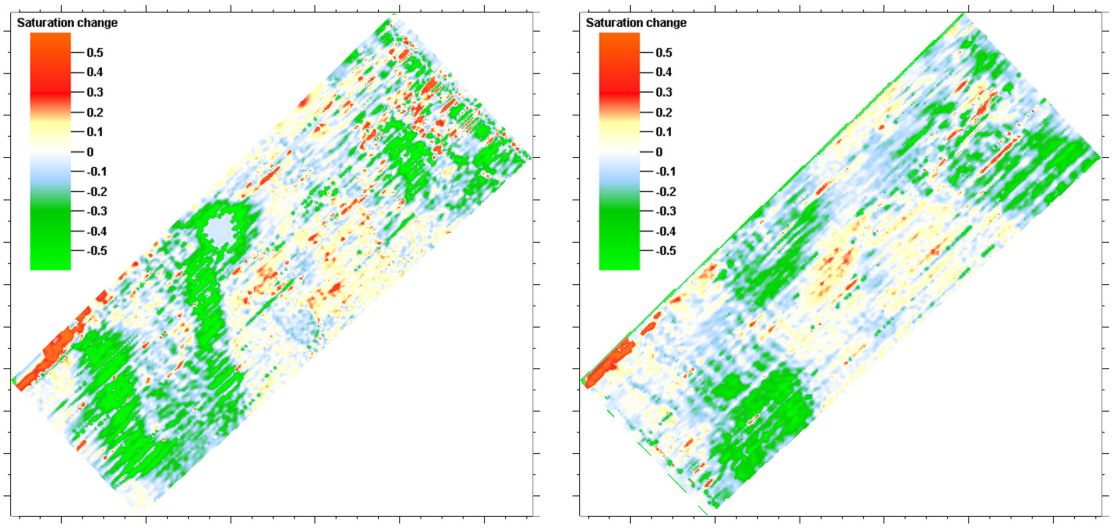

(a) (b)

Figure A.9: The oil saturation change estimate using poor repeat time-lapse data depends on the attribute combination used: (a) attribute combination number 11 (b) attribute combination number 16.

to compare the inversion result with the true reservoir change is not given in reality and will make it difficult to decide on the best attribute combination to use. Various other sources of time-lapse seismic noise, such as non-repeated multiples, source signature variation, water velocity changes or sail line dependent swell noise can further impact the calibration and inversion process. On the other hand, the calibration results might improve if more wells are used. The number of wells is limited to three in the current study and it is acknowledged that this is indeed a small number. To conclude this section, it has to be mentioned that no method has been suggested so far that allows one to assess possible calibration errors due to data uncertainty and therefore identifies usable attribute combinations, even in the presence of noise.

A.3 Estimation of the pressure change in the case of small absolute pressure variation

It is briefly mentioned in Section 3.7 that the small pressure change at the Nelson Field is beyond the detection ability of the multi-attribute pressure and saturation

change inversion technique. Two figures illustrate the problem for an inversion in case of a dominant saturation change signal where the pressure change estimate is influenced by the saturation change (Figure A.10). The saturation change imprint on the estimated pressure change is clearly seen whether using the ideal- or poor repeated time-lapse data, Figure A.10(a) and A.10(b), respectively. The actual

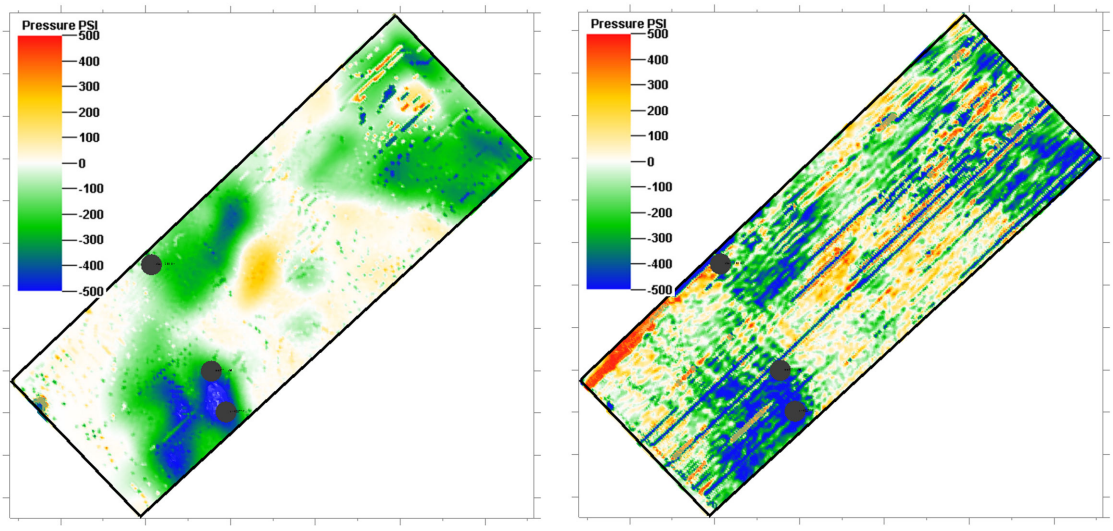

(a) (b)

Figure A.10: Estimate of the pressure change using data from (a) the ideal repeat monitor survey and (b) the poor repeat survey.

pressure change from the simulation model, however, is not resolved (Figure 3.26). This pressure change estimate is not trustworthy, thus it is not taken into consideration while inverting for the oil saturation change. Moreover, it is found that the saturation change estimates do not differ whether the pressure change is neglected during the inversion or honoured in the inversion. This shows that the pressure change has only a marginal influence on the seismic attribute for the Nelson Field study.

Appendix B

Layer stripping workflow and discussion of earlier simple application by Spetzler and Øyvind (2006)

This appendix discusses the practical aspects of how to estimate the reflectivity change from post-stack seismic data using the spectral ratio.

B.1 Calculating the spectral ratio from post-stack seismic data

Assume a seismic record in the time domain starting at time zero with two seismic events recorded, event $e_1 = e(t_1)$ at the two way traveltime t_1 and event $e_2 = e(t_2)$ at the two way traveltime t_2 (Figure B.1(a)). These two reflection events are equivalently described in the frequency domain instead of the time domain, indicated by the red box in Figure B.1(a) (for example, a fast Fourier Transform (FFT) will perform the mapping of the events from the time to the frequency domain). Moreover, this seismic record is the equivalent of the generalised reflectivity, r_D^{02}, of a

stacked layered medium with reflections occurring at two interfaces. Any source and receiver terms are neglected initially in this analysis. The super script 02 represents the reflectivity for the complete region from the surface, index 0, down to the second interface, index 2. According to Section 4.1, the total seismic response,

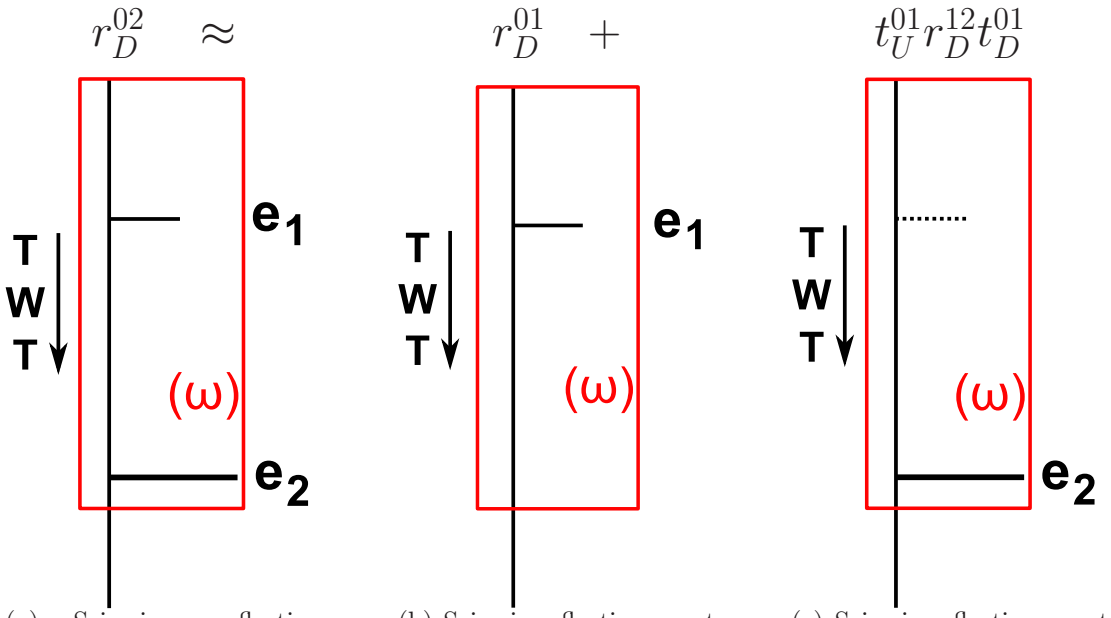

(a) Seismic reflection events e_1 and e_2

(b) Seismic reflection event e_1

(c) Seismic reflection event e_2

Figure B.1: Schematic representation of the generalised reflection addition rule used in order to generate a seismic trace consisting of two reflection events, e_1 and e_2.

r_D^{02}, is the addition of the generalised reflectivity of the first layer r_D^{01} and the second layer, $t_U^{01} r_D^{12} t_D^{01}$, indicated at the top of Figure B.1(b) and B.1(c), respectively. Figure B.1(b) represents the seismic response for the first layer, thus shows only the event, $e(t_1)$. Figure B.1(c) outlines how the reflection response of the second layer is constructed. In the later case, interface 1 is marked with a dashed line, indicating that only transmission effects, t_U^{01} and t_D^{01}, are considered at this interface, whereas the reflection at interface 2 is causing the seismic event, $e(t_2)$. However, the problem is that real data always contain both events, e_1 and e_2, in the seismic trace. Therefore, it is not possible to separate the response into its two constituents by taking the FFT of the complete seismic trace (red box in Figure B.1(a)) The situation as shown in Figure B.1(c) where a reflection occurs at one specific interface and transmission at the remaining interfaces does not occur in reality and the usage

of the FFT has to be adjusted accordingly.

Figure B.2 consequently illustrates how the plane wave propagation in stratified media is used in order to derive each factor of the generalised reflectivity summation from the recorded seismic trace in the time domain. This figure sketches an idealised

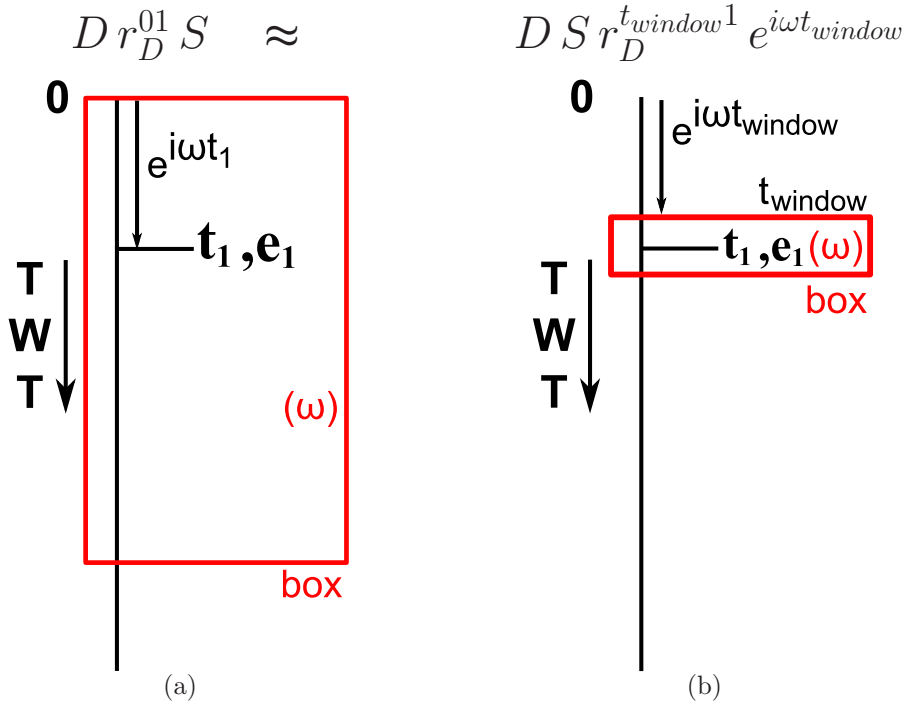

Figure B.2: Schematic representation of breaking the generalised reflectivity into its additive parts for the first reflection event, e_1, of the layered media.

seismic trace of the first reflection event, e_1, in the time domain, as recorded at t_1 (TWT). Hence, the generalised reflectivity, r_D^{01}, is the product of the source and receiver term with the reflectivity, $D\,r_D^{01}\,S$, in the frequency domain. The red box encloses the part of the time series that is transferred into the frequency domain, which includes the local reflection event at interface 1 and the time delay due to propagating from the surface down and up again. However, these effects can be approximated when the seismic reflection event is transferred within a narrow time window into the frequency domain (Figure B.2(b)). Nevertheless, the time window around the reflection event, e_1, has to be large enough to capture the full wavelet. No time delay due to the wave propagation from the surface to the onset of the time window is taken into account in this case. However, a time delay due to propagation is equivalent to a phase shift, $e^{i\omega t_{window}}$, because plane waves are considered. Therefore, this phase shift is multiplied with the Fourier transform of the windowed

signal, $E_1(\omega)$, in order to obtain an approximate representation of the time series event in the frequency domain, as in Figure B.2(a). This phase shift is determined by the difference between time zero and the time of the onset of the window, t_{window}. Nevertheless, the small time window centred around the seismic response creates errors in the frequency domain, because the time series is sharply truncated at both ends. Ringing in the frequency domain is the result, which is known as Gibbs Phenomenon. The windowed time series needs to be tapered on both sides, which reduces the error, but widens the spectrum. Hence, calculating the Fourier transform of the time series within such a narrow tapered window around the reflection signal and subsequently adjusting the phase to account for the wave propagation is an approximation. This does not fully substitute the Fourier transform calculated in a large time window. Figure B.3 illustrates the equivalent for the case of the second reflection event, e_2, and therefore presents an approximation to recover the $t_U^{01} r_D^{12} t_D^{01}$ term from the seismic time series recorded at the surface. Figure B.3(a) represents

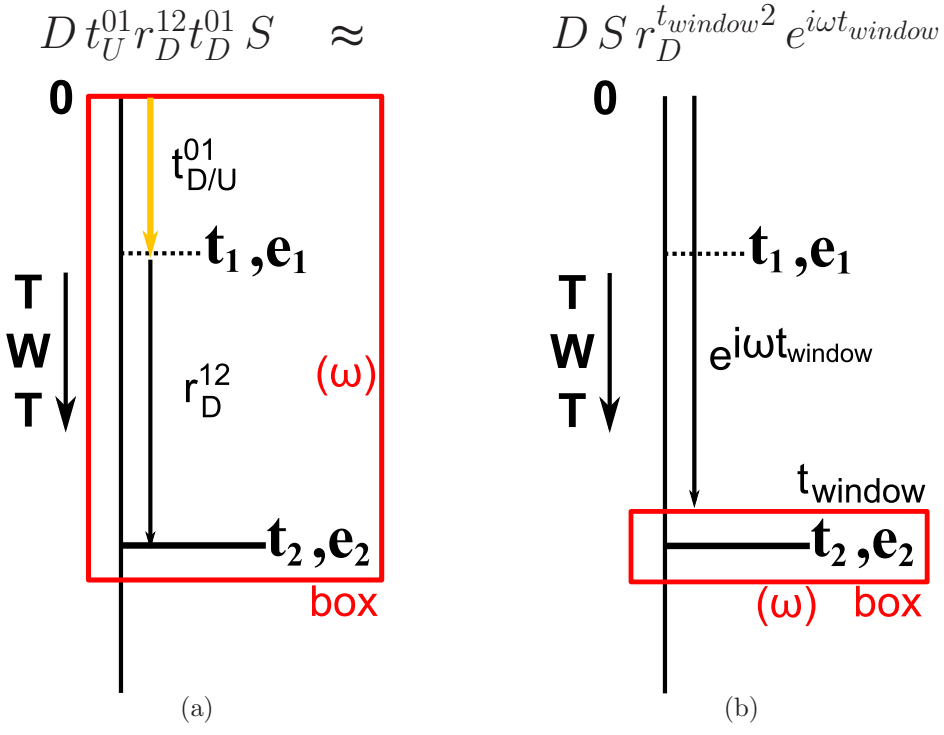

Figure B.3: Schematic representation of breaking the generalised reflectivity into its additive parts for the second reflection event, e_2, of the layered media.

transmission only at interface 1 (dashed line) and reflection at interface 2. In this hypothetical situation, the reflection event in the time domain, e_2 is transferred into

the frequency domain by taking the Fourier transform of the time series within the red box (Figure B.3(a)). Hence, the reflection event 2 represented in the frequency domain, $E_2(\omega)$, is expressed as: $E_2(\omega) = D\, t_U^{01} r_D^{12} t_D^{01}\, S$. On the other hand, a real seismic trace records the reflection event e_1 at earlier times as well, thus taking the Fourier transform of the complete trace does not result in the expression for $E_2(\omega)$, but rather for the generalised reflectivity of the stack of layers. Therefore, to obtain only $E_2(\omega)$ the reasoning is similar to the previous case. All transmission and reflection effects are naturally included in the wavelet e_2 recorded at time t_2. Hence, the Fourier transform of the wavelet inside the narrow time window in Figure B.3(b) includes these transmission and reflection effects, as well as the phase shift from the window onset to the reflection, $D\, r_D^{t_{window} t_2}\, S$. The reflection event 2 is approximated in the frequency domain, $E_2(\omega)$, by applying the Fourier transform to the reflection event extracted in a narrow, tapered time window and adjusting the phase to consider the additional phase shift: $D\, S\, r_D^{t_{window} 2}\, e^{i\omega t_{window}}$. The individual terms of the generalised reflectivity of this two layer example (Figure B.4) are thus approximated from the complete seismic trace by calculating the Fourier transform of the individual reflection events in a narrow time window and multiplying a phase shift to account for the propagation in between reflection events.

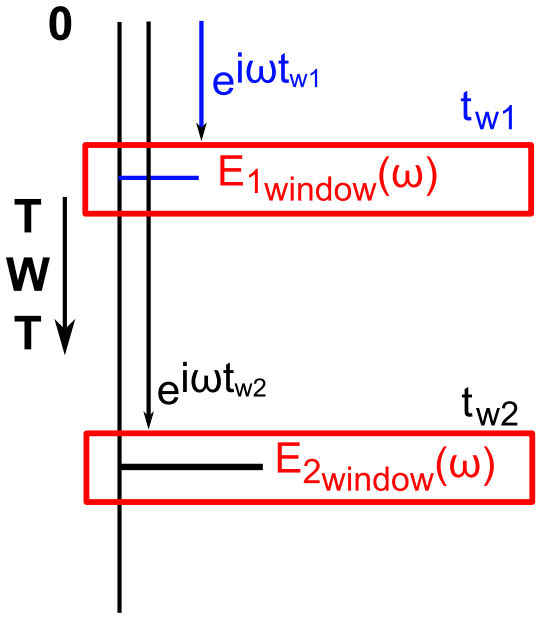

Figure B.4: Decomposition of a seismic reflection series into the terms forming the generalised reflectivity.

This general two layer case is easily expanded into a multi-layer case. These extracted terms labelled as $E_n(\omega)$, with n referring to the different reflection events are equivalent to the terms B_3, B_4 and M_3, M_4, used previously. The spectral ratio and the reservoir reflectivity change (Equation 4.15) can thus be estimated.

B.2 Practical workflow for the layer stripping approach

The theory of calculating the spectral ratios from stacked data is discussed in the previous section. A brief overview of the practical workflow, from picking seismic events to calculating the Fourier transform is given in this section. The general workflow used to derive the spectral ratio is outlined in Table B.1. First, the selected

pick seismic reflection event (time domain)
⇓
extract seismic data inside a window centred around the picked event
⇓
FFT of extracted time series
⇓
adjust the phase using the picked traveltime of the reflection event
⇓
calculate the spectral ratio (frequency domain)

Table B.1: The workflow for calculating the spectral ratio using seismic reflection events.

reflection events are picked in the synthetic post-stack seismic data generated from the ray-tracing model with the Mio-Pliocene channel as well as the Quaternary channel in the overburden. The two way traveltimes for the horizon picks are then exported into an ascii file and later used to correct the phase, before forming the spectral ratios (Equation 4.13). Figure B.5 shows one inline section through a

post-stack seismic data cube and the orange line marks the traveltime picks of the Sele reflection event. Subsequently, the seismic data inside a 32ms window centred

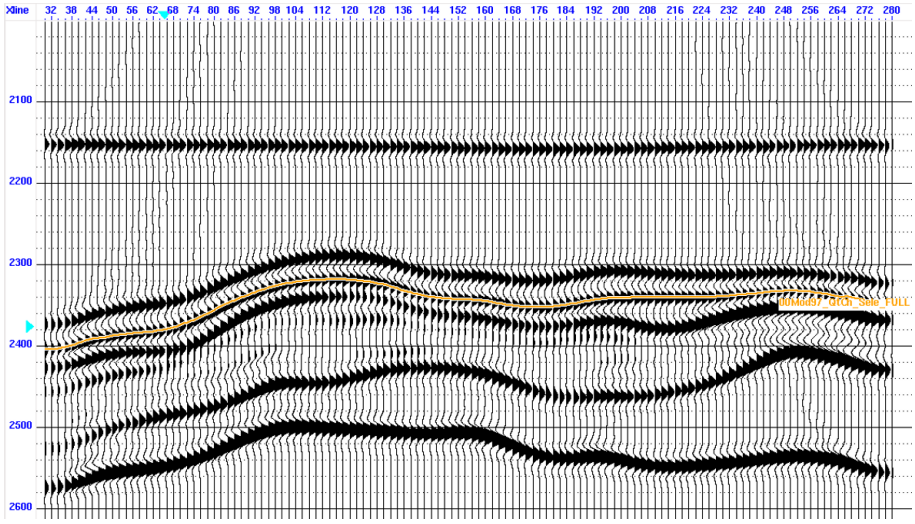

Figure B.5: Inline section of seismic data showing the Sele reflection traveltime being picked for further analysis.

around the picked Sele reflection event are extracted and exported as SEG-Y file (Figure B.6). This extracted time series of the Sele reflection event is then tapered at the edges using a cosine function and in turn transferred to the frequency domain by a Fast Fourier Transform. The picked two way traveltime is used to calculate the phase shifts for each of the discrete frequencies in the FFT which are in turn multiplied with the fourier transformed of the Sele reflection event. The previously discussed Figures B.2 and B.3 illustrate this step as well. The above described steps

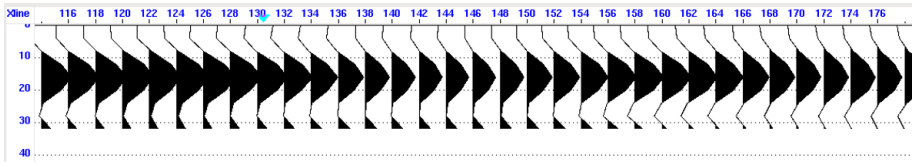

Figure B.6: Extracted seismic data inside a 32ms time window centred around the Sele peak reflection event.

are in turn done for all traces, thus the reflection events are transformed from the time domain into the frequency domain. The spectral ratio is then computed by multiplication and division of these complex valued Fourier transforms.

B.3 Published approach using the spectral ratio method

The spectral ratio method has also been reportedly used by Spetzler and Øyvind (2006) in order to separate overburden effects from the time-lapse signal similar to the study presented in this chapter. Their approach consists of using upgoing and downgoing wavefields as described by Wapenaar and Berkhout (1989), whereas the spectral ratio presented in this chapter is derived using the generalised reflectivity approach described by Kennett (1983). Spetzler and Øyvind (2006) test the spectral ratio on a simple 2D model, where non-repeatability is introduced by a geomechanically changing overburden and a constant shift of the source and receiver positions. Furthermore, the authors estimate the change in reflection coefficient at two separate interfaces from pre-stack as well as near offset post-stack gathers. The fit of the estimated reflectivity change at interface 6 to the theoretical one is good, however, they obtain poor estimates at interface 7 (Figure B.7).

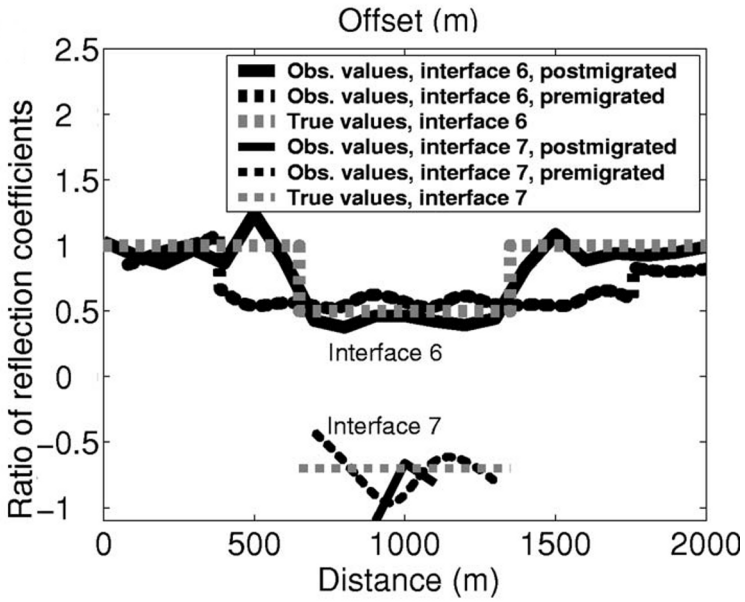

Figure B.7: Pre- and post-stack estimated reflectivity change at interface 6 and 7 from synthetic 2D time-lapse data (from Spetzler and Øyvind (2006)).

In addition to this simple synthetic example, the authors apply the spectral ratio method to real 2D seismic data from the Troll West field, offshore Norway. The reflectivity change estimated at two reflectors in the reservoir is very spiky and strongly

varies around a mean value of one (Figure B.8). Hence, their conclusion is that a change of ±10% indicates that there are no significant time-lapse effects. These

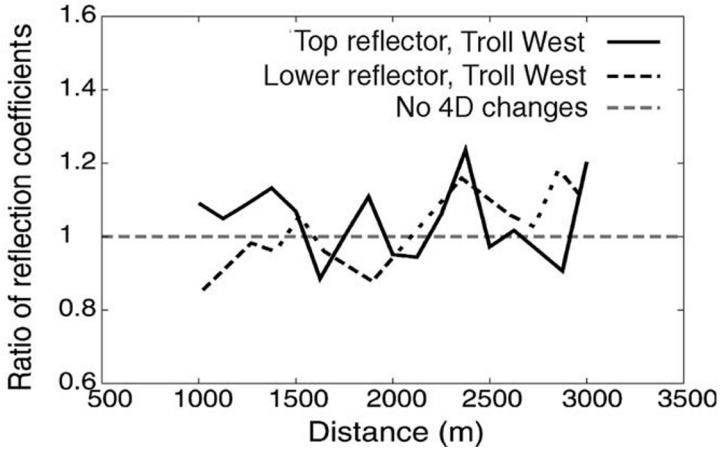

Figure B.8: Estimate of reflectivity change at the Troll West field for two reflectors in the gas province (from Spetzler and Øyvind (2006)).

results have to be compared to the study outlined in this chapter where changes as low as 2% are recovered from the seismic data, However, it is acknowledged that synthetic data are used. Spetzler and Øyvind (2006) calculated the spectral ratio also for the gas-fluid interface of the Troll West data, where no lateral change in reflectivity is to be expected. The result is poor and the spectral ratio fails to estimate the reflectivity change correctly. Moreover, the estimated reflectivity change is highly unstable and estimates vary between 0.6 and 1.2 (Figure B.9).

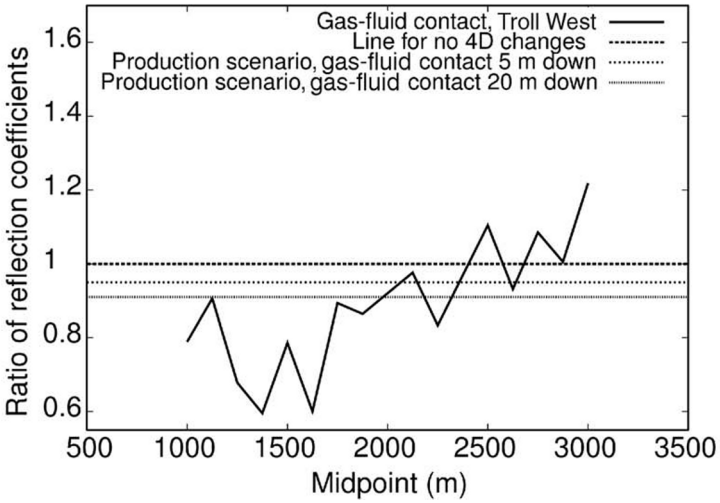

Figure B.9: Estimate of reflectivity change at the gas-fluid interface at the Troll West field (from Spetzler and Øyvind (2006)).

These results do not compare to the reflectivity change estimated for the Sele horizon presented in section 4.2, where the reflectivity changes derived by the spectral ratio barely exceed an absolute error of 0.05 for a laterally non-varying reflection event. Therefore, it is considered that the implementation of the spectral ratio as presented in this chapter is an improvement over the described application by Spetzler and Øyvind (2006), which is not sufficiently convincing and furthermore has not been tested in a full 3D framework.

References

Aki, K. and Richards, P. (2002). *Quantitative Seismology*. Freeman, San Francisco, Calif., second edition.

Al-Maskeri, Y. (2005). *Quantitative 4D Seismic for the Analysis of Reservoir Heterogeneity and Connectivity*. Ph.D., Heriot-Watt University.

Alterman, Z., Aboudi, J., and Karal, F. (1970). Pulse propagation in a laterally heterogeneous solid elastic sphere. *Geophysical Journal International*, 21(3):243–260.

Anderson, J., Cartwright, J., Drysdall, S., and Vivian, N. (2000). Controls on turbidite sand deposition during gravity-driven extension of a passive margin: examples from Miocene sediments in Block 4, Angola. *Marine and Petroleum Geology*, 17(10):1165–1203.

Angelov, P., Arts, R., and Wapenaar, K. (2007). 4D Seismic Pore Pressure Inversion - The Effect of Production Induced Overburden Changes. In *69nd Mtg.*, page P076, London, UK. Eur. Assn. Geosci. Eng.

Anvik, H. and Gibson, W. (1987). Drilling and Workover Experiences in the Greater Ekofisk Area. In *SPE/IADC Drilling Conference*, New Orleans, Louisiana.

Armstrong, T., McAteer, J., and Connolly, P. (2001). Removal of overburden velocity anomaly effects for depth conversion. *Geophys. Prosp.*, 49(01):79–99.

Bancroft, J. (2007). *A Practical Understanding of Pre- and Poststack Migrations*, volume 2 of *Course Notes Series*. Soc. of Expl. Geophys.

Barkved, O. and Kristiansen, T. (2005). Seismic time-lapse effects and stress changes: Examples from a compacting reservoir. *The Leading Edge*, 24:1244–1248.

Batzle, M. and Wang, Z. (1992). Seismic properties of pore fluids. *Geophysics*, 57(11):1396–1408.

Baysal, E., Kosloff, D., and Sherwood, J. (1983). Reverse time migration. *Geophysics*, 48(11):1514–1524.

Beaubouef, R. T., Garfield, T., and F.J., G. (1998). Seismic stratigraphy of depositional sequences: High resolution images from a passive margin slope setting, offshore West Africa. *AAPG Bulletin*, 82:1890.

Behrens, M., Brain, J., van Waarde, J., and Beckers, J. Kechichian, J. (2009). Breathing New Life into a Declining Field - 4D and Integration at Gannet D. In *71st Mtg.* Eur. Assn. Geosci. Eng.

Berndt, C., Bünz, S., and Mienert, J. (2003). Polygonal fault systems on the mid-Norwegian margin: a long-term source for fluid flow. *Geological Society, London, Special Publications*, 216(1):283–290.

Bertrand, A. and MacBeth, C. (2003). Seawater velocity variations and realtime reservoir monitoring. *The Leading Edge*, 22(4):351–355.

Bertrand, A., McQuaid, S., Bobolecki, R., Leiknes, S., and Ro, H. (2005). A high resolution workflow for 4D-friendly analysis: application to gas-oil contact monitoring at Troll West. In *75th Ann. Internat. Mtg.*, pages 2422–2425. Soc. of Expl. Geophys.

Bittleston, S., Canter, P., Hillesund, Ø., and Welker, K. (2000). Marine seismic cable steering and control. In *62nd Mtg.*, pages L–16, Glasgow, Scotland. Eur. Assn. Geosci. Eng.

Boyd-Gorst, J., Fail, P., and Pointing, L. (2001). 4-D time lapse reservoir monitoring of Nelson Field, Central North Sea: Successful use of an integrated rock physics model to predict and track reservoir production. *The Leading Edge*, 20(12):1336–1350.

Brevik, I. (1999). Rock model based inversion of saturation and pressure changes from time lapse seismic data. *SEG Technical Program Expanded Abstracts*, 18(1):1044–1047.

Byerley, G., Pedersen, J., Roervik, K., Ranaweera, K., and A., J. (2006). Reducing risk and monitoring water injection using time-lapse (4D) seismic at the Ekofisk field. In *76rd Ann. Internat. Mtg.*, pages 3210–3214. Soc. of Expl. Geophys.

Calvert, R. (2005a). 4D technology: where are we, and where are we going? *Geophys. Prosp.*, 53:161–171.

Calvert, R. (2005b). *Insights and methods for 4D reservoir monitoring and characterization: 2005 Distinguished Instructor Short Course*, volume no. 8 of *Distinguished instructor series*. Society of Exploration Geophysicists, Tulsa, Okla.

Calvert, R., Hatchell, P., and Jones, C. (2002). 4D acquisition geometry requirements and QA. In *64th Mtg.*, pages A–17. Eur. Assn. Geosci. Eng.

Calvert, R. and Wills, P. (2003). The case for 4D monitoring with sparse OBC. In *65th Mtg.*, pages A–15. Eur. Assn. Geosci. Eng.

Carcione, J. M., Herman, G. C., and ten Kroode, A. P. E. (2002). Seismic modeling. *Geophysics*, 67(4):1304–1325.

Chen, C.-T. and Millero, F. J. (1977). Speed of sound in seawater at high pressures. *The Journal of the Acoustical Society of America*, 62(5):1129–1135.

Chin, L. Y. and Nagel, N. B. (2004). Modeling of Subsidence and Reservoir Compaction under Waterflood Operations. *International Journal of Geomechanics*, 4(1):28–34.

Coléou, T., Hoeber, H., and Lecerf, D. (2002). Multivariate geostatistical filtering of time-lapse seismic data for an improved 4-D signature. *SEG Technical Program Expanded Abstracts*, 21(1):1662–1665.

Corzo, M. (2009). *Quantitative analysis of a dynamically compacting reservoir*. Ph.D. dissertation submitted, Heriot-Watt University.

Corzo, M. and MacBeth, C. (2006). Towards accurate quantitative monitoring of compacting reservoirs using time-lapse seismic. *SEG Technical Program Expanded Abstracts*, 25(1):3190–3194.

Cox, B. and Hatchell, P. (2008). Straightening out lateral shifts in time-lapse seismic. *First Break*, 26:93–98.

Curtis, T., Smith, P., Combee, L., and Olafsen, W. (2002). Acquisition of highly repeatable seismic data using active streamer steering. *SEG Technical Program Expanded Abstracts*, 21(1):81–84.

Del Grosso, V. A. (1974). New equation for the speed of sound in natural waters (with comparisons to other equations). *The Journal of the Acoustical Society of America*, 56(4):1084–1091.

Dix, C. H. (1955). Seismic Velocities from surface measurements. *Geophysics*, 20(1):68–86.

Domes, F., MacBeth, C., and Brain, J. (2009). The Influence of Overburden on Time-Lapse Saturation Interpretation. In *71th Mtg.*, page Y002, Amsterdam, Netherlands. Eur. Assn. Geosci. Eng.

Dong, W., Bouchon, M., and Toksöz, M. N. (1995). Borehole seismic-source radiation in layered isotropic and anisotropic media: Boundary element modeling. *Geophysics*, 60(3):735–747.

Ebaid, H., Tura, A., Nasser, M., Hatchell, P., Smit, F., Payne, N., Herron, D., Stanley, D., Kaldy, J., and Barousse, C. (2008). First dual-vessel high-repeat GoM 4D survey shows development options at Holstein Field. *The Leading Edge*, 27(12):1622–1625.

Eikeberg, O.-A. and Rigmor, M. (2002). 1D modelling - a quantitative tool in 4D analysis on Troll West oil province? In *64th Mtg.*, page P314. Eur. Assn. Geosci. Eng.

Eiken, O., Aronsen, H., Furre, A., Klefstad, L., Nordby, L., Osdal, B., and Skaar, M. (2003a). Seismic Monitoring of the Heidrun, Norne and Midgard Fields Using Steerable Streamers. In *65th Mtg.*, page A30, Stavanger, Norway. Eur. Assn. Geosci. Eng.

Eiken, O., Aronsen, H., Furre, A.-K., Klefstad, L., Nordby, L., and Osdal, B. (2002). Repeated seismic surveys from the Norwegian Sea using new streamer technology. In *72nd Ann. Internat. Mtg.* Soc. of Expl. Geophys.

Eiken, O., Brevik, I., Arts, R., Lindeberg, E., and Fagerviki, K. (2000). Seismic monitoring of CO_2 injected into a marine acquifer. In *70th Ann. Internat. Mtg.* Soc. of Expl. Geophys.

Eiken, O., Haugen, G., Schonewille, M., and Duijndam, A. (2003b). A proven method for acquiring highly repeatable towed streamer seismic data. *Geophysics*, 68(4):1303–1309.

Fabricius, I., Røgen, B., and Gommesen, L. (2007). How depositional texture and diagenesis control petrophysical and elastic properties of samples from five North Sea chalk fields. *Petroleum Geoscience*, 13(1):81–95.

Fehmers, G., Hunt, K., Brain, J., Bergler, S., Kaestner, U., Schutjens, P., and Burrell, R. (2007). Curlew D - Pushing the boundaries of 4D depletion signal in a gas condensate field, UK Central North Sea. In *69th Mtg.*, page P074, London, UK. Eur. Assn. Geosci. Eng.

Fjær, E., Holt, R., Horsrud, P., Raaen, A., and Risnes, R. (2008). *Petroleum related rock mechanics*, volume 53 of *Developments in petroleum science*. Elsevier, 2 edition.

Floricich, M. (2006). *An engineering-consistent approach for pressure and saturation estimation from time-lapse seismic data*. Ph.D., Heriot-Watt University.

Floricich, M., MacBeth, C., Stammeijer, J., Evans, A., and Dijksman, N. (2006a). Determination of a seismic and engineering consistent petro-elastic model for time-lapse seismic studies: Application to the Schiehallion Field. In *76th Ann. Internat. Mtg.* Soc. of Expl. Geophys.

Floricich, M., MacBeth, C., Stammeijer, J., Staples, R., Evans, A., and Dijksman, C. (2006b). A new technique for pressure - saturation separation from time-lapse seismic - Schiehallion case study. In *68th Mtg.*, page E017, Vienna, Austria. Eur. Assn. Geosci. Eng.

Floricich, M., MacBeth, C., and Staples, R. (2005). An engineering-driven approach for separating pressure and saturation using 4D seismic: application to a Jurassic reservoir in the UK North Sea. *SEG Technical Program Expanded Abstracts*, 24(1):2464–2467.

Furre, A., Bakken, E., and Nordby, L. (2005). Heidrun time-lapse 2001-2004: further improvement of reservoir understanding. In *67th Mtg.*, page P101, Stavanger, Norway. Eur. Assn. Geosci. Eng.

Furre, A., Munkvold, F., and Nordby, L. (2003). Improving reservoir understanding using time-lapse seismic at the Heidrun field. In *65th Mtg.*, page A20, Stavanger, Norway. Eur. Assn. Geosci. Eng.

Fyfe, A., Gregersen, U., Jordt, H., Rundberg, Y., Eidvin, T., Evans, D., Stewart, D., Hovland, M., and Andresen, P. (2003). Oligocene to Holocene. *The millennium atlas: Petroleum geology of the central and northern North Sea: The Geological Society (London)*, pages 279–287.

Gassmann, F. (1951a). Elastic waves through a packing of spheres. *Geophysics*, 16(04):673–685. Errata in GEO-17-2-0399 Errata in GEO-18-1-0269.

Gassmann, F. (1951b). Über die Elastizität poröser Medien. *Vierteljahresschrift der Naturforschenden Gesellschaft in Zürich*, 96:1–23.

Gauer, P., Sylte, J., and Nagel, N. (2002). Ekofisk Field Well Log Decompaction. In *SPE/ISRM Rock Mechanics Conference*.

Gilbert, F. and Backus, G. (1966). Propagator matrices in elastic wave and vibration problems. *Geophysics*, 31(2):326–332.

Goulty, N. (2003). Reservoir stress path during depletion of Norwegian chalk oilfields. *Petroleum Geoscience*, 9(3):233–241.

Guilbot, J. and Smith, B. (2002). 4-D constrained depth conversion for reservoir compaction estimation: Application to Ekofisk Field. *The Leading Edge*, 21(03):302–308.

Hall, S., MacBeth, C., Barkved, O., and Wild, P. (2005). Cross-matching with interpreted warping of 3D streamer and 3D ocean-bottom-cable data at Valhall for time-lapse assessment. *Geophys. Prosp.*, 53:283–297.

Hatchell, P. (2000). Fault whispers: Transmission distortions on prestack seismic reflection data. *Geophysics*, 65(02):377–389.

Hatchell, P. and Bourne, S. (2005). Rocks under strain: Strain-induced time-lapse time shifts are observed for depleting reservoirs. *The Leading Edge*, 24(12):1222–1225.

Hatchell, P., Kawar, R., and Savitski, A. (2005). Integrating 4D seismic, geomechanics and reservoir simulation in the Valhall oil field. In *67th Mtg.*, page C012, Madrid, Spain. Eur. Assn. Geosci. Eng.

Hawkins, K., Ben-Brahim, L., Howe, S., Tindle, C., Hollingworth, S., Taylor, N., Joffroy, G., Conroy, G., and Onaisi, A. (2007). Production-Induced Stresses from Timelapse Timeshifts - A Geomechanics Case Sstudy from the Franklin & Elgin Fields. In *69th Mtg.*, page D004, London, UK. Eur. Assn. Geosci. Eng.

Hermansen, H., Thomas, L., and Aasbøe, B. (1997). Twenty Five Years of Ekofisk Reservoir Management. In *SPE Annual Technical Conference*, number SPE 38927, pages 873–885.

Herwanger, J. (2008). R We There Yet? In *70th Mtg.*, page 1029, Rom, Italy. Eur. Assn. Geosci. Eng.

Hodgson, N., MacBeth, C., Duranti, L., Rickett, J., and Nihei, K. (2007). Inverting for reservoir pressure change using time-lapse time strain: Application to Genesis Field, Gulf of Mexico. *The Leading Edge*, 26:649–652.

Holhjem, A. (1998). Introduction - Why Redevelopment of Ekofisk. In *Offshore Technology Conference*, Houston, Texas.

Holt, R. and Fjær, E. (2003). Wave velocities in shales - A rock physics model. In *65th Mtg.*, pages C–13, Stavanger, Norway. Eur. Assn. Geosci. Eng.

Holt, R., Sønstebø, E., and Horsrud, P. (1996). Acoustic velocities of North Sea Shales. In *58th Mtg.*, page C027, Amsterdam, The Netherlands. Eur. Assn. Geosci. Eng.

Horsrud, P. (2001). Estimating Mechanical Properties of Shale from Empirical Correlations. *SPE Drilling & Completion*, 16(2):68–73.

Horsrud, P., Sønstebø, E., and Bøe, R. (1998). Mechanical and petrophysical properties of North Sea shales. *International Journal of Rock Mechanics and Mining Sciences*, 35(8):1009 – 1020.

Houbiers, M., Arntsen, B., Mispel, J., Hager, E., Brown, G., and Hill, D. (2008). Full Azimuth Seismic Modelling in the Norwegian Sea. In *78rd Ann. Internat. Mtg.* Soc. of Expl. Geophys.

Hudson, T., Regel, B., Bretches, J., Condon, P., Rickett, J., Cerney, B., and Inderwiesen, P. (2005). Genesis Field, Gulf of Mexico, 4-D project status and preliminary lookback. In *75rd Ann. Internat. Mtg.* Soc. of Expl. Geophys.

Janssen, A., Byerley, G., Ediriweera, K. K., Hope, T. A., Rasmussen, K. B., and Westeng, K. (2006a). Simulation-driven seismic modeling applied to the design of a reservoir surveillance system for Ekofisk Field. *The Leading Edge*, 25(9):1176–1185.

Janssen, A. L., Smith, B. A., and Byerley, G. W. (2006b). Measuring velocity sensitivity to production-induced strain at the Ekofisk Field using time-lapse time-shifts and compaction logs. *SEG Technical Program Expanded Abstracts*, 25(1):3200–3204.

Japsen, P., Bruun, A., Fabricius, I., Rasmussen, R., Vejbæk, O., Pedersen, J., Mavko, G., Mogensen, C., and Høier, C. (2004). Influence of porosity and pore fluid on acoustic properties of chalk: AVO response from oil, South Arne Field, North Sea. *Petroleum Geoscience*, 10(4):319–330(12).

Kelly, K. and Marfurt, K., editors (1990). *Numerical Modeling Of Seismic Wave Propagation*. Number 13 in Geophysical reprint series. Society of Exploration Geophysicists.

Kelly, K. R., Ward, R. W., Treitel, S., and Alford, R. M. (1976). Synthetic Seismograms: A Finite Difference Approach. *Geophysics*, 41(1):2–27.

Kennett, B. (1983). *Seismic wave propagation in stratified media*. Cambridge University Press.

Kennett, B. and Harding, A. (1985). Is ray theory adequate for reflection seismic modelling? (A survey of modelling methods). *First Break*, 3(1):9–14.

Kim, S. and Cook, R. (1999). 3-D traveltime computation using second-order ENO scheme. *Geophysics*, 64(6):1867–1876.

Klett, T. R. and Gautier, D. L. (2005). Reserve growth in oil fields of the North Sea. *Petroleum Geoscience*, 11:179–190(12).

Kommedal, J., Barkved, O., and Henneberg, K. (2005). Repeatability using a premanantely installed seismic array. In *67th Mtg.*, Madrid, Spain. Eur. Assn. Geosci. Eng.

Korneev, V., Goloshubin, G., Daley, T., and Silin, D. (2004). Seismic low-frequency effects in monitoring fluid-saturated reservoirs. *Geophysics*, 69(2):522–532.

Koster, K., Gabriels, P., Hartung, M., Verbeek, J., Deinum, G., and Staples, R. (2000). Time-lapse seismic surveys in the North Sea and their business impact. *The Leading Edge*, 19(03):286–293.

Kragh, E. and Christie, P. (2002). Seismic repeatability, normalized rms, and predictability. *The Leading Edge*, 21(7):640–647.

Krebes, E. (2004). Seismic Forward Modeling. *CSEG Recorder*, pages 28–39.

Kristiansen, P., Christie, P., Bouska, J., O'Donovan, A., Westwater, P., and Thorogood, E. (2000). Foinaven 4D: Processing and analysis of two designer 4Ds. *SEG Technical Program Expanded Abstracts*, 19(1):1456–1459.

Kvalheim, A., Sandrø, I., Skogland, S., Vinje, V., and Carpenter, M. (2007). Impact of time and depth imaging methods on quantitative 4D reservoir management. In *69th Mtg.*, page H017, London, UK. Eur. Assn. Geosci. Eng.

Landrø, M. (1999a). Discrimination between pressure and fluid saturation changes from time lapse seismic data. *SEG Technical Program Expanded Abstracts*, 18(1):1651–1654.

Landrø, M. (1999b). Repeatability issues of 3-D VSP data. *Geophysics*, 64(6):1673–1679.

Landrø, M. (2001). Discrimination between pressure and fluid saturation changes from time-lapse seismic data. *Geophysics*, 66(3):836–844.

Landrø, M., Solheim, O., Hilde, E., Ekren, B., and Strønen, L. (1999). The Gullfaks 4D seismic study. *Petroleum Geoscience*, 5:213–226.

Landrø, M. and Stammeijer, J. (2004). Quantitative estimation of compaction and velocity changes using 4D impedance and traveltime changes. *Geophysics*, 69(4):949–957.

Liu, E., Crampin, S., and Hudson, J. A. (1997). Diffraction of seismic waves by cracks with application to hydraulic fracturing. *Geophysics*, 62(1):253–265.

Lonergan, L. and Cartwright, J. A. (1999). Polygonal faults and their influence on deep-water sandstone reservoir geometries, Alba Field, United Kingdom central North Sea. *AAPG Bulletin*, 83(3):410–432.

Lumley, D., Meadows, M., Cole, S., and Adams, D. (2003). Estimation of reservoir pressure and saturations by crossplot inversion of 4D seismic attributes. In *73rd Ann. Internat. Mtg.*, pages 1513–1516. Soc. of Expl. Geophys.

Lysmer, J. and Drake, L. (1972). A finite element method for seismology. *Methods in Computational Physics*, 11:181–216.

MacBeth, C., Floricich, M., and Soldo, J. (2006). Going quantitative with 4D seismic analysis. *Geophys. Prosp.*, 54:303–317.

MacBeth, C., Stephen, K., and McInally, A. (2005). The 4D seismic signature of oil-water contact movement due to natural production in a stacked turbidite reservoir. *Geophys. Prosp.*, 53:183–203.

Magesan, M., Depagne, S., Nixon, K., Regel, B., Opich, J., Rogers, G., and Hudson, T. (2005). Seismic processing for time-lapse study: Genesis field, Gulf of Mexico. *The Leading Edge*, 24(4):364–373.

Malme, T., Landrø, M., and Mittet, R. (2005). Overburden distortions - implications for seismic AVO analysis and time-lapse seismic. *J. Geophys. Eng.*, 2:81–89.

Manafov, R., Holt, R., and Fjær, E. (2007). Temperature Sensitivity of Wave Velocities in Shales. In *69th Mtg.*, page F030, London. Eur. Assn. Geosci. Eng.

Mavko, G., Mukerji, T., and Dvorkin, J. (2009). *The rock physics handbook*. Cambridge Univ. Press.

McInally, A., Redondo-López, T., Garnham, J., Kunka, J., Brooks, D., Stenstrup-Hansen, L., Barclay, F., and Davies, D. (2003). Optimizing 4D fluid imaging. *Petroleum Geoscience*, 9:91–101.

Menghini, M. (1989). Compaction Monitoring in the Ekofisk Area Chalk Fields. *Journal of Petroleum Technology*, 41(7):735–739.

Misaghi, A., Landrø, M., and Petersen, S. (2007). Overburden complexity and repeatability of seismic data: Impacts of positioning errors at the Oseberg field, North Sea. *Geophys. Prosp.*, 55:365–379.

Morice, S., Svendsen, M., Larsen, I., and Kristiansen, P. (2000). 4D-Ready Towed-Streamer Data and the Foinaven Benchmark. In *SPE Annual Technical Conference and Exhibition*, pages 63136–MS. SPE.

Muniz, E., da Fontoura, S., and Soares, A. (2005). CU Triaxial Tests on North Sea Shale. In *40th Symposium on Rock Mechanics (USRMS)*, pages ARMA/USRMS 05–814.

Naess, O. (2007). The Relationship between Geometrical Repeatability and Seismic Trace Repeatability in 4D. In *69th Mtg.*, page P066, London, UK. Eur. Assn. Geosci. Eng.

Olden, P., Corbett, P., Westerman, R., Somerville, J., Smart, B., and Koutsabeloulis, N. (2001). Modeling combined fluid and stress change effects in the seismic response of a producing hydrocarbon reservoir. *The Leading Edge*, 20(10):1154–1163.

Østmo, S., Furre, A.-K., Hansen, O. R., Eiken, O., and El Ouair, Y. (2007). Assessment of time-lapse seismic repeatability using repeated test lines at the Kristin field. *SEG Technical Program Expanded Abstracts*, 26(1):2924–2928.

Porter, M., Sprague, A., Sullivan, M., Jennette, D., Beaubouef, R., Garfield, T., Rossen, C., Sickafoose, D., Jensen, G., Friedmann, S., and Mohring, D. (2006). Stratigraphic Organization and Predictability of Mixed Coarse-and Fine-grained Lithofacies Successions in a Lower Miocene Deep-water Slope-channel System, Angola Block 15. *AAPG Memoir / SEPM Special Publication*, 88:281.

Reeckmann, S., Wilkin, D., and Flannery, J. (2003). Kizomba, a Deep-Water Giant Field, Block 15 Angola. *Giant Oil and Gas Fields of the Decade, 1990-1999*, 78:227–236.

Renoux, E. and Lacombe, C. (2005). Effect of Navigation Attributes on 4D Seismic Repeatability. In *67th Mtg.*, page C014, Madrid, Spain. Eur. Assn. Geosci. Eng.

Rhett, D. (1998). Ekofisk revisited: a new model of Ekofisk reservoir geomechanical behavior. *SPE/ISRM Rock Mechanics in Petroleum Engineering*, pages 367–375.

Rickett, J., Duranti, L., Hudson, T., Regel, B., and Hodgson, N. (2007). 4D time strain and the seismic signature of geomechanical compaction at Genesis. *The Leading Edge*, 26:644–647.

Rickett, J. and Lumley, D. (2001). Cross-equalization data processing for time-lapse seismic reservoir monitoring: A case study from the Gulf of Mexico. *Geophysics*, 66(4):1015–1025.

Ritchie, B., Macgregor, A., Strudley, A., and Goto, R. (2002). The impact of new 4D seismic technology on the Magnus Field. In *64th Mtg.*, page A20, Florence, Italy. Eur. Assn. Geosci. Eng.

Ross, C., Cunningham, G., and Weber, D. (1996). Inside the crossequalization black box. *The Leading Edge*, 15(11):1233–1240.

Røste, T., Stovas, A., and Landrø, M. (2005). Estimation of layer thickness and velocity changes using 4D prestack seismic data. In *67th Mtg.*, page C010, Madrid, Spain. Eur. Assn. Geosci. Eng.

Schiøtt, C., Bertrand-Biran, V., Hansen, H., Koutsabeloulis, N., and Westeng, K. (2008). Time-lapse inversion and geomechanical modelling of the South Arne field. *First Break*, 26:85–91.

Schutjens, P. (2005). Reservoir Monitoring With Seismic Timeshifts: Geomechanical Modeling For Its Application in Stacked Pay. In *International Petroleum Technology Conference*, page IPTC 10511.

Sheriff, R. and Geldart, L. (1995). *Exploration seismology*. Cambridge Univ. Press Cambridge.

Sigit, R., Morse, P., and Kimber, K. (1999). 4-D seismic that works: A successful large scale application, Duri Steamflood, Sumatra, Indonesia. In *69th Ann. Internat. Mtg.*, pages 2055–2058. Soc. of Expl. Geophys.

Smit, F., Brain, J., and Watt, K. (2005). Repeatability monitoring during marine 4D streamer acquisition. In *67th Mtg.*, page C015, Madrid, Spain. Eur. Assn. Geosci. Eng.

Smith, B., Sylte, J., Clausen, C., and Guilbot, J. (2002). Ekofisk 4D Seismic-Influence on Flow Simulation and Compaction Modeling. In *Offshore Technology Conference*.

Spetzler, J. and Øyvind, K. (2006). Discrimination between phase and amplitude attributes in time-lapse seismic streamer data. *Geophysics*, 71(4):9–19.

Staples, R., Cook, A., Braisby, J., Hodgson, B., and Mabillard, A. (2006a). Integration of 4D seismic data and the dynamic reservoir model reveal new targets in Gannet C. *The Leading Edge*, 25(9):1126–1133.

Staples, R., Ita, J., Nash, R., Hague, P., and Burrell, R. (2007). Using 4D Seismic Data and Geomechanical Modelling to Understand Pressure Depletion in HPHT Fields of the Central North Sea. In *69th Mtg.*, page A025, London, UK. Eur. Assn. Geosci. Eng.

Staples, R., Stammeijer, J., Jones, S., Brain, J., Smit, F., and Hatchell, P. (2006b). Time-Lapse (4D) Seismic Monitoring - Expanding Applications. In *CSPG-CSEG-CWLS Convention*, pages 181–189.

Sulak, R. and Danielsen, J. (1989). Reservoir aspects of Ekofisk subsidence. *Journal of Petroleum Technology*, 41(7):709–716.

Sylte, J., Thomas, L., Rhett, D., Bruning, D., and Nagel, N. (1999). Water induced compaction in the Ekofisk field. In *SPE Annual Technical Conference and Exhibition*, number 18278, Houston.

Tang, M., Ross, R., and Walker, R. (2007). Lessons through time in 4D seismic. *first break*, 25:79–86.

Taylor, N., Ben-Brahim, L., Tindle, C., Joffroy, G., Hubans, C., and Onaisi, A. (2007). Elgin-Franklin 4D seismic - Encouraging results for reservoir monitoring & developement planning. In *69th Mtg.*, page A026, London, UK. Eur. Assn. Geosci. Eng.

Theune, U., Schmitt, D., and Rokosh, D. (2003). Feasibility study of time-lapse seismic monitoring for heavy oil reservoir development - The rock-physical basis. In *73rd Ann. Internat. Mtg.*, pages 1418–1421. Soc. of Expl. Geophys.

Tura, A., Barker, T., Cattermole, P., Collins, C., Davis, J., Hatchell, P., Koster, K., Schutjens, P., and Wills, P. (2005). Monitoring primary depletion reservoirs using amplitudes and time shifts from high-repeat seismic surveys. *The Leading Edge*, 24(12):1214–1221.

van Gestel, J.-P., Kommedal, J. H., Barkved, O. I., Mundal, I., Bakke, R., and Best, K. D. (2008). Continuous seismic surveillance of Valhall Field. *The Leading Edge*, 27(12):1616–1621.

Vidale, J. E. (1990). Finite-difference calculation of traveltimes in three dimensions. *Geophysics*, 55(5):521–526.

Vinje, V., Iversen, E., Åstebøl, K., and Gjøystdal, H. (1996a). Estimation of multivalued arrivals in 3D models using wavefront construction – Part I. *Geophys. Prosp.*, 44:819–842.

Vinje, V., Iversen, E., Åstebøl, K., and Gjøystdal, H. (1996b). Part II: Tracing and Interpolation. *Geophys. Prosp.*, 44:843–858.

Vinje, V., Iversen, E., and Gjoystal, H. (1993). Traveltime and amplitude estimation using wavefront construction. *Geophysics*, 58(08):1157–1166.

Wapenaar, C. and Berkhout, A. (1989). *Elastic wave field extrapolation: redatuming of single-and multi-component seismic data*. Elsevier.

Whyatt, M., Bowen, J., and Rhodes, D. (1992). The Nelson Field: a successful application of a developement geoseismic model in North Sea exploration. In Hardman, R., editor, *Exploration Britain: Geological insights for the next decade*, Special Publication 67, pages 283–305. Geological Society, London.

Wingfield, R. (1990). The origin of major incisions within the Pleistocene deposits of the North Sea. *Marine Geology*, 91(1-2):31–52.

Yudovich, A., Chin, L., and Morgan, D. (1989). Casing Deformation in Ekofisk. *Journal of Petroleum Technology*, 41(7):729–734.

Zoeppritz, K. (1919). Über Reflexion und Durchgang seismischer Wellen durch Unstetigkeitsflächen. *Nachrichten der Königlichen Gesellschaft der Wissenschaften zu Göttingen*, Mathematisch-Physikalische Klasse:66–84.